

# Capillary Effects on Fluid Transport in Granular Media

ZHONGZHENG WANG

B.Eng (Hons)



THE UNIVERSITY OF  
**SYDNEY**

Supervisors: Yixiang Gan, Jean-Michel Pereira  
Associate Supervisor: Kapil Chauhan

A thesis submitted in fulfilment of  
the requirements for the degree of  
Doctor of Philosophy

School of Civil Engineering  
Faculty of Engineering  
The University of Sydney  
Australia

8 August 2021

## **Statement of Originality**

This is to certify that to the best of my knowledge, the content of this thesis is my own work. This thesis has not been submitted for any degree or other purposes.

I certify that the intellectual content of this thesis is the product of my own work and that all the assistance received in preparing this thesis and sources have been acknowledged.

[REDACTION]

Zhongzheng Wang 08/08/2021

## **Abstract**

Fluid transport phenomena in granular media are of great importance due to various natural and industrial applications, including CO<sub>2</sub> sequestration, enhanced oil recovery, remediation of contamination, and water infiltration into soil. Although numerous studies exist in the literature with aims to understand how fluid properties and flow conditions impact the transport process, some key mechanisms at microscale are often not considered due to simplifications of physical phenomenon and geometry, limited computational resources, or limited temporal/spacial resolution of existing imaging techniques.

In this Thesis, we investigate fluid transport phenomena in granular media with a focus on the capillary effects. We move from relatively simple scenario on patterned surfaces to more complex granular media, tackling a variety of liquid-transport related problems that all have extensive industrial applications. The bulk of this Thesis is composed of six published papers. Each chapter is prefaced by an introductory section presenting the motivation for the corresponding paper and its context within the greater body of work.

In order to explain the characteristics of fluid transport in porous media observed at macroscopic scale, physical mechanisms at micro and pore scale must be understood. When liquid comes into contact with rough grains with irregular shapes, depending on surface feature and liquid properties, the liquid may progressively fill the grooves of the surface, or get pinned at sharp corners, which consequently results in deviation of the effective contact angle from the intrinsic one. These phenomena occurring at nano/micro-scale are captured and incorporated into the pore-network model and lattice Boltzmann method to investigate multiphase displacement process. At pore scale, by considering different invasion instability modes, we study the collective impact of contact angles and pore geometry by numerical simulation, unifying the effects of wettability and topological disorder of porous media. At macroscopic scale, the influence of capillary forces from liquid bridges on the packing structure of wet granular assembly is experimentally studied. A model is proposed based on

energy balance to predict the resulting packing fraction, which is validated by results from experiments and past literature. Finally, drying experiments are conducted to investigate the evolution of liquid distribution and solid structure during evaporation process.

This Thesis reveals the impact of some previously neglected physical phenomena at microscale on the fluid transport in granular materials, providing new insights and methodology for describing and modelling fluid transport process in porous media.

## List of Publication

Journal articles:

[1] Wang, Z., Owais, A., Neto, C., Pereira, J.-M., Gan, Y. (2021). Enhancing Spontaneous Droplet Motion on Structured Surfaces with Tailored Wedge Design. *Adv. Mater. Interfaces*, 8, 2000520. **(Chapter 3)**

[2] Wang, Z., Pereira, J.-M., & Gan, Y. (2021). Effect of grain shape on quasi-static fluid-fluid displacement in porous media. *Water Resources Research*, 57, e2020WR029415. **(Chapter 4)**

[3] Wang, Z., Chauhan, K., Pereira, J.-M., & Gan, Y. (2019). Disorder characterization of porous media and its effect on fluid displacement. *Physical Review Fluids*, 4(3), 034305. **(Chapter 5)**

[4] Wang, Z., Pereira, J.-M., & Gan, Y. (2020). Effect of wetting transition during multiphase displacement in porous media. *Langmuir*, 36(9), 2449–2458. **(Chapter 5)**

[5] Wang, Z., Pereira, J.-M., & Gan, Y. (2021). Packing of wet monodisperse spheres. *Powder Technology*, 378, 60–64. **(Chapter 6)**

[6] Wang, Z., Maillet, B., Pereira, J.-M., & Gan, Y. (2021). Towards the end of drying of granular materials: Enhanced evaporation and drying-induced collapse. *Water Resources Research*, 57, e2021WR030125. **(Chapter 6)**

[7] Shi, Z., Wang, Z., & Gan, Y. (2021). Effects of topological disorder in unsaturated granular media via a pore-scale lattice Boltzmann investigation. *Advances in Water Resources*, 149, 103855.

[8] Wei, D., Wang, Z., Pereira, J.-M., & Gan, Y. (2021). Permeability of uniformly graded 3d printed granular media. *Geophysical Research Letters*, 48(5).

## Conference presentations

- (1) “Multiphase Displacement in Disordered Porous Media: An Investigation Using the Multi-component Lattice Boltzmann Method”. The 10th International Conference on Computational Methods. 2019
- (2) “Fluid-fluid Displacement in Rough Granular Media: Effect of Wetting Transition”. InterPore2020.
- (3) “Effect of grain shape on quasi-static fluid-fluid displacement in porous media”. InterPore2021.

## **Acknowledgements**

Firstly, I would like to take this opportunity to express my sincere gratitude to my supervisor, A/Professor Yixiang Gan, for his support, advice, and patience. Actually, much of my motivation for pursuing a PhD originates from the amazing experience of conducting research activities under his supervision during my undergraduate study. I have learnt a great deal from Yixiang, which helped shape not only my view on academics but on life in general.

I would also like to thank my supervisor, Professor Jean-Michel Pereira, who provided insightful suggestions, discussions, and extensive assistance arranging experiments for my research. I feel very fortunate to have received tremendous support from Jean-Michel, making my stay in France a wonderful experience.

In addition, the valuable suggestions and discussion on my research from Dr. Kapil Chauhan and Professor Chiara Neto are deeply appreciated. I also enjoyed the collaborations with Dr. Benjamin Maillet, Dr. Deheng Wei, Dr Zhang Shi, Dr. Ahmed Owais on a variety of projects, from whom I have learnt many things. Further, I want to thank the technical team at Navier Laboratory in France, including Mr. Emmanuel De Laure, Mr. Baptiste Chabot, Mr. Xavier Boulay, and Mr. Loïc Lesueur, for their support and assistance on my experiments. I acknowledge the fruitful discussions with many of my colleagues, including Dr. Si Suo, Mr. Yanyao Bao, Ms. Zi Ying, and Mr. Xu Wang.

Finally, I would like to thank my family for their unconditional love, support, and encouragement throughout my life. I also want to thank all health workers, including doctors and nurses, who are the frontliners for the battle against Covid-19.

## Contents

<b>Statement of Originality</b>	<b>ii</b>
<b>Abstract</b>	<b>iii</b>
<b>List of Publication</b>	<b>v</b>
<b>Acknowledgements</b>	<b>vii</b>
<b>Contents</b>	<b>viii</b>
<b>Chapter 1 Introduction</b>	<b>1</b>
<b>Chapter 2 Literature Review</b>	<b>5</b>
2.1 Wetting on Rough Surfaces .....	5
2.2 Sharp Edge Pinning .....	8
2.3 Liquid Bridges in Granular Materials .....	10
2.4 Multiphase Flow in Porous media .....	12
2.5 Numerical Modelling .....	13
2.5.1 Lattice Boltzmann Method .....	14
2.5.2 Pore-Network Models .....	17
2.6 Summary .....	18
<b>Chapter 3 Spontaneous Droplet Motion on Structured Surfaces</b>	<b>20</b>
<b>Chapter 4 Effect of Grain Shape on Quasi-Static Fluid-Fluid Displacement</b>	<b>29</b>
<b>Chapter 5 Multiphase Flow modified by Wettability and Disorder</b>	<b>41</b>
5.1 Effect of Wetting Transition during Fluid Displacement Process .....	42
5.2 Disorder Characterization and its Effects on Fluid Displacement .....	53
5.3 Summary .....	67



<b>Chapter 6 Packing and Drying of Unsaturated Granular Material</b>	<b>68</b>
6.1 Packing of Wet Spheres .....	69
6.2 Drying of Loosely Packed Wet Granular Materials .....	75
6.3 Summary .....	90
<b>Chapter 7 Conclusions and Future Work</b>	<b>91</b>
<b>Bibliography</b>	<b>95</b>

## CHAPTER 1

### **Introduction**

---

Due to molecular attraction, the interface between different fluids has the tendency of minimizing its surface area, which is the phenomenon of surface tension. As a result, there exists a pressure difference across the interface between the two fluids, which can consequently impact how fluids and the surrounding solid matrix behave. Water striders (*Gerridae*) “walking” on water, spontaneous rise of liquid in narrow tubes, and droplet freely sliding on the surface of lotus leaf, are all manifestation of capillary forces. Particularly, the effect of capillary forces can be increasingly significant when the length scale becomes small, such as in subsurface granular materials and fibrous porous medium within fuel cells. Clearly, understanding the capillary effect on fluid transport is of paramount importance due to its involvement in various natural and industrial processes, such as enhanced oil recovery, carbon dioxide sequestration, fuel cell design, and water infiltration into soils (Blunt et al., 1993; Nadim et al., 2000; Lipiec et al., 2006; Szulczewski et al., 2012; Lake et al., 2014; Matter et al., 2016).

Despite extensive investigations on the impact of fluid properties and flow conditions on multiphase flow exist in the literature, some challenges remain. Firstly, physical mechanisms at the scale of grain surface due to presence of roughness and sharp corners are often neglected in theoretical analyses and numerical simulations, such as the phenomena of Cassie-Wenzel wetting transition and pinning of menisci at sharp edges. This leads to inaccurate capture of transient effective contact angles during fluid-fluid displacement process, where the effective contact angle has already been identified as one of the key controlling parameters determining the displacement patterns of multiphase flow. Secondly, the influence of topological features of pore space on fluid invasion process, compared with fluid properties and flow conditions, has received much less attention. For example, both the characterisation and impact of

topological disorder of porous media on fluid displacement remain relatively unexplored. Further, the combined influence of liquid and experimental procedure on the packing structure of wet granular materials, as well as the subsequent drying process, require further studies. In this Thesis, we investigate these problems using experimental and numerical methods, aiming to bridge the connection between observations at macroscopic scale and physical mechanisms at surface and grain scale. The research objectives are listed below:

- Understand the effect of disorder, particle shape, and surface roughness on fluid-fluid displacement process in porous media. (Chapter 4 & Chapter 5)
- Develop rigorous pore-network model that can be applied to porous media with grains of different shapes. (Chapter 4)
- Probe the factors that controls the spontaneous droplet movement on structured surfaces and explore the different shapes for enhancing the motion. (Chapter 3)
- Seek a universal law for description of the packing of wet granular materials for different particle sizes and free fall heights, and investigate the subsequent drying processes. (Chapter 6)

The Literature Review (Chapter 2) starts with the theories and experiments on the wetting behaviour of liquid on rough surfaces. Then, the phenomenon of contact line pinning at sharp edges is discussed, and its relevant natural and industrial applications are reviewed. This is followed by moving into more complex systems, i.e., porous media, where the focus is placed on the mutual influence of fluids and solids: how liquid affects the structure and mechanical response of solid matrix; and how topological features and physical properties of solids impact fluid transport. Finally, we touch on some state-of-the-art numerical modelling methods that have been employed to study the transport phenomena in porous media.

In Chapter 3, we begin with a relatively simple system: a water droplet on a surface. It is demonstrated that with a careful design of the substrate structure, the spontaneous directional movement of a droplet can be achieved. This is done by creating a free energy gradient on the surface through utilizing the sharp edge pinning phenomenon, which can drive the droplet without external energy input. We further investigate how the motion can be enhanced using an

experimentally validated model, providing insights in surface structure design for optimizing droplet transport, which has many engineering applications including fog harvesting, water-oil separation, and microfluidic devices (Bai et al., 2010; Zheng et al., 2010; Li et al., 2013; Bai et al., 2014; Cao et al., 2014; Zamuruyev et al., 2014; Tani et al., 2015; Wang et al., 2015; Zhu et al., 2016; Al-Khayat et al., 2017; Li et al., 2017; Morrissette et al., 2017; Tian et al., 2017; Zhao et al., 2017; Luo et al., 2018; Si et al., 2018).

In Chapter 4, an extended pore-network model is developed to probe the effect of particle shapes on quasi-static fluid-fluid displacement processes in porous media. By incorporating the aforementioned sharp edge pinning effect into the model, we are able to carry out efficient numerical simulations under a wide range of wetting conditions and different particle shapes, and demonstrate the profound influence of particle shapes through analysing several key characteristic metrics during the multiphase displacement process. The proposed algorithm significantly extends the capability of this type of pore-network methods, i.e., the interface tracking algorithms, that were previously only applied to spherical grains (Cieplak et al., 1988, 1990).

Chapter 5 consists of two sections studying multiphase flows both using the multi-component lattice Boltzmann method (Shan et al., 1993, 1995; Kruger et al., 2017). In the first part, based on existing experimental observations, a theory describing the time-dependent contact angle due to Cassie-Wenzel wetting transition on rough surfaces is proposed, which is then incorporated into the lattice Boltzmann method for simulations of fluid-fluid displacement processes. The effect of wetting transition is highlighted through comparing displacement efficiency and mobilisation of trapped ganglia under different characteristic time of wetting transition. The second part focuses on the role of topology. Specifically, a disorder index is proposed to quantitatively characterise the topological disorder of the porous media. A phase diagram of invasion morphology under different disorders and wetting conditions is obtained by systematic simulations. Through analysing the instability modes at pore scale, the effects of wettability and topological disorder on multiphase flow is unified.

In Chapter 6, we move to diffusive mass transport in porous media. We firstly present a simple experimental method for generation of wet granular materials with desired packing

fraction. Through considering the relative importance of gravitational and capillary forces, from an energy perspective, a model is derived to predict the final packing fraction given material properties and packing condition, which is verified by experimental results. Using the proposed sample preparation method, we then study the drying process of un-saturated granular materials with a low initial water content, which is relatively unexplored in the literature. Using various experimental tools, including high-resolution camera, analytical balance, and nuclear magnetic resonance technique, the evolution of solid structure and also the liquid distribution during evaporation process is captured. We observe the drying-induced collapse of granular materials, and the statistics of these collapse events provide insights on the role of Kelvin effect near the end of evaporation process, which explains the observed enhancement in drying rate, deviating from the classical theory of diffusion limited evaporation (Brutsaert et al., 1995; Shokri et al., 2011).

The last Chapter provides several concluding remarks on this Thesis, including discussions on the challenging questions remaining in the field and potential future works.

## CHAPTER 2

### Literature Review

---

This Chapter begins with looking at theories and experiments of wetting behaviour of liquid on surfaces with roughness features or sharp edges, and their relevant natural and industrial applications are reviewed. This is followed by moving into more complex systems, i.e., porous media, where the effects of capillary forces due to liquid bridges on the mechanical behaviour of granular materials are reviewed. Then, the current understanding of influence of fluid properties and flow conditions on fluid-fluid displacement process is discussed. Finally, we touch on some numerical modelling methods, with focus on the pore-network models and the lattice Boltzmann method, that have been employed to study the transport phenomena in porous media.

#### 2.1 Wetting on Rough Surfaces

The wetting phenomenon, occurring when a liquid being in contact with a solid surface, is ubiquitous in nature and industrial applications. The wetting behaviour is governed by the surface energies between different phases. On a chemically homogeneous smooth surface, in the case of complete wetting, i.e., the spreading parameter  $S = \gamma_{SG} - (\gamma_{SL} + \gamma_{LG}) > 0$ , where  $\gamma_{SG}$ ,  $\gamma_{SL}$ , and  $\gamma_{LG}$  denote the interfacial tension between solid-gas, solid-liquid, and liquid-gas phases, respectively, the liquid wets the surface completely. Note that the interfacial tension between liquid and gas phases is more commonly known as “surface tension”. When  $S < 0$ , however, the contact angle  $\theta$ , defined as the angle measured within the liquid phase at the liquid-solid-gas contact line (“triple line”) is described by the Young’s equation:

$$\cos \theta = \frac{\gamma_{SG} - \gamma_{SL}}{\gamma_{LG}}, \quad (2.1)$$

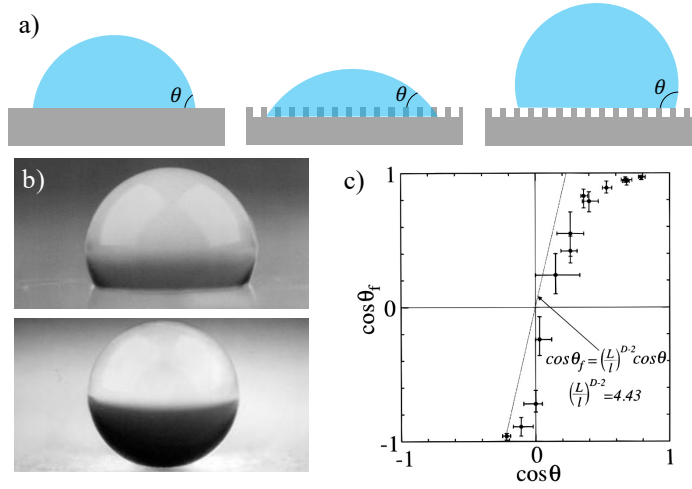


FIGURE 2.1: Wetting on rough surfaces. (a) Schematic of a droplet on a solid substrate. From left to right: partial wetting on an ideal smooth surface, Wenzel state on rough surface, and Cassie-Baxter state on rough surface. (b) The apparent contact angle becomes greater on rough surfaces (bottom) than the one on smooth surface (top), adapted from (Onda et al., 1996). (c) Apparent contact angle on fractal rough surface  $\theta_f$  vs intrinsic contact angle  $\theta$ , adapted from (Onda et al., 1996).

which can be easily derived by applying force balance at the triple line. This angle measured on an ideal smooth surface is also called the intrinsic contact angle  $\theta_0$ . When roughness is present on the solid surface, the apparent contact angle may deviate from the intrinsic one, depending on the surface features and wetting state (Fig. 2.1(a)). If the liquid completely fills the grooves of the surface, i.e., in Wenzel state, the apparent contact angle can be calculated as (Wenzel, 1936):

$$\cos \theta = r \cos \theta_0, \quad (2.2)$$

with  $r$  the roughness ratio, defined as the total area divided by the projected area of the rough surface. Since  $r \geq 1$ , Eqn. (2.2) indicates that the wettability is always enhanced with the presence of roughness, i.e., more hydrophobic (hydrophilic) for intrinsically hydrophobic (hydrophilic) wetting conditions. As shown in Fig. 2.1(b), the surface becomes super-hydrophobic for rough surface (bottom photo), compared with the smooth one (top photo). Fig. 2.1(c) shows the theoretical and experimental results of contact angles on fractal rough surfaces (Onda et al., 1996; Shibuichi et al., 1996). If, however, air is trapped between solid-liquid interface, the apparent contact angle is determined by Cassie-Baxter equation

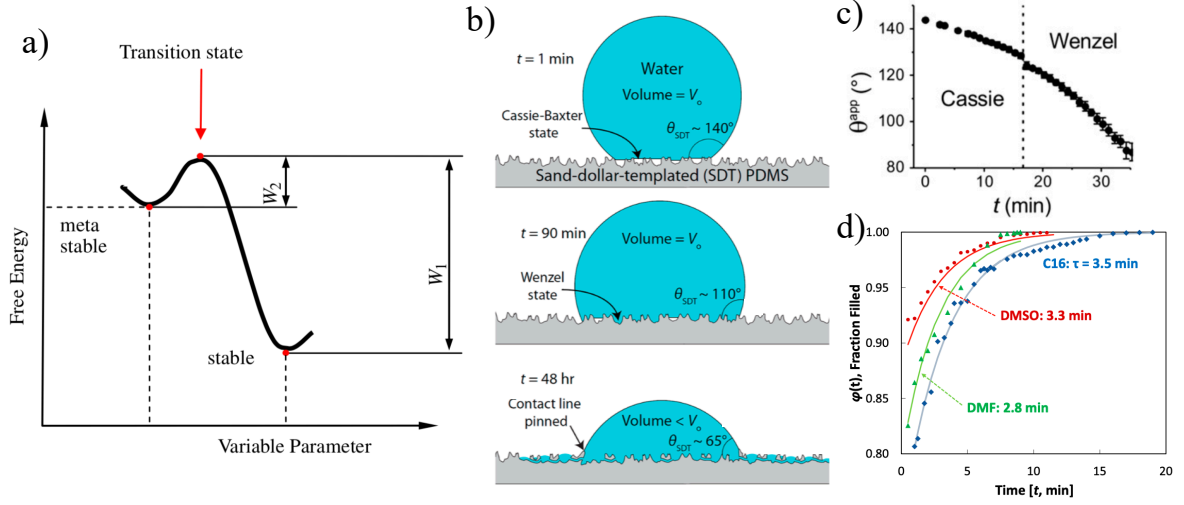


FIGURE 2.2: Cassie-Wenzel wetting transition. (a) Schematic showing the energy barrier that needs to be overcome to transition from meta-stable Cassie-Baxter wetting state to Wenzel state, adapted from (Bormashenko, 2015) (b) The progress of wetting transition on rough PDMS is accompanied by significant variation in apparent contact angle, adapted from (Mishra et al., 2016). (c) Evolution of apparent contact angle of droplet on structured surface with micro-pillars, adapted from (Papadopoulos et al., 2013). (d) Effect of volatility on the time-dependent cavity-filling rate, adapted from (Seo et al., 2018).

(Cassie et al., 1944; Marmur, 2003; He et al., 2004):

$$\cos \theta = r\phi \cos \theta_0 + 1 - \phi, \quad (2.3)$$

with  $\phi \in [0, 1]$  the fraction of projected solid-liquid contact area. Note that with  $\phi = 1$ , Eqn. (2.3) reduces to Eqn. (2.2). Efforts have been devoted to investigate the factors that determine which wetting state will take place, including the intrinsic wettability of the surface and surface roughness features (Feng et al., 2008; Bormashenko, 2015; Cho et al., 2020).

Further, the transition of wetting state from Cassie-Baxter to Wenzel state has been subjected to extensive investigations through both numerical and experimental methods (Moulinet et al., 2007; Sbragaglia et al., 2007; Zhao, 2007; Peters et al., 2009; Oliveira et al., 2011; Lopes et al., 2013; Papadopoulos et al., 2013; Mishra et al., 2016; Seo et al., 2018). From an energy perspective, there exists an energy barrier that needs to be overcome for the transition to take place (Fig. 2.2(a)), and the magnitude of the energy barrier is found to depend on geometry



of micro-structures (Yoshimitsu et al., 2002; Nosonovsky, 2007; Nosonovsky et al., 2008; Bahadur et al., 2009; Amabili et al., 2016; Domingues et al., 2017; Arunachalam et al., 2019), intrinsic contact angle (Seo et al., 2018), size of surface features (Butt et al., 2015), hydrodynamic pressure (Zheng et al., 2005), line tension (Bormashenko et al., 2013), and concentration of dissolved air in water (Seo et al., 2018). Greater energy barrier corresponds to increasing stability of Cassie-Baxter state, resulting in slower transition to Wenzel state. The speed of wetting transition can vary dramatically, depending on the aforementioned factors and also the liquid properties, such as interfacial tension and viscosity (Moulinet et al., 2007; Sbragaglia et al., 2007; Peters et al., 2009; Seo et al., 2018). As a result, the macroscopic contact angle can vary in a time-dependent manner (Fig. 2.2(b,c)), such as the experimental observations on rough PDMS plates by Mishra et al (Mishra et al., 2016). Seo et al (Seo et al., 2018) identified factors affecting the transition speed using bright-field and confocal fluorescence microscopy. Understanding the wetting behaviour on rough surfaces is of great importance in surface science due to its various practical applications such as product design (Wang et al., 2020a). Further, since for most natural grains, the surface is not perfectly smooth and surface roughness is often present, understanding the influence of surface roughness on the multiphase displacement process in porous media has been gaining increasing amount of focus in recent years (Babadagli et al., 2015; Hu et al., 2019b; Ju et al., 2019; Mehmani et al., 2019; Tanino et al., 2020; Liu et al., 2021; Zhang et al., 2021). In Chapter 5, the impact of Cassie-Wenzel wetting transition on multiphase flow in porous media will be investigated using the multi-component lattice Boltzmann method. Focus is placed on how the time-dependent effective contact angle (as a result of wetting transition) can modify the displacement processes.

## **2.2 Sharp Edge Pinning**

Due to inhomogeneity of surfaces, the triple line can be pinned at a specific location while undergoing motion. This pinning phenomenon can be attributed to several potential reasons, including variation in (i) chemical composition of the surface (leading to increase in intrinsic contact angle as per Eqn. (2.1)) (Alheshibri et al., 2013); (ii) surface roughness (leading to

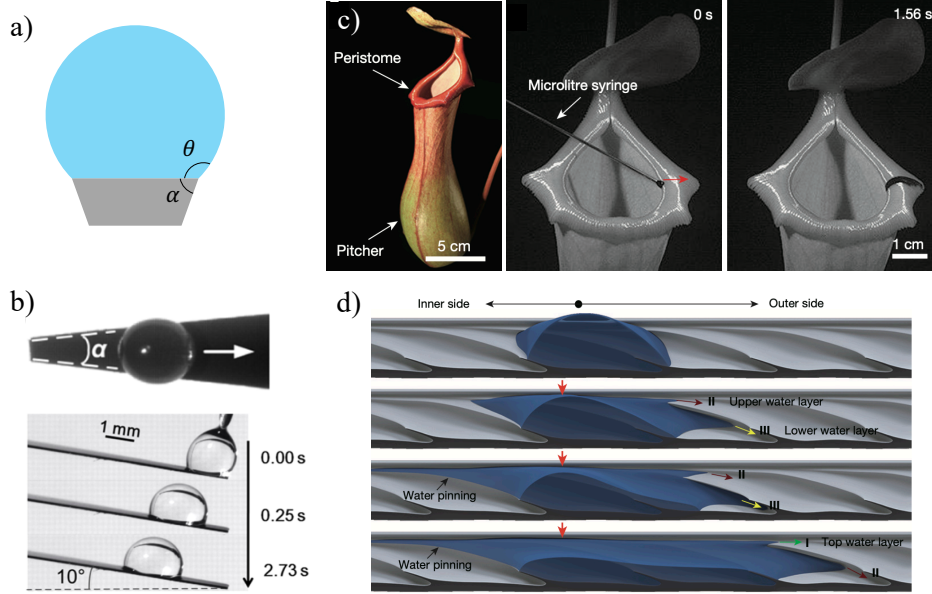


FIGURE 2.3: Sharp edge pinning phenomenon. (a) Schematic showing the pinning of the triple contact line at the sharp corner. (b) Spontaneous directional movement of droplet utilising the sharp edge pinning effect. Motion towards the anti-gravitational direction is achieved without external energy input, adapted from (Zheng et al., 2017). (c) and (d) Photos and schematic showing the mechanisms of continuous unidirectional spreading of liquid on the rim of the pitcher of *Nepenthes alata*, adapted from (Chen et al., 2016).

increase in apparent contact angle as per Eqn. (2.3)); or (iii) local surface geometry in the form of the presence of a sharp corner (Fig. 2.3(a)). The last scenario is of particular interest as it can be described purely by a geometrical extension of Young-Dupre equation (Gibbs, 1961; Oliver et al., 1977), from which the equilibrium state of apparent contact angle  $\theta$  measured within the invading fluid at the triple line can be determined by:

$$\theta_0 \leq \theta \leq \theta_0 + (180^\circ - \alpha), \quad (2.4)$$

with  $\theta_0$  and  $\alpha$  the intrinsic contact angle and the angle subtended by the two surfaces forming the edge, respectively. This sharp edge pinning phenomenon has been observed on surfaces in natural systems, such as *Nepenthes alata*, which aids the continuous unidirectional liquid transport (Chen et al., 2016) (Fig. 2.3(c,d)). This phenomenon has also been utilised to design microfluidic devices to achieve spontaneous liquid transport, where the pinning effect results in a net positive capillary force, driving the movement of liquid without external energy input

(Tan et al., 2016; Zheng et al., 2017; Chatterjee et al., 2018) (e.g., Fig. 2.3(b)). In Chapter 3, by utilising the sharp edge pinning phenomenon, we theoretically and experimentally demonstrate the spontaneous movement of a droplet under the driving force from interfacial tension, and reveal key factors influencing the transport distance.

In more complex systems such as porous media, the pinning of meniscus (interface between two liquids) at sharp edges of grains during multiphase flow leads to a wide distribution of measured contact angle even in chemically homogeneous porous media (AlRatrou et al., 2018; Blunt et al., 2019, 2021). Since the contact angle has been identified as one of the key controlling factors for fluid-fluid displacement processes (Crisp et al., 1948; Purcell, 1950; Cieplak et al., 1990; Mason et al., 1994; Holtzman et al., 2015; Trojer et al., 2015; Jung et al., 2016; Zhao et al., 2016; Primkulov et al., 2018; Ran et al., 2018; Wang et al., 2019, 2020b), it is vital to consider the sharp edge pinning phenomenon in both theoretical analysis and numerical models, since this phenomenon can modify the apparent contact angles that determine the pore-scale invasion mechanisms (Cieplak et al., 1988, 1990; Holtzman et al., 2015), especially for grains with non-smooth surfaces.

### **2.3 Liquid Bridges in Granular Materials**

In granular materials, it has been found that the existence of liquid can impact the mechanical properties of the solid matrix (Cho et al., 2001; Fournier et al., 2005; Scheel et al., 2008a; Scheel et al., 2008b; Lu et al., 2009; Fall et al., 2014). Specifically, with increasing amount of liquid, different regimes have been identified for partially saturated granular materials, including pendular, funicular, and capillary regimes (Wu et al., 1984; Yuan et al., 0000). At pendular regime, liquid bridges form between particles (Fig. 2.4(a)), resulting in a negative pressure within the liquid, exerting attractive force between the particles such that the originally cohesionless granular materials start to behave as if they were cohesive (Fig. 2.4(e)). The force due to liquid bridge depends on various liquid properties and geometrical conditions, such as interfacial tension, separation distance between grains, surface roughness, contact angle, and volume of liquid (Weigert et al., 1999; Rabinovich et al., 2005; Butt, 2008; Butt et al., 2009). In the case of vanishing separation distance, i.e., between contacting grains, the

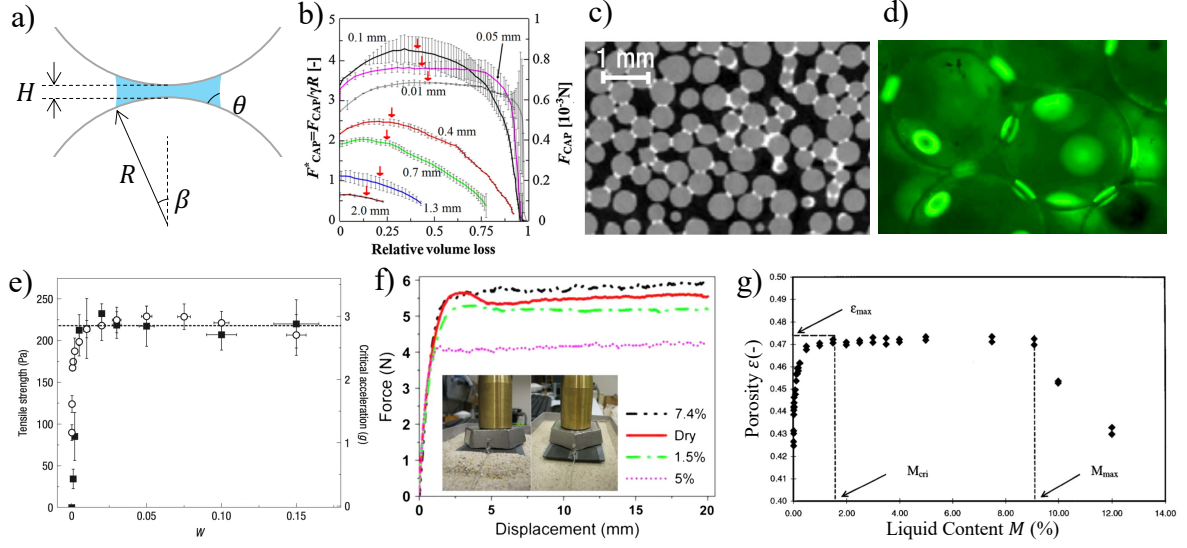


FIGURE 2.4: Liquid bridges in granular materials. (a) Schematic of a liquid bridge between two spherical particles. (b) Measured capillary force of a single liquid bridge as a function of relative volume loss during evaporation for different separation distances, adapted from (Mielniczuk et al., 2014). (c) visualisation of capillary bridges in granular materials using X-ray tomography, adapted from (Scheel et al., 2008b). (d) visualisation of capillary bridge using confocal microscopy, adapted from (Fournier et al., 2005). (e) Tensile strength (filled squares) and critical acceleration (open circles) of a wet granular pile at different volumetric water content, adapted from (Scheel et al., 2008b). (f) Force-displacement curves for wet and dry Iranian sand, adapted from (Fall et al., 2014). (g) Porosity of packed granular media using standard pouring method for different liquid content, adapted from (Feng et al., 2000).

capillary force can be estimated by (Halsey et al., 1998; Rabinovich et al., 2005; Butt et al., 2009):

$$F_c = 2\pi\gamma R \cos \theta, \quad (2.5)$$

where  $\gamma$  is the interfacial tension,  $R$  is the radius, and  $\theta$  is the contact angle. It is interesting to see that Eqn. (2.5) implies the magnitude of the force is insensitive to the volume of liquid. This is because that at relatively low water content, with increase in liquid volume, the increase in liquid-solid contact area balances with decrease in Laplace pressure (Halsey et al., 1998; Rabinovich et al., 2005; Butt, 2008; Butt et al., 2009), which has been confirmed by experiments (Scheel et al., 2008b; Mielniczuk et al., 2014) (Fig. 2.4(b)). However, if more liquid is added into the granular material, liquid bridges start to coalesce, forming liquid clusters with greater volume accompanied by decrease in capillary pressure, reducing

the cohesive force. As a result, the macroscopic properties of granular materials, such as friction (Fig. 2.4(f)), packing fraction (Fig. 2.4(g)), and shear strength, have non-monotonic relationship with the liquid content (Wu et al., 1984; Feng et al., 1998, 2000; Fall et al., 2014). In Chapter 6, a simple experimental procedure is presented for generation of wet granular assembly with different packing fraction. We then develop a model based on energy balance to describe the results of packing fractions of different particle sizes and free fall heights. The effects of capillary forces within the liquid bridges are further investigated in a series of drying experiments..

## 2.4 Multiphase Flow in Porous media

According to the the pioneering studies by Lenormand et al (Lenormand et al., 1988, 1989), patterns of multiphase flow strongly depend on the capillary number (i.e., relative strength of viscous force to capillary force) and the viscosity ratio of the two fluids. Fig. 5(a) shows the phase diagram of invasion morphology under different flow conditions and fluid properties, including capillary fingering, viscous fingering, and stable displacement. Further, the profound influence of wettability (i.e., contact angle) has been demonstrated both numerically and experimentally (i.e., Fig. 2.5(b)) (Crisp et al., 1948; Purcell, 1950; Cieplak et al., 1990; Mason et al., 1994; Holtzman et al., 2015; Trojer et al., 2015; Jung et al., 2016; Zhao et al., 2016; Primkulov et al., 2018; Ran et al., 2018; Wang et al., 2019, 2020b).

From a pore-scale perspective, Cieplak & Robbins (Cieplak et al., 1988, 1990) explain the transitions between macroscopic invasion patterns by the pore scale instability events (Fig. 2.5(c)), and the non-local cooperative pore filling event, or overlap event, is found to stabilize the invasion front. The occurrence and effect of overlap event is further explored by Holtzman et al (Holtzman et al., 2015) via a pore-network model across a wide range of wetting conditions and flow conditions (Fig. 2.5(d)). Other factors such as topological disorder and grain shapes and roughness have been subjected to active research (Holtzman et al., 2010; Hu et al., 2019a) (Fig. 2.5(e)). In Chapter 5, we propose an index to characterize the disorder of the porous media, and conduct systematic simulations of multiphase flow across a wide range of contact angles and disorder. It is found that increase in contact angles

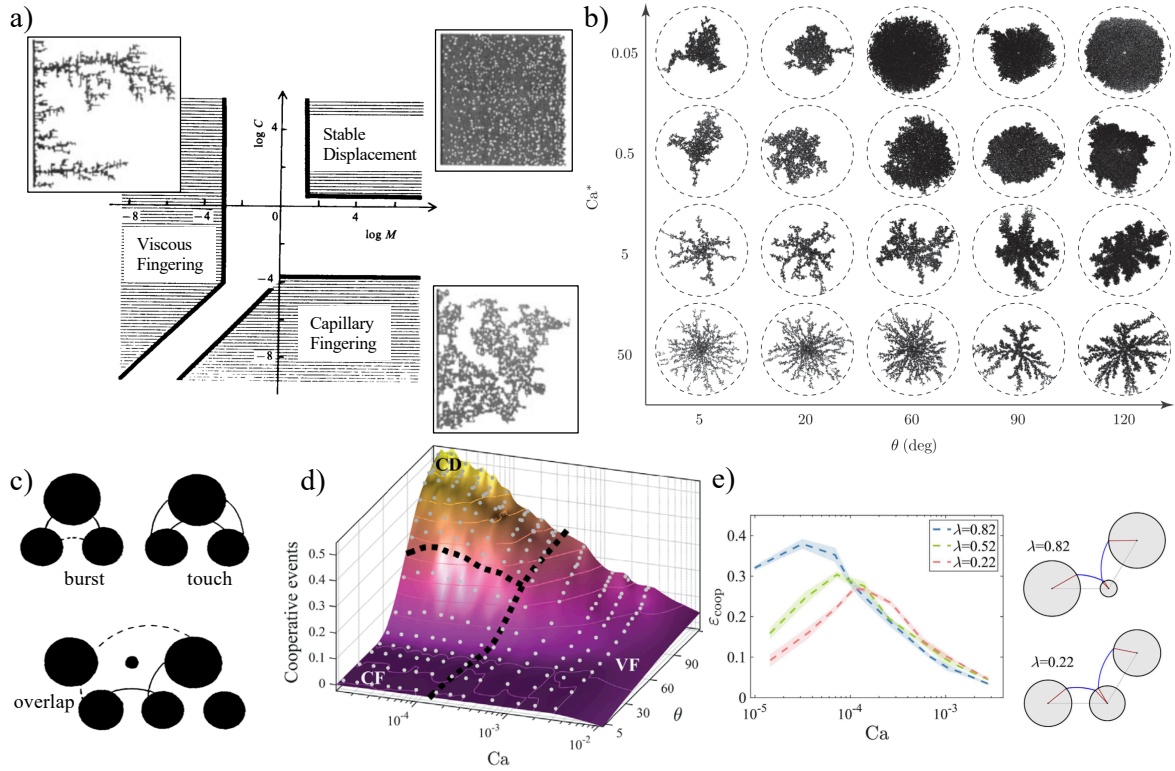


FIGURE 2.5: Multiphase flow in porous media. (a) Phase diagram of multiphase flow.  $C$  and  $M$  denote capillary number and viscosity ratio, respectively, adapted from (Lenormand et al., 1988). (b) Invasion morphologies of radial injection experiments on Hele-Shaw cells under varied capillary number and wetting conditions, adapted from (Trojer et al., 2015). (c) Schematic showing the pore-scale instability events considered in the PNM, adapted from (Cieplak et al., 1988). (d) The frequency of the cooperative pore-filling events (or overlap) under different capillary number and wetting conditions, adapted from (Holtzman et al., 2015). (e) The frequency of the cooperative pore-filling events for porous media with different disorder  $\lambda$ , with  $\lambda$  the width of the uniform distribution of particle diameters  $d \in [1 - \lambda, 1 + \lambda]\bar{d}$ , adapted from (Holtzman, 2016).

and disorder collaboratively destabilises the displacement processes, which is because the greater fluctuations in the local capillary resistance.

## 2.5 Numerical Modelling

As a supplement to experiments, various numerical methods have been developed to simulate transport of fluids, including molecular dynamics (MD) at atomic scale (Amabili et al., 2016;

Prakash et al., 2016; Amabili et al., 2017; Tinti et al., 2017), classical Navier-Stokes equation solvers such as finite volume (FV) method, meso-scale methods such as the Lattice Boltzmann Method (LBM) (Shan et al., 1996; Guo et al., 2002; Chen et al., 2014; Liu et al., 2015; Kruger et al., 2017) and smoothed-particle hydrodynamics (SPH) (Bandara et al., 2013; Bao et al., 2019), and the pore-network method (PNM) based on simplified pore geometry and/or flow conditions.

Among these methods, LBM has been extensively used for simulation of single and multiphase flows due to its capability of handling complex geometries and also being able to be massively parallelised. The PNM, on the other hand, has been applied in various investigations of macroscopic invasion patterns due to its significantly lower computational cost. Therefore, these two methods will be discussed in more detail in the following sections.

### 2.5.1 Lattice Boltzmann Method

Originated from the lattice gas model, the lattice Boltzmann method is based on solving the Boltzmann equation. It can be shown that the Navier-Stokes equation can be recovered through Chapman-Enskog analysis (Mohamad, 2011; Kruger et al., 2017). The basic quantity of LBM is the discrete velocity distribution function  $f_i(\mathbf{x}, t)$ , or particle population, and the discretized Boltzmann equation is:

$$f_i(\mathbf{x} + \mathbf{c}_i \Delta t, t + \Delta t) = f_i(\mathbf{x}, t) + \Omega_i(\mathbf{x}, t), \quad (2.6)$$

which indicates that the particles move with a velocity  $\mathbf{c}_i$  to a neighboring point during each  $\Delta t$ . Also, they are affected by the collision operator  $\Omega_i(\mathbf{x}, t)$ , through which the particles among population  $f_i$  are redistributed. One of the simplest and efficient collision operator, the Bhatnagar-Gross-Krook (BGK) scheme, is

$$\Omega_i(\mathbf{x}, t) = -\frac{f_i - f_i^{eq}}{\tau} \Delta t, \quad (2.7)$$

which relaxes the population toward the equilibrium state  $f_i^{eq}$  at a rate defined by the

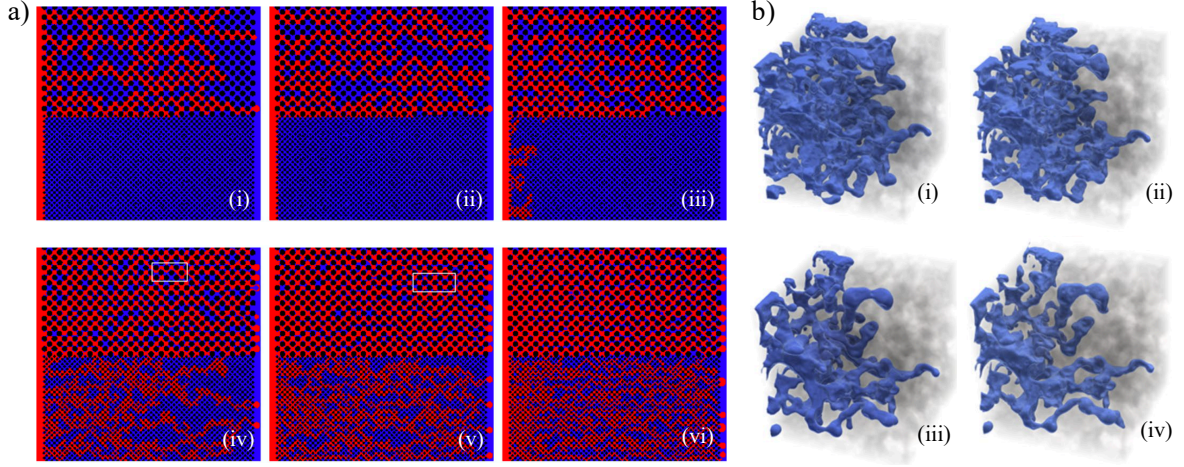


FIGURE 2.6: Lattice Boltzmann simulations of multiphase flow. Invading fluid is injected front the left in all subplots. (a) Final fluid distributions (steady-state) in the dual-permeability microfluidic system using LBM. (i-vi) correspond to capillary number of  $\log(Ca) = \{-4.36, -4.16, -4.06, -3.59, -3.36, -3.06\}$ , adapted from (Liu et al., 2014). (b) Non-wetting fluid distribution at breakthrough time using LBM. (i-iv) correspond to viscosity ratio  $M = \{15, 10, 1, 0.5\}$ , adapted from (Bakhshian et al., 2019).

relaxation time  $\tau$ . The equilibrium distribution function is given by:

$$f_i^{eq}(\mathbf{x}, t) = \omega_i \rho \left[ 1 + \frac{\mathbf{u} \cdot \mathbf{c}_i}{c_s^2} + \frac{(\mathbf{u} \cdot \mathbf{c}_i)^2}{2c_s^4} - \frac{\mathbf{u} \cdot \mathbf{u}}{2c_s^2} \right], \quad (2.8)$$

with  $\omega_i$  the weight for the  $i$ th direction. For application in multiphase problems, different approaches have been proposed to introduce the interactions between different phases, including the free-energy model (Swift et al., 1995, 1996), color-fluid model (Gunstensen et al., 1991), and Shan-Chen (SC) model (Shan et al., 1993, 1995). In SC model, the inter-particle force is introduced as:

$$F^{SC(\sigma)}(\mathbf{x}) = -\psi^{(\sigma)}(\mathbf{x}) \sum_{\bar{\sigma} \neq \sigma} G_{\bar{\sigma}\sigma} \sum_i \omega_i \psi^{(\bar{\sigma})}(\mathbf{x} + \mathbf{c}_i \Delta t) \mathbf{c}_i \Delta t, \quad (2.9)$$

with  $\psi^{(\sigma)}$  the "effective" density function for  $\sigma$  component, and  $G$  is a simple scalar that controls the strength of the interaction. The interactions with solid boundary including description of contact angles can be achieved by adopting different fictitious wall densities (Huang et al., 2007). Although the BGK collision scheme is simple to implement and comparatively efficient, it suffers from limited stability and accuracy under certain conditions,



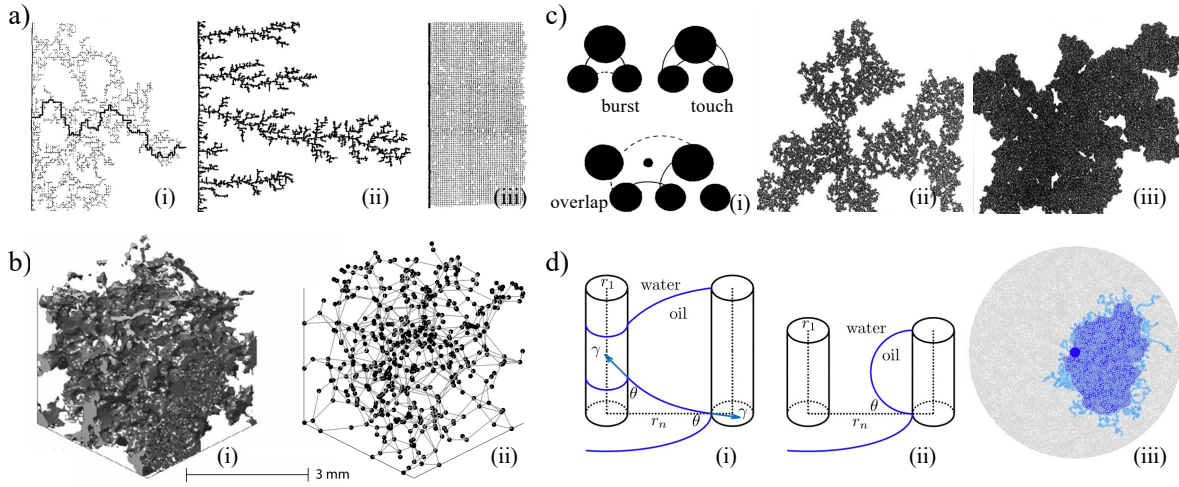


FIGURE 2.7: Pore-network modelling for multiphase flow. (a) Simulation of fluid-fluid displacement using (i) invasion percolation, (ii) diffusion limited aggregation (DLA), and (iii) anti-DLA, adapted from (Lenormand et al., 1988). (b-i) 3D image of sandstone and (b-ii) generated topologically equivalent network representation, adapted from (Valvatne et al., 2004). (c) Interface tracking algorithm proposed by Cieplak & Robbins (Cieplak et al., 1988, 1990). (i) Pore-scale instability events, (ii) invasion morphology for contact angle of  $179^\circ$  (drainage), and (iii) invasion morphology for contact angle of  $58^\circ$  (weak imbibition), adapted from (Cieplak et al., 1988). (d) The extended PNM for consideration of 3D effects. (i) Corner flow event, (ii) capillary bridge event, (iii) invasion morphology of radial injection PNM simulation at breakthrough for contact angle of  $40^\circ$  with dark blue and light blue regions representing fully invaded pores and partially invaded pores, respectively, adapted from (Primkulov et al., 2018).

especially when the density and viscosity ratios start to deviate from unity. To overcome these problems, two-relaxation-time (TRT) and multi-relaxation time (MRT) collision operators have been proposed (Kruger et al., 2017). Fig. 2.6 show examples of LBM simulation for multiphase flow across different Capillary numbers and viscosity ratios. Further development and extensions of the LBM has been subjected to extensive studies, such as high-order LBM for improved stability and accuracy (From et al., 2019, 2020), and macroscopic LBM for reduced computational cost (Chen et al., 2017; Zhou, 2021).

### 2.5.2 Pore-Network Models

Since most numerical methods based on solving Navier-Stokes equations are computationally demanding, and macroscopic invasion morphology observed in experiments often cannot be reproduced due to limited computational resources, the pore-network method offers a rigorous and computationally efficient way to study the displacement processes. Fig. 2.7(a) shows the simulated invasion morphology of capillary fingering, viscous fingering, and stable displacement via invasion percolation (IP) (Wilkinson et al., 1983), diffusion limited aggregation (DLA) (Witten et al., 1981), and anti-DLA, respectively (Lenormand et al., 1988). Further development based on these simple algorithms include consideration of trapping (Masson et al., 2014) and gravity (Wilkinson, 1984; Frette et al., 1992; Meakin et al., 1992; Chaouche et al., 1994), and volume capacitance model to capture the size of Haines jumps (Måløy et al., 1992; Furuberg et al., 1996). Although these algorithms are simple to implement and very efficient, only qualitative agreement at extreme flow conditions (vanishing viscous/capillary effect) can be obtained. Besides, the impact of wettability is not captured.

Another approach to simulate multiphase flow involves firstly constructing pore space based on either artificially generated or realistic CT scans of porous media, where the pores and throats are represented by equivalent simple geometries, such as spheres and cylinders (Blunt, 1998; Valvatne et al., 2004; Blunt, 2017). The local capillary entry pressure can be estimated as:

$$P_c = \frac{2\sigma \cos \theta}{r}, \quad (2.10)$$

with  $\sigma$  the interfacial tension,  $r$  the equivalent radius of the pore/throat space. The pore/throat is invaded if the pressure within invading phase is greater than  $P_c$ . This means that the non-local cooperative pore filling event is not captured, unless extra invasion criterion such as the stochastic model is included to modify the calculation of  $P_c$  based on local filling configurations (Blunt, 2017).

In the work by Cieplak & Robbins (Cieplak et al., 1988, 1990), a PNM model is proposed by considering the basic pore-scale instability events, where both the local burst/touch events

and non-local overlap events can be captured, and the fluid-fluid interface motion during the displacement process is tracked. Their results show that decrease in contact angle promotes the overlap events, which smoothens the invasion front, and consequently reduces the trapping events of defending phase. Recent advances based on this algorithm include incorporation of viscous effects (Holtzman et al., 2015; Primkulov et al., 2019), and consideration of corner flow under extreme wetting condition in the quasi-static regime (Primkulov et al., 2018). In Chapter 4, we will further extend the work of Cieplak & Robbins by expanding the applicability of the PNM, such that multiphase flow in porous media of arbitrary grain shapes can be simulated. Based on the new PNM, we investigate the effect of particle shape on multiphase flow.

## 2.6 Summary

The fundamentals and recent advances of the wetting and transport phenomena have been reviewed with focus on the effect of capillary force on both surfaces and in porous media. Although significant progress has been achieved in terms of general understanding of the role of wettability and geometrical features, many challenges still remain. For the Cassie-Wenzel wetting transition on rough surfaces with features of nano/micrometer size, although extensive experimental works have been conducted, there lacks more quantitative description of the transition process from a theoretical point of view. Further, how the time-dependent behaviour of the contact angle would impact the multiphase displacement process in granular materials remains unexplored.

Besides, there is a need to further understand the liquid transport process on engineered surfaces, such as those patterned surfaces that utilise the sharp edge pinning effect to achieve spontaneous droplet transport. More accurate description of the transport phenomenon can help understand and also aid the design and optimization process of microfluidic devices. Understanding fluid behaviour at sharp edges can also facilitate the development of PNM, especially for capturing the pinning of menisci at pore scale, thus to account for irregular particle shapes other than circles as in many works of the past literature.

Finally, although it is known that the behaviour of granular materials can be modified with the presence of liquid, further quantitative investigations on how capillary forces alter the packing structure of granular materials is needed. At the same time, how the packing structure of granular materials in turn impact the transport phenomenon through either multiphase displacement processes or evaporation is worth studying. In the following chapters, we present studies in the form of six published papers, as the bulk of this Thesis, to tackle some of these problems in detail.

## CHAPTER 3

### **Spontaneous Droplet Motion on Structured Surfaces**

---

In this Chapter, we aim to probe the factors that controls the spontaneous droplet movement on structured surfaces and explore the different shapes for enhancing the motion. Inspired by the sharp edge pinning phenomenon, we design and manufacture a substrate on which the spontaneous movement of droplets can be achieved. We develop a theoretical model for the description of the droplet movement process, and verify it based on experimental results. Then, using the validated model combined with theoretical analysis from an energy perspective, the factors determining the movement process are identified, and guidelines for optimising wedge shape for spontaneous droplet transport are provided.

Corresponding paper: Wang, Z., Owais, A., Neto, C., Pereira, J.-M., Gan, Y. (2021). Enhancing Spontaneous Droplet Motion on Structured Surfaces with Tailored Wedge Design. *Adv. Mater. Interfaces*, 8, 2000520.

I was the primary researcher and author of this paper, being supervised by A/Prof. Yixiang Gan, Prof. Chiara Neto, and Prof. Jean-Michel Pereira.

# Enhancing Spontaneous Droplet Motion on Structured Surfaces with Tailored Wedge Design

Zhongzheng Wang, Ahmed Owais, Chiara Neto, Jean-Michel Pereira, and Yixiang Gan\*

Spontaneous liquid transport has a wide variety of applications, including fog harvesting, microfluidics, and water-oil separation. Understanding of the droplet movement dynamics on structured surfaces is essential for enhancing the transport performance. In this work, a theoretical model describing the movement process of droplets on surfaces with prescribed wedge shapes is developed. Agreement is observed between the predictions from the model and experimental results. Through theoretical analysis and quantitative comparison between the transport performance of different wedge shapes, the factors affecting the movement process are identified and guidelines for wedge shape optimization for spontaneous droplet transport are provided.

## 1. Introduction

Spontaneous directional transport of liquid has many applications, such as fog harvesting,<sup>[1–9]</sup> water-oil separation,<sup>[10–12]</sup> and microfluidic devices.<sup>[13–16]</sup> One ubiquitous phenomenon of liquid transport without external energy input is the capillary rise driven by surface tension.<sup>[17–21]</sup> Efforts have been made to achieve spontaneous droplet motion by introducing a capillary pressure gradient on solid surfaces. This can be achieved by creating a wettability gradient through chemical or thermal treat-

ment,<sup>[22–25]</sup> roughness gradient through varying the spacial roughness ratio,<sup>[8,26–30]</sup> or surface structural gradient.<sup>[2,3,31–37]</sup> It has also been shown that spontaneous motion can be achieved between non-parallel<sup>[38–40]</sup> or flexible plates.<sup>[41]</sup> Besides, Chen et al.<sup>[42]</sup> demonstrated the continuous unidirectional liquid spreading on the peristome surface of *Nepenthes alata*, which inspired many surface designs for liquid transport.<sup>[43–45]</sup> Among these different approaches to induce spontaneous liquid motion, surfaces with wedge-shaped pattern with width gradient turn out to be effective and relatively simple to manufacture.<sup>[1,46–49]</sup> Motion on these wedge-shaped

surfaces is driven by the interfacial tension due to the droplet confinement and deformation near the tip to drive the droplet, that is, a non-zero net capillary force acting along the three-phase contact line of the droplet. From an energy perspective, the existence of a free Gibbs energy gradient leads to the self-propelled motion of the droplet. Alheshibri et al.<sup>[46]</sup> illustrated the unidirectional spreading phenomena of water droplets on heterogeneous hydrophobized Cu and hydrophilic Al surfaces and analyzed the criteria for liquid transport using the force balance. Through simulation and experiments, Tan et al.<sup>[50]</sup> investigated the enhancement of water collection using wedge-shaped gradient surfaces. Zheng et al.<sup>[48]</sup> developed a governing equation describing the droplet motion on wedge-shaped surfaces. However, there are still several challenges remaining, including the enhancement of velocity and/or distance of the transportation, and precise control of the movement.<sup>[35]</sup>

In this work, a theoretical model is developed to describe the droplet movement on surfaces with arbitrary wedge shapes. Different from previous works where the straight edges are considered,<sup>[46,48,50]</sup> the proposed model is applicable to wedges with edges described by a given profile function  $\gamma = \gamma(x)$ . Experiments were conducted to compare with model predictions. Then, based on the model, we make a quantitative comparison of liquid transport performance on surfaces with different shapes. Finally, through theoretical analysis, we identify the factors affecting the distance of the transportation and provide guidelines for wedge shape design for optimized spontaneous liquid transport.

## 2. Theoretical Model

The governing equation for droplet motion on the surface with curved-wedge pattern described by a known profile function

Z. Wang, Dr. Y. Gan  
School of Civil Engineering  
The University of Sydney  
Sydney, NSW 2006, Australia  
E-mail: yixiang.gan@sydney.edu.au

Z. Wang, Prof. J.-M. Pereira  
Navier, Ecole des Ponts  
Univ Gustave Eiffel, CNRS  
Marne-la-Vallée 77455, France

Dr. A. Owais, Prof. C. Neto  
School of Chemistry and The University of Sydney Nano Institute  
The University of Sydney  
Sydney, NSW 2006, Australia

Dr. A. Owais  
Sydney Analytical  
The University of Sydney  
Sydney, NSW 2006, Australia

Dr. A. Owais  
Renewable Energy Science and Engineering Department  
Faculty of Postgraduate Studies for Advanced Sciences (PSAS)  
Beni-Suef University  
Beni-Suef 62511, Egypt

 The ORCID identification number(s) for the author(s) of this article can be found under <https://doi.org/10.1002/admi.202000520>.

DOI: 10.1002/admi.202000520

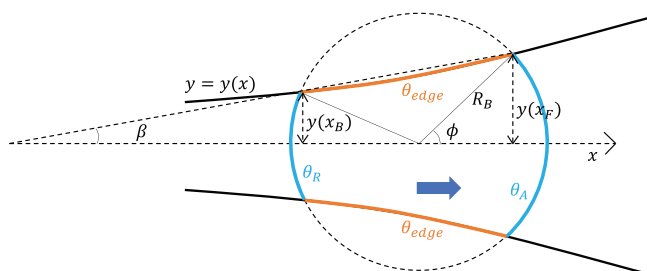


**Figure 1.** Top view schematic for droplet motion on the wedges with the edge described by profile function  $y = y(x)$ . The direction of droplet motion is indicated by the blue arrow.

$y = y(x)$ , as shown in **Figure 1**, can be derived through Newton's second law:

$$\rho V \frac{d^2 x}{dt^2} = F_c - (F_v + F_h + F_g) \quad (1)$$

where  $F_c$  is the actuation force from the interfacial tension, acting along the edges as indicated by orange curves in **Figure 1**.  $F_v$  is the resisting force from viscous dissipation,  $F_h$  is the force due to the presence of contact angle hysteresis, and  $F_g$  represents the force from gravity. The driving capillary force,  $F_c$ , can be calculated through integrating the capillary pressure along the edges:

$$F_c = -4\gamma \sin \beta \int_{\phi}^{\frac{\pi}{2} + \beta} R_B \frac{\cos \theta_{\text{edge}}}{\sin(\theta - \beta)} d\theta \quad (2)$$

where  $\gamma$  is the interfacial tension between liquid and air,  $\beta$  is the half opening angle,  $R_B$  is the base radius of the droplet,  $\theta_{\text{edge}}$  is the contact angle along the edge due to the sharp edge effect,<sup>[51]</sup> which can be determined by individually depositing droplet on circular plates with a series of radii.<sup>[48]</sup> For a given wedge shape, the droplet volume must be large enough for the droplet to be in contact with the edges in order to initiate the movement. Therefore, given the local minimum wedge width  $2\gamma_m$  and contact angle  $\theta$ , in the limiting case of no contact angle hysteresis, the base diameter of the droplet needs to be larger than the wedge width, that is,  $2R_B > 2\gamma_m$ , where

$$R_B = \sqrt[3]{\frac{3V \sin \theta}{(2 + \cos \theta)(1 - \cos \theta)^2 \pi}}, \text{ or, the droplet volume needs}$$

to satisfy  $V > \frac{\gamma_m^3 (2 + \cos \theta)(1 - \cos \theta)^2 \pi}{3 \sin \theta}$ . It is assumed that the

droplet shape remains approximately spherical during the motion. This is true when the size of the droplet is smaller than the capillary length, defined as  $l_c = \sqrt{\gamma / (\Delta \rho g)}$ , where  $\gamma$  is the interfacial tension,  $\Delta \rho$  denotes the density difference, and  $g$  is the gravitational acceleration. For a water droplet placed on a silicon wafer at room temperature,  $l_c \approx 2.7$  mm, which corresponds to droplet volumes being smaller than 7  $\mu\text{L}$ . For a spherical droplet placed on a large smooth substrate, the value of static contact angle along the triple line is between the values of the advancing and receding contact angle. If the size of the substrate is gradually decreased, the apparent contact angle will increase due to sharp edge

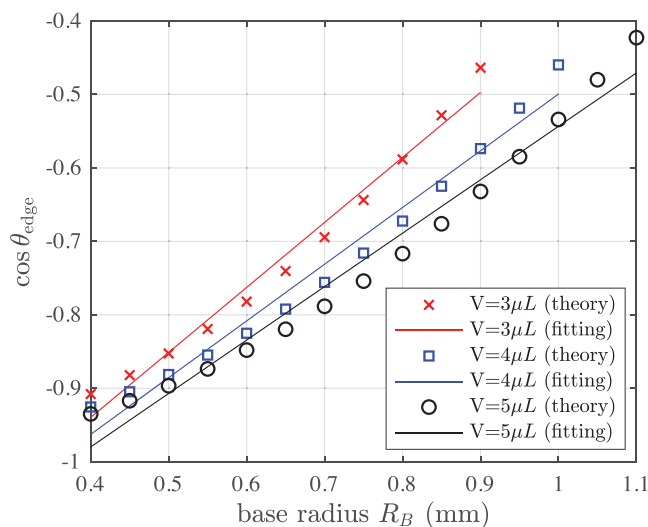


**Figure 2.** The cosine of contact angle along the edge  $\cos \theta_{\text{edge}}$  as a function of  $R_B$  for droplets with volumes  $V = [3, 4, 5] \mu\text{L}$  (crosses, squares, and circles, respectively) and their corresponding linear fitting (solid lines).

pinning effect,<sup>[51]</sup> eventually being larger than the advancing contact angle. Therefore, the value of  $\theta_{\text{edge}}$  can be determined geometrically, which can be represented as a function of the volume of the droplet and the base radius  $R_B$  (or the width of the wedge). **Figure 2** shows  $\cos \theta_{\text{edge}}$  as a function of  $R_B$  for droplets of volumes  $V = [3, 4, 5] \mu\text{L}$  with a contact angle of  $\theta = 115^\circ$  (on smooth surface without wedge), and the corresponding relationship can be linearly fitted:  $\cos \theta_{\text{edge}} = a_1 R_B + a_2$ .

Then, using the linearly fitted expression for  $\cos \theta_{\text{edge}}$ , Equation (2) can be integrated and  $F_c$  can be expressed as

$$F_c = 4\gamma R_B \sin \beta \sin(2\psi) \times \left[ \frac{a_1 R_B \sin(2\psi)}{8} (\sec^2 \psi - \csc^2 \psi + 4 \ln(\tan \psi)) - a_2 \cot(2\psi) \right] \quad (3)$$

with

$$\psi = (\phi - \beta) / 2 \text{ and } \phi = \min \left( \beta + \arcsin \left( \frac{x_0 \sin \beta}{R_B} \right), \frac{\pi}{2} + \beta \right) \quad (4)$$

For curved edges with given shape  $y(x)$ ,  $\beta$  varies with the location of base circle:

$$\beta = \arctan \left( \frac{y(x_F) - y(x_B)}{x_F - x_B} \right) \quad (5)$$

where  $x_F$  and  $x_B$  are the  $x$  coordinates of intersections between  $y(x)$  and base circle at the front and back, respectively (**Figure 1**). The resisting force due to the presence of the contact angle hysteresis,  $F_h$ , is calculated as:

$$F_h = k\gamma (y(x_B) \cos \theta_R - y(x_F) \cos \theta_A) \quad (6)$$

where  $k$  is a parameter accounting on the geometrical effect of the droplet with a typical range of  $[1, \pi]$ .<sup>[52]</sup> Here, a  $k$  value of

1 will be used here for simplicity. The force due to viscous dissipation is given by

$$F_v = \eta A \frac{v}{d}, \quad (7)$$

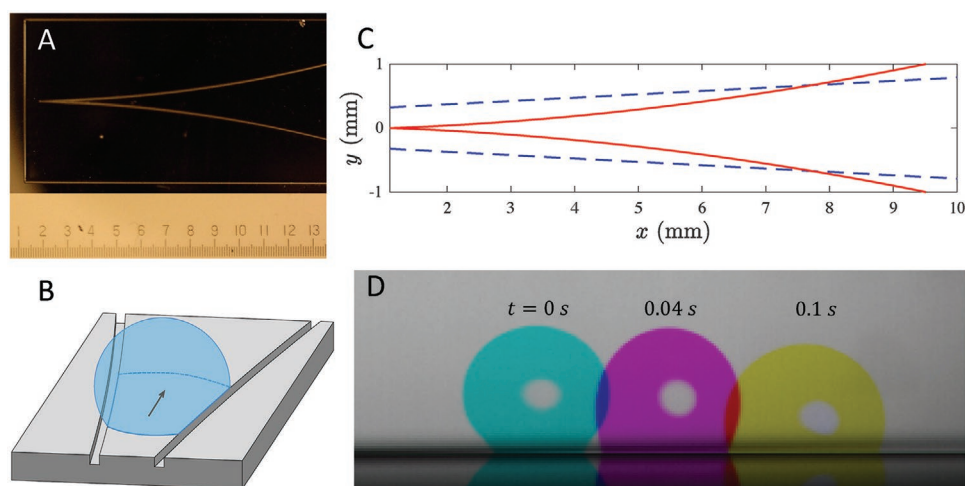
where  $\eta$  is the liquid viscosity,  $d$  is the thickness of the thin boundary layer, and  $A$  is the contact area between the droplet and substrate (area enclosed by blue and orange lines in Figure 1.) Equation (7) indicates that the force due to viscosity increases as the droplet moves along the wedge due to larger droplet-substrate contact area  $A$ , further slowing down the movement.<sup>[47,53]</sup> Finally, the force due to gravity with an inclination angle  $\theta_{\text{incline}}$  is  $F_g = \rho V g \sin \theta_{\text{incline}}$ . Here,  $\theta_{\text{incline}}$  is defined as the angle between the surface and horizontal direction. Although  $\theta_{\text{incline}} = 0$  in all our experiments, it is included here for generality. Therefore, given a wedge shape with profile function  $y = y(x)$ , after obtaining all the forces, the description of droplet movement can be obtained by numerically solving Equation (1).

### 3. Experiments and Results

Surfaces with different patterns were manufactured by cryo-etching a silicon (Si) wafer using a standard photoresist to dig a 98  $\mu\text{m}$ -deep frame featuring the borders of the wedges. The designed wedges can be described by the profile functions  $y = 0.009775x^2 + 0.01534x - 0.03014$  (in mm, will be referred as the curved wedge) and  $y = \tan(3^\circ)x + 0.2661$  (in mm, the straight wedge). The shapes of the wedges are indicated by the red-solid lines (curved wedge) and blue-dashed lines (straight wedge) in Figure 3C, respectively. The Si wedges were coated by a self-assembled monolayer of octadecyltrichlorosilane (OTS) according to the method published by Brzoska et al.<sup>[54]</sup> Si wafers were thoroughly cleaned by successive sonication in ethanol and acetone, then blown with dry high purity nitrogen,

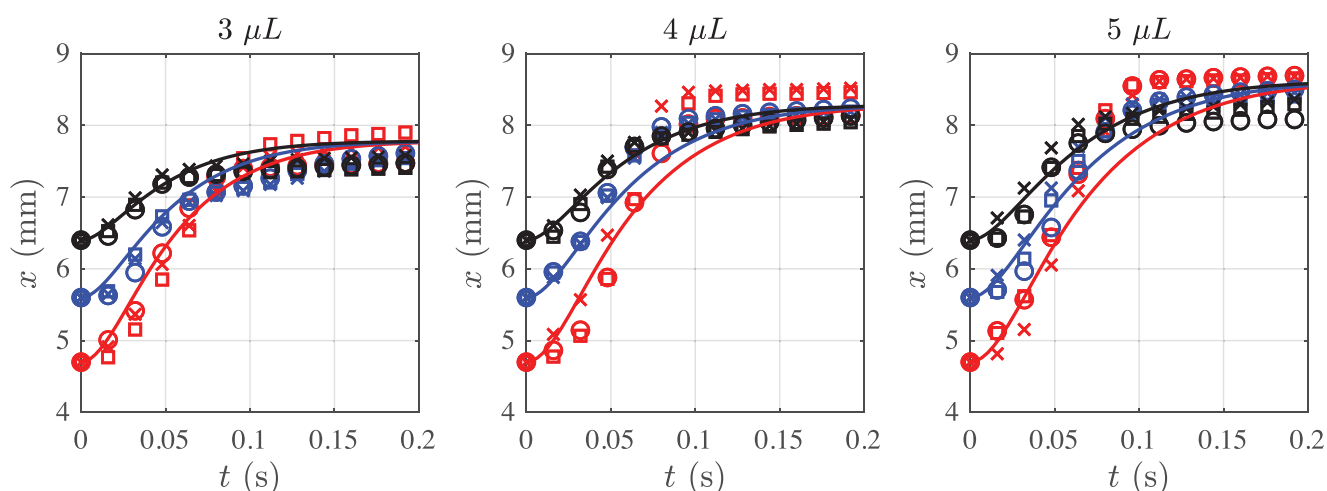
then exposed to  $\text{CO}_2$  snow jet to remove particulates, then plasma-treated in air for 30 s. Next, the cleaned Si wafers were immersed in OTS solutions in toluene (3 mm) for 15 min under dry conditions (RH < 10%). Finally, the coated surfaces were sonicated in pure toluene to remove physisorbed layers of OTS. The coated surfaces exhibited advancing angle  $\theta_A$  and receding angle  $\theta_R$  of  $115^\circ \pm 1^\circ$  and  $97^\circ \pm 1^\circ$  on a smooth surface measured by goniometer (KSV Cam 200), respectively. A photograph and a schematic showing the top view and side view of curve wedge are shown in Figures 3A and 3B, respectively. Droplets with volumes of 3, 4, and 5  $\mu\text{L}$  were formed using a precise syringe and placed onto the structured surface with different initial locations. The movement of droplets were recorded with a time interval of 0.016 s, and subsequent data analysis was carried out in MATLAB. A 4- $\mu\text{m}$  droplet moving on the curved wedge is shown in Figure 3D. Four videos showing the movement of droplets of 3, 4, and 5  $\mu\text{L}$  with three different starting locations for both curved and straight wedges are provided in Supporting Information.

Figure 4 shows the locations of droplets with volumes  $V = [3, 4, 5]$   $\mu\text{L}$  (with 0.8% relative error) as a function of time on curved wedge during the first 0.2 s. Points are the results from the experiments with initial droplet location  $x_0 = [4.7, 5.6, 6.4]$  mm ( $\pm 0.1$  mm). For each experimental condition, point shapes represent results retrieved from three different repetitions. It is found that the droplets experience fast movement during the first 0.1 second. Similar values of final location  $x_{\text{final}}$  can be observed for droplets with the same volume. The final location is further away with increasing droplet size. In order to check the validity of the model, the boundary thickness  $d$  needs to be determined experimentally. However, due to low viscosity of water and limited substrate size, it is difficult for droplets to reach constant speed on the surface at a certain tilting angles. Therefore, using one set of experimental data with droplet size of 3  $\mu\text{L}$  and  $x_0 = 4.7$  mm,  $d$  can be fitted by minimizing the residuals between data from model and experiments, which are found to be  $4 \times 10^{-6}$  m. This value was then used in the model to



**Figure 3.** A) Photograph of the top view of the curved wedge. B) 3D schematic of a moving droplet on the curved wedge. C) Straight (blue-dashed line) and curved (red-solid line) wedges described by the profile function  $y = \tan(3^\circ)x + 0.2661$  and  $y = 0.009775x^2 + 0.01534x - 0.03014$ , respectively ( $x$  and  $y$  are in mm). D) Snapshots of a video during movement of a 4- $\mu\text{L}$  droplet on the curved wedge. The color is added to show the droplet advancement at different times.





**Figure 4.** Motion of water droplets on the curved wedge during the first 0.2 s starting at different initial locations  $x_0 = [4.7, 5.6, 6.4]$  mm for droplet volumes  $V = [3, 4, 5]$   $\mu\text{L}$ . Points show the experimental results (three repeated experiments are marked with different symbols for each  $x_0$  location), and solid lines represent predictions from the model.

produce the fits shown as solid lines in Figure 4, which shows good agreements between model prediction and experimental results. For 4- and 5- $\mu\text{L}$  droplets, one can notice slight underestimation of droplet velocity, especially for small initial location  $x_0$ , and the underestimation is more significant in larger droplets. We attribute this phenomenon to the effect of inertia: upon detachment of droplet from the needle, it is observed in the experiments that the droplets are squeezed and bounce on impact with the surface, leading to larger contact line length along the wedge, and consequently larger driving force  $F_c$ . We anticipate the effect of bouncing is more significant 1) for larger droplets, 2) during early stage of droplet motion, and 3) for wedges with smaller opening angle, where  $F_c$  is more sensitive to the contact line length.

On straight wedges, the model underestimates the velocity during the early stage of movement associated with droplet bouncing effect, and fails to provide satisfactory predictions for droplet motion. This may attribute to, as discussed previously, the smaller local opening angle on the straight wedge (constant  $6^\circ$ ) compared with the curved wedge (varies from  $11^\circ$  to  $20^\circ$  during droplet movement). However, as shown in Figure 5, good agreement on the final location  $x_{\text{final}}$  can be observed for both curved and straight wedges, where the errorbars represent the standard deviation. A systematic study on the evaluation of gravitational effect on spontaneous droplet motion can be conducted through incorporating established theory,<sup>[55]</sup> which, however, is beyond the scope of current work.

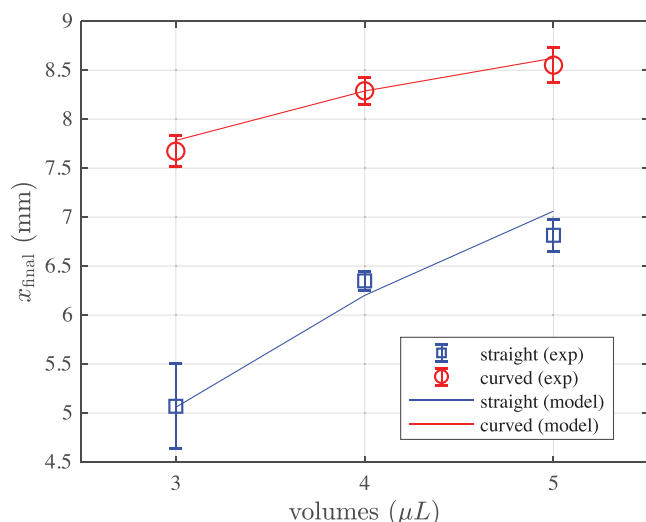


**Figure 5.** Final droplet location as a function of volumes for straight (blue-squares) and curved (red-circles) wedges. The final location is recorded after more than 10 s of initial droplet motion, where no further movement can be detected. Solid lines are predictions from the model. Error bars represent standard deviation.

#### 4. Tailored Design for Droplet Transport

In this section, surfaces with different wedge shape designs are compared quantitatively based on the proposed model. Then, we analyze the droplet motion from an energy perspective, deriving the equation for calculating maximum traveled distance within a prescribed time and identifying factors that influence the movement process. Finally, we summarize the results and provide design guidelines for droplet transport on surfaces with wedge-shaped patterns.

Three distinct wedge shapes with profile functions  $\gamma_1 = 0.0375x^{0.823}$  (concave),  $\gamma_2 = 0.075x^{1.00}$  (straight, opening angle  $\alpha = 8^\circ$ ), and  $\gamma_3 = 0.150x^{1.177}$  (convex), are shown in Figure 6A. The corresponding driving force  $F_c$  for droplets with volumes 3 and 4  $\mu\text{L}$  as a function of  $x$  are shown in Figure 6B. The previously determined  $d$  was used for the calculations. Although the wedge shapes are visually similar, it is observed that the forces due to capillary pressure are significantly different, where concave wedge has the maximum initial  $F_c$ , whereas  $F_c$  of convex wedge decreases more slowly. We can also conclude that  $F_c$  increases with increasing droplet volume for a given wedge shape due to larger edge contact length. Figure 6C,D shows

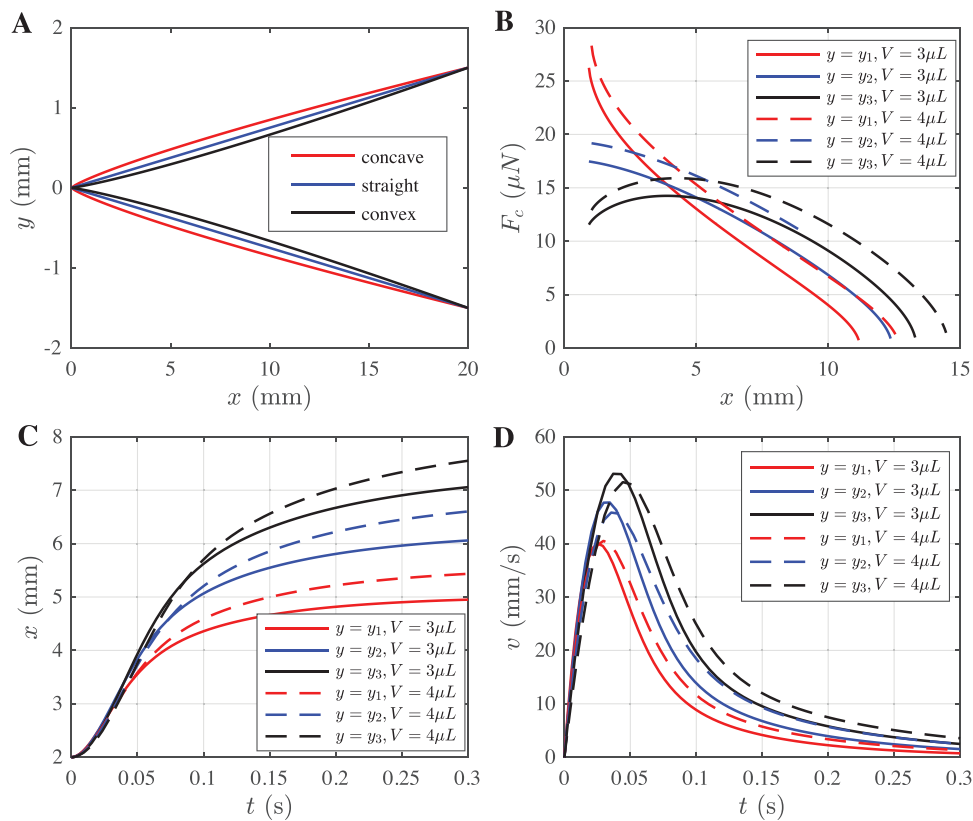


**Figure 6.** A) Shapes of convex (black), straight (blue), and concave (red) wedge shapes and their corresponding profile functions. B) The corresponding driving force  $F_c$  as a function of location on different surfaces. Solid and dashed lines represent the forces for 3 and 4  $\mu\text{L}$  droplets, respectively. C, D) Location and velocity as a function of time.

the corresponding location and velocity as a function of time. Note that during the experiments, it was found that there exists a minimum value for the initial location  $x_0$  depending on the droplet volume and width of the wedge, smaller than which the droplet cannot be placed stably onto the wedge. However, for simplicity, we assume the droplets can be placed at an initial location  $x_0 = 2$  mm. It can be seen that droplets on the convex wedge travel furthest. One can also notice that the terminal location  $x_f$  increases as the volume of droplets becomes larger, consistent with the experiments.

In order for a droplet to move “spontaneously”, it needs to be placed at an initial state with high free Gibbs energy  $G_{\text{initial}}$ . After the motion,  $G$  decreases by  $\Delta G$ , ending at  $G_{\text{final}}$ . The amount of change in Gibbs energy  $\Delta G$  is the total available actuation energy for droplet movement, which is the energy input  $E_{\text{input}}$  as

$$E_{\text{input}} = \Delta G = G_{\text{initial}} - G_{\text{final}} \quad (8)$$

The Gibbs free energy  $G$  from the interfacial energetic terms can be calculated by

$$G = \gamma_{SL}A_{SL} + \gamma_{SG}A_{SG} + \gamma_{LG}A_{LG} \quad (9)$$

where the subscripts,  $LS$ ,  $LG$ , and  $SG$ , stand for liquid-solid, liquid-gas, and solid-gas, respectively.  $\gamma$  is the interfacial tension. With the total surface area of the droplet

$A_{\text{drop}} = A_{LS} + A_{LG}$  and the total surface area of wedge,  $A_{\text{wedge}} = A_{SL} + A_{SG}$ , by applying Young’s equation:

$$G = G^* - \gamma_{LG}A_{LS}(1 + \cos\theta) \quad (10)$$

where  $G^* = A_{\text{wedge}}\gamma_{SG} + \gamma_{LG}A_{\text{drop}}$ , and  $\theta$  is the equilibrium contact angle. If we assume the total surface area of the droplet,  $A_{\text{drop}}$ , remains constant during the movement, then  $G^*$  can be treated as a constant, and the total energy input  $E_{\text{input}}$  can be simplified as

$$E_{\text{input}} = \gamma_{LG}(A_{LS,\text{final}} - A_{LS,\text{initial}})(1 + \cos\theta) \quad (11)$$

where  $A_{LS,\text{final}}$  and  $A_{LS,\text{initial}}$  are the final and initial contact area between droplet and the substrate, respectively, indicated by the area enclosed by blue and orange lines in Figure 1. Equation (11) implies that in order to increase the available  $E_{\text{input}}$ , apart from choosing liquids with larger surface tension, we can decrease  $A_{LS,\text{initial}}$  by placing the droplet near the wedge tip or reducing the initial local opening angle, and increase  $A_{LS,\text{final}}$  by increasing the final local opening angle.

During the movement process from initial position  $x_0$  to final position  $x_f$ ,  $E_{\text{input}}$  is dissipated due to viscosity, forces from contact angle hysteresis, or converted into gravitational energy. Therefore, the energy budget can be written as

$$E_{\text{input}} = \int_{x_0}^{x_f} \left[ F_v \left( x, \frac{dx}{dt} \right) + F_h(x) + F_g \right] dx \quad (12)$$

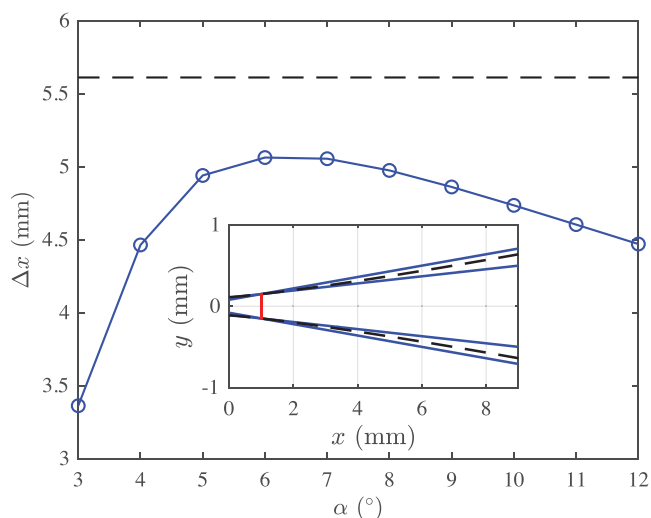


**Figure 7.** Total traveled distance  $\Delta x$  for straight (blue-dot line) as a function of opening angle  $\alpha$ . The  $\Delta x$  for the convex wedge (black-dashed line) is added for comparison. The inset shows the wedge shapes for curved (black-dashed line) and straight wedges for  $\alpha = [5^\circ, 8^\circ]$ . The solid-red line marks the initial location of the droplet.

Equation (12) shows that the energies dissipated due to contact angle hysteresis and gravity (for  $\theta_{\text{incline}} \geq 0$ ) increases monotonically with total traveled distance  $\Delta x$ , independent of the movement velocity. Therefore, in order to more “efficiently” use the available energy and achieve further traveled distance within a prescribed time  $t_0$ , the term  $E_v$  needs to be minimized. As the viscous force is a linear function of velocity  $v$ , the optimal movement strategy is to keep a constant speed  $v = L/t_0$  (see Appendix). Thus, the theoretical maximum traveled distance  $L_{\text{max},t_0}$  can be calculated by solving

$$\Delta x_{\text{max},t_0} = \frac{E_{\text{input}}}{F_v + F_h + F_g} = \frac{\gamma(1 + \cos\theta)(A_{LS,\text{final}} - A_{LS,\text{initial}})}{F_v + F_h + F_g} \quad (13)$$

In the case of unlimited time, or  $t_0 \rightarrow \infty$ , the wedge should have a shape, based on Equation (3), such that the  $F_c$  is slightly larger than  $F_h + F_g$ , so the droplet moves with infinitesimal velocity, minimizing  $E_v \approx 0$  and achieving maximum traveled distance. Equation (13) also explains why a convex wedge is better in terms of droplet transportation as shown in Figure 6C. On the one hand, a convex wedge geometrically has smaller  $A_{LS,\text{initial}}$  and larger  $A_{LS,\text{final}}$ , resulting in larger  $E_{\text{input}}$ . A smaller local opening angle near the tip (where both the droplet-edge contact length and the contact angles are large) and larger local opening angle further away suit the need for maintaining a constant velocity.

**Figure 7** shows the comparison of the performances of straight wedges with different opening angles ( $\alpha \in [3^\circ, 12^\circ]$ ) and convex wedge with a profile function  $\gamma = 0.15x^{1.2}$  for total traveled distance  $\Delta x$ . The droplet has a volume of  $4 \mu\text{L}$  with an initial location  $x_0 = 1 \text{ mm}$  and wedge width of  $0.3 \text{ mm}$  for all cases. It is observed that there is a non-monotonic relationship between the opening angle and  $\Delta x$ . The driving force  $F_c$  for a straight wedge with  $\alpha = 3^\circ$  is so small and the droplet stops early. As  $\alpha$  increases,  $F_c$  increases, resulting in larger  $\Delta x$ , reaching a maximum at around  $\alpha = 7^\circ$ , after which  $\Delta x$  decreases due to smaller

contact length between droplet and edge. The black-dashed line in Figure 7 indicates that the  $\Delta x$  for the convex wedge is greater than all straight wedge shapes, showing a clear improvement due to the change of wedge geometry. The inset in Figure 7 shows the comparison of shapes of convex wedge (black-dashed line) and straight wedges (blue-solid lines) with  $\alpha = [5^\circ, 8^\circ]$ . It should be pointed out that the optimum shape of wedge does not necessarily satisfy a power law profile function, and the exact profile needs to be determined by solving Equations (13) and (3) with consideration of all resisting forces, especially the wedge-shape-dependent force from contact angle hysteresis.

Therefore, for given set material properties, that is, contact angles, liquid viscosity, contact angle hysteresis, the transport distance of spontaneous droplet motion on structured surfaces can be enhanced through increasing both the available actuation energy (Equation (11)) and efficiency of energy usage (Equations (12) and (13)). On the other hand, if one aims for achieving a high transport velocity during a short distance, it has been demonstrated that droplet movements with larger wedge local opening angle (concentrated energy release) and smaller size of droplet (more relatively significant contributions from the capillary force) are faster.<sup>[34,46,48]</sup> Note that all these material parameters can be identified from experimental data, as demonstrated in this work. In addition, other methods targeting the improvement of material properties can be used to further enhance the liquid transport, in particular, reducing the contact angle hysteresis by surface coating.

## 5. Conclusion

A theoretical model for the description of spontaneous directional droplet motion on structured surfaces is developed, which is applicable for surfaces with arbitrary wedge shapes. Experiments have also been conducted for validation purposes. Good agreements are observed between the predictions from the model and experimental results. Through quantitative comparison of droplet motion on surfaces with different shapes and theoretical analysis, we found wedges with convex shapes have the potential of performing significantly better than straight ones in terms of total traveled distance due to larger energy input and more efficient energy usage. The theoretical framework developed here enables a tailored design for achieving targeted modes of droplet motion. Our work deepens the understanding of spontaneous liquid transport on surfaces with wedge-shaped gradient and provides insights on surface design to enhance the effective transport distance. Further optimized designs are warranted based on the proposed theoretical analyses.

## Appendix

### Minimization of Linearly Velocity-Dependent Energy Dissipation

To travel a distance  $L$  within time  $t_0$ , assume the resistance force  $f = kv$  where  $k$  is a constant. The total energy dissipation

$$E = \int_0^L f dx = k \int_0^L v dx \quad (\text{A.1})$$

Case 1:  $v = \frac{L}{t_0} = \bar{v}$ , the total dissipated energy

$$E_1 = k\bar{v}L \quad (\text{A.2})$$

Case 2:  $v = \bar{v} + v^*(t)$ , where  $v^*(t)$  is the velocity deviation from  $\bar{v}$ . Since the total traveled distance is still  $L$ :

$$L = \int_0^{t_0} v dt = \int_0^{t_0} (\bar{v} + v^*) dt = L + \int_0^{t_0} v^* dt \quad (\text{A.3})$$

we have

$$\int_0^{t_0} v^* dt = 0 \quad (\text{A.4})$$

Consider  $dx = v dt = (\bar{v} + v^*) dt$ , the dissipated energy

$$\begin{aligned} E_2 &= k \int_0^L v dx = k\bar{v}L + k \int_0^{t_0} [\bar{v}v^* + (v^*)^2] dt \\ &= k\bar{v}L + k\bar{v} \int_0^{t_0} v^* dt + k \int_0^{t_0} (v^*)^2 dt \end{aligned} \quad (\text{A.5})$$

From Equation (A.4), the second term on the right hand side becomes zero. Thus,

$$E_2 = k\bar{v}L + k \int_0^{t_0} (v^*)^2 dt \geq k\bar{v}L = E_1 \quad (\text{A.6})$$

The above equation indicates velocity function for case 2 cannot be more efficient than case 1, and the equal sign holds only if  $v^* = 0$ .

## Supporting Information

Supporting Information is available from the Wiley Online Library or from the author.

## Acknowledgements

This work was financially supported by Australian Research Council (Projects DP170102886) and The University of Sydney SOAR Fellowship.

## Conflict of Interest

The authors declare no conflict of interest.

## Keywords

capillary force, droplet transport, spontaneous movement, wedge-shaped gradient

Received: March 24, 2020

Published online:

[1] H. Bai, L. Wang, J. Ju, R. Sun, Y. Zheng, L. Jiang, *Adv. Mater.* **2014**, *26*, 5025.

[2] M. Cao, J. Ju, K. Li, S. Dou, K. Liu, L. Jiang, *Adv. Funct. Mater.* **2014**, *24*, 3235.

[3] H. Bai, X. Tian, Y. Zheng, J. Ju, Y. Zhao, L. Jiang, *Adv. Mater.* **2010**, *22*, 5521.

[4] Y. Zheng, H. Bai, Z. Huang, X. Tian, F. Q. Nie, Y. Zhao, J. Zhai, L. Jiang, *Nature* **2010**, *463*, 640.

[5] H. Zhu, Z. Guo, W. Liu, *Chem. Commun.* **2016**, *52*, 3863.

[6] Y. Tian, P. Zhu, X. Tang, C. Zhou, J. Wang, T. Kong, M. Xu, L. Wang, *Nat. Commun.* **2017**, *8*, 1080.

[7] H. Luo, Y. Lu, S. Yin, S. Huang, J. Song, F. Chen, F. Chen, C. J. Carmalt, I. P. Parkin, *J. Mater. Chem. A* **2018**, *6*, 5635.

[8] K. O. Zamuruyev, H. K. Bardaweel, C. J. Carron, N. J. Kenyon, O. Brand, J. P. Delplanque, C. E. Davis, *Langmuir* **2014**, *30*, 10133, PMID: 25073014.

[9] O. Al-Khayat, J. K. Hong, D. M. Beck, A. I. Minett, C. Neto, *ACS Appl. Mater. Interfaces* **2017**, *9*, 13676, PMID: 28224792.

[10] K. Li, J. Ju, Z. Xue, J. Ma, L. Feng, S. Gao, L. Jiang, *Nat. Commun.* **2013**, *4*, 2276.

[11] C. Li, L. Wu, C. Yu, Z. Dong, L. Jiang, *Angew. Chem., Int. Ed.* **2017**, *56*, 13623.

[12] B. Wang, W. Liang, Z. Guo, W. Liu, *Chem. Soc. Rev.* **2015**, *44*, 336.

[13] M. Tani, R. Kawano, K. Kamiya, K. Okumura, *Sci. Rep.* **2015**, *5*, 10263.

[14] J. M. Morrisette, P. S. Mahapatra, A. Ghosh, R. Ganguly, C. M. Megaridis, *Sci. Rep.* **2017**, *7*, 1800.

[15] Y. Zhao, H. Wang, H. Zhou, T. Lin, *Small* **2017**, *13*, 1601070.

[16] Y. Si, C. Yu, Z. Dong, L. Jiang, *Curr. Opin. Colloid Interface Sci.* **2018**, *36*, 10.

[17] M. M. Weislogel, *J. Fluid Mech.* **2012**, *709*, 622.

[18] T. Yu, J. Zhou, M. Doi, *Soft Matter* **2018**, *14*, 9263.

[19] M. M. Weislogel, J. A. Baker, R. M. Jensen, *J. Fluid Mech.* **2011**, *685*, 271.

[20] V. T. Gurumurthy, D. Rettenmaier, I. V. Roisman, C. Tropea, S. Garoff, *Colloids Surf., A* **2018**, *544*, 118.

[21] V. T. Gurumurthy, I. V. Roisman, C. Tropea, S. Garoff, *J. Colloid Interface Sci.* **2018**, *527*, 151.

[22] M. K. Chaudhury, G. M. Whitesides, *Science* **1992**, *256*, 1539.

[23] M. Zhang, L. Wang, Y. Hou, W. Shi, S. Feng, Y. Zheng, *Adv. Mater.* **2015**, *27*, 5057.

[24] Y. y. Song, Y. Liu, H. b. Jiang, S. y. Li, C. Kaya, T. Stegmaier, Z. w. Han, L. q. Ren, *Nanoscale* **2018**, *10*, 3813.

[25] Y. Hou, L. Gao, S. Feng, Y. Chen, Y. Xue, L. Jiang, Y. Zheng, *Chem. Commun.* **2013**, *49*, 5253.

[26] Y. Kita, C. Mackenzie Dover, A. Askounis, Y. Takata, K. Sefiane, *Soft Matter* **2018**, *14*, 9418.

[27] J. Li, Q. H. Qin, A. Shah, R. H. A. Ras, X. Tian, V. Jokinen, *Sci. Adv.* **2016**, *2*, e1600148.

[28] C. Liu, J. Sun, J. Li, C. Xiang, L. Che, Z. Wang, X. Zhou, *Sci. Rep.* **2017**, *7*, 7552.

[29] J. T. Yang, J. Chen, K. J. Huang, J. J. Yeh, *J. Microelectromech. Syst.* **2006**, *15*, 697.

[30] J. T. Yang, Z. H. Yang, C. Y. Chen, D. J. Yao, *Langmuir* **2008**, *24*, 9889, PMID: 18683962.

[31] P. Galatola, *Phys. Rev. Fluids* **2018**, *3*, 103601.

[32] S. Chatterjee, P. Sinha Mahapatra, A. Ibrahim, R. Ganguly, L. Yu, R. Dodge, C. M. Megaridis, *Langmuir* **2018**, *34*, 2865, PMID: 29377702.

[33] J. Ju, H. Bai, Y. Zheng, T. Zhao, R. Fang, L. Jiang, *Nat. Commun.* **2012**, *3*, 1247.

[34] C. Lv, C. Chen, Y. C. Chuang, F. G. Tseng, Y. Yin, F. Grey, Q. Zheng, *Phys. Rev. Lett.* **2014**, *113*, 026101.

[35] J. Li, Z. Guo, *Nanoscale* **2018**, *10*, 13814.

[36] K. H. Chu, R. Xiao, E. N. Wang, *Nat. Mater.* **2010**, *9*, 413.

[37] S. Deng, W. Shang, S. Feng, S. Zhu, Y. Xing, D. Li, Y. Hou, Y. Zheng, *Sci. Rep.* **2017**, *7*, 45687.

[38] M. Ataei, T. Tang, A. Amirfazli, *J. Colloid Interface Sci.* **2017**, *492*, 218.

[39] M. Ataei, H. Chen, A. Amirfazli, *Langmuir* **2017**, *33*, 14674, PMID: 29148812.

[40] Y. Huang, L. Hu, W. Chen, X. Fu, X. Ruan, H. Xie, *Langmuir* **2018**, *34*, 4484, PMID: 29575897.

- [41] A. T. Bradley, F. Box, I. J. Hewitt, D. Vella, *Phys. Rev. Lett.* **2019**, *122*, 074503.
- [42] H. Chen, P. Zhang, L. Zhang, H. Liu, Y. Jiang, D. Zhang, Z. Han, L. Jiang, *Nature* **2016**, *532*, 85.
- [43] H. Chen, L. Zhang, P. Zhang, D. Zhang, Z. Han, L. Jiang, *Small* **2017**, *13*, 1601676.
- [44] C. Li, H. Dai, C. Gao, T. Wang, Z. Dong, L. Jiang, *Proc. Natl. Acad. Sci.* **2019**, *116*, 12704.
- [45] P. Zhang, L. Zhang, H. Chen, Z. Dong, D. Zhang, *Adv. Mater.* **2017**, *29*, 1702995.
- [46] M. H. Alheshibri, N. G. Rogers, A. D. Sommers, K. F. Eid, *Appl. Phys. Lett.* **2013**, *102*, 174103.
- [47] U. Sen, S. Chatterjee, R. Ganguly, R. Dodge, L. Yu, C. M. Megaridis, *Langmuir* **2018**, *34*, 1899, PMID: 29323498.
- [48] Y. Zheng, J. Cheng, C. Zhou, H. Xing, X. Wen, P. Pi, S. Xu, *Langmuir* **2017**, *33*, 4172, PMID: 28398753.
- [49] C. Zhang, B. Zhang, H. Ma, Z. Li, X. Xiao, Y. Zhang, X. Cui, C. Yu, M. Cao, L. Jiang, *ACS Nano* **2018**, *12*, 2048, PMID: 29346727.
- [50] X. Tan, Y. Zhu, T. Shi, Z. Tang, G. Liao, *J. Micromech. Microeng.* **2016**, *26*, 115009.
- [51] J. Oliver, C. Huh, S. Mason, *J. Colloid Interface Sci.* **1977**, *59*, 568.
- [52] A. ElSherbini, A. Jacobi, *J. Colloid Interface Sci.* **2006**, *299*, 841.
- [53] B. S. Yilbas, A. Al-Sharafi, H. Ali, N. Al-Aqeeli, *RSC Adv.* **2017**, *7*, 48806.
- [54] J. B. Brzoska, I. B. Azouz, F. Rondelez, *Langmuir* **1994**, *10*, 4367.
- [55] Y. C. Jung, B. Bhushan, *Langmuir* **2009**, *25*, 9208, PMID: 19441842.

## CHAPTER 4

### **Effect of Grain Shape on Quasi-Static Fluid-Fluid Displacement**

---

In this Chapter, we aim to understand the effect of particle shape on fluid-fluid displacement process in porous media. Following the previous chapter on the sharp edge pinning phenomenon, we incorporate it into the pore-network model originally proposed by Cieplak & Robbins (Cieplak et al., 1988, 1990) for simulations of multiphase displacement process in the quasi-static regime. The proposed algorithm also includes the volume capacitance model (Måløy et al., 1992; Furuberg et al., 1996) to capture both the evolution of capillary pressure signal and sizes of Haines jumps. We conduct systematic simulations across a wide range of wetting conditions and particle shapes, revealing profound influence of particle shape on multiphase flow via analysis of various metrics during displacement.

Corresponding paper: Wang, Z., Pereira, J.-M., & Gan, Y. (2021). Effect of grain shape on quasi-static fluid-fluid displacement in porous media. *Water Resources Research*, 57, e2020WR029415.

I was the primary researcher and author of this paper, being supervised by A/Prof. Yixiang Gan and Prof. Jean-Michel Pereira.

# Water Resources Research

## RESEARCH ARTICLE

10.1029/2020WR029415

## Effect of Grain Shape on Quasi-Static Fluid-Fluid Displacement in Porous Media

Zhongzheng Wang<sup>1,2</sup> , Jean-Michel Pereira<sup>2</sup> , and Yixiang Gan<sup>1,3</sup> 

<sup>1</sup>School of Civil Engineering, The University of Sydney, Sydney, NSW, Australia, <sup>2</sup>Navier, Ecole des Ponts, Université Gustave Eiffel, CNRS, Marne-la-Vallée, France, <sup>3</sup>The University of Sydney Nano Institute (Sydney Nano), The University of Sydney, Sydney, NSW, Australia

### Key Points:

- A novel pore-network model algorithm is developed to probe the effect of grain shape on multiphase displacement in porous media
- Systematic simulations are conducted using the proposed algorithm across a wide range of wetting conditions and particle shapes
- Through analyzing various metrics during displacement, the results highlight the profound influence of particle shape on multiphase flow

### Supporting Information:

Supporting Information may be found in the online version of this article.

### Correspondence to:

Y. Gan,  
yixiang.gan@sydney.edu.au

### Citation:

Wang, Z., Pereira, J.-M., & Gan, Y. (2021). Effect of grain shape on quasi-static fluid-fluid displacement in porous media. *Water Resources Research*, 57, e2020WR029415. <https://doi.org/10.1029/2020WR029415>

Received 12 DEC 2020  
Accepted 15 MAR 2021

**Abstract** We study how grain shapes impact multiphase flow in porous media in the quasi-static regime using an extended pore-network model. The algorithm allows the explicit determination of different types of pore-scale instabilities and tracks the interface motion during the fluid-fluid displacement process. It also includes the volume capacitance model, such that both the evolution of capillary pressure signal and sizes of Haines jumps can be captured. Further, it considers the pinning of menisci at sharp edges of grains, through which the distribution of effective contact angles can be obtained. Simulations are carried out across a wide range of wetting conditions for different particle shapes. Our results show that the effective contact angle distribution during displacement widens as the grain becomes more angular, which consequently modifies the macroscopic fluid invasion morphology. By analyzing various characteristic metrics during displacement, including capillary pressure signal, Haines jump size distribution, and fractal dimension, our results highlight the profound influence of particle shape on the multiphase flow.

## 1. Introduction

Fluid-fluid displacement in porous media is a common phenomenon encountered in a wide range of natural and industrial processes, such as water infiltration into soil (Lipiec et al., 2006), carbon sequestration (Matter et al., 2016; Szulczewski et al., 2012), enhanced oil recovery (Blunt et al., 1993; Lake et al., 2014), and remediation of contamination in aquifer systems (Nadim et al., 2000). As indicated by the pioneering works by Lenormand et al. (1988) and Lenormand and Zircon (1989), the multiphase displacement patterns strongly depend on the capillary number (i.e., relative strength of viscous force to capillary force) and the viscosity ratio of the two fluids, and a phase diagram including capillary fingering, viscous fingering, and stable displacement was presented. Since then, extensive efforts have been devoted to further investigation of how fluid properties, flow conditions, and topological characteristics of the porous media modify the invasion morphology (Armstrong et al., 2014; Holtzman, 2016; Hu et al., 2019; Ju et al., 2020; Rabbani et al., 2018; Wang et al., 2019; Xu et al., 2014; Yortsos et al., 1997). Specifically, both numerical and experimental works have revealed the profound influence of wettability (i.e., contact angle) in two-phase flows (Cieplak & Robbins, 1990; Crisp & Thorpe, 1948; Holtzman & Segre, 2015; Jung et al., 2016; Mason & Morrow, 1994; Primkulov et al., 2018; Purcell, 1950; Ran et al., 2018; Trojer et al., 2015; Wang et al., 2019, 2020; Zhao et al., 2016). However, the effective contact angle, as one of the key controlling factors, is often unknown prior to the displacement process due to the complex geometry of pore space. Even for chemically homogeneous porous media, a wide distribution of contact angles has been observed due to the roughness and pinning of menisci at sharp edges (AlRatrou et al., 2018; Blunt et al., 2019, 2021). Therefore, it is important to understand how particle shape affects the effective contact angles, which can consequently alter the pore-scale instability events and macroscopic invasion morphology (AlRatrou et al., 2018; Cieplak & Robbins, 1990; Geistlinger & Zulficar, 2020; Holtzman & Segre, 2015; Zulficar et al., 2020).

In the quasi-static regime of multiphase flow where capillary force dominates the displacement, various numerical approaches have been developed to supplement experiments, including Navier-Stokes equation solvers and pore-network models. The methods of the latter category have been successfully applied in the investigation of macroscopic invasion patterns due to significantly less computational cost (Blunt, 1998, 2001; Cieplak & Robbins, 1988, 1990; Holtzman, 2016; Holtzman & Segre, 2015; Hu et al., 2019; Primkulov et al., 2018). A subclass of pore-network models, the interface tracking algorithm, initially proposed by

Cieplak and Robbins (1988) and Robbins (1988, 1990) and recently extended by Primkulov et al. (2018) for consideration of corner flow, has been found successful in reproducing multiphase displacement experiments in Hele-Shaw cells (Chapuis et al., 2008; Holtzman, 2016; Holtzman & Segre, 2015; Ran et al., 2018; Trojer et al., 2015; Zhao et al., 2016). This method captures the pore-scale invasion mechanisms by taking into account the local pore geometry, including the cooperative pore-filling event, which stabilizes the invasion during imbibition (Cieplak & Robbins, 1988, 1990; Holtzman & Segre, 2015). However, up to now, this type of pore-network model is applicable to perfectly spherical particles, whereas grains with irregular shapes are prevalent in natural systems such as sand packs, and solid walls characterized by surface with sharp edges due to manufacturing limitations are encountered in microfluidics. These non-smooth surfaces can often lead to pinning of menisci during the displacement process, which results in effective contact angles deviating from the intrinsic one, altering the capillary resistance at local pore/throat. It is worth noting that surface roughness has also proven influential on the effective contact angle during the fluid-fluid displacement process (AlRatrouf et al., 2018; Chen et al., 2018; Mehmani et al., 2019; Zulfiqar et al., 2020). One option to distinguish the impact from particle shape and roughness on contact angle is whether the effect is transient. Due to surface roughness, the effective contact angle can change as the liquid fills the grooves of the surface, leading to a time-dependent behavior of contact angle. This phenomenon has been extensively observed in experiments (Mishra et al., 2016; Moulinet & Bartolo, 2007; Papadopoulos et al., 2013; Sbragaglia et al., 2007; Seo et al., 2018), where the effective contact angle could be described by the Wenzel or Cassie-Baxter model, depending on the wetting states (Cassie & Baxter, 1944; Gao & Yan, 2009; Marmur, 2003; Wenzel, 1936). On the other hand, the pinning of the meniscus at sharp edges (Gibbs, 1961; Oliver et al., 1977), is a thermodynamically stable configuration. In the current study, we thus focus on the latter phenomenon in the quasi-static displacement process.

Here, we develop an extended pore-network model (called EPONM) to probe the effect of particle shape on quasi-static fluid-fluid displacement. The model incorporates the explicit determination of basic pore-scale instabilities based on the study of Cieplak and Robbins (1988, 1990). It also includes the volume capacitance model (Furuberg et al., 1996; Måløy et al., 1992), which allows us to capture both the evolution of capillary pressure signal and sizes of Haines jumps. Different from the original algorithm where the volume capacitance is a prescribed constant (Furuberg et al., 1996; Måløy et al., 1992), it is calculated based on local pore geometries without extra assumptions. More importantly, the sharp edge pinning effect is added to consider the pinning of the menisci (Gibbs, 1961; Oliver et al., 1977). Our results for different grain shapes indicate that increase in angularity leads to wider distribution of contact angles, which explains the observed greater fluctuations in capillary pressure. Besides, it is found that compared with more spherical particles, the mean capillary pressure for angular grains is greater in drainage whereas smaller in imbibition. We quantify and analyze the correlation between grain shape and size distribution of Haines jumps, interfacial length, and fractal dimension across a wide range of wetting conditions. The implications of our findings are then discussed.

## 2. Extended Pore-Network Model

To model the two-dimensional (2D) flow patterns observed in Hele-Shaw cells filled with vertical posts (Hu et al., 2019; Primkulov et al., 2018; Trojer et al., 2015; Zhao et al., 2016) with controlled particle shapes, the porous medium is represented by polygons (instead of circles in past studies) placed on 2D triangular lattice. The invading fluid is injected from the center of the simulation domain. Based on a purely geometrical extension of Young-Dupre equation (Gibbs, 1961; Oliver et al., 1977), the equilibrium state of effective contact angle  $\theta$  measured within the invading fluid at the triple line follows:

$$\theta_0 \leq \theta \leq \theta_0 + (180^\circ - \alpha), \quad (1)$$

where  $\theta_0$  and  $\alpha$  are the intrinsic contact angle and the angle subtended by the two surfaces forming the edge, respectively (Figure 1a). Since in this work the focus is placed on the regime of quasi-static displacement, the advancement of liquid front is governed by capillary force, and the viscous effect is ignored.

In the framework of interface tracking algorithm, the menisci move forward through two types of advancements: (1) pressure-driven events and (2) spontaneous events (relaxation). With a constant injection velocity boundary condition, the capillary pressure builds up accompanied by change in shapes in menisci,



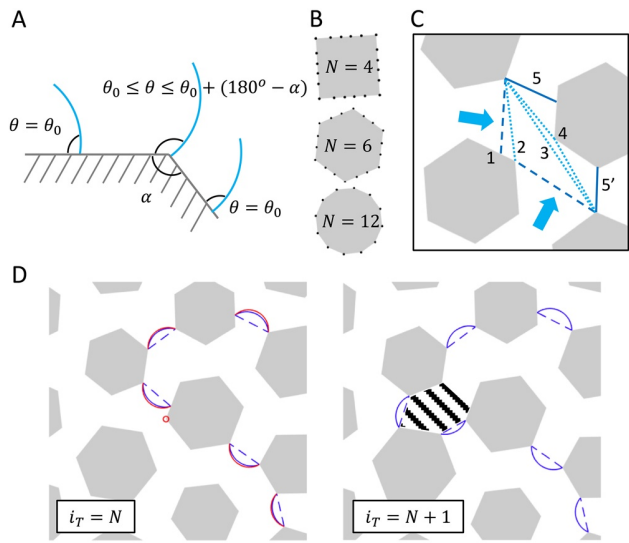


**Figure 1.** (a) Pinning of menisci at corners leads to greater effective contact angle. (b) Investigated grain shapes in this work with the different number of edges  $N$ . The black dots represent the mesh points. (c) Schematic showing different invasion types. {1–2, 2–3, 3–4, 4–5(5')} correspond to {unpin, overlap, touch, unpin} events, respectively. Blue arrows mark the movement direction of menisci. (d) Snapshots of invasion morphology at two consecutive steps. Blue-solid lines represent menisci after relaxation of the previous step. Red-solid lines represent menisci at the critical state (in this case an unpin event marked by the red circle will take place). The shaded area is invaded, accompanied by retraction of menisci from red lines at  $i_T = N$  to blue lines at  $i_T = N + 1$ .

until either the meniscus jumps toward the next mesh point due to the local contact angle being greater than the upper bound according to Equation 1 (*unpin* event), or the meniscus touches other grain, forming two new menisci (*touch* event). Regarding the fineness of the mesh, the number of mesh points needed per edge is denoted by  $M = E/N$ , with  $E$  the effective number of mesh points per grain and  $N$  the number of edges a grain has. It is found that  $E = 24$  is sufficient for the studied grain shapes, leading to the corresponding number of mesh points per edge  $M = 6, 4,$  and  $2$  for square, hexagon, and dodecagon, respectively (Figure 1b). This is verified by checking both the macroscopic invasion morphology and pore-scale instability events (see the supporting information for the mesh sensitivity test). After each pressure-driven event, the newly invaded area is subtracted from the total volume capacitance (Furuberg et al., 1996; Måløy et al., 1992; area between red and blue-dashed lines in Figure 1d), from which the pressure within the invading fluid is updated according to the remaining volume capacitance, that is, redistributing the total volume back to each active meniscus assuming all are at thermodynamic equilibrium, that is, all have the same curvature. Then, potential *overlap* events and further advancement events including *unpin* and/or *touch* are checked and executed. This process is carried out until the smallest capillary resistance at the invasion front is greater than the remaining pressure within the invading fluid. Note that after each time step, trapping is checked and all menisci that belong to trapped regions are deactivated to prevent any further movement. Figure 1c shows the schematic of several advancement steps initialized by a pressure-driven *unpin* event. Figure 1d shows local snapshot of invasion morphology at two consecutive time steps. The blue-solid lines denote the menisci shape after the previous relaxation step, and red-solid lines denote the menisci shape associated with the next minimum critical capillary pressure. The

flow chart of the algorithm is shown in Figure 2. More details on the algorithm, such as the calculation of critical capillary pressure, determination of instability modes, and conversion between pressure and volume can be found in the supporting information.

To investigate the effect of particle shapes, squares, hexagons, and dodecagons were chosen as representative grains with decreasing angularity (Figure 1b). The one-by-one rectangular simulation domain contains in total 7,520 particles placed on triangular lattice, corresponding to 94 columns of 80 vertically aligned grains with constant porosity of  $0.5912 \pm 0.0005$  (see a sample packing structure in Figure 3a). Disorder is introduced by (i) inducing 10% variation in particle size with a uniform distribution and (ii) random rotation of particles in  $(0^\circ, 360^\circ)$ . The capillary pressure signal, total injected fluid volume (area in 2D), and size of Haines jump are recorded at each step, until the invasion front reaches the boundary. Simulations were carried out for each particle shape with five randomly generated porous media under contact angles ranging from  $45^\circ$  to  $165^\circ$  with  $15^\circ$  increment. For displacement processes with contact angles below  $45^\circ$ , the 3D phenomenon corner flow starts to appear (Primkulov et al., 2018; Zhao et al., 2016), which is currently not captured in the model, and thus those processes are not covered in the present study.

A typical evolution of the invasion front until breakthrough for hexagonal grains with an intrinsic contact angle of  $\theta_0 = 120^\circ$  is shown in Figure 3a. Crimson represents the initial stage whereas yellow indicates the late times. The displacement pattern contains rather ramified structures with significant trapping, which represents the capillary fingering in drainage. Figure 3b(i) shows the evolution of the dimensionless capillary pressure calculated as the curvature  $P_c^* = 1/r^*$ , with  $r^*$  being the radius of the meniscus. The pressure-driven events and spontaneous events are marked by red circles and yellow cross, respectively. Clearly, multiple spontaneous events can take place following a pressure-driven event, which is a manifestation of a Haines jump. In the limit of vanishing capillary number, Haines jump can be regarded as effectively instantaneous compared with the speed of fluid injection at the inlet. Thus, after conversion from step into time, which is expressed as volume of injected area normalized by the average pore area, Figure 3b(ii) shows

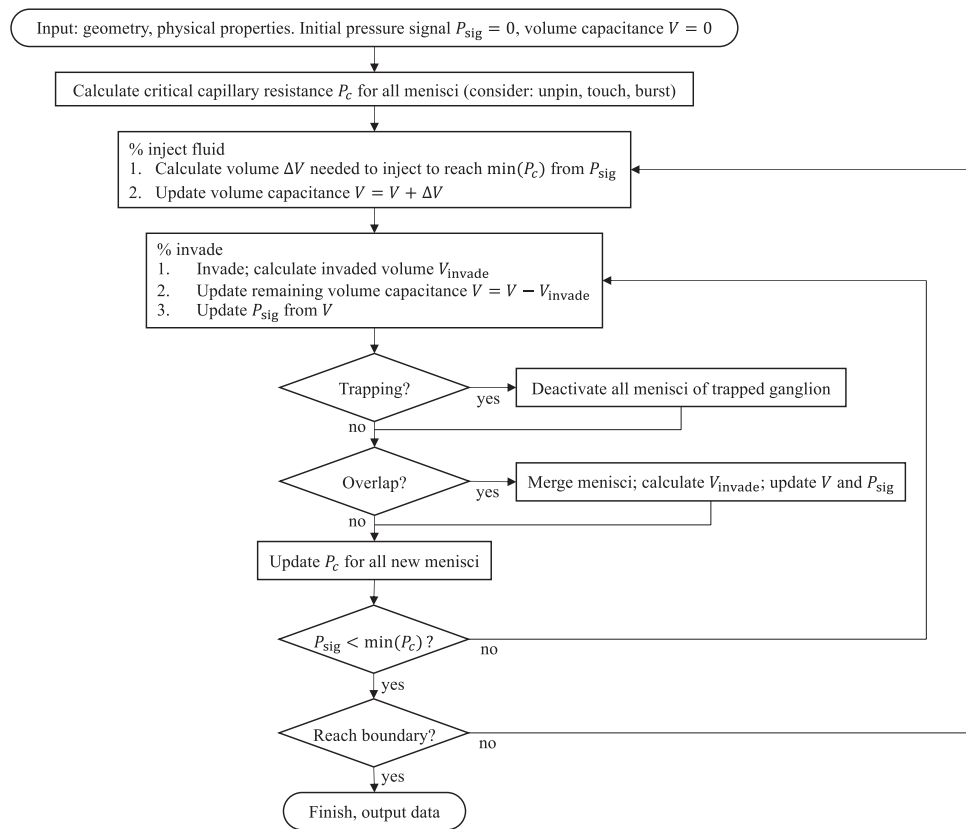


**Figure 2.** Flow chart of the pore-network model.

the pressure signal as a function of  $A_{inj}^*$ . The  $P_c^*$  values at same invasion progress are marked by the same number in Figures 3b(i) and 3b(ii). Specifically, the processes marked by (1–2) and (2–3) represent a fast Haines jump accompanied by drop in pressure, and slow injection of invading fluid until the next critical  $P_c^*$  is reached, respectively. Figure 3b(iii) shows  $P_c^*$  signal for the whole simulation. Similar pressure signal signatures in a stick-slip manner have been observed in experiments at quasi-static condition (Furuberg et al., 1996; Måløy et al., 1992; Moura et al., 2020).

### 3. Results and Discussion

The phase diagram of the displacement patterns across a wide range of contact angles for different particle shapes is shown in Figure 4a. The invasion morphology for medium with dodecagons at  $\theta_0 = 45^\circ$  is compact with rather smooth front. This hexagonal shape is a direct result of the grain placement in the triangular lattice, which has been observed in the previous study (Holtzman, 2016; Lenormand, 1990). However, with increase in angularity, despite the displacement pattern is still relatively stable without trapping, the invasion front becomes more irregular, indicating a shift of the dominance of local pore geometry from lattice structure toward grain shape. The results at  $\theta_0 = 60^\circ$  demonstrate similar trend, with trapping events starting to occur for angular grains. With the increase of  $\theta_0$ , the displacement patterns experience a transition from compact displacement to capillary fingering. The distribution of the normalized throat size  $L_t^*$ , calculated as the shortest distance between adjacent grains divided by the throat size of the volume equivalent spheres, is shown in Figure 4b. Although the media have similar grain size distribution (10% variation with uniform distribution) and arrangement (placed on triangular lattice), the  $L_t^*$  distribution varies drastically for different grain shapes, with wider span for more angular grains, similar to the effect from increasing topological disorder (Wang et al., 2019). Another influence of particle shape is the smaller average throat

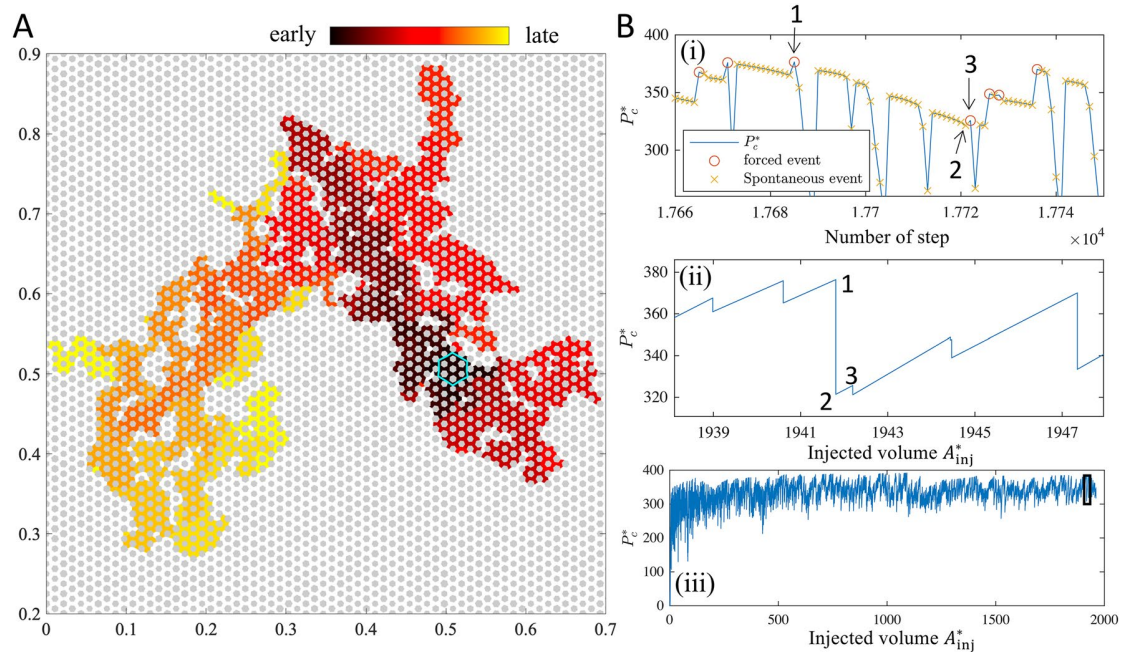


**Figure 3.** (a) Invasion morphology with hexagon grains (Number of edges  $N = 6$ ) and  $\theta_0 = 120^\circ$ . The color represents displacement patterns at different steps. The initial positions of menisci are shown as cyan lines. (b) Process of capillary pressure signal: (i) Evolution of dimensionless capillary pressure calculated as the local curvature  $P_c^* = 1/r^*$  in terms of number of step. Red circle marks the critical capillary pressure, where the pressure-driven advancement occurs. Yellow crosses represent the consequent spontaneous events (relaxation). (ii) Conversion from step into time expressed in terms of injected fluid area  $A_{inj}^*$  which is normalized by the average pore area. The time for Haines jump is regarded as instantaneous, that is, only the start and end of  $P_c^*$  are “felt” at the inlet. The  $P_c^*$  values at same invasion progress are marked by the same number in (i) and (ii). (iii) Capillary pressure signal during the whole simulation. The black box is (ii).

size as angularity increases, despite almost constant porosity. For media filled with dodecagons, the average throat size is close to 1, that is, the average throat size is similar to media with perfect spheres, which implies that the shape of dodecagons can be regarded as very close to spherical particles. Figure 4c shows the effective contact angle distribution  $\theta$  at the end of displacement (after the final relaxation process when invasion front reaches the boundary) for the case with an intrinsic contact angle  $\theta_0 = 120^\circ$ . Note that there is one effective contact angle per triple line (and thus two per meniscus). Due to the sharp edge pinning effect, the distribution narrows for grains with decreasing angularity. In the case of perfect spheres, one can expect a single value of  $\theta = \theta_0$  according to Equation 1. Therefore, Figures 4b and 4(c) summarize the important influences of particle angularity on pore geometry features and contact angle distribution, which will consequently impact the capillary pressure signal and invasion morphology.

### 3.1. Capillary Pressure Signal

As indicated in Figure 5a, the evolution of dimensionless capillary pressure  $P_c^*$  shows larger fluctuations for media with squares compared with more spherical grains (dodecagons), implying greater randomness in local capillary resistance. At the same time, larger mean value is observed with increasing  $\theta_0$ , which is a direct result of greater curvature of menisci. The distribution of  $P_{start}^*$ , the avalanches starting pressure, can also be directly obtained from the simulation (Figure 5b), where  $P_{start}^*$  is the capillary pressure at pressure-driven event (red circle in Figure 3b(i)). For experiments conducted using spherical glass beads in drainage,  $P_{start}^*$  is found to distribute within a relatively narrow region (Furuberg et al., 1996; Måløy et al., 1992; Moura et al., 2020). The  $P_{start}^*$  distribution is linked to the total volume capacitance stored in all active menisci (Furuberg et al., 1996), which reflects the characteristics of pore geometry. For spherical grains with given packing structure, the capillary resistance is distinct between “pore” and “throat,” leading to the fact that the avalanches are likely to initialize (and finish) at same location and consequently similar  $P_{start}^*$ . As the shape of particle becomes more angular, the distribution of  $P_{start}^*$  widens as a result of increased impact from

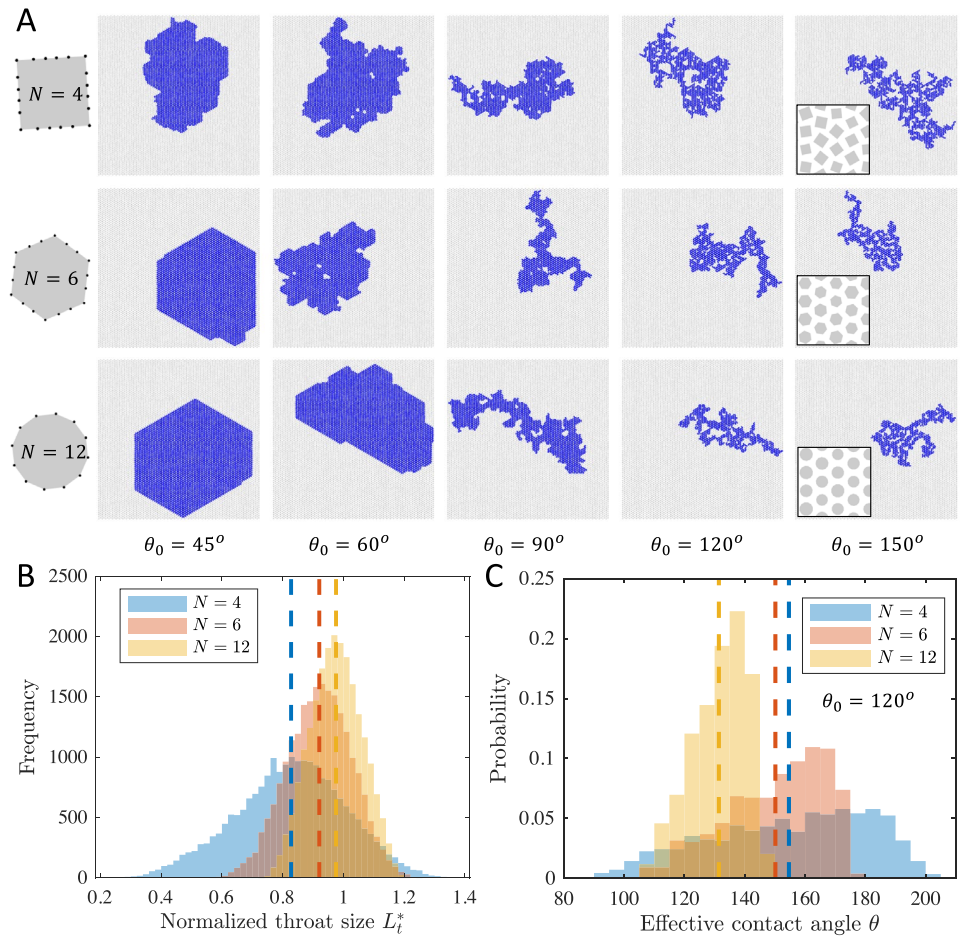


**Figure 4.** (a) Displacement patterns at the end of the simulation for different wettability conditions and grain shapes. Blue color represents the invading fluid injected from the center of domain. Gray color represents grains. Insets in the last column show the typical grain arrangement of a zoomed region. The simulation ends when the invading fluid reaches the boundary. (b) Distribution of normalized throat size for a typical set of porous media of different grain shapes, calculated as the shortest distance between adjacent grains divided by the throat size of volume equivalent spheres. (c) Contact angle distribution of one typical simulation at the end of simulation with an intrinsic contact angle  $\theta_0 = 120^\circ$  for different grain shapes. The dashed lines mark the average value for the corresponding data.

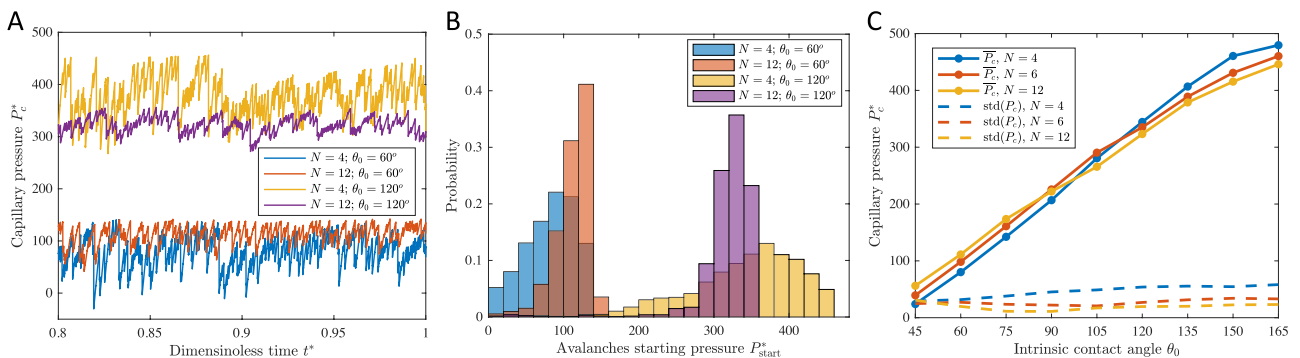


**Figure 5.** (a) Capillary pressure signals  $P_c^*$  for media with squares and dodecagons at  $\theta_0 = 60^\circ$  and  $\theta_0 = 120^\circ$ . Only last 20% of invasion is plotted for visualization purpose. (b) Corresponding avalanches starting pressure  $P_{start}^*$  distribution for cases in (a), which is the  $P_c^*$  at pressure-driven event (red circle in Figure 3b(i)). (c) Mean and standard deviation in  $P_c^*$  for all grain shapes and wettability conditions. Values are calculated from five individual simulations.

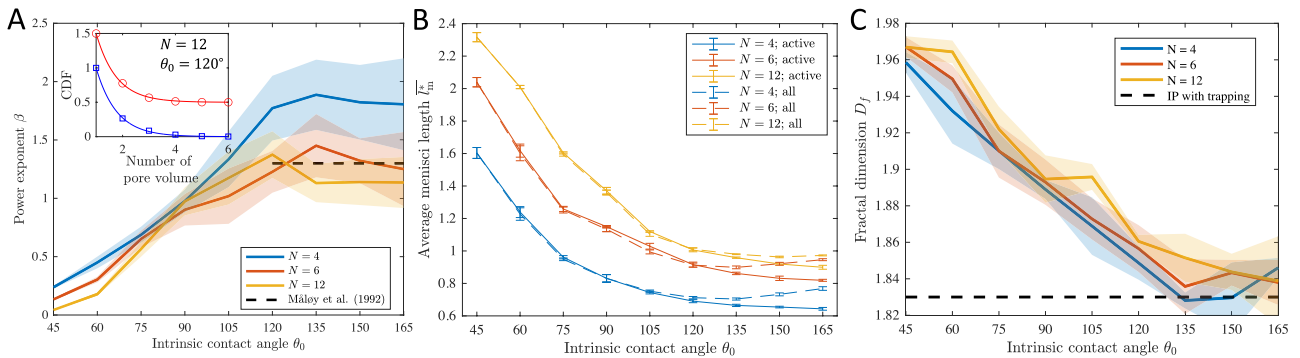


**Figure 6.** (a) Power exponent  $\beta$  for different grain shapes and wetting conditions. The black-dashed line is from Måløy et al. (1992) in drainage experiment with glass beads (since the contact angle is not reported, it is assumed that  $\theta_0 > 120^\circ$ ). Inset: Cumulative Haines jump sizes (blue squares) and intervals (red circles) distribution for a typical simulation at  $N = 12$  with  $\theta_0 = 120^\circ$ . The intervals distribution is shifted by 0.5 for visualization purpose. Lines represent exponential fitting with 1.29 and 1.30 for jump sizes and interval sizes, respectively. (b) The normalized average meniscus width  $l_m^*$  as a function of intrinsic contact angle. Solid (dashed) lines represent values calculated from active (all) menisci. (c) Fractal dimension calculated using the box-counting method as a function of intrinsic contact angle, with shaded area showing the standard deviation of five simulations.

random orientations of grains and pinning of menisci, which is clearly demonstrated in Figure 5b. Figure 5c depicts the mean and standard deviation of  $P_c^*$  for all grain shapes and wettability with each value calculated from five individual simulations. As expected, the average capillary pressure increases with increasing contact angle, and the fluctuations in capillary pressure are found to be larger for more angular grains across all wetting conditions. Besides, it can be observed that  $P_c^*$  is greater (smaller) for angular grains in drainage (imbibition) conditions, with a crossover at around  $\theta_0 \approx 90^\circ$ , which can be attributed to the change in pore and throat size distribution. It is well understood that the throat (pore) size controls the invasion process in drainage (imbibition). Figure 4c indicates that greater angularity leads to smaller average throat size, and in the meantime greater average pore size (as the porosity is the same), which explains the observed higher capillary pressure in drainage and lower capillary pressure in imbibition.

### 3.2. Haines Jumps and Patterns Characteristics

The size of Haines jump can be obtained as the area filled between two pressure-driven events (shaded area in Figure 1d), where filling events of single and multiple pores are observed. Both the cumulative pressure jump sizes and intervals distributions during drainage experiments have been found to follow an exponential law (Furuberg et al., 1996; Måløy et al., 1992), which is consistent with the simulation results (inset in Figure 6a). The time interval between two jumps is expressed as the injected area of invading fluid, and the area of invading fluid is expressed in terms of number of average pore volume, calculated as the total pore space divided by the number of pores. Note that the distribution of the cumulative intervals is shifted upwards by 0.5 for visualization purpose. The power exponent  $\beta$ , which is regarded as a signature of the displacement process (Furuberg et al., 1996; Måløy et al., 1992), is plotted for different grain shapes and wetting conditions (Figure 6a). It is shown that  $\beta$  increases with the intrinsic contact angle, reaching a plateau at around  $\theta_0 = 120^\circ$ . Also, in general, the angularity positively correlates with the power exponent. The power exponent  $\beta$  from Måløy et al. (1992) in drainage experiment with glass beads is added as black-dashed line for comparison. Since the contact angle was not reported, it is assumed that  $\theta_0 > 120^\circ$ . Their value of  $\beta$  is close to the less angular grains (hexagons and dodecagons), which is consistent with the fact that glass beads are comparatively round and smooth.

The average meniscus width  $l_m^*$  (or the average throat size where menisci are present), normalized by the throat size of porous medium of same porosity filled with mono-dispersed spheres, can reveal the distribution of menisci sizes for different particle shapes and wetting conditions. Figure 6b shows  $l_m^*$  as a function of intrinsic contact angle for different angularities with or without consideration of menisci belonging to trapped region. For all active menisci (solid lines),  $l_m^*$  decreases with increasing  $\theta_0$ , reflecting stronger stability of pinned meniscus at small throat. Besides, despite constant porosity for all simulations, the average

meniscus size is found to be smaller in angular grains as a result of (i) wider distribution of throat sizes (Figure 4b), and (ii) greater capacity of pinning (upper bound in Equation 1) as the local corner becomes sharper, leading to wider distribution of effective contact angles (Figure 4c). If both active and inactive menisci are considered, however, a non-monotonic relationship is observed. This is a result of incompressibility of the trapped ganglia that prevent the menisci from further advancement and ultimately being pinned at narrower throats. Due to increased amount of trapping at larger contact angle (see Figure 4a), this effect becomes significant at extreme non-wetting condition that leads to increase in  $l_m^*$ . This also implies that the pressure within the trapped ganglia could be lower than the capillary pressure signal measured at the inlet.

To quantify the displacement patterns, the fractal dimension  $D_f$ , as a measurement of the degree to which a pattern fills space, is calculated using the box-counting method. Figure 6c demonstrates the transition from stable displacement with a  $D_f$  of around 1.96 toward the regime of capillary fingering with  $D_f \approx 1.84$ , which is consistent with previously documented values of 1.96 and 1.83 for compact growth and invasion percolation, respectively (Blunt, 2017; Lenormand & Zarcone, 1989; Primkulov et al., 2018; Trojer et al., 2015; Wilkinson & Willemsen, 1983; Zhao et al., 2016). Furthermore, in spite of considerable variation (standard deviation, represented by the shaded area), an early transition toward capillary fingering, that is, smaller  $D_f$  at the same  $\theta_0$ , can be observed for grains with greater angularity, which confirms the qualitative observation in the displacement patterns in Figure 4a. This could be partially explained by, apart from the variation in local pore structure, the increase of average effective contact angles in angular grains assemblies due to sharp edge pinning effect, which is evident in Figure 4c.

In this study, though we considered simplified particle shapes (regular polygons), more general and complex shapes can be easily implemented by changing the coordinates of grain vertices and updating the local corner angles accordingly. Also, it is possible to consider the viscous effect by incorporating, for example, the recently proposed moving capacitor model (Primkulov et al., 2019). Furthermore, in the current work, the change in distribution of effective contact angle and throat size has been regarded as a direct result of variation in particle shape (Figures 4b and 4c), as simultaneous variations in these two quantities, under fixed porosity, are inevitable with change in particle shape. It could be interesting to solely look at the impact of menisci pinning phenomena at sharp edges by excluding the change in throat (or pore) size distribution, although this would lead to different overall porosity of samples. Note that, for the choice of particle shapes investigated in this study, square grain is chosen as the most angular case instead of triangle. This is because that with current porosity 0.5912, there will be overlaps of grains, if the shape is triangle, when they are randomly rotated. Since the porosity is already relatively large and we do not want to further increase it, also, we try to avoid manually specifying extra criterion during media generation and ensure fully random (homogeneous and isotropic) porous media, the most angular shape for current grain arrangement and porosity without grain overlap is square. On the other hand, dodecagon is used to represent circular grain, as the algorithm is not capable of doing perfect circles since the calculation of critical capillary pressure and advancement of menisci is based on discretization of the grains, and perfect circles correspond to infinite number of mesh points. Nevertheless, it was shown that the case for dodecagon is close to circle, as the average throat size is very close to the porous media filled with perfect circles (Figure 4b).

#### 4. Conclusions

In conclusion, we presented the EPONM to probe the effect of grain shapes on quasi-static fluid-fluid displacement in porous media. The model incorporates the mechanisms of pore-scale instabilities (Cieplak & Robbins, 1988, 1990), volume capacitance model (Furuberg et al., 1996; Måløy et al., 1992), and sharp edge pinning effect (Gibbs, 1961; Oliver et al., 1977). This allows us to reproduce the multiphase flow patterns across a wide range of wetting conditions for different grain shapes. The algorithm, with further extension, that is, mainly on geometry description and generalization on determination of instability modes, should be applicable to porous media with arbitrary grain shape/location, such as reconstructed pore geometry from scan of rocks, offering a rigorous approach for investigation of how topological features modify the multiphase displacement in porous media.

At the pore scale, increase in grain angularity not only introduces greater heterogeneity in pore geometry, but also amplifies the effect of menisci pinning at corners. This is directly reflected by the variations in distributions of throat sizes (Figure 4b) and effective contact angles (Figure 4c), which consequently impact both the mean value and fluctuation of the capillary pressure signal (Figure 5a). Macroscopically, an earlier transition from stable displacement toward the regime of capillary fingering is observed both qualitatively from the invasion morphology (Figure 4a) and quantitatively as indicated by the fractal dimension (Figure 6c). Various characteristic metrics have been calculated for comparison with past experimental works, including the distribution of avalanches starting pressure, Haines jump size, and interval. Reasonable agreement is observed, and impacts of grain shape are discussed. In particular, under the condition of same porosity for all studied cases, the average size of menisci is found to be smaller in porous media with angular grains, showing a tendency of pinning at narrower throats as a result of wider distribution of throat sizes (Figure 4b) and greater pinning strength (Equation 1).

Our results have provided independent corroboration of wide distribution of contact angles observed experimentally in mineralogically homogeneous porous media. The profound influences of grain shape are highlighted by systematically analyzing the displacement processes, deepening the understanding of the interplay between pore geometry and wettability. The proposed pore-network model offers an efficient approach for the investigation of multiphase flow in natural porous media.

## Data Availability Statement

Data sets associated with this work are available online (<https://doi.org/10.6084/m9.figshare.13369733>).

## Acknowledgments

This work was financially supported by the Australian Research Council (Projects DP170102886) and The University of Sydney SOAR Fellowship. Y. Gan acknowledges the financial support of Labex MMCD (ANR-11-LABX-022-01) for his stay at Laboratoire Navier at ENPC. Z. Wang thanks Ms Zi Ying for fruitful discussion.

## References

- AlRatrou, A., Blunt, M. J., & Bijeljic, B. (2018). Wettability in complex porous materials, the mixed-wet state, and its relationship to surface roughness. *Proceedings of the National Academy of Sciences of the United States of America*, *115*(36), 8901–8906. <https://doi.org/10.1073/pnas.1803734115>
- Armstrong, R. T., Georgiadis, A., Ott, H., Klemin, D., & Berg, S. (2014). Critical capillary number: Desaturation studied with fast x-ray computed microtomography. *Geophysical Research Letters*, *41*, 55–60. <https://doi.org/10.1002/2013GL058075>
- Blunt, M., Fayers, F., & Orr, F. M. (1993). Carbon dioxide in enhanced oil recovery. *Energy Conversion and Management*, *34*(9), 1197–1204. (Proceedings of the International Energy Agency Carbon Dioxide Disposal Symposium).
- Blunt, M. J. (1998). Physically-based network modeling of multiphase flow in intermediate-wet porous media. *Journal of Petroleum Science and Engineering*, *20*(3), 117–125. [https://doi.org/10.1016/S0920-4105\(98\)00010-2](https://doi.org/10.1016/S0920-4105(98)00010-2)
- Blunt, M. J. (2001). Flow in porous media pore-network models and multiphase flow. *Current Opinion in Colloid & Interface Science*, *6*(3), 197–207. [https://doi.org/10.1016/S1359-0294\(01\)00084-X](https://doi.org/10.1016/S1359-0294(01)00084-X)
- Blunt, M. J. (2017). *Multiphase flow in permeable media: A pore-scale perspective*. Cambridge University Press. <https://doi.org/10.1017/9781316145098>
- Blunt, M. J., Alhosani, A., Lin, Q., Scanziani, A., & Bijeljic, B. (2021). Determination of contact angles for three-phase flow in porous media using an energy balance. *Journal of Colloid and Interface Science*, *582*, 283–290. <https://doi.org/10.1016/j.jcis.2020.07.152>
- Blunt, M. J., Lin, Q., Akai, T., & Bijeljic, B. (2019). A thermodynamically consistent characterization of wettability in porous media using high-resolution imaging. *Journal of Colloid and Interface Science*, *552*, 59–65. <https://doi.org/10.1016/j.jcis.2019.05.026>
- Cassie, A. B. D., & Baxter, S. (1944). Wettability of porous surfaces. *Transactions of the Faraday Society*, *40*, 546–551. <http://dx.doi.org/10.1039/TF9444000546>
- Chapuis, O., Prat, M., Quintard, M., Chane-Kane, E., Guillot, O., & Mayer, N. (2008). Two-phase flow and evaporation in model fibrous media: Application to the gas diffusion layer of PEM fuel cells. *Journal of Power Sources*, *178*(1), 258–268. <https://doi.org/10.1016/j.jpowsour.2007.12.011>
- Chen, Y.-F., Wu, D.-S., Fang, S., & Hu, R. (2018). Experimental study on two-phase flow in rough fracture: Phase diagram and localized flow channel. *International Journal of Heat and Mass Transfer*, *122*, 1298–1307. <https://doi.org/10.1016/j.ijheatmasstransfer.2018.02.031>
- Cieplak, M., & Robbins, M. O. (1988). Dynamical transition in quasistatic fluid invasion in porous media. *Physical Review Letters*, *60*, 2042–2045. <https://doi.org/10.1103/PhysRevLett.60.2042>
- Cieplak, M., & Robbins, M. O. (1990). Influence of contact angle on quasistatic fluid invasion of porous media. *Physical Review B: Condensed Matter*, *41*, 11508–11521. <https://doi.org/10.1103/PhysRevB.41.11508>
- Crisp, D. J., & Thorpe, W. H. (1948). The water-protecting properties of insect hairs. *Discussions of the Faraday Society*, *3*, 210–220. <http://dx.doi.org/10.1039/DF9480300210>
- Furuberg, L., Måløy, K. J., & Feder, J. (1996). Intermittent behavior in slow drainage. *Physical Review E - Statistical Physics, Plasmas, Fluids, and Related Interdisciplinary Topics*, *53*, 966–977. <https://doi.org/10.1103/PhysRevE.53.966>
- Gao, N., & Yan, Y. (2009). Modeling superhydrophobic contact angles and wetting transition. *Journal of Bionic Engineering*, *6*(4), 335–340. [https://doi.org/10.1016/S1672-6529\(08\)60135-3](https://doi.org/10.1016/S1672-6529(08)60135-3)
- Geistlinger, H., & Zulfiqar, B. (2020). The impact of wettability and surface roughness on fluid displacement and capillary trapping in 2D- and 3D-porous media. Part 1: Wettability-controlled phase transition of trapping efficiency in glass beads packs. *Water Resources Research*, *56*(10), e2019WR026826. <https://doi.org/10.1029/2019WR026826>
- Gibbs, J. W. (1961). *The scientific papers* (Vol. 1). New York, NY: Dover Publications.

- Holtzman, R. (2016). Effects of pore-scale disorder on fluid displacement in partially-wettable porous media. *Scientific Reports*, 6, 36221. <https://doi.org/10.1038/srep36221>
- Holtzman, R., & Segre, E. (2015). Wettability stabilizes fluid invasion into porous media via nonlocal, cooperative pore filling. *Physical Review Letters*, 115, 164501. <https://doi.org/10.1103/PhysRevLett.115.164501>
- Hu, R., Lan, T., Wei, G.-J., & Chen, Y.-F. (2019). Phase diagram of quasi-static immiscible displacement in disordered porous media. *Journal of Fluid Mechanics*, 875, 448–475. <https://doi.org/10.1017/jfm.2019.504>
- Ju, Y., Gong, W., Chang, W., & Sun, M. (2020). Effects of pore characteristics on water-oil two-phase displacement in non-homogeneous pore structures: A pore-scale lattice Boltzmann model considering various fluid density ratios. *International Journal of Engineering Science*, 154, 103343. <https://doi.org/10.1016/j.ijengsci.2020.103343>
- Jung, M., Brinkmann, M., Seemann, R., Hiller, T., Sanchez de La Loma, M., & Herminghaus, S. (2016). Wettability controls slow immiscible displacement through local interfacial instabilities. *Physical Review Fluids*, 1, 074202. <https://doi.org/10.1103/PhysRevFluids.1.074202>
- Lake, L. W., Johns, R., Rossen, B., & Pope, G. (2014). *Fundamentals of enhanced oil recovery*. Society of Petroleum Engineers.
- Lenormand, R. (1990). Liquids in porous media. *Journal of Physics: Condensed Matter*, 2(S), SA79–SA88. <https://doi.org/10.1088/0953-8984/2/s/008>
- Lenormand, R., Touboul, E., & Zarcone, C. (1988). Numerical models and experiments on immiscible displacements in porous media. *Journal of Fluid Mechanics*, 189, 165–187. <https://doi.org/10.1017/s0022112088000953>
- Lenormand, R., & Zarcone, C. (1989). Capillary fingering: Percolation and fractal dimension. *Transport in Porous Media*, 4(6), 599–612. <https://doi.org/10.1007/BF00223630>
- Lipiec, J., Ku, J., Slowiska-Jurkiewicz, A., & Nosalewicz, A. (2006). Soil porosity and water infiltration as influenced by tillage methods. *Soil and Tillage Research*, 89(2), 210–220. <https://doi.org/10.1016/j.still.2005.07.012>
- Måløy, K. J., Furuberg, L., Feder, J., & Jøssang, T. (1992). Dynamics of slow drainage in porous media. *Physical Review Letters*, 68, 2161–2164. <https://doi.org/10.1103/PhysRevLett.68.2161>
- Marmur, A. (2003). Wetting on hydrophobic rough surfaces: To be heterogeneous or not to be? *Langmuir*, 19(20), 8343–8348. <https://doi.org/10.1021/la0344682>
- Mason, G., & Morrow, N. R. (1994). Effect of contact angle on capillary displacement curvatures in pore throats formed by spheres. *Journal of Colloid and Interface Science*, 168(1), 130–141. <https://doi.org/10.1006/jcis.1994.1402>
- Matter, J. M., Stute, M., Snæbjörnsdóttir, S. Ó., Oelkers, E. H., Gislason, S. R., Aradóttir, E. S., et al (2016). Rapid carbon mineralization for permanent disposal of anthropogenic carbon dioxide emissions. *Science*, 352(6291), 1312–1314. <https://doi.org/10.1126/science.aad8132>
- Mehmani, A., Kelly, S., Torres-Verdn, C., & Balhoff, M. (2019). Residual oil saturation following gas injection in sandstones: Microfluidic quantification of the impact of pore-scale surface roughness. *Fuel*, 251, 147–161. <https://doi.org/10.1016/j.fuel.2019.02.118>
- Mishra, H., Schrader, A. M., Lee, D. W., Gallo, A., Chen, S.-Y., Kaufman, Y., et al. (2016). Time-dependent wetting behavior of PDMS surfaces with bioinspired, hierarchical structures. *ACS Applied Materials & Interfaces*, 8(12), 8168–8174. <https://doi.org/10.1021/acsami.5b10721>
- Moulinet, S., & Bartolo, D. (2007). Life and death of a fakir droplet: Impalement transitions on superhydrophobic surfaces. *The European Physical Journal E*, 24(3), 251–260. <https://doi.org/10.1140/epje/i2007-10235-y>
- Moura, M., Mly, K. J., Flekky, E. G., & Toussaint, R. (2020). Intermittent dynamics of slow drainage experiments in porous media: Characterization under different boundary conditions. *Frontiers in Physics*, 7(217), 10.3389/fphy.2019.00217
- Nadim, F., Hoag, G. E., Liu, S., Carley, R. J., & Zack, P. (2000). Detection and remediation of soil and aquifer systems contaminated with petroleum products: An overview. *Journal of Petroleum Science and Engineering*, 26(1), 169–178.
- Oliver, J., Huh, C., & Mason, S. (1977). Resistance to spreading of liquids by sharp edges. *Journal of Colloid and Interface Science*, 59(3), 568–581. [https://doi.org/10.1016/0021-9797\(77\)90052-2](https://doi.org/10.1016/0021-9797(77)90052-2)
- Papadopoulos, P., Mammen, L., Deng, X., Vollmer, D., & Butt, H.-J. (2013). How superhydrophobicity breaks down. *Proceedings of the National Academy of Sciences of the United States of America*, 110(9), 3254–3258. <https://doi.org/10.1073/pnas.1218673110>
- Primkulov, B. K., Pahlavan, A. A., Fu, X., Zhao, B., MacMinn, C. W., & Juanes, R. (2019). Signatures of fluid-fluid displacement in porous media: Wettability, patterns and pressures. *Journal of Fluid Mechanics*, 875, R4. <https://doi.org/10.1017/jfm.2019.554>
- Primkulov, B. K., Talman, S., Khaleghi, K., Rangriz Shokri, A., Chalaturnyk, R., Zhao, B., et al. (2018). Quasistatic fluid-fluid displacement in porous media: Invasion-percolation through a wetting transition. *Physical Review Fluids*, 3, 104001. <https://doi.org/10.1103/PhysRevFluids.3.104001>
- Purcell, W. (1950). Interpretation of capillary pressure data. *Journal of Petroleum Technology*, 2(08), 11–12. <https://doi.org/10.2118/950369-G>
- Rabbani, H. S., Or, D., Liu, Y., Lai, C.-Y., Lu, N. B., Datta, S. S., et al. (2018). Suppressing viscous fingering in structured porous media. *Proceedings of the National Academy of Sciences of the United States of America*, 115, 4833–4838. <https://doi.org/10.1073/pnas.1800729115>
- Ran, H., Jiamin, W., Zhibing, Y., Yi-Feng, C., & Tetsu, T. (2018). Wettability and flow rate impacts on immiscible displacement: A theoretical model. *Geophysical Research Letters*, 45(7), 3077–3086. <https://doi.org/10.1002/2017GL076600>
- Sbragaglia, M., Peters, A. M., Pirat, C., Borkent, B. M., Lammertink, R. G. H., Wessling, M., & Lohse, D. (2007). Spontaneous breakdown of superhydrophobicity. *Physical Review Letters*, 99, 156001. <https://doi.org/10.1103/PhysRevLett.99.156001>
- Seo, D., Schrader, A. M., Chen, S.-Y., Kaufman, Y., Cristiani, T. R., Page, S. H., et al. (2018). Rates of cavity filling by liquids. *Proceedings of the National Academy of Sciences of the United States of America*, 115(32), 8070–8075. <https://doi.org/10.1073/pnas.1804437115>
- Szulcowski, M. L., MacMinn, C. W., Herzog, H. J., & Juanes, R. (2012). Lifetime of carbon capture and storage as a climate-change mitigation technology. *Proceedings of the National Academy of Sciences of the United States of America*, 109(14), 5185–5189. <https://doi.org/10.1073/pnas.1115347109>
- Trojer, M., Szulcowski, M. L., & Juanes, R. (2015). Stabilizing fluid-fluid displacements in porous media through wettability alteration. *Physical Review Applied*, 3, 054008. <https://doi.org/10.1103/PhysRevApplied.3.054008>
- Wang, Z., Chauhan, K., Pereira, J.-M., & Gan, Y. (2019). Disorder characterization of porous media and its effect on fluid displacement. *Physical Review Fluids*, 4, 034305. <https://doi.org/10.1103/PhysRevFluids.4.034305>
- Wang, Z., Pereira, J.-M., & Gan, Y. (2020). Effect of wetting transition during multiphase displacement in porous media. *Langmuir*, 36(9), 2449–2458. <https://doi.org/10.1021/acs.langmuir.9b03780>
- Wenzel, R. N. (1936). Resistance of solid surfaces to wetting by water. *Industrial & Engineering Chemistry*, 28(8), 988–994. <https://doi.org/10.1021/ie50320a024>
- Wilkinson, D., & Willemsen, J. F. (1983). Invasion percolation: A new form of percolation theory. *Journal of Physics A: Mathematical and General*, 16(14), 3365–3376. <https://doi.org/10.1088/0305-4470/16/14/028>



- Xu, W., Ok, J. T., Xiao, F., Neeves, K. B., & Yin, X. (2014). Effect of pore geometry and interfacial tension on water-oil displacement efficiency in oil-wet microfluidic porous media analogs. *Physics of Fluids*, *26*(9), 093102. <https://doi.org/10.1063/1.4894071>
- Yortsos, Y. C., Xu, B., & Salin, D. (1997). Phase diagram of fully developed drainage in porous media. *Physical Review Letters*, *79*, 4581–4584. <https://doi.org/10.1103/PhysRevLett.79.4581>
- Zhao, B., MacMinn, C. W., & Juanes, R. (2016). Wettability control on multiphase flow in patterned microfluidics. *Proceedings of the National Academy of Sciences of the United States of America*, *113*(37), 10251–10256. <https://doi.org/10.1073/pnas.1603387113>
- Zulfiqar, B., Vogel, H., Ding, Y., Golmohammadi, S., Kehler, M., Reuter, D., & Geistlinger, H. (2020). The impact of wettability and surface roughness on fluid displacement and capillary trapping in 2D- and 3D-porous media: Part 2: Combined effect of wettability, surface roughness, and pore space structure on trapping efficiency in sand packs and micromodels. *Water Resources Research*, *56*(10), e2020WR027965. <https://doi.org/10.1029/2020WR027965>

## CHAPTER 5

### **Multiphase Flow modified by Wettability and Disorder**

---

Multiphase flow in porous media is commonly encountered in a wide range of natural and industrial processes, such as water infiltration into soil (Lipiec et al., 2006), carbon geosequestration (Szulczewski et al., 2012; Matter et al., 2016), enhanced oil recovery (Blunt et al., 1993; Lake et al., 2014), and remediation of contamination in aquifer systems (Nadim et al., 2000). Although there are extensive studies on the role of wettability on multiphase flow, the effect of disorder remains relatively unexplored. In this chapter, we study the fluid-fluid displacement process numerically using the lattice Boltzmann method, with focus placed on unifying the effect of wetting condition and topological disorder of porous media.

## 5.1 Effect of Wetting Transition during Fluid Displacement Process

The first paper in this chapter includes the development of a theory describing the time-dependent behaviour of apparent contact angle due to Cassie-Wenzel wetting transition. The theory is then incorporated into the multi-component lattice Boltzmann method for simulation of fluid-fluid displacement process. By introducing a dimensionless time ratio  $Dy$ , the relative speed of pore invasion event and wetting transition can be represented. Systematic simulations are conducted across a wide range of  $Dy$ . We analyse the displacement process focusing on the displacement efficiency and statistics of trapped defending phase at different  $Dy$ . We show that the total pressure gradient due to both viscous and capillary effects needs to be considered for consistent description of ganglia mobilization events.

Corresponding paper: Wang, Z., Chauhan, K., Pereira, J.-M., & Gan, Y. (2019). Disorder characterization of porous media and its effect on fluid displacement. *Physical Review Fluids*, 4(3), 034305.

I was the primary researcher and author of this paper, being supervised by A/Prof. Yixiang Gan and Prof. Jean-Michel Pereira.

# Effect of Wetting Transition during Multiphase Displacement in Porous Media

Zhongzheng Wang, Jean-Michel Pereira, and Yixiang Gan\*

Cite This: *Langmuir* 2020, 36, 2449–2458

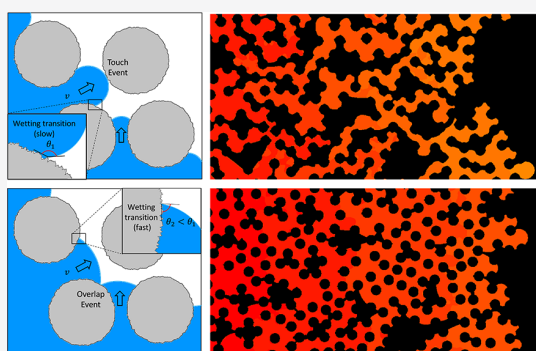
Read Online

ACCESS |

Metrics &amp; More

Article Recommendations

**ABSTRACT:** The effects of wettability on multiphase displacement in porous media have been studied extensively in the past, and the contact angle is identified as an important factor influencing the displacement patterns. At the same time, it has been found that the effective contact angle can vary drastically in a time-dependent manner on rough surfaces due to the Cassie–Wenzel wetting transition. In this study, we develop a theoretical model at the pore scale describing the apparent contact angle on a rough interface as a function of time. The theory is then incorporated into the lattice Boltzmann method for simulation of multiphase displacement in disordered porous media. A dimensionless time ratio,  $Dy$ , describing the relative speed of the wetting transition and pore invasion is defined. We show that the displacement patterns can be significantly influenced by  $Dy$ , where more trapped defending ganglia are observed at large  $Dy$  values, leading to lower displacement efficiency. We investigate the mobilization of trapped ganglia through identifying different mobilization dynamics during displacement, including translation, coalescence, and fragmentation. Agreement is observed between the mobilization statistics and the total pressure gradient across a wide range of  $Dy$  values. Understanding the effect of the wetting transition during multiphase displacement in porous media is of importance for applications such as carbon geosequestration and oil recovery, especially for porous media where solid surface roughness cannot be neglected.



## INTRODUCTION

Fluid–fluid displacement in porous media is an important phenomenon in many natural processes and engineering applications, including water infiltration into soils,<sup>1</sup> enhanced oil recovery,<sup>2,3</sup> and carbon geosequestration.<sup>4,5</sup> The displacement patterns are influenced by the characteristics of solid and liquid phases, including pore size distribution and topological disorder, fluid properties, and flow conditions.<sup>6–13</sup> When gravity is negligible, the multiphase displacement is governed by the interplay between capillary and viscous forces, which can be described by the capillary number  $Ca = \frac{\mu v}{\sigma}$ , where  $\mu$  is the viscosity of defending fluid,  $v$  is the characteristic velocity of invading fluid, and  $\sigma$  is the interfacial tension between the fluids. Besides, wettability, or contact angle, also has significant impacts on the displacement process. Here, the contact angle is measured within the invading fluid. When the contact angle of the invading phase becomes smaller, the invasion front tends to be stabilized due to increased occurrence of cooperative pore-filling events,<sup>14–16</sup> which leads to higher displacement efficiency. When the contact angle further decreases, however, the displacement efficiency may decrease due to corner flow.<sup>12,17,18</sup>

It has been found that the wettability of solids can vary in a wide range due to direct ionic bonding, Coulomb interactions,

and precipitation.<sup>19</sup> A recent study by AlRatrouf et al.<sup>20</sup> showed that the apparent contact angle is correlated with the surface roughness, being lower on rougher surfaces, which results from the accumulation of water in crevices. Mehmani et al.<sup>21</sup> investigated the effects of pore-scale roughness on displacement processes in sandstones, and they also found that increase in roughness results in smaller effective contact angle, which consequently stabilizes the displacement and facilitates the recovery process. However, in a study on two-phase flow displacement in rough fracture by Chen et al.,<sup>22</sup> as the surface becomes rougher, an increase in the apparent contact angle was observed during the multiphase displacement process. The relationship between apparent contact angle and surface roughness can be determined using the Wenzel or Cassie–Baxter model, depending on the wetting states.<sup>23–26</sup> If the invading fluid is partially in contact with the surface, i.e., some defending phase is trapped in the crevices due to limited relaxation time in a relatively fast displacement process, the apparent contact angle will become larger according to the

Received: December 9, 2019

Revised: February 17, 2020

Published: February 18, 2020

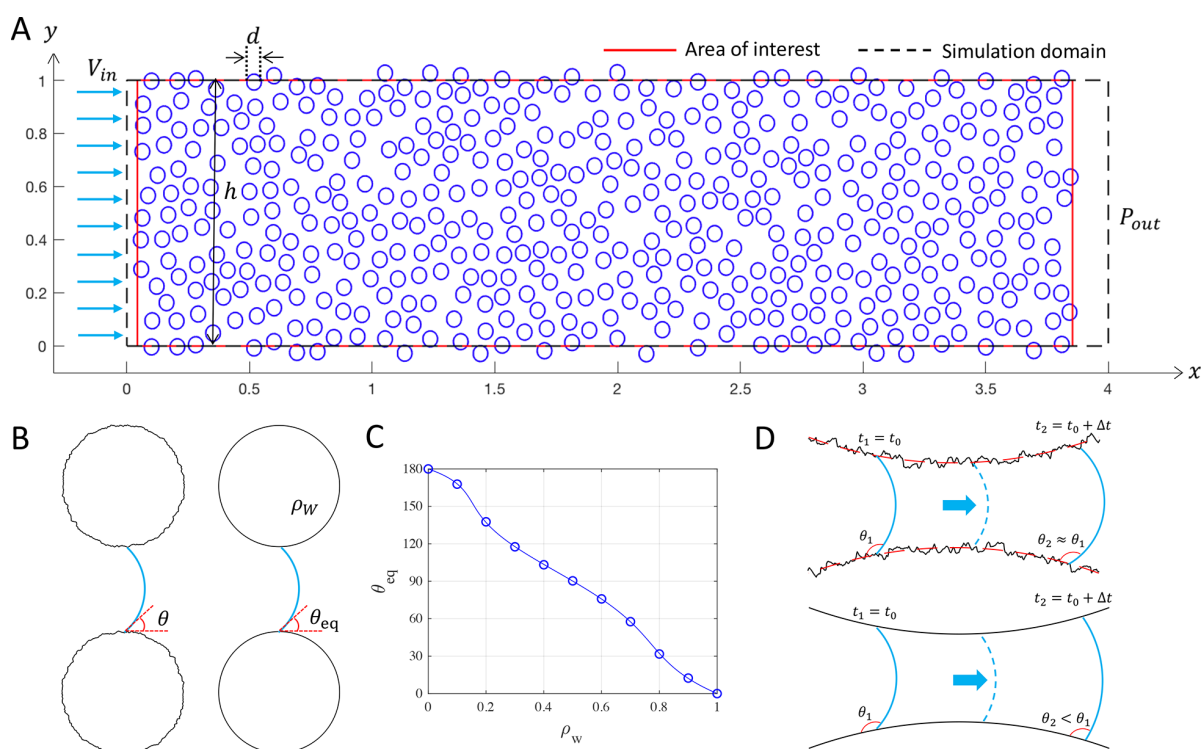


**Figure 1.** (A) Our simulated porous medium contains in total 440 circular obstacles with diameter  $d = 0.06$ . The area enclosed by the black dashed line is the simulated area, while our results and analysis are based on the area of interest to exclude the empty space near the boundaries, which is marked by the red solid line. The invading fluid is injected from the left with a constant velocity  $V_{in}$ . Constant pressure boundary condition is set at the outlet. Periodic boundary condition is imposed at top and bottom of the simulation area. (B) Schematic of actual rough grains with an effective contact angle  $\theta$  (left) and equivalent grains in simulations with an equilibrium contact angle  $\theta_{eq} = \theta$  (right). (C) Equilibrium contact angle  $\theta_{eq}$  as a function of the fictitious wall density  $\rho_w$ . Blue circles represent simulation results, and the solid line is the corresponding fitting curve using a sixth order polynomial. (D) Schematic showing the induced error in contact angle during invasion due to simplification on wettability of grains. (top) Under constant velocity, with homogeneous surface features, the effective contact angle on the rough surface is expected to be a constant. (bottom) The effective contact angle decreases due to the simplification, leading to underestimation of the contact angle at a latter stage of local pore invasion.

Cassie–Baxter equation. If the invading fluid moves slowly such that it can completely fill the grooves on the surface, it is called a Wenzel state, leading to a smaller apparent contact angle for intrinsically water-wet media. The equilibrium contact angle can be determined by the modified Cassie–Baxter equation:<sup>24–26</sup>

$$\cos \theta_{eq} = r_w \phi \cos \theta_0 + \phi - 1 \quad (1)$$

where  $\phi \in [0, 1]$  is the proportion of projected liquid–solid contact area (in the case of two-fluid displacement in porous media,  $\phi$  is the proportion of projected invading fluid–grain contact area);  $r_w$  is the surface roughness ratio greater than or equal to 1, defined as the total area divided by the apparent area; and  $\theta_0$  is the intrinsic contact angle.

The aforementioned transition of wetting states, or Cassie–Wenzel wetting transition, has been investigated extensively through both experiments and simulations.<sup>27–35</sup> The energy barrier that needs to be overcome for the transition to take place is found to be dependent on the geometry of microstructures,<sup>36–42</sup> size of surface features,<sup>43</sup> hydrodynamic pressure,<sup>44</sup> line tension,<sup>45</sup> intrinsic contact angle,<sup>31</sup> and concentration of dissolved defending phase in the invading phase.<sup>31</sup> A larger energy barrier corresponds to increased stability of the Cassie–Baxter state, leading to slower transition to the Wenzel state. The typical time for the wetting transition

to completion ranges from seconds to days, depending on the aforementioned factors and liquid properties, including interfacial tension and viscosity.<sup>28–31</sup> It has been also found that hierarchical surface structure can dramatically increase the stability of the Cassie state, slowing the transition.<sup>46–48</sup> On the other hand, external excitations, such as vibration, can help in overcoming the energy barrier, accelerating the wetting transition.<sup>49–51</sup> Mishra et al.<sup>27</sup> demonstrated that the apparent contact angle changes from around 140 to 60° due to the wetting transition on rough polydimethylsiloxane (PDMS) plates as the time of the contact increases. Seo et al.<sup>31</sup> experimentally showed a logarithmic relation between the intrinsic contact angle and the average time required for pore filling. As a result, the effective contact angle during multiphase fluid displacement in porous media with rough grains can be vastly influenced by the wetting state. The contact angle has an impact on the morphology of the invading fluid and the geometry of the menisci, which determines when, where, and whether a pore-filling event will take place. Usually the pore-filling events, e.g., two menisci merging, happen instantly. Since in contrast the time scale of the change in contact angle is not instantaneous, the local wettability is kept unchanged during pore-filling events. The available time for the progress of the wetting transition is related to the local speed of pore invasion, which can be controlled by the injection velocity. Therefore,

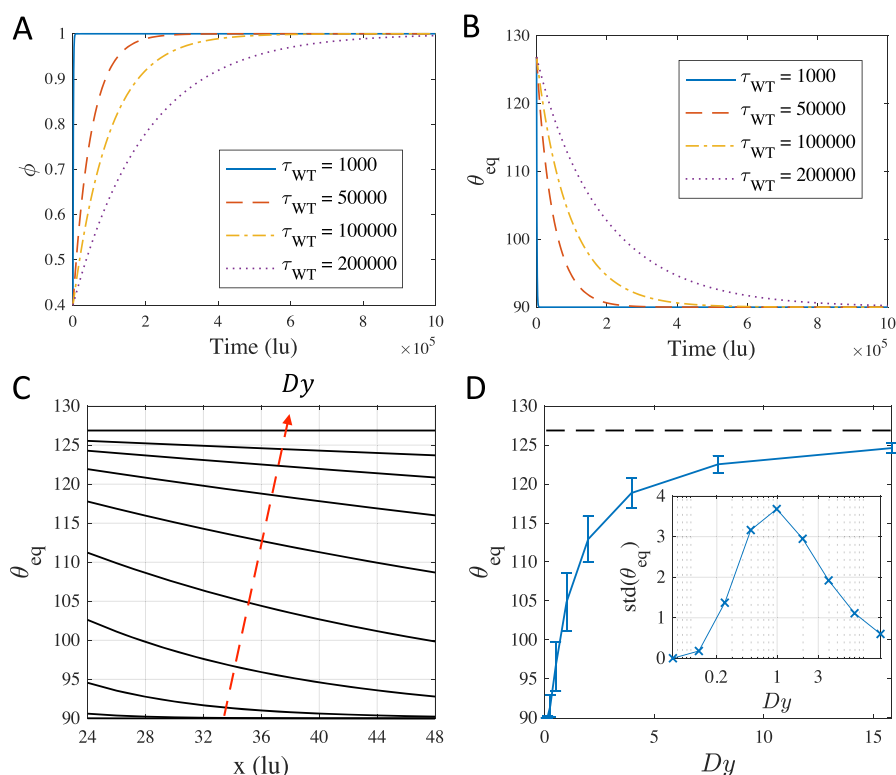


**Figure 2.** Time dependence of (A) liquid–solid contact proportion  $\phi$  and (B) equilibrium contact angle  $\theta_{eq}$ , under different characteristic times of wetting transition  $\tau_{WT}$ . Note that time is in lattice unit (lu). (C) Equilibrium contact angle “experienced” by the invasion front along the latter half of particle ( $d = 48$  lu). The red dashed arrow indicates the direction of increasing  $Dy = \{0.1, 0.2, 0.4, 0.8, 1.6, 3.2, 6.4, 12.8, \infty\}$ . (D) Average equilibrium contact angle  $\theta_{eq}$  as a function of  $Dy$ ; the error bar indicates the standard deviation. The black dashed line shows the value of  $\theta_{eq}$  with  $Dy = \infty$  with a standard deviation of zero. The inset shows the standard deviation of  $\theta_{eq}$  vs  $Dy$  in a semilog plot.

we hypothesize the existence of a competition between the progresses of pore invasion and wetting transition, which influences the effective contact contact angle during the advancement of the invading fluid, consequently affecting the multiphase displacement patterns.

In this work, a theoretical model describing the local apparent contact angle for each individual grain as a function of time is proposed. This model is then incorporated into the lattice Boltzmann method for simulation of multiphase displacement in porous medium, such that the wettability of each individual grain in the medium depends on the time of contact between the solid and the invading fluid. To characterize the dynamic effect of wetting transition in multiphase displacement, we define a dimensionless parameter  $Dy = \frac{\tau_{WT}}{\tau_{PI}}$ , where  $\tau_{WT}$  and  $\tau_{PI}$  are the characteristic times of wetting transition and pore invasion, respectively. Then, we study how the time-dependent behavior of the contact angle influences the multiphase displacement process in porous media.

## METHODOLOGY

**Media Geometry and Simulation Method.** The medium is a rectangular domain filled with circular obstacles to simulate the solid phase (Figure 1A). Through varying the diameter of the obstacle  $d$ , the porosity of the medium can be controlled. Initially, these obstacles are regularly placed on a triangular lattice, and the spacial disorder is introduced by iterative Monte Carlo movement of each obstacle with an

apparent diameter  $d_{app} = \lambda d$ . In this study we fix  $\lambda = 1.2$ . The detailed process has been explained in a previous study.<sup>11</sup> With the choice of a periodic domain with  $x \in [0.0433, 3.8538]$  and  $y \in [0, 1]$  filled with 440 obstacles having a diameter of 0.06, the overall porosity is  $\Phi = 0.674$ .

The conventional Shan–Chen multiphase lattice Boltzmann method with D2Q9 lattice is adopted for our two-dimensional (2D) numerical simulations.<sup>52,53</sup> In this study, the Bhatnagar–Gross–Krook (BGK) approach is preferred to the multi-relaxation-time (MRT) one due to extra computational resources and complexity required for the latter.<sup>54</sup> We choose a mesh size of  $800 \times 3200$  lu<sup>2</sup> (lu, lattice unit) for the simulation area such that at least 10 lattices are in between the smallest throat to ensure the grid is fine enough.<sup>55</sup> The invading and defending fluids both have a density of 1 lu. The kinematic viscosity  $\nu$  for both fluids is 0.1667 lu, leading to a viscosity ratio of 1. The interfacial tension can be calculated using the Young–Laplace equation, which is  $\sigma = 0.215$  lu. The invading fluid is injected from the left with a constant velocity of  $V_{in} = 0.002$  lu, leading to a capillary number  $Ca = \frac{V_{in} t_{def}}{\sigma} = 0.0016$ . Comparing with past literature,<sup>10,16</sup> this implies that the flow process is under a viscous dominated regime. However, since both fluids have the same viscosity and the displacement is neither favorable (viscous stabilizing effect) nor unfavorable (viscous fingering), the influence of surface tension is still expected, which is shown in the next section.

The pore scale Reynolds number  $Re = \frac{(V_{in} / \Phi) \bar{L}_t}{\nu} = 0.57$ , where  $\bar{L}_t = 32$  lu is the average throat size. The outlet pressure

at the right end is set to be a constant of 0.33 lu. Periodic boundary condition is applied at the top and bottom of the simulation area. The effective contact angle of spherical grains with rough surfaces is simulated by an equivalent contact angle on smooth grains as shown in Figure 1B.

In the Shan–Chen multiphase scheme, the contact angle can be tuned by adjusting the fictitious wall density  $\rho_w$ , a parameter which influences the interaction strength between liquid and solid.<sup>53,54,56</sup> Figure 1C shows the equilibrium contact angle as a function of  $\rho_w$ . It can be seen that  $\theta_{eq}$  monotonically decreases from 180 to 0° with the increase of  $\rho_w$  from 0 to 1. For simplicity, a sixth order polynomial is used for describing this relationship, which is shown as the solid line in Figure 1C.

**Time-Dependent Wetting Transition Model.** In order to quantitatively relate the progress of the wetting transition to time, the Arrhenius equation with an activation energy being the adhesion energy is used in a recent study by Seo et al.<sup>31</sup> Here, we use a similar approach to consider the rate of the Cassie–Wenzel wetting transition:

$$\frac{\partial A_{\text{wenzel}}}{\partial t} = A_{\text{cassie}}k = (A_{\text{total}} - A_{\text{wenzel}})k, \quad (2)$$

with  $k = Ce^{-E_a/RT}$

where  $C$  (unit, 1/s) is the pre-exponential factor which can be a function of fluid viscosity and surface geometry;  $E_a$  is the activation energy, which has been shown to be a function of intrinsic contact angle and interfacial tension;<sup>31</sup> and  $A_{\text{wenzel}}$  and  $A_{\text{cassie}}$  are the surface areas under the Wenzel state and the Cassie state, respectively. After solving the partial differential equation, we arrive at

$$\frac{A_{\text{wenzel}}}{A_{\text{total}}} = \phi = 1 + (\phi_0 - 1)e^{-kt} \quad (3)$$

where  $\phi_0$  is the initial liquid–solid contact fraction at  $t = 0$ . It should be pointed out that three distinct regimes have been identified during wetting, including (1) rapid spreading stage after several milliseconds of initial contact;<sup>57,58</sup> (2) groove-filling stage controlled by local forces, which is the focus in the current study; and (3) evaporation and condensation stage.<sup>31</sup> Equation 3 concerns the second stage; therefore, it is appropriate to assume a nonzero  $\phi_0$  after the first stage. The parameter  $k$  can be regarded as a transition rate, which is inversely proportional to the characteristic time of wetting transition  $\tau_{\text{WT}} = 1/k$ ; then we have

$$\phi = 1 + (\phi_0 - 1)e^{-t/\tau_{\text{WT}}} \quad (4)$$

Figure 2A shows the evolution of  $\phi$  with an initial solid–liquid contact fraction  $\phi_0 = 0.4$  for different characteristic times of wetting transition  $\tau_{\text{WT}}$ . Small values of  $\tau_{\text{WT}}$  correspond to cases where fast groove-filling events take place, and  $\phi$  quickly approaches 1, transiting to the Wenzel state. As  $\tau_{\text{WT}}$  increases, the speed of the wetting transition slows down, but  $\phi$  also ultimately approaches 1 as time increases. For intrinsically hydrophobic rough surfaces with a thermodynamically stable Cassie state,  $\tau_{\text{WT}} = \infty$ , which means the Cassie–Wenzel wetting transition will not occur spontaneously. Figure 2B shows the time evolution of the equilibrium contact angle calculated from eq 1 with a roughness ratio  $r_w = 1.1$ . In all cases  $\theta_{eq}$  decreases from 126.9 to 90.2°. Note that, as mentioned previously, the value of the characteristic time of wetting transition  $\tau_{\text{WT}}$  is a function of both surface features and fluid properties. However, in the current work, to limit our

investigation to the effects of the wetting transition during multiphase displacement, we do not aim to formulate theories on the characteristic time of the wetting transition. Instead,  $\tau_{\text{WT}}$  values are prescribed, covering a wide range of values.

To incorporate eq 4 into the lattice Boltzmann method, for each individual grain, the fictitious wall density is updated as a function of contact time  $t_c$  iteratively. The contact time can be calculated by  $t_c = T_i - T_i^c$ , where  $T_i$  and  $T_i^c$  are the current time step and the time step when the invading fluid comes into contact with the grain, respectively. The event of contact is detected by scanning all peripheral lattices of a grain. A value of 0 is adopted for  $t_c$  when there is no contact. Figure 2B shows how the equilibrium contact angle changes with solid–liquid contact time  $t_c$  at each individual grain for different characteristic times of wetting transition. This implies that the effective equilibrium contact angles can be different along the invasion front, depending on the invasion velocity. For a faster invasion front, corresponding to the situation where invasion takes place quickly and the time available for the wetting transition is limited, the equilibrium contact angle is larger. Therefore, the heterogeneity in the time scale of pore invasion can be simulated during multiphase displacement, where an invasion front with faster velocity experiences a larger effective contact angle. It is important to point out that, in order to significantly reduce the computation cost, we assume the wettability of a single grain to be homogeneous; i.e., all the peripheral lattices of one grain are updated together and have the same value of  $\rho_w$ . Realistically, it is not the case since the wetting state of one single grain can vary depending on the location; i.e., the contact angle would only change in the immediate vicinity of the contact line such that freshly covered sections of the grain would initially have high corresponding contact angles. Therefore, this assumption leads to underestimation of the contact angle for regions that have not been touched by invading fluid, while their neighbor lattices on the same grain have. However, when there is a large difference between the characteristic times of wetting transition and pore invasion, this error reduces significantly, which will be further discussed next. Note that, although in this work we focus on the Cassie–Baxter wetting transition, other theories describing different mechanisms affecting the contact angles such as the use of surface-active agents (e.g., surfactants, nanoparticles, etc.) can also be incorporated into the lattice Boltzmann method using a similar approach, which is however beyond the scope of the current work.

The rate of local pore invasion is quantified by defining the characteristic time of pore invasion:

$$\tau_{\text{PI}} = \frac{d}{V_{\text{in}}/\Phi} \quad (5)$$

where  $d = 48$  lu is the grain diameter. With  $V_{\text{in}} = 0.002$  lu and  $\Phi = 0.674$ ,  $\tau_{\text{PI}}$  is calculated to be 16 164 lu. Then, the ratio of time scales of wetting transition and pore invasion  $Dy$  is defined as

$$Dy = \frac{\tau_{\text{WT}}}{\tau_{\text{PI}}} \quad (6)$$

A large value of  $Dy$  represents cases where local pore invasion proceeds much faster than the wetting transition, where the defending fluid is trapped in the crevices of grains, leading to a larger contact angle due to the Cassie wetting state. Smaller

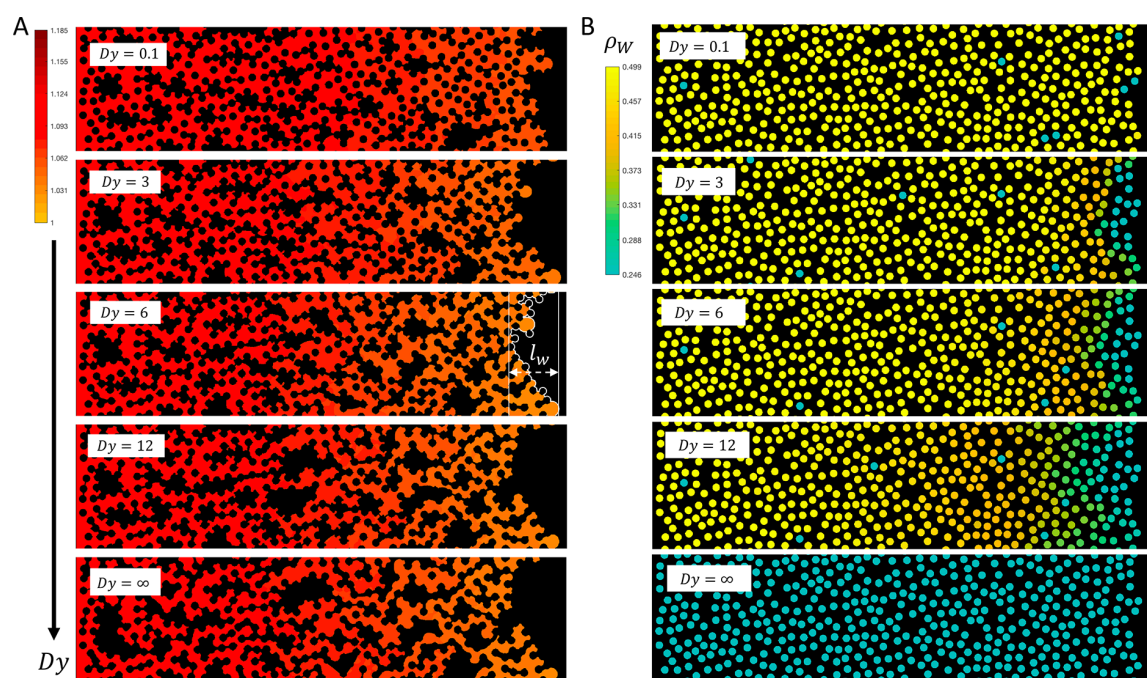


**Figure 3.** (A) Displacement patterns at percolation under varying  $Dy$ . The white solid curve at  $Dy = 6$  marks front length  $l_f$  along the invasion front. The length of the dashed arrow is front width  $l_w$ . The black color shows the location of defending fluid and grains, while the red color shows the density fluctuation of invading fluid, which represents pressure variation in the lattice Boltzmann method. (B) Wettability distribution at percolation for different values of  $Dy$ . Larger  $Dy$  indicates slower process of wetting transition compared with pore invasion. Colors represent values of the fictitious wall density  $\rho_w$ .

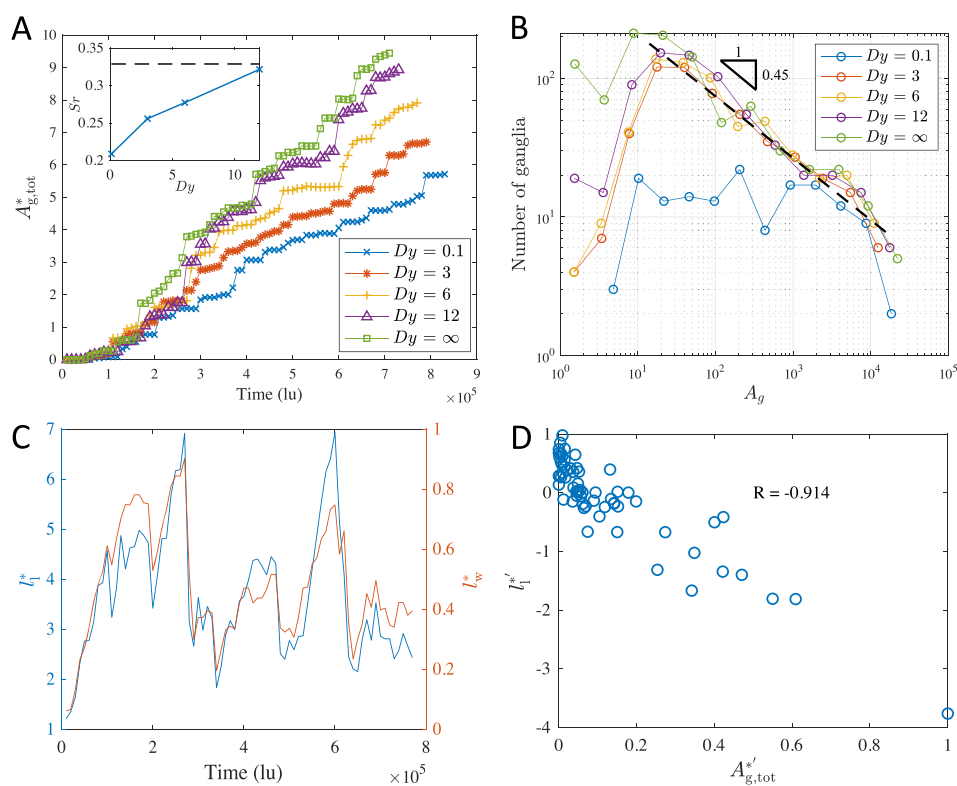


**Figure 4.** (A) Evolution of normalized total trapped ganglia area  $A_{g,tot}^*$ . The inset shows the final residual saturation of defending fluids  $S_r$  for different  $Dy$  values. The dashed line corresponds to the value of  $S_r$  with  $Dy = \infty$ . (B) Number of ganglia as a function of ganglia size  $A_g$ . (C) Evolution of normalized interfacial length  $l_f^*$  and width  $l_w^*$  for  $Dy = 6$ . (D) Correlation between the derivatives of  $A_{g,tot}^*$  and  $l_f^*$  for  $Dy = 6$ . The correlation coefficient is  $R = -0.914$ . For other cases,  $R = \{-0.858, -0.761, -0.909, -0.895\}$  for  $Dy = \{0.1, 3, 12, \infty\}$ , respectively.



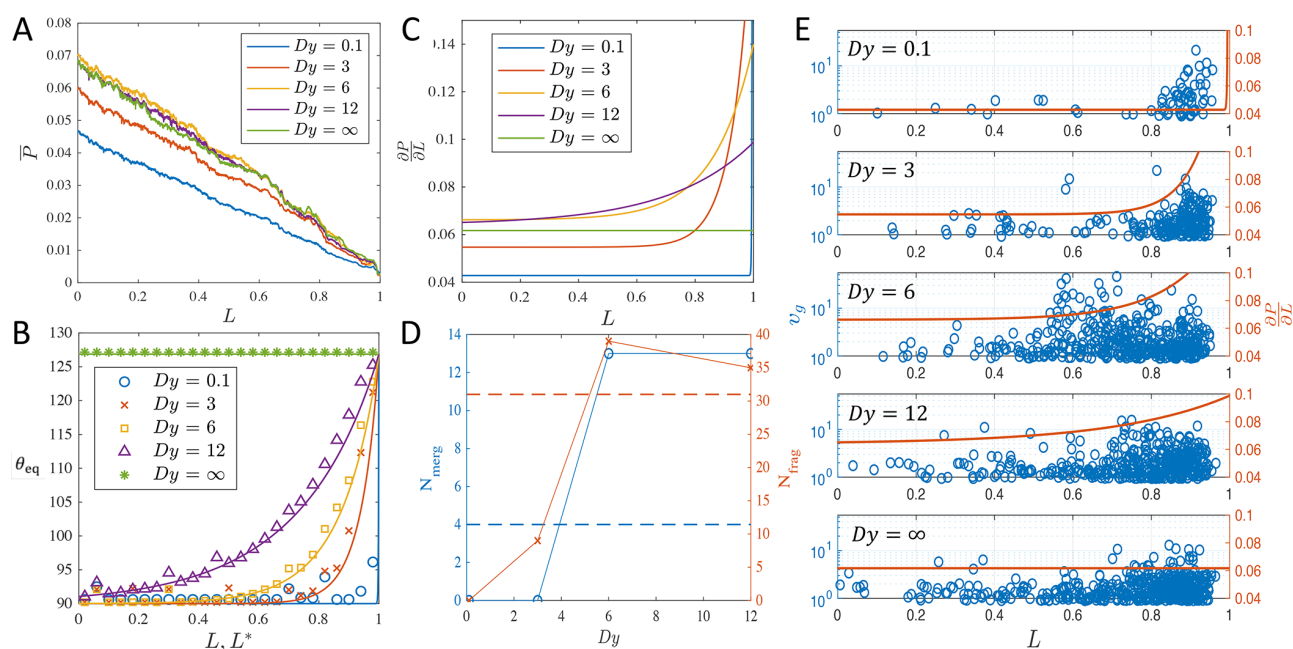


**Figure 5.** (A) Pressure distribution of invading fluid in lattice unit at percolation  $\bar{P}$  in lattice unit along  $x$ -direction, which is averaged along  $y$ -direction. (B) Equilibrium contact angle  $\theta_{eq}$  from theory (lines, plotted against  $L$ ) and simulations (symbols, plotted against  $L^*$ ) for different  $Dy$  values. (C) Total pressure gradient along  $L$  for different  $Dy$  values. (D) Number of events of merging ( $N_{merg}$ ) and fragmentation ( $N_{frag}$ ) at different  $Dy$  values. The dashed lines correspond to values with  $Dy = \infty$ . (E) Distribution of  $v_g$ , an indication of mobilized ganglia, along  $L$  from simulations (blue circular circles), and the total pressure gradient in lattice unit from theory (red solid lines).

values of  $Dy$  indicate a fast wetting transition toward the Wenzel state.

Since homogeneous roughness feature is assumed and  $Dy$  is fixed during each individual simulation, the same effective contact angle is expected during the whole displacement process, despite some local variations depending on the invasion dynamics. However, due to the assumption on the simplified wettability of each grain as mentioned before, instead of having similar equilibrium contact angles  $\theta_{eq}$ 's, the  $\theta_{eq}$  that is actually "experienced" by the invasion front will tend to decrease as the invasion front advances along each individual grain, as shown in Figure 1D. This error in contact angle may influence the pore-scale mechanisms during displacement, including burst, touch, and overlap.<sup>11,18,59</sup> Consider the rear side of one throat, i.e., after the invasion front passing through the minimum throat with adjacent grains and one of the pore-scale mechanisms is about to take place, Figure 2C shows the equilibrium contact angle at the invasion front along the latter half of the grain ( $d = 48$  lu), assuming a constant velocity  $v = V_{in}/\Phi$ . The red dashed arrow shows the direction of increasing  $Dy = \{0.1, 0.2, 0.4, 0.8, 1.6, 3.2, 6.4, 12.8, \infty\}$ . It is observed that all  $\theta_{eq}$ 's have the decreasing tendency except for infinite  $Dy$ . Figure 2D and the inset show the average and standard deviation of equilibrium contact angle  $\theta_{eq}$  as a function of  $Dy$ , respectively. Clearly, the error reaches a maximum at  $Dy \approx 1$ , indicating a comparable time scale between the wetting transition and pore invasion, and decreases as  $Dy$  moves away from 1. Therefore, we choose  $\tau_{WT} = 10^4 \times \{0.1, 5, 10, 20, \infty\}$ , which gives the corresponding  $Dy \approx \{0.1, 3, 6, 12, \infty\}$ . Note that, in order to have a wide range of  $Dy$  values, it is also possible to fix  $\tau_{WT}$  while changing  $\tau_{PI}$  through changing, for example, the injection velocity  $V_{in}$ . Nevertheless, we choose to fix  $\tau_{PI}$  because (1) the computation cost greatly increases with low  $V_{in}$ , (2) the numerical stability

of simulation decreases with large  $V_{in}$ , and (3) change in  $V_{in}$  results in different  $Ca$  values, which introduces extra variables such as the effect from the dynamic contact angle hysteresis due to viscous dissipation.<sup>60–63</sup>

## RESULTS AND DISCUSSION

**Displacement Efficiency.** The displacement patterns at percolation for five different  $Dy$  values are shown in Figure 3A, which qualitatively demonstrates the influence of wetting transition speed on the invasion morphology. The trapped defending fluid and grains are represented by black color. Red color shows the invading fluid. With increase in  $Dy$ , or larger characteristic time of wetting transition, it is observed that the invasion front becomes less stable and a larger amount of defending fluid is trapped inside the medium.

In order to quantitatively reveal the effect of  $Dy$ , Figure 4A shows the evolution of total area of trapped ganglia  $A_{g,tot}^*$ , which is defined by  $A_{g,tot}^* = A_{g,tot}/(dh)$ , where  $d$  and  $h$  are the grain diameter and injection width in lattice unit, respectively, and  $A_{g,tot}$  is the total area of trapped ganglia in lattice unit. Here, "ganglia" refers to the trapped clusters of defending fluid, although different names may be used according to the cluster size.<sup>64</sup> Stepwise increases in  $A_{g,tot}^*$  are observed, corresponding to individual trapping events. When the wetting transition progresses slowly during the displacement process (corresponding to large  $Dy$ ), the contact angle at pore scale becomes larger due to more defending fluids trapped in the surface grooves. This increase in effective contact angle suppresses cooperative pore-filling events, promoting trapping,<sup>16,65</sup> consistent with past results.<sup>11–14,16</sup> Moreover, the volume of trapped ganglia for cases with large  $Dy$  ( $Dy = 12$ , slow wetting transition) can be very close to the one with  $Dy = \infty$  where the wetting transition does not take place. However, from Figure 3B, there are significant differences in the wettability

distribution between  $Dy = 12$  and  $Dy = \infty$  except for the region near the invasion front. This implies that changes in contact angles behind the invasion front do not have a significant impact on the total trapping volumes, although they may affect the redistribution of the trapped ganglia. Figure 4A also shows that the simulation time (or percolation time) for different  $Dy$  values ranges from  $7 \times 10^5$  to  $8.5 \times 10^5$  time steps, which correspond to an actual time of around 20 h using 16 CPUs. The inset shows the residual saturation of defending fluid  $S_r$  for different  $Dy$  values. The black dashed line represents the  $S_r$  value with  $Dy = \infty$ . It is worth noting that it is possible to observe further reduction in residual saturation for porous media due to the connectivity of the defending phase trapped in the crevices of the pore space. But this phenomenon can only take place after breakthrough.<sup>66</sup>

The interfacial length in lattice unit  $l_l$  can be defined as the total front length between the defending fluid and the union of invading fluid and grains, as shown by the white solid curve in Figure 3A. The normalized value can be calculated as  $l_l^* = l_l/h$ . The interfacial width  $l_w$  is the span of  $l_l$  in the direction of injection, indicated by the dashed double arrow. It can also be normalized by  $l_w^* = l_w/h$ . Figure 4C shows the changes of interfacial length (blue curve) and width (red curve) during the displacement for the case with  $Dy = 6$ . It can be seen that they both fluctuate around a value while having a similar trend. Figure 4D shows the correlation between the derivatives of  $A_{g,tot}^*$  and  $l_l^*$ , which are denoted by  $A_{g,tot}^{*'} and  $l_l^{*'}$ , respectively. A correlation coefficient of  $R = -0.914$  is found, indicating that, for each trapping event, the total trapped area increases, while both  $l_l$  and  $l_w$  decrease, smoothing the invasion front. The patterns observed in Figure 4C,D also appear similarly in other cases with different  $Dy$  values ( $R = \{-0.858, -0.761, -0.909, -0.895\}$  for  $Dy = \{0.1, 3, 12, \infty\}$ , respectively).$

**Ganglia Size Distribution.** Figure 4B shows the ganglia size distribution for different  $Dy$  values at percolation. In the size range from 10 to  $10^4$  lu, a power-law relation is present between the number of ganglia and ganglia size for all simulation results except  $Dy = 0.1$ . In the case of  $Dy = 0.1$ , the effective contact angle is smaller than in other cases such that fewer trapping events occur during displacement, consequently leading to fewer trapped ganglia. The value of the exponent of the power-law relation, or the slope of the black dashed line as in Figure 4B, is associated with structure of the pore network, and a wide range of values have been observed.<sup>67</sup> In this case an exponent of  $-0.45$  is seen, indicated by the black triangle. Note that there are upper and lower bounds for the power-law relation of the distribution due to the limited size of the simulation domain and the minimum pore size, respectively. One can notice the large deviations of ganglia number at small  $A_g$ , where fewer trapping events occur at lower  $Dy$  values, implying that the wetting transition facilitates the stable displacement.

**Ganglia Mobilization.** We also look at the mobilization of trapped ganglia during the two-phase flow. The trapped defending phase can be mobilized due to the momentum transfer from the invading phase when viscous drag plays an important role.<sup>64</sup> Figure 5A shows the pressure distribution of invading fluid in lattice unit at percolation along the normalized length of area of interest  $L$  for different  $Dy$  values, where each value is averaged along the transverse direction. Overall, linear viscous pressure drop can be observed for all  $Dy$  values, with larger viscous pressure gradient for larger  $Dy$  values, although the difference is not significant for  $Dy > 3$ .

However, viscous pressure alone is not sufficient for describing the mobilization of trapped ganglia, since the spacial wettability gradient can also exert pressure onto the defending phase due to the time-dependent local contact angles. Figure 3B shows the wettability distribution of the porous medium at percolation. The colors represent the values of the fictitious wall density  $\rho_w$ , which is a direct function of contact angles according to Figure 1C. A wettability transition zone can be seen in the diagram, and the width of the transition zone is affected by  $Dy$ . For a more quantitative representation of the wettability distribution, symbols in Figure 5B show the equilibrium contact angle  $\theta_{eq}$  along  $L$  with a bin size of 0.04, which is again averaged in the transverse direction from the simulation results. To compare with theory, a Lagrangian length scale needs to be introduced to convert time into spacial information:

$$L^* = 1 - \frac{T_r V_{in}}{\phi(1 - S_r) X_{AOI}} \quad (7)$$

where  $X_{AOI}$  is the longitudinal length of area of interest in lattice unit. Note that  $L^* = 1$  represents the location of invasion front, whereas  $L^* < 1$  represents the location  $1 - L^*$  behind the invasion front. Then, the theoretical spacial wettability distribution is plotted with  $L^*$  as solid lines in Figure 5B. It can be seen that the theory matches well with the simulation results. Since the contact angle is larger near the front, from the perspective of defending fluid, this wettability gradient should facilitate the mobilization. To combine the pressure gradient from both viscous drag and interfacial tension, the total pressure gradient can be estimated as

$$\frac{\partial P}{\partial L} = \frac{\partial P_{vis}}{\partial L} + \frac{2\sigma}{\bar{L}_t} \frac{\partial(\cos \theta)}{\partial L} \quad (8)$$

where  $\bar{L}_t$  is the average throat size. Figure 5C shows the total pressure gradient  $\partial P/\partial L$  along  $L$  for different  $Dy$  values. It is interesting to see that although the effective contact angle and total trapped defending ganglia are the largest for  $Dy = \infty$ , due to the contribution from wettability change, the corresponding pressure gradient fails to dominate others, especially near the invasion front, whereas cases with  $Dy = 6$  and  $Dy = 12$  show larger pressure gradients, implying higher driving force for ganglia mobilization.

To verify our hypothesis, or the driving force for mobilizing ganglia, the distance of movement in lattice unit of each ganglion within a certain period (in this case 1000 time steps) or the characteristic velocity of ganglia  $v_g$  is plotted as blue circles in Figure 5E for different  $Dy$  values. These movements of an individual ganglion, or translation events, are a direct reflection of ganglia mobilization. The corresponding total pressure gradient is also shown as a red solid line. We can see concentrated mobilization events near the invasion front for all  $Dy$  values at  $L \approx 0.9$ . This is simply a technical issue due to the fact that we have more data near the invasion front during the injection process. Qualitatively, it can be seen that the distribution of  $v_g$  reasonably agrees with the total pressure gradient  $\partial P/\partial L$ .

During the displacement process, apart from translation events, the trapped defending fluid can also experience other types of dynamics, including coalescence where two ganglia merge into one, and fragmentation where one ganglion becomes two. The number of occurrences of these events should provide an indication on the ganglia mobilization.

Figure 5D shows the number of merging and fragmentation events for different  $Dy$  values. A nonmonotonic relationship can be observed, and the trapped ganglia are more “active” with  $Dy = \{6, 12\}$ , consistent with the results from Figure 5E. It is important to point out that the extent of influence due to change in contact angle can be different based on fluid property and flow conditions. For example, Holtzman and Segre<sup>16</sup> showed that further decreases in contact angle below  $60^\circ$  in the capillary dominated regime do not have a significant impact on the frequency of cooperative pore-filling events. The impact of variation in contact angle is also found to be dependent on porosity and disorder.<sup>68</sup> Besides, during flow processes in the viscous dominant regime with a viscosity ratio much larger or smaller than 1 (either stable displacement or viscous fingering), the effect of interfacial tension will diminish compared with viscous pressure; consequently, the impact on displacement patterns due to change in contact angle is expected to decrease. Also note that the events of ganglia motion, merging, and fragmentation are reported up to the time of percolation. Longer simulations are likely to introduce additional events until steady state is reached. However, since the main purpose of the current work is to compare the ganglia mobilization for the same geometry to highlight the effect of  $Dy$ , we did not further investigate the post-breakthrough behavior.

## CONCLUSIONS

The nontrivial correlation between the apparent contact angle and surface roughness in multiphase displacement is identified. We attribute the different behaviors of the apparent contact angle to the relaxation time available for the progress of the wetting transition, which is constrained by the speed of pore invasion. A theoretical model describing the time scale of the Cassie–Wenzel wetting transition is developed, where the equilibrium contact angle can be directly related to time. Then the model is incorporated into the lattice Boltzmann method for simulation of multiphase displacement in disordered porous media.

To quantitatively describe the competition between two characteristic pore-scale processes of wetting transition and pore invasion, a dimensionless time ratio,  $Dy$ , describing the relative speed of these two mechanisms is defined. We show that the displacement patterns can be significantly influenced by  $Dy$  at percolation, where more trapped defending ganglia are observed at large  $Dy$  due to either fast invasion velocity or slow wetting transition, leading to lower displacement efficiency. Through studying different mobilization dynamics of trapped ganglia, including translation, coalescence, and fragmentation, agreement is shown between the mobilization statistics and the total pressure gradient, considering the effects of both viscous drag and capillary pressure.

Our study reveals the possible significant effect of injection velocity and surface roughness on the transient contact angle during displacement in porous media, which consequently affects displacement patterns. We also want to emphasize the potential underestimation of the effective contact angle during displacement, as the experimentally measured correlation between the contact angle and roughness after the displacement process has been completed could be inaccurate due to subsequent wetting transition and fluid redistribution.

## AUTHOR INFORMATION

### Corresponding Author

**Yixiang Gan** – School of Civil Engineering, The University of Sydney, Sydney 2006, New South Wales, Australia;  
orcid.org/0000-0002-9621-0277; Email: yixiang.gan@sydney.edu.au

### Authors

**Zhongzheng Wang** – School of Civil Engineering, The University of Sydney, Sydney 2006, New South Wales, Australia; Navier, Ecole des Ponts, Université Gustave Eiffel, CNRS, 77420 Marne-la-Vallée, France

**Jean-Michel Pereira** – Navier, Ecole des Ponts, Université Gustave Eiffel, CNRS, 77420 Marne-la-Vallée, France

Complete contact information is available at:

<https://pubs.acs.org/10.1021/acs.langmuir.9b03780>

### Notes

The authors declare no competing financial interest.

## ACKNOWLEDGMENTS

This work was financially supported by the Australian Research Council (Projects DP170102886) and The University of Sydney SOAR Fellowship. Y.G. acknowledges the financial support of Labex MMCD(ANR-11-LABX-022-01) for his stay at Laboratoire Navier at ENPC. This research was undertaken with the assistance of the HPC service at The University of Sydney.

## REFERENCES

- (1) Lipiec, J.; Kuś, J.; Słowińska-Jurkiewicz, A.; Nosalewicz, A. Soil porosity and water infiltration as influenced by tillage methods. *Soil Tillage Res.* **2006**, *89*, 210–220.
- (2) Lake, L. *Fundamentals of Enhanced Oil Recovery*; SPE continuing education; Society of Petroleum Engineers: 1986.
- (3) Blunt, M.; Fayers, F.; Orr, F. M. Carbon dioxide in enhanced oil recovery. *Energy Convers. Manage.* **1993**, *34*, 1197–1204.
- (4) Szulczewski, M. L.; MacMinn, C. W.; Herzog, H. J.; Juanes, R. Lifetime of carbon capture and storage as a climate-change mitigation technology. *Proc. Natl. Acad. Sci. U. S. A.* **2012**, *109*, 5185–5189.
- (5) Matter, J. M.; Stute, M.; Snæbjörnsdóttir, S. Ó.; Oelkers, E. H.; Gislason, S. R.; Aradóttir, E. S.; Sigfusson, B.; Gunnarsson, I.; Sigurdardóttir, H.; Gunnlaugsson, E.; Axelsson, G.; Alfredsson, H. A.; Wolff-Boenisch, D.; Mesfin, K.; Taya, D. F. d. l. R.; Hall, J.; Dideriksen, K.; Broecker, W. S. Rapid carbon mineralization for permanent disposal of anthropogenic carbon dioxide emissions. *Science* **2016**, *352*, 1312–1314.
- (6) Lenormand, R.; Touboul, E.; Zarcone, C. Numerical models and experiments on immiscible displacements in porous media. *J. Fluid Mech.* **1988**, *189*, 165–187.
- (7) Armstrong, R. T.; Georgiadis, A.; Ott, H.; Klemin, D.; Berg, S. Critical capillary number: Desaturation studied with fast X-ray computed microtomography. *Geophys. Res. Lett.* **2014**, *41*, 55–60.
- (8) Yortsos, Y. C.; Xu, B.; Salin, D. Phase Diagram of Fully Developed Drainage in Porous Media. *Phys. Rev. Lett.* **1997**, *79*, 4581–4584.
- (9) Rabbani, H. S.; Or, D.; Liu, Y.; Lai, C.-Y.; Lu, N. B.; Datta, S. S.; Stone, H. A.; Shokri, N. Suppressing viscous fingering in structured porous media. *Proc. Natl. Acad. Sci. U. S. A.* **2018**, *115*, 4833–4838.
- (10) Holtzman, R. Effects of Pore-Scale Disorder on Fluid Displacement in Partially-Wettable Porous Media. *Sci. Rep.* **2016**, *6*, 36221.
- (11) Wang, Z.; Chauhan, K.; Pereira, J.-M.; Gan, Y. Disorder characterization of porous media and its effect on fluid displacement. *Phys. Rev. Fluids* **2019**, *4*, 034305.

- (12) Zhao, B.; MacMinn, C. W.; Juanes, R. Wettability control on multiphase flow in patterned microfluidics. *Proc. Natl. Acad. Sci. U. S. A.* **2016**, *113*, 10251–10256.
- (13) Trojer, M.; Szulcowski, M. L.; Juanes, R. Stabilizing Fluid-Fluid Displacements in Porous Media Through Wettability Alteration. *Phys. Rev. Appl.* **2015**, *3*, 054008.
- (14) Cieplak, M.; Robbins, M. O. Influence of contact angle on quasistatic fluid invasion of porous media. *Phys. Rev. B: Condens. Matter Mater. Phys.* **1990**, *41*, 11508–11521.
- (15) Jung, M.; Brinkmann, M.; Seemann, R.; Hiller, T.; Sanchez de La Lama, M.; Herminghaus, S. Wettability controls slow immiscible displacement through local interfacial instabilities. *Phys. Rev. Fluids* **2016**, *1*, 074202.
- (16) Holtzman, R.; Segre, E. Wettability Stabilizes Fluid Invasion into Porous Media via Nonlocal, Cooperative Pore Filling. *Phys. Rev. Lett.* **2015**, *115*, 164501.
- (17) Hu, R.; Wan, J.; Yang, Z.; Chen, Y.-F.; Tokunaga, T. Wettability and Flow Rate Impacts on Immiscible Displacement: A Theoretical Model. *Geophys. Res. Lett.* **2018**, *45*, 3077–3086.
- (18) Primkulov, B. K.; Talman, S.; Khaleghi, K.; Rangriz Shokri, A.; Chalaturnyk, R.; Zhao, B.; MacMinn, C. W.; Juanes, R. Quasistatic fluid-fluid displacement in porous media: Invasion-percolation through a wetting transition. *Phys. Rev. Fluids* **2018**, *3*, 104001.
- (19) Morrow, N. R. Wettability and Its Effect on Oil Recovery. *JPT, J. Pet. Technol.* **1990**, *42*, 1476–1484.
- (20) AlRatrou, A.; Blunt, M. J.; Bijeljic, B. Wettability in complex porous materials, the mixed-wet state, and its relationship to surface roughness. *Proc. Natl. Acad. Sci. U. S. A.* **2018**, *115*, 8901–8906.
- (21) Mehmani, A.; Kelly, S.; Torres-Verdin, C.; Balhoff, M. Residual oil saturation following gas injection in sandstones: Microfluidic quantification of the impact of pore-scale surface roughness. *Fuel* **2019**, *251*, 147–161.
- (22) Chen, Y.-F.; Wu, D.-S.; Fang, S.; Hu, R. Experimental study on two-phase flow in rough fracture: Phase diagram and localized flow channel. *Int. J. Heat Mass Transfer* **2018**, *122*, 1298–1307.
- (23) Wenzel, R. N. Resistance of solid surfaces to wetting by water. *Ind. Eng. Chem.* **1936**, *28*, 988–994.
- (24) Cassie, A. B. D.; Baxter, S. Wettability of porous surfaces. *Trans. Faraday Soc.* **1944**, *40*, 546–551.
- (25) Marmur, A. Wetting on Hydrophobic Rough Surfaces: To Be Heterogeneous or Not To Be. *Langmuir* **2003**, *19*, 8343–8348.
- (26) Gao, N.; Yan, Y. Modeling Superhydrophobic Contact Angles and Wetting Transition. *Journal of Bionic Engineering* **2009**, *6*, 335–340.
- (27) Mishra, H.; Schrader, A. M.; Lee, D. W.; Gallo, A.; Chen, S.-Y.; Kaufman, Y.; Das, S.; Israelachvili, J. N. Time-Dependent Wetting Behavior of PDMS Surfaces with Bioinspired, Hierarchical Structures. *ACS Appl. Mater. Interfaces* **2016**, *8*, 8168–8174.
- (28) Moulinet, S.; Bartolo, D. Life and death of a fakir droplet: Impalement transitions on superhydrophobic surfaces. *Eur. Phys. J. E: Soft Matter Biol. Phys.* **2007**, *24*, 251–260.
- (29) Peters, A. M.; Pirat, C.; Sbragaglia, M.; Borkent, B. M.; Wessling, M.; Lohse, D.; Lammertink, R. G. H. Cassie-Baxter to Wenzel state wetting transition: Scaling of the front velocity. *Eur. Phys. J. E: Soft Matter Biol. Phys.* **2009**, *29*, 391–397.
- (30) Sbragaglia, M.; Peters, A. M.; Pirat, C.; Borkent, B. M.; Lammertink, R. G. H.; Wessling, M.; Lohse, D. Spontaneous Breakdown of Superhydrophobicity. *Phys. Rev. Lett.* **2007**, *99*, 156001.
- (31) Seo, D.; Schrader, A. M.; Chen, S.-Y.; Kaufman, Y.; Cristiani, T. R.; Page, S. H.; Koenig, P. H.; Gizaw, Y.; Lee, D. W.; Israelachvili, J. N. Rates of cavity filling by liquids. *Proc. Natl. Acad. Sci. U. S. A.* **2018**, *115*, 8070–8075.
- (32) Lopes, D. M.; Ramos, S. M. M.; de Oliveira, L. R.; Mombach, J. C. M. Cassie-Baxter to Wenzel state wetting transition: a 2D numerical simulation. *RSC Adv.* **2013**, *3*, 24530–24534.
- (33) de Oliveira, L. R.; Lopes, D. M.; Ramos, S. M. M.; Mombach, J. C. M. Two-dimensional modeling of the superhydrophobic behavior of a liquid droplet sliding down a ramp of pillars. *Soft Matter* **2011**, *7*, 3763–3765.
- (34) Zhao, X. Wetting transition of water on graphite: Monte Carlo simulations. *Phys. Rev. B: Condens. Matter Mater. Phys.* **2007**, *76*, 041402.
- (35) Papadopoulos, P.; Mammen, L.; Deng, X.; Vollmer, D.; Butt, H.-J. How superhydrophobicity breaks down. *Proc. Natl. Acad. Sci. U. S. A.* **2013**, *110*, 3254–3258.
- (36) Domingues, E. M.; Arunachalam, S.; Mishra, H. Doubly Reentrant Cavities Prevent Catastrophic Wetting Transitions on Intrinsically Wetting Surfaces. *ACS Appl. Mater. Interfaces* **2017**, *9*, 21532–21538.
- (37) Amabili, M.; Giacomello, A.; Meloni, S.; Casciola, C. M. Intrusion and extrusion of a liquid on nanostructured surfaces. *J. Phys.: Condens. Matter* **2017**, *29*, 014003.
- (38) Arunachalam, S.; Das, R.; Nauruzbayeva, J.; Domingues, E. M.; Mishra, H. Assessing omniphobicity by immersion. *J. Colloid Interface Sci.* **2019**, *534*, 156–162.
- (39) Bahadur, V.; Garimella, S. V. Preventing the Cassie-Wenzel Transition Using Surfaces with Noncommunicating Roughness Elements. *Langmuir* **2009**, *25*, 4815–4820.
- (40) Nosonovsky, M. Multiscale Roughness and Stability of Superhydrophobic Biomimetic Interfaces. *Langmuir* **2007**, *23*, 3157–3161.
- (41) Nosonovsky, M.; Bhushan, B. Patterned Nonadhesive Surfaces: Superhydrophobicity and Wetting Regime Transitions. *Langmuir* **2008**, *24*, 1525–1533.
- (42) Yoshimitsu, Z.; Nakajima, A.; Watanabe, T.; Hashimoto, K. Effects of Surface Structure on the Hydrophobicity and Sliding Behavior of Water Droplets. *Langmuir* **2002**, *18*, 5818–5822.
- (43) Butt, H.-J.; Vollmer, D.; Papadopoulos, P. Super liquid-repellent layers: The smaller the better. *Adv. Colloid Interface Sci.* **2015**, *222*, 104–109.
- (44) Zheng, Q.-S.; Yu, Y.; Zhao, Z.-H. Effects of Hydraulic Pressure on the Stability and Transition of Wetting Modes of Superhydrophobic Surfaces. *Langmuir* **2005**, *21*, 12207–12212.
- (45) Bormashenko, E.; Whyman, G. On the Role of the Line Tension in the Stability of Cassie Wetting. *Langmuir* **2013**, *29*, 5515–5519.
- (46) Bormashenko, E.; Gendelman, O.; Whyman, G. Superhydrophobicity of Lotus Leaves versus Birds Wings: Different Physical Mechanisms Leading to Similar Phenomena. *Langmuir* **2012**, *28*, 14992–14997.
- (47) Wu, H.; Yang, Z.; Cao, B.; Zhang, Z.; Zhu, K.; Wu, B.; Jiang, S.; Chai, G. Wetting and Dewetting Transitions on Submerged Superhydrophobic Surfaces with Hierarchical Structures. *Langmuir* **2017**, *33*, 407–416.
- (48) Michael, N.; Bhushan, B. Hierarchical roughness makes superhydrophobic states stable. *Microelectron. Eng.* **2007**, *84*, 382–386.
- (49) Bormashenko, E.; Pogreb, R.; Whyman, G.; Erlich, M. Cassie-Wenzel Wetting Transition in Vibrating Drops Deposited on Rough Surfaces: Is the Dynamic Cassie-Wenzel Wetting Transition a 2D or 1D Affair. *Langmuir* **2007**, *23*, 6501–6503.
- (50) Bormashenko, E.; Pogreb, R.; Whyman, G.; Erlich, M. Resonance Cassie-Wenzel Wetting Transition for Horizontally Vibrated Drops Deposited on a Rough Surface. *Langmuir* **2007**, *23*, 12217–12221.
- (51) Bormashenko, E.; Pogreb, R.; Stein, T.; Whyman, G.; Erlich, M.; Musin, A.; Machavariani, V.; Aurbach, D. Characterization of rough surfaces with vibrated drops. *Phys. Chem. Chem. Phys.* **2008**, *10*, 4056–4061.
- (52) Shan, X.; Chen, H. Lattice Boltzmann model for simulating flows with multiple phases and components. *Phys. Rev. E: Stat. Phys., Plasmas, Fluids, Relat. Interdiscip. Top.* **1993**, *47*, 1815–1819.
- (53) Shan, X.; Doolen, G. Multicomponent Lattice-Boltzmann Model with Interparticle Interaction. *J. Stat. Phys.* **1995**, *81*, 379–393.
- (54) Kruger, T.; Kusumaatmaja, H.; Kuzmin, A.; Shardt, O.; Silva, G.; Viggien, E. M. *LBM - The Principles and Methods*; Springer: 2017.

- (55) Raiskinmäki, P.; Shakib-Manesh, A.; Jäsberg, A.; Koponen, A.; Merikoski, J.; Timonen, J. Lattice-Boltzmann Simulation of Capillary Rise Dynamics. *J. Stat. Phys.* **2002**, *107*, 143–158.
- (56) Huang, H.; Thorne, D. T.; Schaap, M. G.; Sukop, M. C. Proposed approximation for contact angles in Shan-and-Chen-type multicomponent multiphase lattice Boltzmann models. *Phys. Rev. E* **2007**, *76*, 066701.
- (57) Bird, J. C.; Mandre, S.; Stone, H. A. Short-Time Dynamics of Partial Wetting. *Phys. Rev. Lett.* **2008**, *100*, 234501.
- (58) Courbin, L.; Bird, J. C.; Reyssat, M.; Stone, H. A. Dynamics of wetting: from inertial spreading to viscous imbibition. *J. Phys.: Condens. Matter* **2009**, *21*, 464127.
- (59) Cieplak, M.; Robbins, M. O. Dynamical Transition in Quasistatic Fluid Invasion in Porous Media. *Phys. Rev. Lett.* **1988**, *60*, 2042–2045.
- (60) Cox, R. G. The dynamics of the spreading of liquids on a solid surface. Part 1 Viscous flow. *J. Fluid Mech.* **1986**, *168*, 169–194.
- (61) Voinov, O. V. Hydrodynamics of wetting. *Fluid Dyn.* **1977**, *11*, 714–721.
- (62) Blake, T.; Haynes, J. Kinetics of liquid-liquid displacement. *J. Colloid Interface Sci.* **1969**, *30*, 421–423.
- (63) Petrov, P.; Petrov, I. A combined molecular-hydrodynamic approach to wetting kinetics. *Langmuir* **1992**, *8*, 1762–1767.
- (64) Zarikos, I.; Terzis, A.; Hassanizadeh, S.; Weigand, B. Velocity distributions in trapped and mobilized non-wetting phase ganglia in porous media. *Sci. Rep.* **2018**, *8*, 13228.
- (65) Blunt, M. J. *Multiphase Flow in Permeable Media: A Pore-Scale Perspective*; Cambridge University Press: 2017.
- (66) Blunt, M. J. Physically-based network modeling of multiphase flow in intermediate-wet porous media. *J. Pet. Sci. Eng.* **1998**, *20*, 117–125.
- (67) Avendaño, J.; Lima, N.; Quevedo, A.; Carvalho, M. Effect of Surface Wettability on Immiscible Displacement in a Microfluidic Porous Media. *Energies* **2019**, *12*, 664.
- (68) Hu, R.; Lan, T.; Wei, G.-J.; Chen, Y.-F. Phase diagram of quasi-static immiscible displacement in disordered porous media. *J. Fluid Mech.* **2019**, *875*, 448–475.

## 5.2 Disorder Characterization and its Effects on Fluid Displacement

The second paper in this chapter focuses on the characterisation of topological disorder of porous media, and its combined effects with wettability on fluid displacement process. A novel disorder index  $I_v$  is proposed based on the Voronoi diagram. Porous media with different  $I_v$  are generated using Monte-Carlo process. Simulations of multiphase flow under different disorder and wetting conditions are carried out, and a phase diagram showing the impact from both factors is produced. By analysing the critical capillary pressure at pore scale, which considers both pore geometry and contact angle, we unify the impact of wettability and topological disorder on multiphase flow.

Corresponding paper: Wang, Z., Pereira, J.-M., & Gan, Y. (2020). Effect of wetting transition during multiphase displacement in porous media. *Langmuir*, 36(9), 2449–2458.

I was the primary researcher and author of this paper, being supervised by A/Prof. Yixiang Gan, Dr. Kapil Chauhan, and Prof. Jean-Michel Pereira.

**Disorder characterization of porous media and its effect on fluid displacement**Zhongzheng Wang,<sup>1,2</sup> Kapil Chauhan,<sup>1</sup> Jean-Michel Pereira,<sup>2</sup> and Yixiang Gan<sup>1,\*</sup><sup>1</sup>*School of Civil Engineering, The University of Sydney, NSW 2006, Australia*<sup>2</sup>*Laboratoire Navier, UMR 8205, Ecole des Ponts ParisTech, IFSTTAR, CNRS, UPE, France*

(Received 19 December 2018; published 29 March 2019)

We investigate the effects of topological disorder and wettability on fluid displacement in porous media. A modified disorder index  $I_v$  is proposed to characterize the disorder of porous media. By changing  $I_v$ , different displacement patterns (stable displacement and fingering) under the same flow condition and fluid property are obtained. We analytically demonstrate how increase in disorder promotes fingering due to uneven distribution of local capillary pressure. It is shown that the displacement efficiency for different wettability conditions and disorder well correlates with the distribution of local capillary pressure. A power-law relation between fluid-fluid interfacial length and saturation of invading fluid is proposed by taking geometry into account, where the parameters in power-law relation can be predicted by the capillary index,  $I_c$ , unifying the effects of topological disorder and wettability.

DOI: [10.1103/PhysRevFluids.4.034305](https://doi.org/10.1103/PhysRevFluids.4.034305)**I. INTRODUCTION**

Displacement of multiphase fluids in porous media is involved in many industrial and natural processes, such as injection of CO<sub>2</sub> into geological formations [1,2], enhanced oil recovery [3,4], remediation of contamination in aquifer systems [5], and water infiltration into soil [6]. Studies have been conducted with a focus on impacts of flow conditions and fluid properties on displacement of multiphase flows [7,8], and effects of gravity [9] and wettability [10–12], while less attention has been paid on correlating the pore-scale disorder of porous media with the fluid displacement.

The displacement patterns, including capillary fingering (CF), viscous fingering (VF), and stable displacement (SD), are primarily controlled by capillary number,  $Ca$ , and viscosity ratio,  $M$ , between the defending and invading fluids [13–18]. When the invading fluid is more viscous than the defending fluid, i.e.,  $M < 1$ , the displacement patterns tend to shift from SD to CF with the decrease of  $Ca$ , indicating the dominance of the interfacial tension. While in the case of  $M > 1$ , increase of  $Ca$  modifies the flow toward VF. At the same time, wettability is also proven to play an important role: Increasing contact angle of invading fluid results in more efficient displacement at all  $Ca$  [19–21], but when the contact angle exceeds a critical value, the trend is reversed due to *corner flow* [12].

Another important factor that influences fluids displacement is disorder of the porous media. For flows dominated by capillary effects (low  $Ca$ ), increase in disorder promotes fingering, leading to a transition from SD to CF [10,22]. While for large  $Ca$  with  $M > 1$ , high disorder modifies the viscous fingerings to become more chaotic instead of having ordered patterns in regular media [13]. When both capillary and viscous effects are important, Holtzman [23] found that increase in disorder leads to higher interfacial area and lower displacement efficiency due to trapping. Holtzman [23] also offer

\*yixiang.gan@sydney.edu.au

subtle observations on effects of disorder by considering both capillary and viscous effects through scaling analysis [23]. However, many pore-scale simulation models assume quasistatic displacement [15], thus not capable of properly simulating dynamic mechanisms which are crucial even in slowly driven systems [21]. Despite a recent improvement of pore-scale simulation on ability of capturing nonlocal nature of interface dynamics [21], some processes during multiphase flow still remain un-captured such as droplet fragmentation [24]. In addition, due to the complex interplay among fluids properties, flow conditions, and topological features, the study of disorder effects on fluid displacement remain an active area of research, and attracts increased attention in the recent years with the help of development in microfluidics and advances in computational methods.

Multiphase flow in porous media has been studied both experimentally using micromodels [12,15,16,25–27] and numerically by a range of simulation methods. Pore-network (PN) models, though computationally efficient, have limited predictive capability and accuracy due to simplification of pore geometries and/or flow equations [28–30]. Statistical models including diffusion-limited aggregation (DLA), anti-DLA, and invasion percolation (IP) have been used to simulate VF, SD, and CF, respectively. However, these “specialized” models cannot capture transitions between different regimes [18,31]. Grid-based methods with interface tracking such as volume of fluid (VOF) method and level set (LS) method have been proposed to study multiphase flow in porous media [32–36]. However, they suffer from numerical instability at the interface when interfacial tension becomes dominant for microdroplets [37]. In addition, they have only been applied to simple pore geometries due to relatively high computational costs. The lattice Boltzmann method (LBM), as a mesoscale method, has been developed into a powerful tool for flow simulation in porous media [38–42]. Comparing to other numerical methods, the LBM is particularly suitable for pore-scale simulation of multiphase flows due to its ability of handling complex geometries and also being able to be massively parallelized. Therefore, it has been applied to study many problems in fluid mechanics [43–45].

In this paper, we investigate the effects of disorder and their coupling with wettability on fluid displacement in porous media. To better describe multiphase flow in porous media, a modified disorder index  $I_v$  is proposed to characterize disordered geometry by reflecting the degree of fluctuation of local porosity. Samples are generated to have distinct values of  $I_v$  for numerical simulations using lattice Boltzmann method. Through controlling the disorder of geometry, we are able to produce different displacement patterns (stable displacement and fingering) under the same capillary number and viscosity ratio, providing new insights toward the conventional displacement phase diagram which is independent on system geometry. We demonstrate how increase in disorder collaborated with interfacial phenomena promote fingering due to uneven distribution of local capillary pressure. It is shown that for different wettability conditions and disorder, the displacement efficiency well correlates with the distribution of local capillary pressure. Finally, a power-law relation between fluid-fluid interfacial length and saturation of invading fluid is constructed. The parameters in power-law relation can be predicted by the capillary index,  $I_c$ , which combines the effects of topological disorder and wettability.

## II. METHOD

### A. Media generation and characterization

Our geometry is a rectangular domain filled with circular obstacles to simulate the solid phase in porous media as shown in Fig. 1. The porosity of the medium, defined as the ratio of void area to total area in the 2D space, is controlled by varying the diameter of the obstacles. These obstacles are initially regularly placed on a triangular lattice.

To characterize the disorder of the medium, we use similar idea from Laubie *et al.* [46] but a different calculation method: Instead of using fixed square meshing in their study of mechanical behavior of solid material (originally named as  $I_d$ ), a Voronoi diagram is constructed for obtaining the local porosity, then a disorder index  $I_v$  can be defined as the corrected standard deviation of local



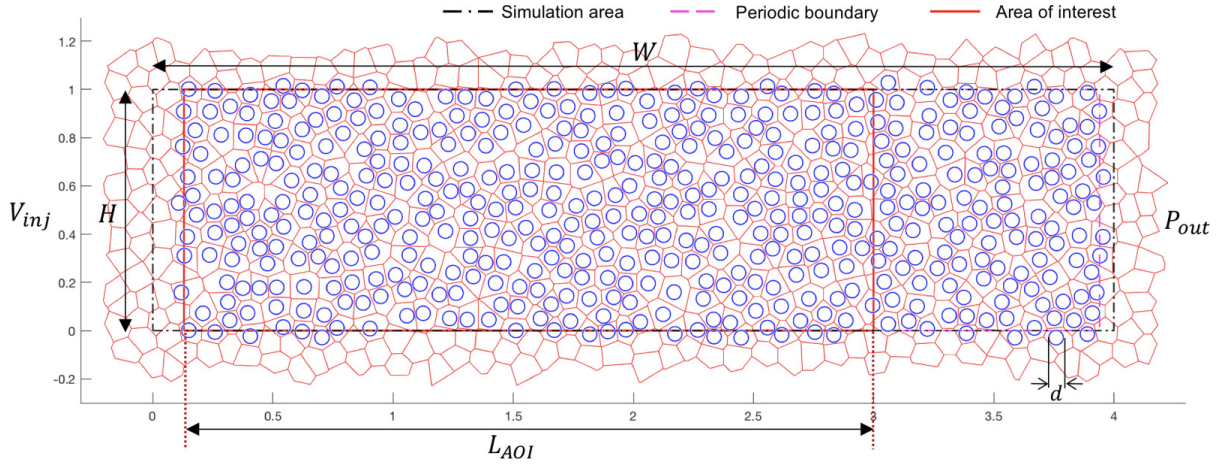


FIG. 1. Our porous medium is composed of 440 circular obstacles with diameter  $d = 0.06$ , which are initially regularly placed on a triangular lattice. The area enclosed by black dot-dash line is the simulated area with injection width  $H$  and longitudinal length  $W$ , while our results and analysis are based on the area of interest ( $L_{AOI}$ ), which is enclosed by red solid line. Geometrical periodicity in horizontal and vertical direction is ensured inside periodic boundary (purple-dashed line). The invading fluid is injected from the left with a constant velocity  $V_{inj}$ . The pressure at the right end is set to be constant  $P_{out}$ . Periodic boundary condition is imposed at top and bottom of the simulation area.

porosity:

$$I_v = \sqrt{\frac{\sum_{n=1}^N (\phi_n - \bar{\phi})^2}{N - 1}}, \quad (1)$$

where  $N$  is the number of obstacles in the domain,  $\phi_n$  is the local porosity within the Voronoi cell, and  $\bar{\phi}$  is the overall porosity of the medium.

Disorder is introduced by Monte Carlo iterative movement of each obstacle with an apparent diameter  $D_{app} = \lambda D$  with  $\lambda \in [1, D_{max}/D]$ , where  $D$  is the original diameter of obstacle and  $D_{max}$  is the maximum diameter to achieve the maximum packing, e.g., ideally  $\frac{\sqrt{3}\pi}{6}$  in 2D, and its value depends on the system dimension and number of obstacles. Thus,  $\lambda = 1$  corresponds to a fully disordered system where no restriction is applied during perturbation except that overlap is avoided, while  $\lambda = D_{max}/D$  corresponds to a regular system where no obstacle is able to move since they are already in contact with each other according to their apparent diameter. Here, we focus on media with obstacles of same size. Periodicity is ensured in both horizontal and vertical direction for obstacle distribution and for the consequent Voronoi diagram in the periodic boundary (Fig. 1). During each time-step, perturbation is applied to each particle, after which the disorder index  $I_v$  is calculated. This process stops when  $I_v$  stabilizes around a certain value for given  $\lambda$  (the fluctuations in  $I_v$  are generally smaller than 5% at the end). Thus,  $I_v = 0$  corresponds to a perfectly ordered system, exhibiting no variation in local porosity; whereas large values of  $I_v$  correspond to disordered systems by reflecting fluctuation of local porosity with respect to fully ordered one. We found that the disorder index  $I_v$  has a monotonic correlation with  $\lambda$ : as  $\lambda$  decreases,  $I_v$  increases and the system becomes more disordered. It is also found that the achievable maximum value of  $I_v$  is dependent on the size of system domain, total number of obstacles, and the overall porosity. With our choice of a simulation domain with a length to width ratio  $W/H = 4$ , and a periodic domain with  $x \in [0.1299, 3.9404]$  and  $y \in [0, 1]$  filled with 440 obstacles having a diameter of 0.06 (corresponding to an overall porosity of 0.6735),  $I_v \in [0, 0.08]$ . Using this method, five geometries with distinct disorder have been generated for simulation with  $I_v = [0, 0.020, 0.036, 0.047, 0.054]$  (see Fig. 2). Generally, with increasing  $I_v$ , the medium becomes more disordered and the variations in throat sizes becomes larger.

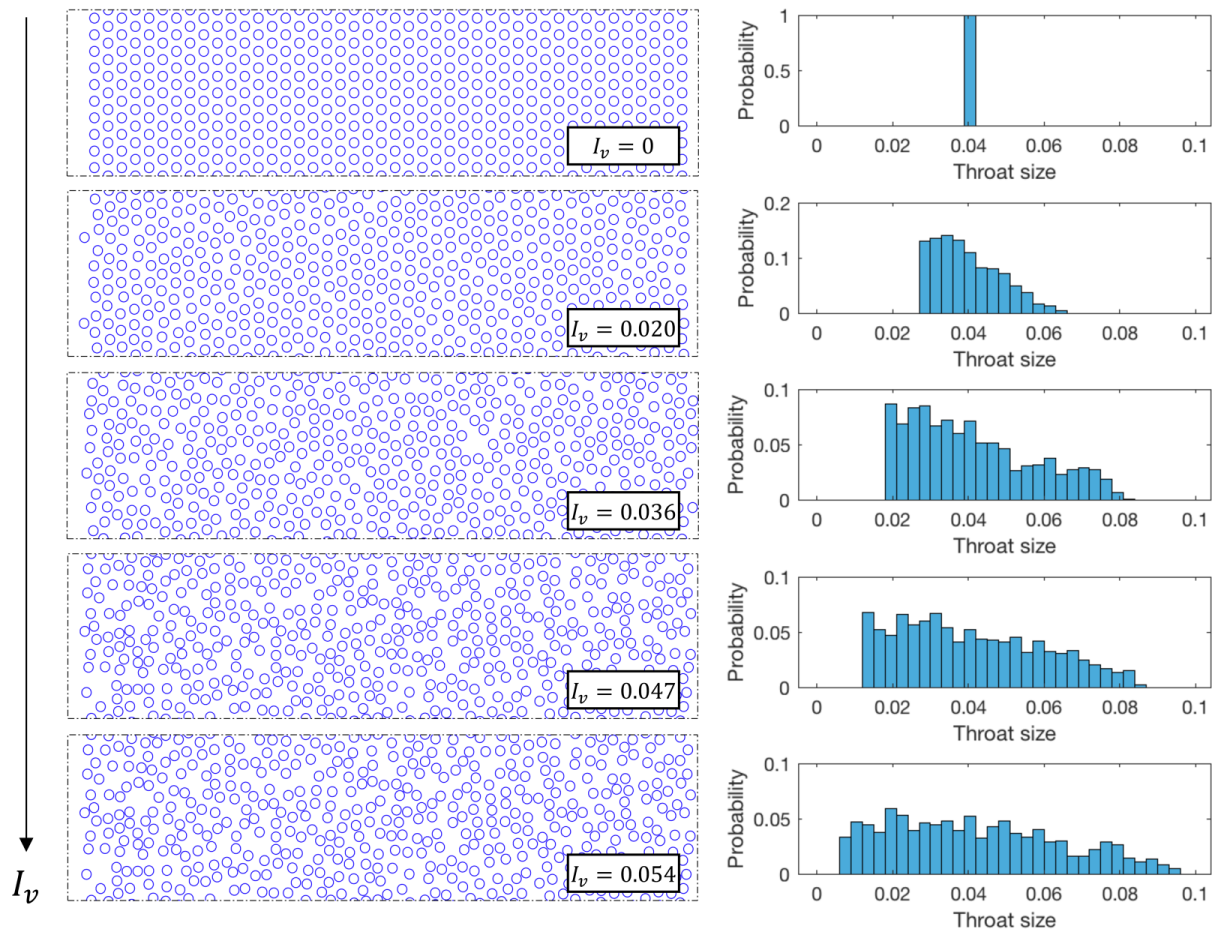


FIG. 2. Generated porous media and corresponding throat size probability distribution. From top to bottom,  $I_v = 0, 0.020, 0.036, 0.047, 0.054$ .

It is necessary to elaborate on reasons to introduce  $I_v$  instead of directly using  $\lambda$  as the disorder parameter [10,23,25,47]. First, although a monotonic relation has been observed between  $\lambda$  and  $I_v$ , from the definitions,  $\lambda$  is a parameter for generating the geometry controlling the minimum distance between obstacles, while  $I_v$  is the parameter for geometry characterization. Second, at the start of perturbation, the disorder of geometry can be quite different (usually in an increasing trend) for the same  $\lambda$ , until a sufficient number of iterations have passed. This is reflected by  $I_v$  having an increasing tendency followed by fluctuation around a constant value, without which it is hard to define how many iterations are “sufficient.” Finally, due to the the construction of Voronoi diagram for calculating  $I_v$ , each local porosity is dependent on its proximity of adjacent obstacles. Therefore, a large  $I_v$  not only reflects the uneven spacial distribution of individual obstacles, but also implies the existence of dense clusters, which has strong influences on regional trapping as we will show in our results.

### B. Simulation method

Standard lattice Boltzmann method with D2Q9 lattice is used for our 2D numerical simulations, which includes streaming and collision steps as

$$f_i(\mathbf{x} + \mathbf{c}_i \Delta t, t + \Delta t) = f_i(\mathbf{x}, t) + \Omega_i(\mathbf{x}, t), \quad (2)$$

where  $f_i$  is the density distribution function in  $i$ th direction. In this study, Bhatnagar-Gross-Krook (BGK) approach was preferred to multirelaxation time (MRT) one due to extra computational

resources and complexity required for the latter [42]. The BGK collision operator is

$$\Omega_i(\mathbf{x}, t) = -\frac{f_i - f_i^{\text{eq}}}{\tau} \Delta t, \quad (3)$$

which relaxes the distribution function towards an equilibrium  $f_i^{\text{eq}}$  at a rate determined by the relaxation time  $\tau$ . The equilibrium distribution function is given by

$$f_i^{\text{eq}}(\mathbf{x}, t) = \omega_i \rho \left[ 1 + \frac{\mathbf{u} \cdot \mathbf{c}_i}{c_s^2} + \frac{(\mathbf{u} \cdot \mathbf{c}_i)^2}{2c_s^4} - \frac{\mathbf{u} \cdot \mathbf{u}}{2c_s^2} \right], \quad (4)$$

where  $\omega_i$  is the weight for the  $i$ th direction. We use Shan-Chen multicomponent model originally proposed by Refs. [38,39]. They introduced an interparticle force as

$$F^{\text{SC}(\sigma)}(\mathbf{x}) = -\psi^{(\sigma)}(\mathbf{x}) \sum_{\tilde{\sigma} \neq \sigma} G_{\tilde{\sigma}\sigma} \sum_i \omega_i \psi^{(\tilde{\sigma})}(\mathbf{x} + \mathbf{c}_i \Delta t) \mathbf{c}_i \Delta t, \quad (5)$$

where  $\psi^{(\sigma)}$  is the “effective” density function for  $\sigma$  component, and  $G$  is a simple scalar that controls the strength of the interaction. To model immiscible fluids, the interaction strength  $G$  must be positive, simulating the repulsive force between different components. By adopting different fictitious wall densities, contact angles can be tuned [48]. Regularized boundary condition proposed by Latt and Chopard [49] is adopted to achieve second-order accuracy. For more detailed information about lattice Boltzmann method, we refer to Mohamad [50] and Kruger *et al.* [42]. We choose a mesh size of  $800 \times 3200$  lu<sup>2</sup> (lu: lattice unit) for the simulation area such that at least 10 lattices are in between the smallest throat to ensure the grid is fine enough [51]. Each time after the generation of media, the minimum throat distance  $r_{\text{min}}$  is determined. To ensure minimum number of lattices  $N_{\text{min}}$  along  $r_{\text{min}}$ , the number of lattices required in vertical direction for the simulation domain is calculated as  $M_v = \frac{N_{\text{min}}}{r_{\text{min}}} \times H$ , and  $M_h = 4 \times M_v$  for horizontal direction, where  $H$  is the height of the simulation domain shown in Fig. 1. Note that this method assumes  $r_{\text{min}}$  and principal directions can be aligned. For example, with  $N_{\text{min}} = 10$  and  $r_{\text{min}} = 0.02$ , the mesh needs to be (at least)  $500 \times 2000$ . Finer mesh is required as the topological disorder increases (reduce in apparent diameter leads to smaller possible  $r_{\text{min}}$ ). After examining all possible cases, we finally choose a mesh of  $800 \times 3200$  to ensure  $N_{\text{min}} = 10$  for all simulation cases. The kinematic viscosities for both fluids are 0.1667 lu. The invading and defending fluids have densities of 1 and 0.8 lu, respectively, leading to a viscosity ratio  $M = 0.8$ . The interfacial tension can be calculated using Young-Laplace equation, which is 0.2152 lu. The invading fluid is injected from the left with a constant velocity of  $V_{\text{inj}} = 0.005$  lu, leading to a capillary number  $\text{Ca} = \frac{V_{\text{inj}} \mu_{\text{def}}}{\gamma} = 0.0031$ . The pore-scale Reynolds number is less than 10. The outlet pressure at the right end is set to be a constant of 0.2667 lu. Periodic boundary condition is applied at top and bottom of the simulation area. Overall, 25 simulations are carried out for five different disorders ( $I_v = 0, 0.020, 0.036, 0.047, 0.054$ ) and five different contact angles ( $\theta = 35^\circ, 62^\circ, 89^\circ, 109^\circ, 128^\circ$ ).

### III. RESULTS AND DISCUSSION

The displacement patterns for different wettability conditions and topological disorder are shown in Fig. 3. These are qualitative demonstrations of effects of wettability and disorder on fluid displacement in porous media. Note that these snapshots correspond to the final stage of simulation, which is when the invading fluid reaches the right end of the periodic boundary (see Fig. 1). Generally, stronger fingering and larger trapped area of defending fluid are observed when the medium becomes more disordered (increasing  $I_v$ ) and more hydrophobic (increasing  $\theta$ ), implying a less efficient displacement, consistent with previous observations [9–12,19–21,23,52]. Figure 3 also demonstrates the “competition” between the destabilizing effect due to uneven distribution of capillary resistance and stabilizing effect from cooperative pore filling events, which have a higher occurrence when contact angle is small. To provide quantitative information about these

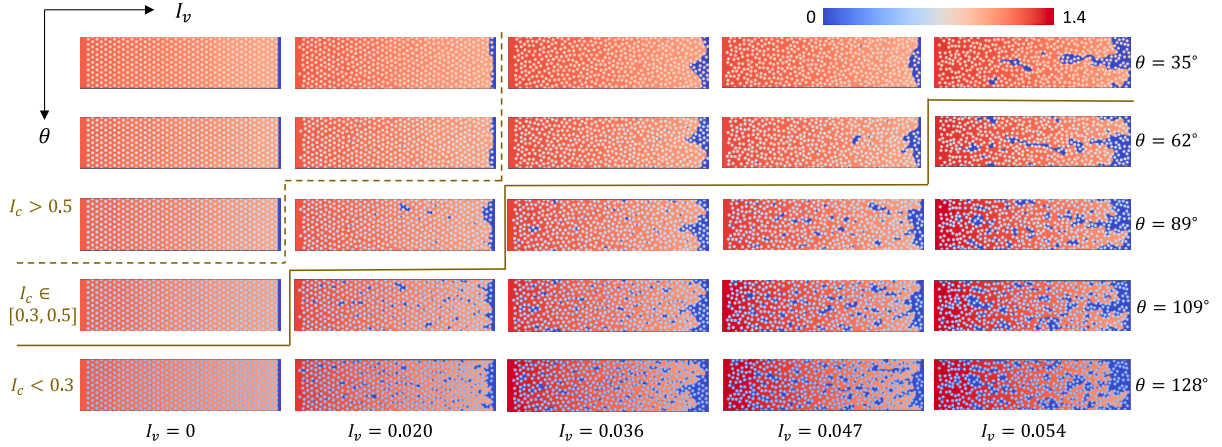


FIG. 3. Displacement patterns (from data of invading fluid) for different disorder (left to right,  $I_v = 0, 0.020, 0.036, 0.047, 0.054$ ) and wettability (top to bottom,  $\theta = 35^\circ, 62^\circ, 89^\circ, 109^\circ, 128^\circ$ ). The color map represents the density of invading fluid in lattice unit. Note that in LBM, the density fields of invading and defending fluids are stored in separate matrices. Here only the matrix storing data of invading fluid is shown. The blue color (density of invading fluid being zero) stands for the location of defending fluid, and the density fluctuation represents the pressure variation.

patterns, the normalized fluid-fluid interfacial length,  $L^* = \frac{\text{interfacial length}}{\text{width of geometry}}$ , is calculated and plotted as a function of saturation of invading fluid  $S$  for each time-step (Fig. 4). Note that to exclude the boundary effect at outlet we conduct representative volume analysis and found an area of interest with  $L_{\text{AOI}} = 3$  well captures the displacement data, so it is within this area (Fig. 1) our results are based on. Figure 4 shows that the rates at which interfacial length increase are larger as the media become more disordered (following the direction of black arrow) for all wettability conditions. This dependence becomes stronger as the contact angle increases, which again can be explained by the stabilizing effect of wettability [20,21]: trapping is mitigated by cooperative pore filling, or overlap, during displacement for disordered media (corresponding to the four collapsed curves for  $\theta = 35^\circ$ ). As the contact angle increases, this “mitigating effect” is reduced such that more trapping events occur, leading to higher interfacial length. Furthermore, we also quantify (a) the residual saturation [Figs. 5(a) and 5(c)] and (b) the ratio of final interfacial length to saturation [Figs. 5(b) and 5(d)] as functions of  $I_v$  and  $\theta$ : increase in  $I_v$  and  $\theta$  leads to decrease in displacement efficiency and increase in interfacial length per unit of saturation. These results again demonstrate the combined impacts of topological disorder and wettability.

To analytically investigate how wettability and disorder cooperate together to influence fluid displacement, we start with the equation that contain the physics of fluid displacement in multiple

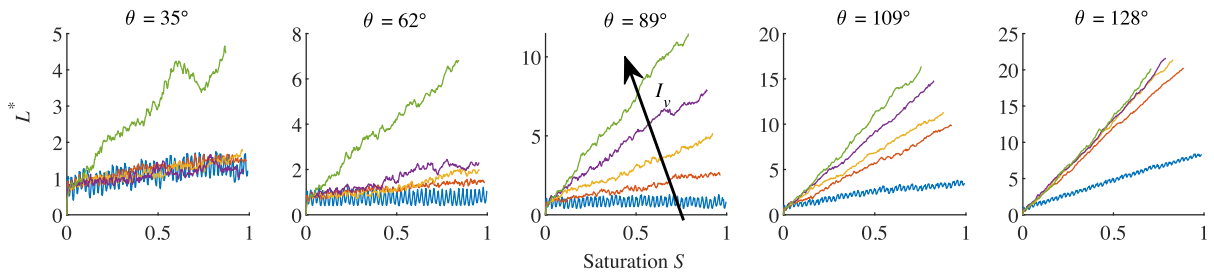


FIG. 4. Normalized fluid-fluid interfacial length ( $L^*$ ) as a function of saturation of invading fluid ( $S$ ) for different wettability and topological disorder. The black arrow indicates the direction of increasing disorder:  $I_v = 0, 0.020, 0.036, 0.047, 0.054$  corresponding to blue, orange, yellow, purple, and green curves, respectively.

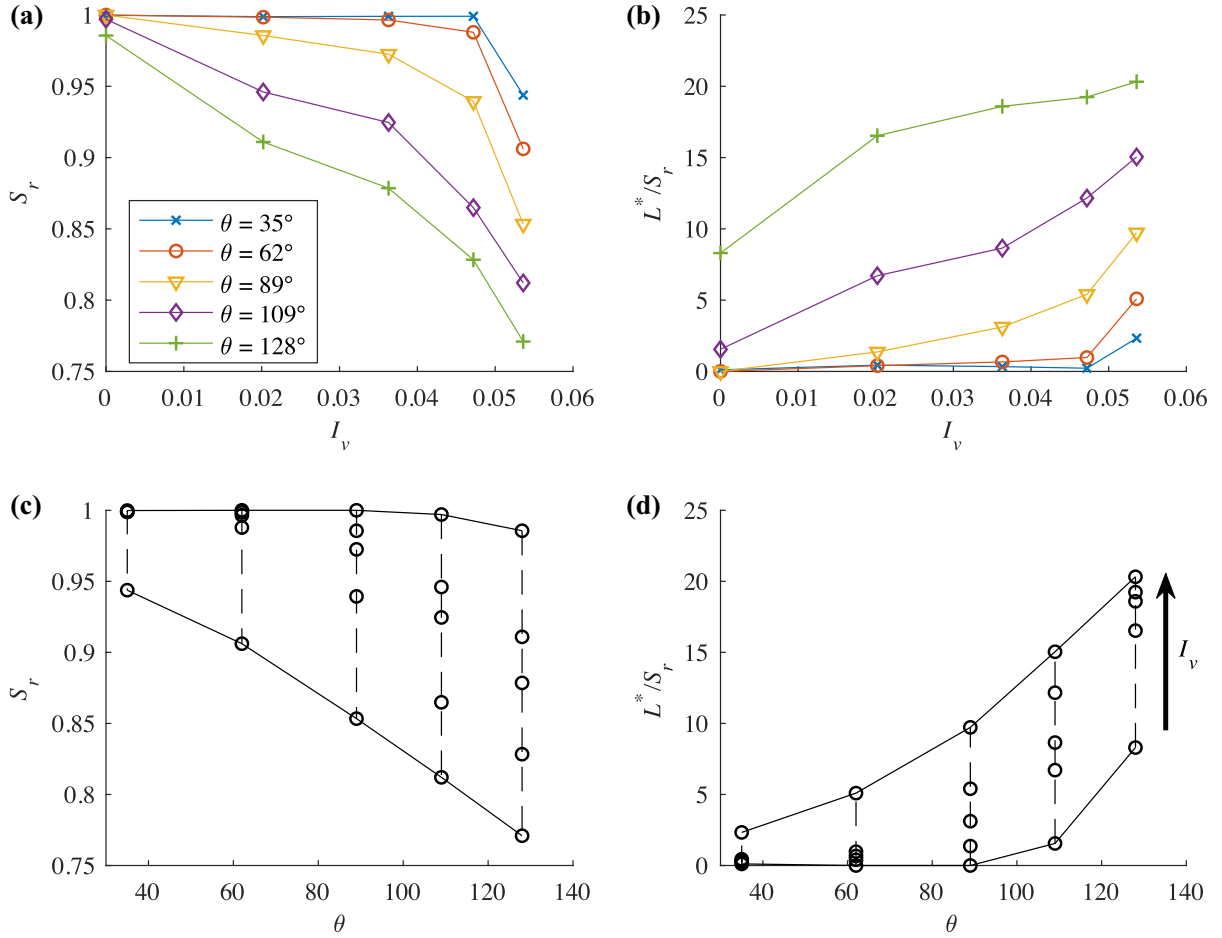


FIG. 5. (a) Final saturation of invading fluid  $S_r$  (or displacement efficiency, which is the fraction of defending fluid that has been displaced from the media at the end of the simulation) as a function of  $I_v$  and  $\theta$ . (b) Final normalized interfacial length  $L^*$  over final saturation  $S_r$  as a function of  $I_v$  and  $\theta$ . (c), (d) Same data set as a function of contact angle  $\theta$  for different topological disorders. Black arrow indicates the direction of increasing values of  $I_v$  from 0 to 0.054.

throats as suggested by Lenormand *et al.* [15]:

$$q = K_1(P - P_{c_1})^+ + K_2(P - P_{c_2})^+ + \dots = \sum_{n=1}^N K_n(P - P_{c_n})^+, \quad (6)$$

where  $q$  is the total flow rate,  $N$  is total number of throats,  $K_n$  is the hydraulic conductance at local pore throat  $n$ ,  $P$  is the pressure difference of invading and defending fluids, and  $P_{c_n}$  is the local capillary pressure providing resistance to the invasion of throat  $n$ . Locally, as long as  $P$  is smaller than  $P_{c_n}$ , there is no displacement. Then, the pressure difference between invading and defending fluids increases as more invading fluid is injected, resulting in  $P > P_{c_n}$  at throat  $n$ , leading to local throat invasion. Thus, in absence of viscous fingering, it is the uneven distribution of local capillary pressure that leads to uneven invasion of pores and consequent trapping and fingering, which ultimately affects the fluid-fluid interfacial length and displacement efficiency. To calculate the maximum allowable capillary pressure  $P_{c,\max}$  before a throat is invaded, we consider three basic pore-scale mechanisms: “burst,” “touch,” and “overlap” [53]. First, the equation for capillary pressure  $P_c$  at throat  $n$  in porous medium filled with circular obstacles of same diameter can be calculated by

$$P_{c_n} = \frac{2\gamma \sin(\alpha + \theta - 90^\circ)}{h_n - d \cos(\alpha)}, \quad (7)$$

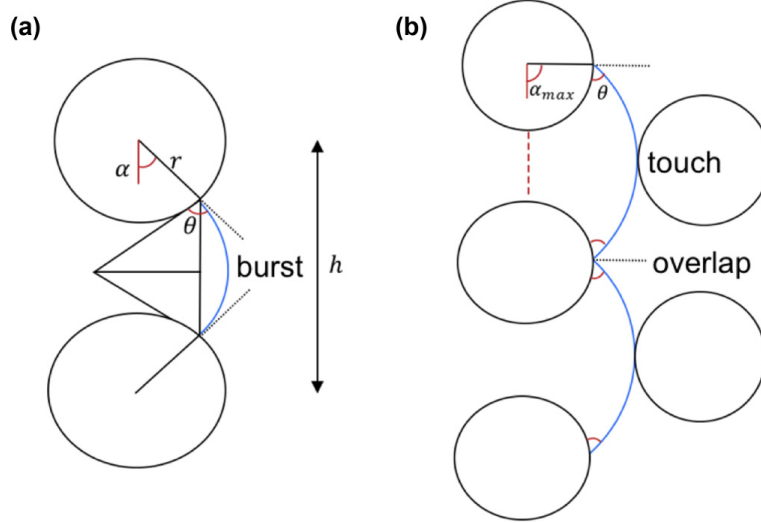


FIG. 6. (a) Schematic figure for calculation of local capillary pressure as a function of center-to-center distance of particle  $h$ , radius  $r$ , contact angle  $\theta$ , and filling angle  $\alpha$ . (b) Schematic figure for calculation of  $\alpha_{\text{crit}}$ , which is the maximum allowable  $\alpha$ , larger than which the local throat being considered (red dashed line) will be invaded.

where  $\gamma$  is the interfacial tension,  $h$  is the center-to-center distance of obstacles,  $d$  is the diameter, and  $\alpha$  is the filling angle shown in Fig. 6(a). Then, we define that the throat is invaded if (i) the front of invading fluid comes in contact with the next obstacle (touch), or (ii)  $\alpha$  reaches  $\alpha_{\text{overlap}}$  corresponding to cooperative pore filling event (overlap), assuming that obstacles are placed on triangular lattices [Fig. 6(b)]. Thus, for given contact angle  $\theta$ , the critical angle  $\alpha_{\text{crit}}$  can be calculated as  $\alpha_{\text{crit}} = \min(\alpha_{\text{touch}}, \alpha_{\text{overlap}})$ , where  $\alpha_{\text{touch}}$  is calculated based on  $\theta$  and  $\alpha_{\text{overlap}} = 90^\circ$ . Different characteristic front shape indicated by  $\alpha_{\text{overlap}}$  may be used by other researchers depending on the porosity of the medium [21]. In our study it is found  $\alpha_{\text{overlap}}$  will not significantly impact the results and  $90^\circ$  is adopted. Finally, for every throat, the  $P_{c,\text{max}}$  can be calculated as

$$P_{c,\text{max}} = \max(P_c), \alpha \in [-90^\circ, \alpha_{\text{crit}}], \quad (8)$$

which is the maximum capillary pressure before the front reaches any of the instability state at burst, touch, or overlap. It is found that log-normal curves can well fit most of the  $P_{c,\text{max}}$  distributions, and the probability distributions of  $P_{c,\text{max}}$  for different  $I_v$  and  $\theta$  are plotted in Fig. 7. It shows that as the medium becomes more disordered, the distribution of  $P_{c,\text{max}}$  spreads out. In the meantime, increase in contact angle of invading fluid amplifies this effect, which further increases the variation in  $P_{c,\text{max}}$ . Thus, the  $P_{c,\text{max}}$  distribution captures the interplay among wettability and geometry of

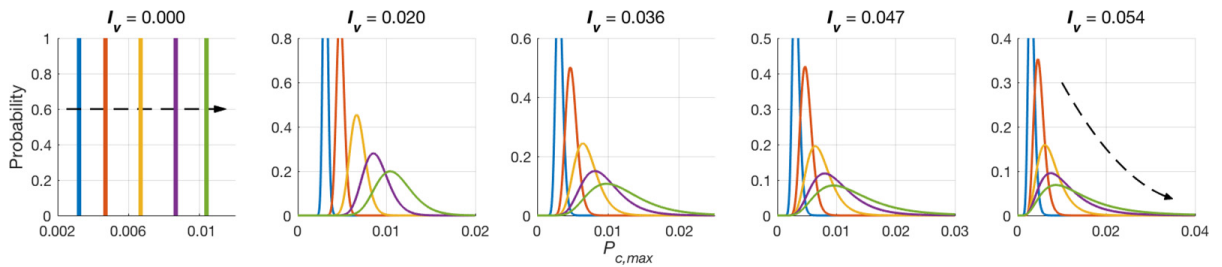


FIG. 7. Probability distribution of local maximum capillary pressure for different disorder and wettability (histogram for  $I_v = 0$  and probability density function for log-normal fitting of other values of  $I_v$ ). Black dashed arrow indicates the direction of increasing contact angle. Blue, orange, yellow, purple, and green colors correspond to  $\theta = 35^\circ, 62^\circ, 89^\circ, 109^\circ, 128^\circ$ , respectively.

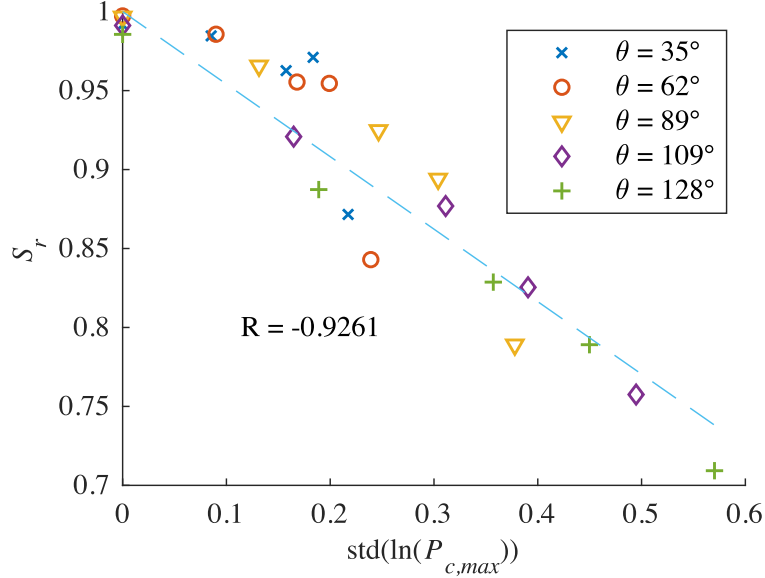


FIG. 8. Final saturation  $S_r$  as a function of standard deviation of logarithm maximum capillary pressure for different topological disorder and wettability.

the system, reflecting the resultant capillary resistance, which should have close relationship with the displacement patterns. To validate this hypothesis, the final saturation of invading fluid  $S_r$ , or displacement efficiency, is plotted against the standard deviation of  $\ln(P_{c,max})$  in Fig. 8 for all our simulation cases. Collapses of curves for different wettability conditions and disorder can be observed, showing a linear relationship with a correlation coefficient  $R = -0.9261$ .

On the other hand, regarding the fluid-fluid interfacial length, Liu *et al.* [54] found that the interfacial length  $L$  and saturation of invading fluid  $S$  can be correlated with a power-law relationship:  $L = kS^\beta$ , where  $k$  and  $\beta$  are fitting parameters depending on the geometry. Here, we propose a modified correlation between interfacial length and saturation assuming a power-law relation between normalized interfacial length  $L^*$  and “injection length”  $vt$ :

$$L^* = \frac{L}{H} = k(vt)^\beta = k(\phi WS)^\beta, \quad (9)$$

where,  $v$  is the injection velocity,  $t$  is time,  $H$  is the injection width (across which the invading fluid is injected),  $\phi$  is porosity,  $W$  is the domain longitudinal length,  $S$  is saturation of invading fluid,  $k$  and  $\beta$  are parameters that can be estimated based on capillary index  $I_c$  depending on system disorder and wettability conditions, which is defined as

$$I_c = \frac{I_{v,max} - I_v}{I_{v,max} - I_{v,min}} \frac{\cos(\theta_{max}) - \cos(\theta)}{\cos(\theta_{max}) - \cos(\theta_{min})}, \quad (10)$$

where  $I_{v,max}$  is the maximum disorder index depending on overall porosity of the geometry and total number of obstacles inside the system, being 0.08 for the current setting.  $I_{v,min} = 0$  is the disorder index for fully ordered system.  $\cos(\theta_{max})$  and  $\cos(\theta_{min})$  are  $-1$  and  $1$ , corresponding to  $\theta = 180^\circ$  and  $\theta = 0^\circ$ , respectively. As we have discussed previously that increase in contact angle and topological disorder promotes fingering, therefore,  $I_c$  is a direct indicator of the collaborative effect due to medium geometry and wettability conditions. A small value of  $I_c$  implies relatively large  $\theta$  and  $I_v$ , which leads to less efficient displacement, while larger values of  $I_c$  would correspond to more stable displacement. We plot the parameters  $\beta$  and  $\ln(k)$  from Eq. (10) as function of  $I_c$  in Fig. 9(a) and found that with  $I_c < 0.5$ , both  $\beta$  and  $\ln(k)$  show a strong linear relation with  $I_c$ , having  $R$  of  $-0.9467$  and  $0.9958$ , respectively. For  $I_c \geq 0.5$ , the displacement patterns are all stable, resulting in small  $\beta$  and large  $\ln(k)$ , indicating weak dependence of  $L^*$  on  $S_r$ :  $L^*$  is only composed of the

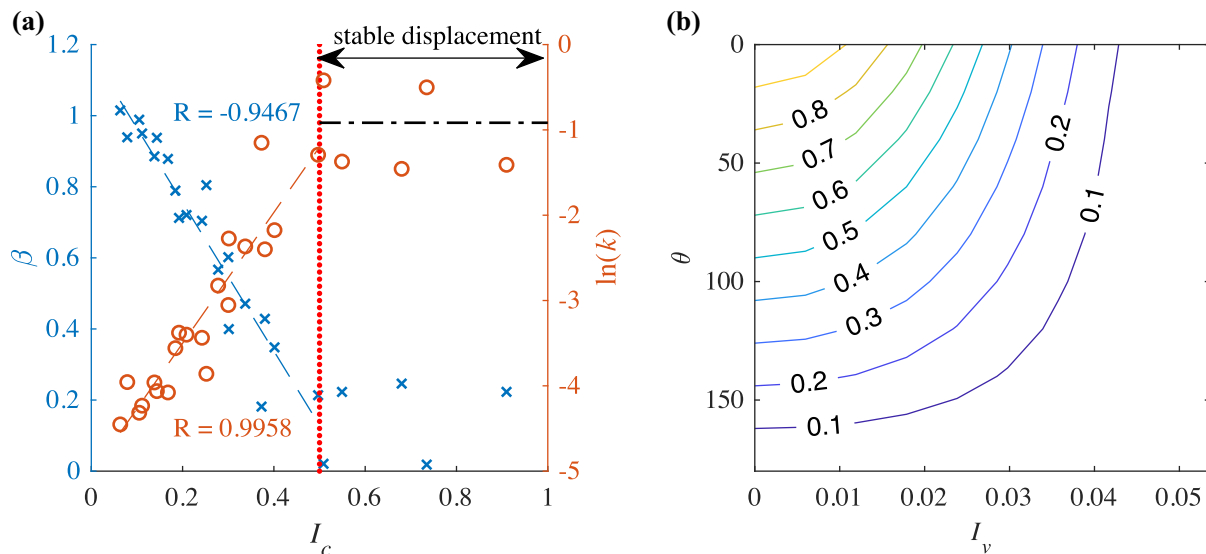


FIG. 9. (a)  $\beta$  (blue cross) and  $\ln(k)$  (orange circle) in Eq. (9) as a function of  $I_c$ . The blue dashed line and orange solid line are the best fit lines for  $\beta$  and  $\ln(k)$ , respectively. Black dashed line indicates the theoretical value for  $\ln(k)$  in perfect stable displacement. (b) Contour plot of  $I_c$  as functions of topological disorder ( $I_v$ ) and wettability ( $\theta$ ).

fluid front, being almost constant during the stable displacement. In Fig. 9(a), the black dashed line and a value of 0 correspond to the theoretical values for  $\ln(k)$  and  $\beta$  for perfect stable displacement. Clearly, it can be seen that  $I_c$  can also be used to classify displacement patterns Fig. 9(b). As shown in Fig. 3, 25 patterns are separated into three regions by the dashed line ( $I_c = 0.5$ ) and solid line ( $I_c = 0.3$ ) depending on the values of  $I_c$ . A smaller value of  $I_c$  implies larger interfacial length per unit of saturation. Note for the left-bottom displacement pattern in Fig. 3, if we zoom in and observe carefully, trapping event actually occurs at every obstacle during which small bubbles are formed, leading to much larger interfacial length between fluids than it appears to be. Overall, the proposed power-law relation [Eq. (9)] together with capillary index  $I_c$  [Eq. (10)] provide a rigorous method to capture the quantitative relation between  $L^*$  and  $S_r$  for different disorder and wettability conditions, offering a reasonable way to predict the value of interfacial length.

In the current study, to focus on the effects of disorder and its coupling with wettability on fluid displacement in porous media, the injecting velocity in all simulations are the same, implying a constant capillary number  $Ca$ . Although the influence of  $Ca$  is not investigated, based on numerous past works, since it is the uneven distribution of capillary pressure that leads to unstable displacement, a decrease in  $Ca$  would make all the displacement patterns shown in Fig. 3 more unstable since the capillary effect would become more significant. We also limit our attention to situations where Saffman-Taylor instability, or viscous fingering, is not present by setting the viscosity ratio  $M = 0.8$ .

#### IV. CONCLUSION

We systematically study the impact of topological disorder and its coupling with wettability on multiphase flow in porous media via fluid-fluid displacement simulation using lattice Boltzmann method. It has been shown that the disorder of porous media and wettability play a significant role on the fluid-fluid displacement patterns. In addition to the overall porosity of the medium, the consideration of an appropriate “disorder index” is required to capture the effects of microstructure on fluid displacement. The modified disorder index  $I_v$  is able to characterize geometries with different disorder by reflecting the degree of fluctuation of local porosity based on Voronoi diagram. Our results show larger contact angle and increasing disorder promote fingering, leading



to larger fluid-fluid interfacial area and lower displacement efficiency. To analytically investigate how wettability and disorder collaboratively influence displacement, we calculate the maximum allowable local capillary pressure  $P_{c,\max}$  based on three pore-scale mechanisms during displacement: burst, touch, and overlap. It is found that the standard deviation of  $\ln(P_{c,\max})$  strongly correlates with the displacement efficiency for all wettability conditions and disorder. We proposed a more general power-law relation and defined the capillary index  $I_c$ , which offers a rigorous way to capture the quantitative relation between  $L^*$  and  $S_r$  for different disorder and wettability conditions.

While in current work we only consider obstacles of same size, for media with different sizes of grains, modified Voronoi diagram can be adopted to generate the disorder index by taking the varying radii into account. We provide qualitative and quantitative insight into how geometrical features and wettability conditions collaboratively impact the fluid displacement, paving the way for further study of disorder and wettability control on multiphase flow in porous media.

### ACKNOWLEDGMENTS

This work was financially supported by Australian Research Council (Project No. DP170102886) and The University of Sydney SOAR Fellowship. Y.G. acknowledges the financial support of Labex MMCD(Grant No. ANR-11-LABX-022-01) for his stay at Laboratoire Navier at ENPC. This research was undertaken with the assistance of the HPC service at The University of Sydney.

- 
- [1] M. L. Szulczewski, C. W. MacMinn, H. J. Herzog, and R. Juanes, Lifetime of carbon capture and storage as a climate-change mitigation technology, *Proc. Natl. Acad. Sci. USA* **109**, 5185 (2012).
  - [2] J. M. Matter, M. Stute, S. Ó. Snæbjörnsdóttir, E. H. Oelkers, S. R. Gislason, E. S. Aradóttir, B. Sigfusson, I. Gunnarsson, H. Sigurdardóttir, E. Gunnlaugsson, G. Axelsson, H. A. Alfredsson, D. Wolff-Boenisch, K. Mesfin, Diana Fernandez de la Reguera Taya, J. Hall, K. Dideriksen, and W. S. Broecker, Rapid carbon mineralization for permanent disposal of anthropogenic carbon dioxide emissions, *Science* **352**, 1312 (2016).
  - [3] L. W. Lake and Society of Petroleum Engineers (US), *Fundamentals of Enhanced Oil Recovery*, SPE continuing education (SPE, Richardson, TX, 1986).
  - [4] M. Blunt, F. J. Fayers, and F. M. Orr, Carbon dioxide in enhanced oil recovery, *Energy Convers. Manage.* **34**, 1197 (1993).
  - [5] F. Nadim, G. E. Hoag, S. Liu, R. J. Carley, and P. Zack, Detection and remediation of soil and aquifer systems contaminated with petroleum products: An overview, *J. Petroleum Sci. Eng.* **26**, 169 (2000).
  - [6] J. Lipiec, J. Kuś, A. Słowińska-Jurkiewicz, and A. Nosalewicz, Soil porosity and water infiltration as influenced by tillage methods, *Soil Tillage Research* **89**, 210 (2006).
  - [7] B. Dong, Y. Y. Yan, W. Li, and Y. Song, Lattice Boltzmann simulation of viscous fingering phenomenon of immiscible fluids displacement in a channel, *Comput. Fluids* **39**, 768 (2010).
  - [8] C. Zhang, M. Oostrom, T. W. Wietsma, J. W. Grate, and M. Warner, Influence of viscous and capillary forces on immiscible fluid displacement: Pore-scale experimental study in a water-wet micromodel demonstrating viscous and capillary fingering, *Energy Fuels* **25**, 3493 (2011).
  - [9] H. Liu, A. J. Valocchi, Q. Kang, and C. Werth, Pore-scale simulations of gas displacing liquid in a homogeneous pore network using the lattice Boltzmann method, *Transp. Porous Media* **99**, 555 (2013).
  - [10] M. Cieplak and M. O. Robbins, Influence of contact angle on quasistatic fluid invasion of porous media, *Phys. Rev. B* **41**, 11508 (1990).
  - [11] B. Dong, Y. Y. Yan, W. Z. Li, and Y. C. Song, Simulation of the influence of surface wettability on viscous fingering phenomenon in porous media, *J. Bion. Eng.* **7**, 267 (2010).
  - [12] B. Zhao, C. W. MacMinn, and R. Juanes, Wettability control on multiphase flow in patterned microfluidics, *Proc. Natl. Acad. Sci. USA* **113**, 10251 (2016).

- [13] J.-D. Chen and D. Wilkinson, Pore-Scale Viscous Fingering In Porous Media, *Phys. Rev. Lett.* **55**, 1892 (1985).
- [14] G. M. Homsy, Viscous fingering in porous media, *Annu. Rev. Fluid Mech.* **19**, 271 (1987).
- [15] R. Lenormand, E. Touboul, and C. Zarcone, Numerical models and experiments on immiscible displacements in porous media, *J. Fluid Mech.* **189** 165 (1988).
- [16] C. Cottin, H. Bodiguel, and A. Colin, Drainage in two-dimensional porous media: From capillary fingering to viscous flow, *Phys. Rev. E* **82**, 046315 (2010).
- [17] C. Odier, B. Levache, E. Santanach-Carreras, and D. Bartolo, Forced Imbibition in Porous Media: A Fourfold Scenario, *Phys. Rev. Lett.* **119**, 208005 (2017).
- [18] Y. C. Yortsos, B. Xu, and D. Salin, Phase Diagram of Fully Developed Drainage in Porous Media, *Phys. Rev. Lett.* **79**, 4581 (1997).
- [19] M. Jung, M. Brinkmann, R. Seemann, T. Hiller, M. Sanchez de La Lama, and S. Herminghaus, Wettability controls slow immiscible displacement through local interfacial instabilities, *Phys. Rev. Fluids* **1**, 074202 (2016).
- [20] M. Trojer, M. L. Szulczewski, and R. Juanes, Stabilizing Fluid-Fluid Displacements in Porous Media Through Wettability Alteration, *Phys. Rev. Appl.* **3**, 054008 (2015).
- [21] R. Holtzman and E. Segre, Wettability Stabilizes Fluid Invasion into Porous Media Via Nonlocal, Cooperative Pore Filling, *Phys. Rev. Lett.* **115**, 164501 (2015).
- [22] H. Liu, Y. Zhang, and A. J. Valocchi, Lattice Boltzmann simulation of immiscible fluid displacement in porous media: Homogeneous versus heterogeneous pore network, *Phys. Fluids* **27**, 052103 (2015).
- [23] R. Holtzman, Effects of pore-scale disorder on fluid displacement in partially-wettable porous media, *Sci. Rep.* **6**, 36221 (2016).
- [24] T. Pak, I. B. Butler, S. Geiger, M. I. J. van Dijke, and K. S. Sorbie, Droplet fragmentation: 3D imaging of a previously unidentified pore-scale process during multiphase flow in porous media, *Proc. Natl. Acad. Sci. USA* **112**, 1947 (2015).
- [25] R. Holtzman and R. Juanes, Crossover from fingering to fracturing in deformable disordered media, *Phys. Rev. E* **82**, 046305 (2010).
- [26] C. Zhang, M. Oostrom, J. W. Grate, T. W. Wietsma, and M. Warner, Liquid CO<sub>2</sub> displacement of water in a dual-permeability pore network micromodel, *Environ. Sci. Technol.* **45**, 7581 (2011).
- [27] W. Xu, J. T. Ok, F. Xiao, K. B. Neeves, and X. Yin, Effect of pore geometry and interfacial tension on water-oil displacement efficiency in oil-wet microfluidic porous media analogs, *Phys. Fluids* **26**, 093102 (2014).
- [28] B. K. Primkulov, S. Talman, K. Khaleghi, A. R. Shokri, R. Chalaturnyk, B. Zhao, C. W. MacMinn, and R. Juanes, Quasistatic Fluid-Fluid Displacement in Porous Media: Invasion-Percolation Through a Wetting Transition, *Phys. Rev. Lett.* **3**, 104001 (2018).
- [29] M. Blunt and P. King, Relative permeabilities from two- and three-dimensional pore-scale network modeling, *Transp. Porous Media* **6**, 407 (1991).
- [30] M. S. Al-Gharbi and M. J. Blunt, Dynamic network modeling of two-phase drainage in porous media, *Phys. Rev. E* **71**, 016308 (2005).
- [31] M. Ferer, C. Ji, G. S. Bromhal, J. Cook, G. Ahmadi, and D. H. Smith, Crossover from capillary fingering to viscous fingering for immiscible unstable flow: Experiment and modeling, *Phys. Rev. E* **70**, 016303 (2004).
- [32] S. Osher and J. A. Sethian, Fronts propagating with curvature-dependent speed: Algorithms based on Hamilton-Jacobi formulations, *J. Comput. Phys.* **79**, 12 (1988).
- [33] H. Huang, P. Meakin, and M. Liu, Computer simulation of two-phase immiscible fluid motion in unsaturated complex fractures using a volume of fluid method, *Water Resour. Res.* **41**, 22 (2005).
- [34] A. Q. Raeini, M. J. Blunt, and B. Bijeljic, Modelling two-phase flow in porous media at the pore scale using the volume-of-fluid method, *J. Comput. Phys.* **231**, 5653 (2012).
- [35] H. A. A. Amiri and A. A. Hamouda, Evaluation of level set and phase field methods in modeling two phase flow with viscosity contrast through dual-permeability porous medium, *Int. J. Multiphase Flow* **52**, 22 (2013).

- [36] H. S. Rabbani, D. Or, Y. Liu, C.-Y. Lai, N. B. Lu, S. S. Datta, H. A. Stone, and N. Shokri, Suppressing viscous fingering in structured porous media, *Proc. Natl. Acad. Sci. USA* **115**, 4833 (2018).
- [37] W. Shyy, R. W. Smith, H. S. Udaykumar, and M. M. Rao, *Computational Fluid Dynamics with Moving Boundaries* (Taylor & Francis, Bristol, PA, 1996).
- [38] X. Shan and H. Chen, Lattice Boltzmann model for simulating flows with multiple phases and components, *Phys. Rev. E* **47**, 1815 (1993).
- [39] X. Shan and G. Doolen, Multicomponent lattice-Boltzmann model with interparticle interaction, *J. Stat. Phys.* **81**, 379 (1995).
- [40] Z. Guo and T. S. Zhao, Lattice Boltzmann model for incompressible flows through porous media, *Phys. Rev. E* **66**, 036304 (2002).
- [41] H. A. A. Amiri and A. A. Hamouda, Pore-scale modeling of nonisothermal two phase flow in 2D porous media: Influences of viscosity, capillarity, wettability, and heterogeneity, *Int. J. Multiphase Flow* **61**, 14 (2014).
- [42] T. Kruger, H. Kusumaatmaja, A. Kuzmin, O. Shardt, G. Silva, and E. M. Viggien, *LBM—The Principles and Methods* (Springer, Berlin, 2017).
- [43] F. Diotallevi, L. Biferale, S. Chibbaro, A. Lamura, G. Pontrelli, M. Sbragaglia, S. Succi, and F. Toschi, Capillary filling using lattice Boltzmann equations: The case of multiphase flows, *Eur. Phys. J. Special Topics* **166**, 111 (2009).
- [44] L. Chen, Q. Kang, Y. Mu, Ya-Ling He, and Wen-Quan Tao, A critical review of the pseudopotential multiphase lattice Boltzmann model: Methods and applications, *Int. J. Heat Mass Transf.* **76**, 210 (2014).
- [45] H. Liu, Q. Kang, C. R. Leonardi, S. Schmieschek, A. Narvaez, B. D. Jones, J. R. Williams, A. J. Valocchi, and J. Harting, Multiphase lattice Boltzmann simulations for porous media applications, *Comput. Geosci.* **20**, 777 (2015).
- [46] H. Laubie, F. Radjai, R. Pellenq, and F.-J. Ulm, Stress Transmission and Failure in Disordered Porous Media, *Phys. Rev. Lett.* **119**, 075501 (2017).
- [47] O. Borgman, P. Fantinel, W. Lühder, L. Goehring, and R. Holtzman, Impact of spatially correlated pore-scale heterogeneity on drying porous media, *Water Resour. Res.* **53**, 5645.
- [48] H. Huang, D. T. Thorne, M. G. Schaap, and M. C. Sukop, Proposed approximation for contact angles in Shan-and-Chen-type multicomponent multiphase lattice Boltzmann models, *Phys. Rev. E* **76**, 066701 (2007).
- [49] J. Latt and B. Chopard, Lattice Boltzmann method with regularized nonequilibrium distribution functions, *Math. Comput. Simul.* **72**, 165 (2006).
- [50] A. A. Mohamad, *LBM—Fundamentals and Engineering Applications with Computer Codes* (Springer, Berlin, 2011).
- [51] P. Raiskinmäki, A. Shakib-Manesh, A. Jäsberg, A. Koponen, J. Merikoski, and J. Timonen, Lattice-Boltzmann simulation of capillary rise dynamics, *J. Stat. Phys.* **107**, 143 (2002).
- [52] H. Ran, W. Jiamin, Y. Zhibing, C. Yi-Feng, and T. Tetsu, Wettability and flow rate impacts on immiscible displacement: A theoretical model, *Geophys. Res. Lett.* **45**, 3077 (2018).
- [53] M. Cieplak and M. O. Robbins, Dynamical Transition in Quasistatic Fluid Invasion in Porous Media, *Phys. Rev. Lett.* **60**, 2042 (1988).
- [54] H. Liu, A. J. Valocchi, C. Werth, Q. Kang, and M. Oostrom, Pore-scale simulation of liquid CO<sub>2</sub> displacement of water using a two-phase lattice Boltzmann model, *Adv. Water Resour.* **73**, 144 (2014).

### **5.3 Summary**

It is demonstrated in this Chapter that the consideration of physical mechanisms at micro-scale (Cassie-Wenzel wetting transition on rough surfaces) and pore-scale (different instability events) is crucial for understanding the displacement patterns of multiphase flow. Specifically, the simulation results indicate that slower wetting transition leads to greater effective contact angles along the invasion front during displacement, which consequently suppress cooperative pore filling events and promote trapping. Additionally, greater fluctuations in distribution of capillary resistance resulted from disordered pore geometry and larger contact angle tend to destabilise the displacement process, leading to smaller sweep efficiency and greater fluid-fluid interfacial area.

## CHAPTER 6

### **Packing and Drying of Unsaturated Granular Material**

---

The packing structure of wet granular materials is of great interest due to its various industrial applications and importance for the understanding of many fundamental physical problems. Additionally, understanding the subsequent drying of partially saturated porous media is also important in food processing, drugs and cosmetics synthesis in the pharmaceutical industries, and soil treatment in agriculture. In this chapter, we experimentally investigate the packing of wet monodisperse spheres, and present a simple experimental procedure to control the resulting packing fraction of the granular assembly. Using the proposed method, we then study the drying process of granular materials with low initial liquid content using image analysis and magnetic resonance imaging technique. These works provide new insights on the packing and drying process of partially saturated granular materials.

## 6.1 Packing of Wet Spheres

The existing description of packing fraction of assembly formed by falling cohesive particles in the literature is from (Yang et al., 2000; Dong et al., 2006, 2012), where the key governing parameter is a dimensionless force ratio, i.e., the ratio of interparticle force to gravity. Greater force ratio corresponds to smaller packing fraction. However, this model does not take the packing method into account. Thus, it cannot capture the process of particle rearrangement due to the potential variations in impact velocities of falling particles. In this section, we present a simple experimental method for generating granular media with controlled falling height, and propose a model from an energy perspective to predict the resulting packing fraction. Good agreement is found between the model and experimental results for both wet particles where capillary force dominates and dry powders where van der Waals forces are essential.

Corresponding paper: Wang, Z., Pereira, J.-M., & Gan, Y. (2021). Packing of wet monodisperse spheres. *Powder Technology*, 378, 60–64.

I was the primary researcher and author of this paper, being supervised by A/Prof. Yixiang Gan and Prof. Jean-Michel Pereira.



## Packing of wet monodisperse spheres

Zhongzheng Wang<sup>a,b</sup>, Jean-Michel Pereira<sup>b</sup>, Yixiang Gan<sup>a,c,\*</sup>

<sup>a</sup> School of Civil Engineering, The University of Sydney, NSW 2006, Australia

<sup>b</sup> Navier, Ecole des Ponts, Univ Gustave Eiffel, CNRS, Marne-la-Vallée, France

<sup>c</sup> The University of Sydney, Nano Institute, The University of Sydney, NSW 2006, Australia

### ARTICLE INFO

#### Article history:

Received 22 July 2020

Received in revised form 15 September 2020

Accepted 30 September 2020

Available online 02 October 2020

#### Keywords:

Granular packing

Monodisperse spheres

Capillary force

Cohesive granular media

### ABSTRACT

We experimentally investigated the packing of wet monodisperse spheres with controlled falling height. The packing fraction are found to decrease with smaller grain size and free fall height. A model describing the effects of interparticle force and falling height on packing fraction is developed by introducing a dimensionless length scale, representing the extent of particle rearrangement towards a denser state due to impacts of falling grains. A universal law is observed for both wet particles where capillary forces dominate and dry powders where van der Waals forces govern the packing behaviour. This study deepens the understanding of packing of cohesive spheres and provide a simple experimental method for generating granular media with tailored packing fraction.

© 2020 Elsevier B.V. All rights reserved.

### 1. Introduction

The random packing of granular materials has been subjected to extensive studies due to its various industrial applications and importance for the understanding of many fundamental physical problems [1–6]. The packing fraction of monodisperse cohesionless frictional particles ranges from ~0.55 (random very loose packing) to ~0.64 (random close packing), depending on the packing method and particle friction coefficient [7–16]. For frictionless particles, O'Hern et al. showed narrowed jamming threshold as the system size increases, approaching 0.648 in 3D, close to random close packing [14,15]. Moreover, studies on the effects of tapping on system of monodisperse spheres attribute the increase of packing fraction to the propagation of ordered packing structure from the boundary [17–19]. On the other hand, the packing fraction is found to decrease with smaller effective gravity or greater friction coefficient [7,12,16]. Further, Farrell et al. experimentally demonstrated how Stokes number controls the approach to the loose packing limit by varying the particle and fluid properties [10]. In the context of statistical mechanics, Ciamarra and Coniglio showed that the granular entropy, which reflects the number of mechanically stable states of volume fraction of a granular assembly, vanishes at upper and lower bound of packing fractions, while reaching a maximum at random loose packing [11]. Their work provided the first-principle definition of the commonly observed random loose packing fraction.

For spheres with diameter typically less than 100  $\mu\text{m}$ , the van der Waals force becomes significant. The attractive interparticle force starts to influence the packing fraction, which have been observed both numerically and experimentally [20–27]. Through imposing a controlled external magnetic field on iron spheres, Forsyth et al. demonstrated lower packing fraction with greater interparticle forces [28], and they concluded that the void fraction of spherical particles depends only on the ratio of interparticle cohesive force to particle weight. Their claim was further confirmed by DEM simulations of settling of fine particles [24,26,29]. In fact, the van der Waals force explains the formation of fragile low density configurations such as quicksand [23,25], and packing fraction as low as 15% has been experimentally created using ballistic deposition [22].

For larger particles, the effect of van der Waals force on packing fraction becomes negligible. However, the addition of liquid strengthens the cohesive force due to formation of liquid bridges [5,6,30–32]. Feng and Yu observed an increase in porosity of mono-sized glass beads when grains are added with water, followed by a plateau regime where porosity is insensitive to liquid content. Finally, the porosity decreases when more water is added. Similar behaviours have been observed in bidisperse and polydisperse systems [34–36]. The origin of these three distinct regimes can be readily understood by the relationship between liquid content and capillary force in granular media. At very low liquid content (asperity or roughness regime [37]), the capillary force increases with liquid volume due to surface roughness. However, further increase in liquid content does not result in additional increase in interparticle force because the increase in liquid-solid contact area balances with decrease in Laplace pressure [30,32,37,38]. This has been experimentally confirmed by measurements of the capillary force due to

\* Corresponding author at: School of Civil Engineering, The University of Sydney, NSW 2006, Australia.

E-mail address: [yixiang.gan@sydney.edu.au](mailto:yixiang.gan@sydney.edu.au) (Y. Gan).

liquid bridge at grain scale and the tensile strength of wet granular pile at macroscopic scale [5,39]. Finally, menisci coalesce before the slurry state where liquid is in excess and no capillary effects exist [33,40,41].

The aforementioned studies of packing of wet cohesive spheres mostly focus on the effects of grain size, interparticle forces, and solid/liquid properties. Less attention has been paid in packing methods, given that most experiments were carried out by pouring grains into the container [27,28,33,42,43]. To systematically probe the influence of packing method on the packing state of granular materials, in this work, a simple experimental method for preparing granular media with desired packing fraction is presented. We investigate the effect of falling height  $h_{\text{fall}}$  on packing fraction of wet monodisperse spherical glass beads with different grain sizes. A previously proposed relation describing the packing fraction [20,21,24] is extended by introducing a dimensionless length scale, representing the degree of compaction due to gravity, where the effects of falling height can be captured.

## 2. Experiments

Glass beads with a density of  $2460 \text{ kg/m}^3$  [44] were mixed with water at an initial volumetric water content  $w_0 = 5 \pm 0.1\%$  to ensure the granular medium is in pendular state and liquid bridges are formed [5,31,44]. Then, the wet grains are placed in a sieve, which was shaken by a vibration machine (Impact SV008 Electromagnetic Sieve Shaker, frequency 50 Hz and intensity 3.3 mm). A cylindrical container with inner diameter  $13.70 \pm 0.01 \text{ mm}$  and inner height  $44.94 \pm 0.12 \text{ mm}$  is placed  $h_{\text{fall}}$  away under the sieve, being supported by struts that are disconnected with the vibration machine. Once the vibration is initialized, wet grains fall progressively from the sieve into the container, similar to a sedimentation process. Fig. 4(a) shows the schematic of the experiment setup. The same equipment has been used in a previous work by Than et al. [44]. Note that in order to ensure a constant  $h_{\text{fall}}$  during the experiments, ideally, the supporting system should move downwards such that the surface of the grains stays at the same level as more grains fall into the container. However, we did not aim to produce such equipment due to extra complexity involved. Once the container is full, the grains in excess were carefully removed using a sharp plate, and medium was weighed before and after drying in an oven overnight at  $105^\circ\text{C}$ . The sieve grid size  $\{0.2, 1, 1.5, 3.15\} \text{ mm}$  were used for glass beads with average diameters  $\{97, 375, 568, 1594\} \mu\text{m}$ , respectively (Fig. 1(c)). These sizes allow passing for maximum of two to three spheres and avoid clusters of grains (namely, aggregates or agglomerates, which leads to less homogeneous packing structure) [40,43,45]. The cumulative grain size distribution determined by laser diffraction technique (using Beckman Coulter Vsm + Ls Variable Speed Fluid Module Plus) is shown in Fig. 1(b). Note that the data for packing of  $97 \mu\text{m}$  wet grains are obtained from Than et al. [44]. For packing of dry grains, given relative large

size of glass beads (generally larger than  $100 \mu\text{m}$ ), the van der Waals force is not expected to significantly affect the packing fraction [26,29,46]. Therefore, the system is simply packed by the pouring method. To ensure there is no formation of liquid bridges at lab condition due to capillary condensation, the water contents at “dry” condition were measured to be less than  $0.03\%$ , being smaller than  $0.07\%$ , at which the liquid bridges start to form [31].

## 3. Results and discussion

Fig. 2 shows the packing fraction  $\rho$  of monodisperse glass beads under dry or wet condition. For dry grains, the packing fraction is close to random loose packing of 0.6, consistent with past observations [33]. There is a slight decrease in  $\rho$  for smaller grains. One may argue this could result from the boundary effects [36,47]. Nevertheless, in the study of packing of cohesionless spheres in cylindrical containers by Zou and Yu [47], both the side-wall effect and top-bottom-wall effect (or thickness effect) lead to decrease in packing fraction for smaller system domain (corresponding to larger grains with the same container), which contradicts the trend in our results. Therefore, the decrease in packing fraction for smaller grains, despite small magnitude, is likely due to van der Waals force [20,26,33]. The packing fraction for wet grains is generally smaller than dry condition, and this decrease is more significant for smaller spheres. In addition, the colorbar shows the effects of free fall height  $h_{\text{fall}}$  on  $\rho$ , with denser packing at greater  $h_{\text{fall}}$ .

Previous studies have demonstrated increases in  $\rho$  with higher liquid content at very low liquid content regime (typically less than  $1 \sim 2\%$  depending on grain size distribution) [33,36,42,43]. However, Fig. 3(a) shows the relationship between  $\rho$  and  $w$  for all grain sizes, where no significant correlation between  $w$  and  $\rho$  can be seen. As discussed before, this is because the medium is in pendular state, and the capillary force due to liquid bridges is not sensitive to variations in water content within this regime [5,33,39]. By rearranging the dataset, Fig. 3(b) more quantitatively shows  $\rho$  as a function of  $h_{\text{fall}}$ . It can be observed that  $\rho$  increases monotonically with  $h_{\text{fall}}$ , ranging from around 0.3 to random loose packing of 0.6 marked by black-dashed line. Although  $\rho$  increases with  $h_{\text{fall}}$  for the investigated range of  $h_{\text{fall}}$ , it is expected the packing fraction will eventually reach a plateau as  $h_{\text{fall}}$  further increases due to either (1) the particle reaches the terminal velocity due to air drag and the kinetic energy is saturated, or (2) the packing fraction approaches 0.6 and the system starts to jam. For  $D = 1594 \mu\text{m}$  grains, the packing fraction is about 0.6 at the smallest  $h_{\text{fall}}$ ; whilst for larger  $h_{\text{fall}} > 150 \text{ mm}$ , bounces were observed and the container could not be completely filled. However, even with greater  $h_{\text{fall}}$  it is expected that the packing fraction will not surpass the value at dry condition as particles are already jammed.

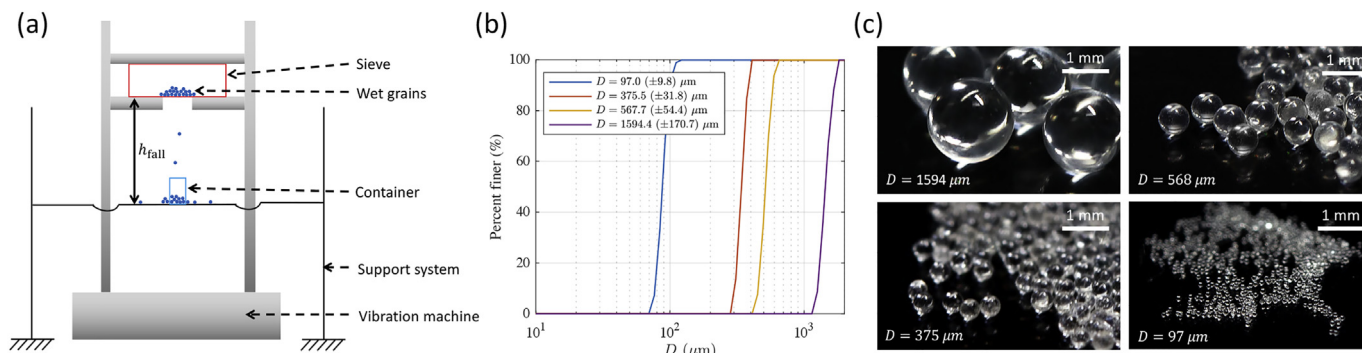
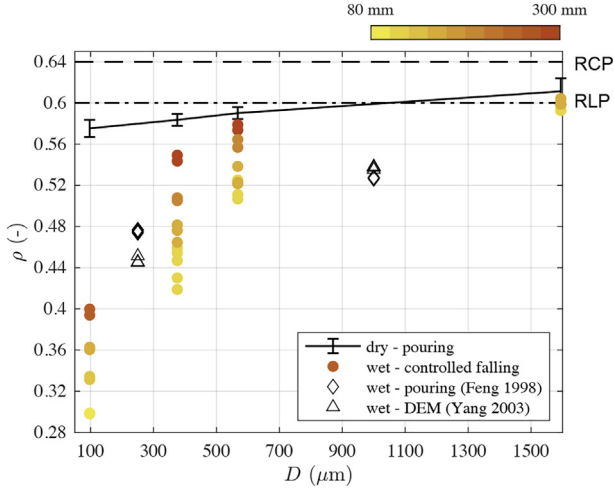


Fig. 1. (a) Schematic of the system for packing of wet spheres. (b) Cumulative grain size distribution. Values in bracket represent standard deviation. (c) Photos of glass beads with different sizes.





**Fig. 2.** Packing fraction  $\rho$  of dry (solid line with errorbar) or wet (circles) monodisperse glass beads. The errorbar represents the standard deviation of 6 measurements. The colorbar represents different free fall height  $h_{fall}$ . Data from literature are added for comparison (experiments using pouring method [33] and DEM simulation [40]). The packing fraction normally observed at random close packing (RCP) and random loose packing (RLP) are marked by dashed line and dash-dot line, respectively.

To quantify the interplay between gravity and interparticle forces on packing fraction, a model has previously been proposed for fine particles [20,24,29]:

$$\rho = \rho_0 (1 - e^{-a \cdot r^b}), \quad (1)$$

where  $\rho_0$  is the packing fraction without the presence of attractive interparticle force with values between random loose packing (0.6) and random close packing (0.64),  $a$  and  $b$  are fitting parameters, and  $r$  is the “force ratio” of the magnitudes of interparticle force to the gravity. As explained by Yang et al. [20], the force ratio,  $r$ , provides a quantitative description of the resistance force restricting the relative movement between particles during formation of a packing. However, the “force ratio” alone is not sufficient in capturing the process of particle rearrangement due to the potential variations in impact velocities of falling particles, which can lead to different numbers of breaks and formations of new liquid bridge bonds within the granular network that withstands the impact. This can be reflected by that fact that Eq. (1) will produce a single value of  $\rho$  for any given grain size with different  $h_{fall}$ .

Therefore, in order to capture the energy state of the falling particle upon impact, a more appropriate approach here is from an energy perspective where an “energy ratio” can be introduced:

$$r_E = \frac{F_{inter} \cdot l}{E_k}, \quad (2)$$

where  $F_{inter}$  is the interparticle force,  $l$  is the characteristic length, representing the displacement during the process of particles rearrangement, and  $E_k$  is the kinetic energy upon impact, which can be approximated as the gravitational potential energy. Here,  $r_E$  represents the proportion of kinetic energy dissipated due to interparticle forces (e.g., through enhanced frictional force from liquid bridges). Therefore,  $r_E$  approaches to unity when the interparticle cohesive forces are significant comparing to gravity. Previous studies have indicated that the ratio of interparticle force to gravity needs to be much larger than one (in the order of 10) in order for the interparticle force to have significant effect on packing fraction [20,29]. This can be explained by the fact that there is no preferred direction in the interparticle force due to random arrangement of grains, unlike gravity [20]. For wet spheres, the capillary force  $F_c$  due to liquid bridges can be calculated as  $F_c = 2\pi\gamma R \cos \theta$  [30,32,37], where  $\gamma$  is the surface tension,  $R$  is the radius, and  $\theta$  is the contact angle. Thus, for the force ratio  $\frac{F_c}{F_g} = \frac{3\gamma \cos \theta}{2R^2 \rho g} \approx 10$  with the average contact angle between glass beads and water  $\theta \approx 60^\circ$  [48] and density of  $2460 \text{ kg}^3/\text{m}$ , an approximate threshold grain size can be obtained as  $D^* = \sqrt{\frac{6\gamma \cos \theta}{10 \rho g}} \approx 950 \mu\text{m}$ . For grain sizes larger than  $D^*$ ,  $r_E \ll 1$ , and it is expected that the packing fraction is close to random loose packing 0.6, insensitive to free fall height, which is confirmed by Fig. 3(b). For grain sizes less than  $D^*$ ,  $r_E$  approaches to 1. Under this regime, a dimensionless length scale can be introduced  $l^* = l/D$ , which reflects the relative displacement during the process of particle rearrangement. Then, with Eq. (2), assuming  $r_E = 1$  for simplicity, one obtains:

$$l^* = \frac{E_k}{F_{inter} \cdot D}. \quad (3)$$

Therefore,  $l^*$  can be regarded as the the degree of compaction due to gravity, i.e., the extent of particle rearrangement towards a denser state from the packing state of diffusion limited aggregation. Either smaller  $E_k$  or greater  $F_{inter}$  lead to decrease in  $l^*$ , implying less compaction and thus looser packing state. It is worth mentioning that, for the case of wet particles with negligible van der Waals force where the interparticle force is mainly from capillary force,  $l^*$  can be thought as a generalization of

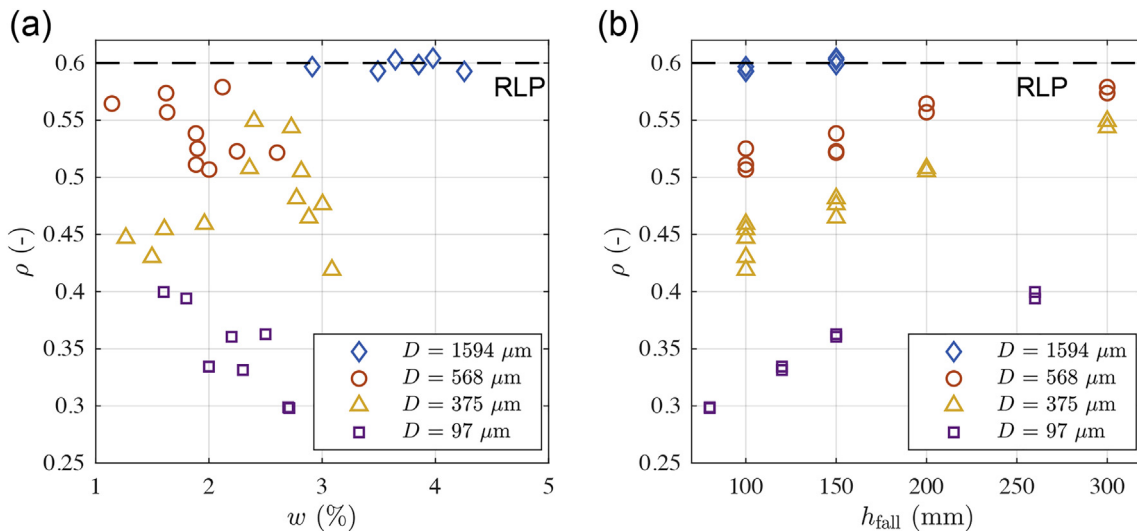


**Fig. 3.** (a) The influence of volumetric water content  $w$  on packing fraction is not significant. (b) Packing fraction  $\rho$  increases with larger height of free fall  $h_{fall}$  for different grain sizes.

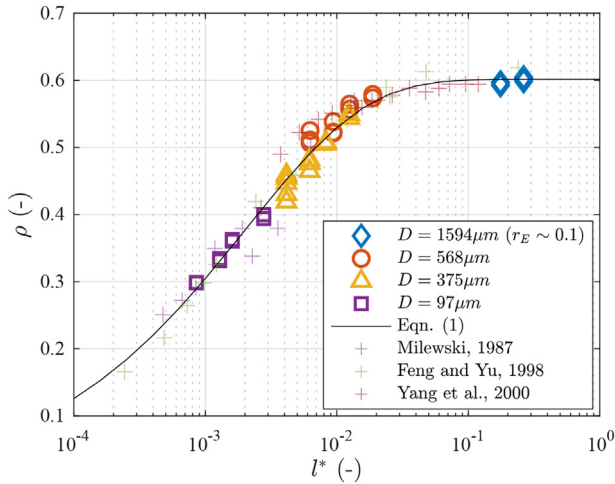


**Fig. 4.** Packing fraction  $\rho$  of wet spheres as a function of  $l^*$  for grains of different sizes and  $h_{\text{fall}}$ . Solid line is from Eq. (1) with  $r$  replaced by  $l^*$ . Data from literature for dry powders are added for comparison where the interparticle force is calculated by Eq. (4).

Weber number  $l^* = \frac{\rho D v^2}{12\gamma \cos\theta} = \frac{We}{12 \cos\theta}$ , which provides a measure of relative importance of inertia compared to surface tension. Fig. 4 plots the packing fraction as a function of  $l^*$ . Collapse of data can be observed for different grain sizes and free fall heights. For grain size larger than  $D^*$ , as mentioned before the forces from liquid bridge will not be the major source of energy dissipation, i.e.,  $r_E \ll 1$ . Therefore,  $r_E = 0.1$  is used as an estimation for  $D = 1594 \mu\text{m}$ . Also, the model from Eq. (1) with  $l^*$  replacing  $r$  are plotted with solid line with fitted  $a = -19.2$ ,  $b = 0.478$  and  $\rho_0 = 0.602$ .

We also check the validity of the model for describing dry grains with diameter less than  $100 \mu\text{m}$  where van der Waals force plays an important role. The attractive van der Waals force between two particles can be calculated by [20,21,29]:

$$F_v = \frac{A}{6} \frac{64R_i^3 R_j^3 (s + R_i + R_j)}{(s^2 + 2R_i s + 2R_j s)^2 (s^2 + 2R_i s + 2R_j s + 4R_i R_j)^2}, \quad (4)$$

where  $R_i, R_j$  are radii of the two spheres,  $A$  is the Hamaker constant that is related to material properties, being  $6.5 \times 10^{-20} \text{ J}$  for glass beads, and  $s$  is the separation distance with typical value of  $1 \times 10^{-10} \text{ m}$  [1,21]. With monodisperse spheres and assuming the separation distance is much less than the grain radius, Eq. (4) reduces to  $F_v = AR/(12s^2)$ . Data from literature of packing of fine powders are shown as “+” signs in Fig. 4. Since we did not find the corresponding falling height for the data, the  $h_{\text{fall}}$  is fitted to be 5 mm. However, this value is likely to be smaller than the typical  $h_{\text{fall}}$  in laboratory conditions. One of the sources of the error could be from the calculation in interparticle forces, especially when the accurate estimation of the separation distance  $s$  can be difficult. This error will lead to a shift of data in the horizontal direction in Fig. 4. Nevertheless, the general shape of the data from literature, which is independent of  $h_{\text{fall}}$  or  $s$ , matches well with the proposed theory.

In the current study of glass beads falling within air, the kinetic energy right before the impact is approximated by the gravitational potential energy. However, if the particles are settling within a surrounding fluid with large viscosity [10,24,29], firstly,  $E_k$  cannot be estimated as the initial gravitational potential energy due to significant viscous dissipation during settlement process. Secondly, the extra viscous resistance during the short period of particle rearrangement upon impact needs to be considered, i.e., the numerator in the expression of  $r_E$  (Eq. (2)) should include extra terms to take into account the effect from the surrounding fluids depending on the fluid property, through which the current theory built on energy conservation can be further extended.

## 4. Conclusions

The packing of wet monodisperse spheres was experimentally studied. Glass beads with different sizes were packed under controlled falling height. It is observed that both grain size and free fall height significantly impact the packing fraction. A dimensionless length scale is introduced, which reflects the extent of particle rearrangement towards a denser state due to impacts from falling grains, extending the existing model for describing the packing fraction of cohesive spheres, where the effect of falling heights can be well captured. Based on the proposed theory, collapses of data are observed for both wet particles where capillary force dominates and dry powders where van der Waals force is essential. Our study deepens the understanding of packing of cohesive spheres and provide a simple experimental method for preparing granular media with desired packing fraction by using the proposed universal law.

## Declaration of Competing Interest

The authors declare that they have no known competing financial interests or personal relationships that could have appeared to influence the work reported in this paper.

## Acknowledgments

This work was financially supported by Australian Research Council (Projects DP170102886) and The University of Sydney SOAR Fellowship. YG acknowledges the financial support of Labex MMCD (ANR-11-LABX-022-01) for his stay at Laboratoire Navier at ENPC. ZW thanks Baptiste Chabot, Xavier Boulay, Loïc Lesueur, and Emmanuel De Laure for the assistance on experiments.

## References

- [1] H. Zhu, Z. Zhou, R. Yang, A. Yu, Discrete particle simulation of particulate systems: Theoretical developments, Chem. Eng. Sci. 62 (2007) 3378–3396 Frontier of Chemical Engineering - Multi-scale Bridge between Reductionism and Holism.
- [2] H. Zhu, Z. Zhou, R. Yang, A. Yu, Discrete particle simulation of particulate systems: a review of major applications and findings, Chem. Eng. Sci. 63 (2008) 5728–5770.
- [3] H. Chen, W. Liu, S. Li, Random loose packing of small particles with liquid cohesion, AIChE J. 65 (2019) 500–511.
- [4] S. Chen, W. Liu, S. Li, A fast adhesive discrete element method for random packings of fine particles, Chem. Eng. Sci. 193 (2019) 336–345.
- [5] M. Scheel, R. Seemann, M. Brinkmann, M. Di Michiel, A. Sheppard, B. Breidenbach, S. Herminghaus, Morphological clues to wet granular pile stability, Nat. Mater. 7 (2008) 189–193.
- [6] M. Scheel, R. Seemann, M. Brinkmann, M.D. Michiel, A. Sheppard, S. Herminghaus, Liquid distribution and cohesion in wet granular assemblies beyond the capillary bridge regime, J. Phys. Condens. Matter 20 (2008), 494236.
- [7] G.Y. Onoda, E.G. Liniger, Random loose packings of uniform spheres and the dilatancy onset, Phys. Rev. Lett. 64 (1990) 2727–2730.
- [8] L. Liu, Z. Zhang, A. Yu, Dynamic simulation of the centripetal packing of mono-sized spheres, Physica A 268 (1999) 433–453.
- [9] X. Cheng, Experimental study of the jamming transition at zero temperature, Phys. Rev. E 81 (2010), 031301.
- [10] G.R. Farrell, K.M. Martini, N. Menon, Loose packings of frictional spheres, Soft Matter 6 (2010) 2925–2930.
- [11] M.P. Ciamarra, A. Coniglio, Random very loose packings, Phys. Rev. Lett. 101 (2008), 128001.
- [12] M. Jerkins, M. Schröter, H.L. Swinney, T.J. Senden, M. Saadatfar, T. Aste, Onset of mechanical stability in random packings of frictional spheres, Phys. Rev. Lett. 101 (2008), 018301.
- [13] A.J. Liu, S.R. Nagel, The jamming transition and the marginally jammed solid, Ann. Rev. Condens. Matter Physics 1 (2010) 347–369.
- [14] C.S. O’Hern, S.A. Langer, A.J. Liu, S.R. Nagel, Random packings of frictionless particles, Phys. Rev. Lett. 88 (2002) 075507.
- [15] C.S. O’Hern, L.E. Silbert, A.J. Liu, S.R. Nagel, Jamming at zero temperature and zero applied stress: the epitome of disorder, Phys. Rev. E 68 (2003), 011306.
- [16] L.E. Silbert, Jamming of frictional spheres and random loose packing, Soft Matter 6 (2010) 2918–2924.
- [17] A.D. Rosato, O. Dybenko, D.J. Horntrop, V. Ratnaswamy, L. Kondic, Microstructure evolution in density relaxation by tapping, Phys. Rev. E 81 (2010), 061301.

- [18] V. Ratnaswamy, A.D. Rosato, D. Blackmore, X. Tricoche, N. Ching, L. Zuo, Evolution of solids fraction surfaces in tapping: simulation and dynamical systems analysis, *Granul. Matter* 14 (2012) 163–168.
- [19] W. Dai, J. Reimann, D. Hanaor, C. Ferrero, Y. Gan, Modes of wall induced granular crystallisation in vibrational packing, *Granul. Matter* 21 (2019) 26.
- [20] R.Y. Yang, R.P. Zou, A.B. Yu, Computer simulation of the packing of fine particles, *Phys. Rev. E* 62 (2000) 3900–3908.
- [21] A. Yu, C. Feng, R. Zou, R. Yang, On the relationship between porosity and interparticle forces, *Powder Technol.* 130 (2003) 70–76.
- [22] J. Blum, R. Schräpler, Structure and mechanical properties of high-porosity macroscopic agglomerates formed by random ballistic deposition, *Phys. Rev. Lett.* 93 (2004), 115503.
- [23] D. Lohse, R. Rauhé, R. Bergmann, D. Meer, Creating a dry variety of quicksand, *Nature* 432 (2005) 689–690.
- [24] K.J. Dong, R.Y. Yang, R.P. Zou, A.B. Yu, Role of interparticle forces in the formation of random loose packing, *Phys. Rev. Lett.* 96 (2006), 145505.
- [25] P.B. Umbanhowar, D.I. Goldman, Low density fragile states in cohesive powders, *Am. J. Phys.* 74 (2006) 720–721.
- [26] R. Yang, R. Zou, K. Dong, X. An, A. Yu, Simulation of the packing of cohesive particles, *Comput. Phys. Commun.* 177 (2007) 206–209 Proceedings of the Conference on Computational Physics 2006.
- [27] E. Parteli, J. Schmidt, C. Blümel, K.-E. Wirth, W. Peukert, T. Pöschel, Attractive particle interaction forces and packing density of fine glass powders, *Sci. Rep.* 4 (2014) 6227.
- [28] A.J. Forsyth, S.R. Hutton, C.F. Osborne, M.J. Rhodes, Effects of interparticle force on the packing of spherical granular material, *Phys. Rev. Lett.* 87 (2001), 244301.
- [29] K.J. Dong, R.Y. Yang, R.P. Zou, A.B. Yu, Settling of particles in liquids: effects of material properties, *AIChE J.* 58 (2012) 1409–1421.
- [30] Y.I. Rabinovich, M.S. Esayanur, B.M. Moudgil, Capillary forces between two spheres with a fixed volume liquid bridge: theory and experiment, *Langmuir* 21 (2005) 10992–10997. 16285763.
- [31] Z. Fournier, D. Geromichalos, S. Herminghaus, M.M. Kohonen, F. Mugele, M. Scheel, M. Schulz, B. Schulz, C. Schier, R. Seemann, A. Skudelný, Mechanical properties of wet granular materials, *J. Phys. Condens. Matter* 17 (2005) S477–S502.
- [32] H.-J. Butt, M. Kappl, Normal capillary forces, *Adv. Colloid Interf. Sci.* 146 (2009) 48–60.
- [33] C. Feng, A. Yu, Effect of liquid addition on the packing of mono-sized coarse spheres, *Powder Technol.* 99 (1998) 22–28.
- [34] R.-P. Zou, C.-L. Feng, A.-B. Yu, Packing density of binary mixtures of wet spheres, *J. Am. Ceram. Soc.* 84 (2001) 504–508.
- [35] R. Zou, J. Xu, C. Feng, A. Yu, S. Johnston, N. Standish, Packing of multi-sized mixtures of wet coarse spheres, *Powder Technol.* 130 (2003) 77–83.
- [36] J.-F. Bruchon, Investigation by Means of X-Ray Computed Tomography of Capillary Collapse in Granular Materials, Theses, Université Paris-Est, 2014. <https://pastel.archives-ouvertes.fr/tel-01124287>.
- [37] T.C. Halsey, A.J. Levine, How sandcastles fall, *Phys. Rev. Lett.* 80 (1998) 3141–3144.
- [38] H.-J. Butt, Capillary forces: influence of roughness and heterogeneity, *Langmuir* 24 (2008) 4715–4721. 18442225.
- [39] B. Mielniczuk, T. Hueckel, M.S.E. Youssoufi, Evaporation-induced evolution of the capillary force between two grains, *Granul. Matter* 16 (2014) 815–828.
- [40] R.Y. Yang, R.P. Zou, A.B. Yu, Numerical study of the packing of wet coarse uniform spheres, *AIChE J.* 49 (2003) 1656–1666.
- [41] N. Mitarai, F. Nori, Wet granular materials, *Adv. Phys.* 55 (2006) 1–45.
- [42] C. Feng, A. Yu, Quantification of the relationship between porosity and interparticle forces for the packing of wet uniform spheres, *J. Colloid Interface Sci.* 231 (2000) 136–142.
- [43] J.Q. Xu, R.P. Zou, A.B. Yu, Packing structure of cohesive spheres, *Phys. Rev. E* 69 (2004), 032301.
- [44] V.-D. Than, P. Aïmedieu, J.-M. Pereira, J.-N. Roux, M. Bornert, A.-M. Tang, Macroscopic one-dimensional compression of wet granular soils by experimental investigation, *E3S Web of Conferences* 9 (2016) 06001.
- [45] J.-F. Bruchon, J.-M. Pereira, M. Vandamme, N. Lenoir, P. Delage, M. Bornert, Full 3d investigation and characterisation of capillary collapse of a loose unsaturated sand using x-ray ct, *Granul. Matter* 15 (2013) 783–800.
- [46] A. Yu, J. Bridgwater, A. Burbidge, On the modelling of the packing of fine particles, *Powder Technol.* 92 (1997) 185–194.
- [47] R. Zou, A. Yu, The packing of spheres in a cylindrical container: the thickness effect, *Chem. Eng. Sci.* 50 (1995) 1504–1507.
- [48] K.A. Klise, D. Moriarty, H. Yoon, Z. Karpyn, Automated contact angle estimation for three-dimensional x-ray microtomography data, *Adv. Water Resour.* 95 (2016) 152–160 Pore scale modeling and experiments.

## **6.2 Drying of Loosely Packed Wet Granular Materials**

In this paper, loosely packed wet granular materials are firstly generated using the experimental procedure reported in previous section. Then, drying experiments are conducted. Via analytical balance, high-resolution camera, and magnetic resonance imaging technique, we obtain the evolution of liquid distribution and packing structure of the granular media during the drying process. An enhancement in evaporation is observed and explained by Kelvin effect. We also observe concentrated drying-induced collapse events near the end of drying process, which implies the existence of liquid bridges in the apparent dry region, providing insights on the drying process of partially saturated granular materials, especially near the end of evaporation.

Corresponding manuscript: Wang, Z., Maillet, B., Pereira, J.-M., & Gan, Y. (2021). Towards the end of drying of granular materials: Enhanced evaporation and drying-induced collapse. *Water Resources Research*, 57, e2021WR030125.

I was the primary researcher and author of this paper, being supervised by A/Prof. Yixiang Gan and Prof. Jean-Michel Pereira.

# Water Resources Research

## RESEARCH ARTICLE

10.1029/2021WR030125

### Key Points:

- Drying-induced collapse of loosely packed granular media is observed and quantified
- NMR technique is used to reveal the distribution of liquid during evaporation
- The existence of liquid in the apparent dry region is evidenced by the concentrated collapse near the end of drying experiment
- The enhancement of evaporation rate is observed and explained by Kelvin effect

### Supporting Information:

Supporting Information may be found in the online version of this article.

### Correspondence to:

J. M. Pereira and Y. Gan,  
[jean-michel.pereira@enpc.fr](mailto:jean-michel.pereira@enpc.fr);  
[yixiang.gan@sydney.edu.au](mailto:yixiang.gan@sydney.edu.au)

### Citation:




Wang, Z., Mailliet, B., Pereira, J.-M., & Gan, Y. (2021). Towards the end of drying of granular materials: Enhanced evaporation and drying-induced collapse. *Water Resources Research*, 57, e2021WR030125. <https://doi.org/10.1029/2021WR030125>

Received 12 APR 2021

Accepted 18 JUN 2021

© 2021. American Geophysical Union.  
 All Rights Reserved.

## Towards the End of Drying of Granular Materials: Enhanced Evaporation and Drying-Induced Collapse

Zhongzheng Wang<sup>1,2</sup> , Benjamin Mailliet<sup>2</sup>, Jean-Michel Pereira<sup>2</sup> , and Yixiang Gan<sup>1,3</sup> 

<sup>1</sup>School of Civil Engineering, The University of Sydney, Sydney, NSW, Australia, <sup>2</sup>Navier, Ecole des Ponts, Univ Gustave Eiffel, CNRS, Marne-la-Vallée, France, <sup>3</sup>The University of Sydney Nano Institute, The University of Sydney, Sydney, NSW, Australia

**Abstract** We experimentally study the drying of loosely packed wet glass beads at low initial water content. The drying rate is found to decrease at the start, corresponding to the decreasing rate period controlled by vapor diffusion, followed by a deviation in drying rate from the diffusion limited evaporation. The propagation of drying front associated with a sharp saturation gradient is identified through both image analysis and magnetic resonance imaging technique. The drying-induced collapse of granular medium is observed and quantified. The concentrated collapse at the end of drying suggests the existence of liquid in the form of liquid bridges in the apparent dry region until the end of drying process. Collapse event is found to be local, that is, a clear boundary can be identified for each collapse event, below which the loosely packed medium remains intact. This indicates the existence of a saturation gradient in the apparent dry region. The drying dynamics and collapse statistics suggest that the observed transition of drying regimes is due to Kelvin effect. This work demonstrates for the first time the drying enhancement phenomenon due to Kelvin effect even for grains with size of hundreds of micrometers, and provides insights on the drying process of partially saturated granular materials, especially near the final period of evaporation.

### 1. Introduction

Drying of porous media is essential in relation with many applications, such as drugs and cosmetics synthesis in the pharmaceutical industry, thermally enhanced oil recovery, and drying of textiles, grains, and food. Particularly, soil drying is of great environmental importance, as it controls the water, energy and solutes transfer between the atmosphere and subsurface. The basic mechanisms of drying of saturated porous media have been identified as two distinguishable stages (Brutsaert & Chen, 1995; Coussot, 2000; Or et al., 2013; Shokri et al., 2009; Lehmann et al., 2008; Yiotis et al., 2012a; Yiotis et al., 2012b; Thiery et al., 2017). In the first stage, although the primary drying front (below which the medium is saturated) is receding into the medium, the evaporation of liquid at the surface is constantly being supplied through capillary flow, leading to a constant evaporation rate, which is limited by the external conditions (i.e., velocity and relative humidity of surrounding air), until either a critical surface water content (Or et al., 2013) or a characteristic depth (Lehmann et al., 2008) is reached. Then, the evaporation enters the second stage, and the drying rate starts to decrease as a result of dominance of vapor diffusion, which is accompanied by the secondary drying front (separating the dry region and capillary flow region) receding into the porous media (Coussot, 2000; Yiotis et al., 2012a, 2012b; Thiery et al., 2017; Shokri & Or, 2011). A schematic showing the drying process of porous media is shown in Figure 1. Efforts have been made to predict this transition mainly through the force balance among capillary, viscous, and gravitational forces, depending on properties of liquid and solid matrix, such as surface tension, viscosity, wettability, and pore size distribution (Coussot, 2000; Or et al., 2013; Lehmann et al., 2008; Yiotis et al., 2012a, 2012b; Thiery et al., 2017; Shokri & Or, 2011). Nevertheless, most existing studies focused on the drying process of initially saturated porous media, and the drying of partially saturated media with low liquid content, especially towards the extreme end of drying, remains relatively unexplored.

For porous media at low water content, that is, in the pendular state (Fournier et al., 2005; Scheel et al., 2008a; Than et al., 2016), water exists mainly in the form of liquid bridges, making the granular material cohesive as a result of the capillary force from liquid bridges (Butt & Kappl, 2009; Fournier et al., 2005; Rabinovich et al., 2005; Scheel et al., 2008a, 2008b). As a result, studies have demonstrated a significant decrease in

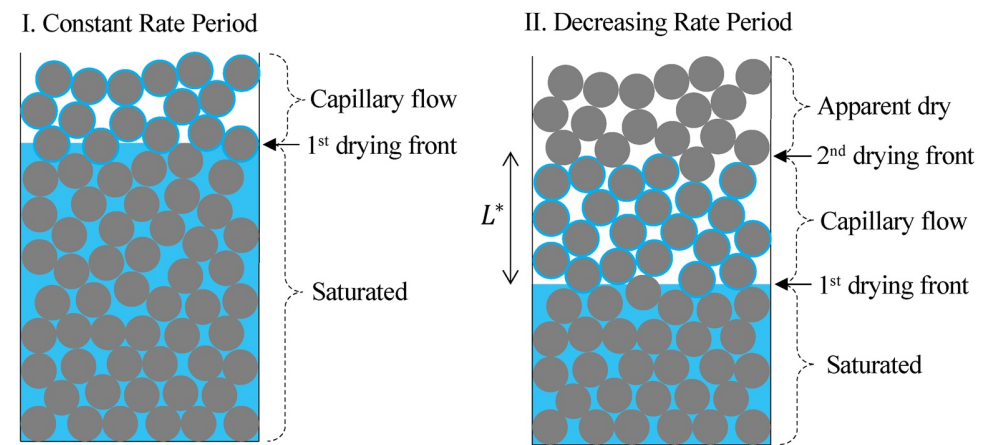


**Figure 1.** Schematic showing the drying process of porous media. In the constant rate period, evaporation of liquid at surface is supplied by capillary flow. After reaching a characteristic length  $L^*$ , the second drying front starts receding into the medium, marking the transition towards decreasing rate period.

packing fraction of wet porous media compared with dry (or fully saturated) media (Feng & Yu, 1998; Mitarai & Nori, 2006; Wang et al., 2021; Yang et al., 2003). This may have several implications for the dynamics of drying processes. First, as reported in the literature, for cohesionless particles with size typically greater than  $100\ \mu\text{m}$  (negligible van der Waals forces), the lower limit of packing fraction is around 0.55 (random very loose packing) (Ciamarra & Coniglio, 2008; Farrell et al., 2010; Jerkins et al., 2008; Onoda & Liniger, 1990; Vo et al., 2020). Therefore, drying-induced collapse may occur in loosely packed wet granular materials (e.g., packing fraction less than 0.55 for mono-sized spheres) as the liquid bridges disappear during evaporation. Besides, since the liquid bridges can be regarded as isolated in the pendular regime, the initial drying stage is expected to be fundamentally different from the saturated case where the connected liquid network can supply liquid towards the medium surface through capillary flow. Particularly, several studies have suggested that, apart from capillary flow, the film flow at grain surface due to adsorption can maintain the connectivity of liquid phase (Tuller & Or, 2001; Tuller & Or, 2005; Wang et al., 2013; Wang et al., 2018). It is thus interesting to examine the potential influence of film flow on the drying process, especially at low initial water content.

In this work, we experimentally investigate the drying of loosely packed wet glass beads at low initial volumetric water content ( $\sim 2\%$ ). Such low initial water is chosen in order to focus on the drying process near the end of drying, which also allows the generation of loosely packed granular assembly and investigation on the drying-induced collapse. The specimen was first prepared with desired packing fraction ( $\sim 0.45$ ) through a recently reported experimental procedure (Than et al., 2016; Wang et al., 2021), after which the drying experiment was conducted. The statistics of collapse events during drying as well as the evolution of liquid distribution were obtained through image analysis and magnetic resonance imaging (MRI) technique, which provide global and local insights on physical mechanisms that govern the drying process.

## 2. Experiments

**Materials and specimen preparation:** Mono-sized glass beads of average diameter  $375.5\ \mu\text{m}$  (standard deviation  $31.8\ \mu\text{m}$ ) are chosen with consideration of a) to exclude the effect from van der Waals forces on packing structure, and b) to have significant decrease in packing fraction once water is added (Feng & Yu, 1998; Mitarai & Nori, 2006; Than et al., 2016; Wang et al., 2021; Yang et al., 2003). The cumulative grain size distribution determined by laser diffraction technique (using Beckman Coulter Vsm + Ls Variable Speed Fluid Module Plus) is shown in Figure 2b. The specimen was mixed thoroughly with water at volumetric water content  $5 \pm 1\%$  (Than et al., 2016; Wang et al., 2021; Bruchon et al., 2013). Then, a sieve containing the wet glass beads was shaken by a vibration machine. A cylindrical container with inner diameter  $13.70 \pm 0.01\ \text{mm}$  and inner height  $44.22 \pm 0.12\ \text{mm}$  was placed under the sieve, which was supported by struts that are disconnected with the vibration machine. Wet grains fell progressively from the sieve

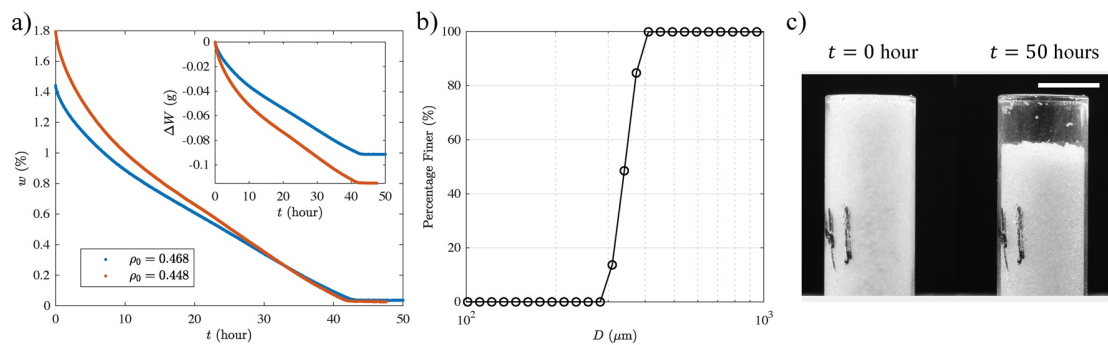


**Figure 2.** (a) Change of volumetric water content as a function of time for two typical experiments with initial packing fractions  $\rho_0 = 0.448$  and  $\rho_0 = 0.468$ . Inset: corresponding specimen weight as a function of time. (b) Cumulative grain size distribution of glass beads with average diameter  $375.5 \mu\text{m}$  (standard deviation  $31.8 \mu\text{m}$ ). (c) Photos of specimen taken at initial and final stages of drying. Scale bar represents 10 mm.

into the container once the vibration starts. The free fall height of grains, that is, the distance between the sieve and the container can be adjusted to control the resulting packing fraction (Wang et al., 2021). After the specimen preparation, the initial volumetric water content and packing fraction were measured to be  $w_0 = 1.7 \pm 0.2\%$  and  $\rho_0 = 0.45 \pm 0.01$ , respectively. With the choice of grain and container size, which leads to a particle diameter-to-container diameter ratio smaller than 0.1, the boundary effect from the container wall can be neglected (Chiapponi, 2017; Wang et al., 2021).

**Drying experiments:** The specimens were dried at laboratory conditions at temperature of  $21 \pm 1^\circ\text{C}$  and 0.55 relative humidity. The weight of each specimen was recorded every minute by an analytical balance (Sartorius CP224S) with nominal resolution of 0.1 mg, and photos were taken every 10 min by a camera (Canon 600D). Generally, the drying experiment under described conditions took around 45 h to complete. The end of drying can be identified once the specimen weight stops changing and remains at a constant value with fluctuations of the resolution of balance (also indicated by the relatively sharp turning point of drying rate, for example, in Figure 2a). The completion of drying process was further verified by comparing the residual water content of specimen, calculated from the weight difference before and after heating in oven overnight at  $105^\circ\text{C}$ , to that of dry specimen in laboratory condition, both of which were  $0.029 \pm 0.001\%$ . The cumulative drift of balance was found to be less than 0.5 mg during the entire experiment.

**MRI profiling experiment:** The nuclear magnetic resonance imaging (MRI), as a non-invasive and non-destructive method, has proven effective in probing the evolution of saturation profile during the evaporation process (Ben Abdelouahab et al., 2019; Coussot, 2020; Thierry et al., 2017). Here, the drying experiments were also conducted to obtain the evolution of 1D saturation profile using MRI (Bruker Minispec mq20 equipped with a field gradient) under similar experimental conditions as a supplement to provide qualitative characterization of the drying process. Due to the limitation on the size of NMR tube for the mini-spectrometer, the specimen size is smaller, that is, inner diameter of 6.9 mm and inner height of 14.5 mm. To remove the grains sticking at the inner wall, vibration is applied to the container such that grains on the wall fall down due to inertia. As a result of the extra vibration, the packing fraction of the granular assembly is around 0.58 for the MRI experiment, equal to the packing fraction of medium packed at dry condition, thus no collapse event is expected during the MRI experiment.

A multi-echo sequence with 128 echos was applied during the evaporation process. The echo time was 7.4 ms, much smaller than the typical relaxation time of the water at 40 ms to avoid a  $T_2$  weighting. The field of view was 20 mm, greater than the specimen height. The number of pixels was 128, corresponding to a spatial resolution of 0.16 mm. An averaging by three pixels was carried out to smooth the data. The recycle delay was 2 s (much greater than the total duration of the multi-echo sequence and typical value of the longitudinal relaxation time  $T_1$  of the water in this specimen) to reach the magnetization equilibrium and to avoid warming of the specimen. The signal was accumulated 128 times in order to increase the signal-to-noise ratio, leading to the cycle period of about 4.3 min. A Fourier transform of each echo and a Gaussian filter were applied. An exponential fit of odd echos for each pixel was done to get the amplitude, which is

**Table 1**  
*List of Experiments*

No. Exp.	$D$ ( $\mu\text{m}$ )	$h_{\text{fall}}$ (mm)	Container	$\rho_0$	Technique
6	376( $\pm 32$ )	100	standard	0.45( $\pm 0.01$ )	camera + balance
1	376( $\pm 32$ )	150	standard	0.53	camera + balance
1	1,594( $\pm 171$ )	100	standard	0.59	camera + balance
1	376( $\pm 32$ )	N.A	small	0.58	NMR

*Note.* From left to right columns: number of experiments, particle diameter (standard deviation in bracket), free fall height for specimen generation, container type, initial packing fraction (standard deviation in bracket), and experimental technique. “standard” corresponds to cylindrical container with inner diameter 13.70 mm and inner height 44.22 mm. “small” corresponds to cylindrical container with inner diameter of 6.9 mm and inner height of 14.5 mm.

proportional to the mass of water corresponding to each pixel. The integration of each 1D profile gives the total NMR signal, which is proportional to the total mass of water.

At the same time, we measured the NMR relaxation through a Carr-Purcell-Meiboom-Gill (Meiboom & Gill, 1958) (CPMG) sequence composed of a first  $\pi/2$ -pulse and 2,500  $\pi$ -pulses during 500 ms distributed in linear intervals. The repetition time is 2 s for relaxation of protons. This sequence was repeated 128 times to increase the signal-to-noise ratio. By means of Inverse Laplace Transform (ILT) with a procedure of non-negative least square fit to the data with Tikhonov regularization (similar to the “Contin” method as in (Provencher, 1982; Whittall & MacKay, 1969)), the transverse relaxation time  $T_2$  distribution can be resolved. We refer to (Coussot, 2020; Faure & Rodts, 2008; Valori et al., 2013) for more details on NMR. Note that the 1D profile and CPMG experiments were carried out intermittently in a loop function, leading to an effective time resolution of around 9.9 min. Table 1 summarizes the experiments conducted in this work.

### 3. Results and Discussion

#### 3.1. Evaporation Rate and Propagation of Drying Front

Figure 2a shows the change in volumetric water content (and specimen weight in the inset) as a function of time for two typical experiments with initial packing fractions of 0.448 and 0.468. For both experiments, the rate of change in weight decreases at the initial stage, entering a roughly linear stage after  $t \approx 15$  h, implying a constant drying period. Note that this observed constant drying regime is different from the one during the “Constant Rate Period” as in Figure 1, where the latter occurs at the beginning of the drying process at high liquid content. Finally, the liquid content does not further change after about 40 h, marking the end of the evaporation. Note that the non-zero liquid content measured at the end of experiment is  $0.029 \pm 0.01\%$ , which is equal to the liquid content of “dry” glass beads at laboratory condition. This is a result of adsorptive forces such that very small amount of liquid can exist at laboratory condition when no liquid is manually added into the media. Figure 2c shows two photos taken at the initial and final stages of drying period, where significant settlement of grains can be seen.

Since the packing fraction is found to be strongly influenced by the interparticle forces (Blum & Schr apler, 2004; Dong et al., 2006; Lohse et al., 2005; Parteli et al., 2014; Umbanhowar & Goldman, 2006; Yu et al., 2003; Yang et al., 2000, 2007), the drying-induced collapse, as explained earlier, originates from the structural instability of the loosely packed granular material once the liquid bridges evaporate, such that the assembly transitions from cohesive state to cohesionless state as the capillary force diminishes. Although it has been argued that decrease in liquid content does not result in variation in interparticle forces from liquid bridge because the decrease in liquid-solid contact area balances with increase in Laplace pressure (Butt, 2008; Butt & Kappl, 2009; Halsey & Levine, 1998; Rabinovich et al., 2005), at very low liquid content (asperity or roughness regime (Halsey & Levine, 1998)), the capillary force decreases sharply with smaller liquid volume due to surface roughness, which has been demonstrated in force measurement experiments in liquid bridges during drying process (Hueckel et al., 2020; Mielniczuk et al., 2014, 2015). This implies the existence of a critical water content at which the collapse will be triggered.



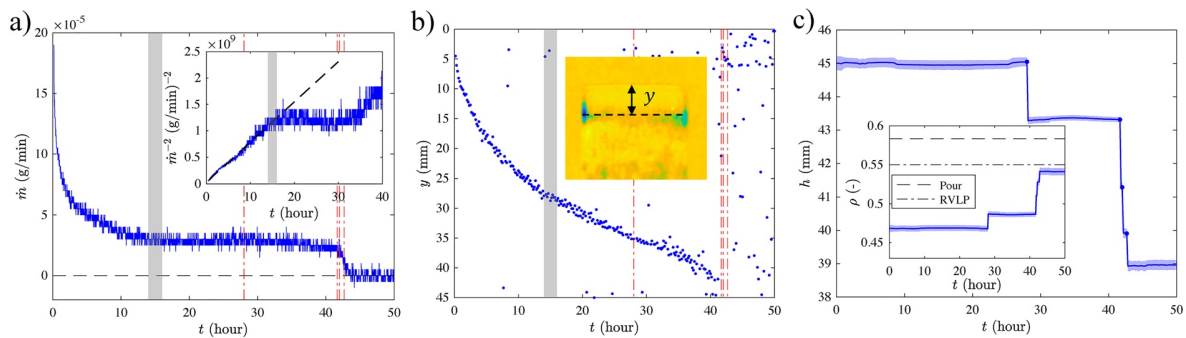


**Figure 3.** Drying dynamics of a typical experiment. (a) Drying rate  $\dot{m}$  as a function of time. Red-dotted lines mark the time of collapse event. Inset:  $\dot{m}^{-2}$  as a function of time. Black-dashed line is the linear regression based on data up to  $t = 15$  h. Gray area represents the transition between drying regimes. (b) Depth of drying front versus time. Inset shows the color map of difference between two consecutive images (only top region is shown for visualization purpose). (c) Height of glass beads specimen versus time. The identified collapse events are shown as blue dots. Inset: evolution of packing fraction calculated based on specimen height. Dashed line and dotted-dashed line represent the packing fractions at dry condition using pouring method (0.58) and random very loose packing (RVLP) state (0.55), respectively. Shaded area represents standard deviation.

Figure 3a more clearly shows that the drying rate  $\dot{m}$  starts to decrease at the beginning of the experiment, entering a roughly constant rate period after 15 h (marked by the gray region). Then  $\dot{m}$  maintains at this level before decreasing to zero at the end of evaporation. To compare the observed drying rate with evaporation controlled by vapor diffusion, the inset plots  $\dot{m}^{-2}$  as a function of time, where a linear relation can be observed during the first 15 h (black-dashed line), consistent with the theory on the basis of Brutsaert & Chen (1995) and experiments during the “second” drying period for initially fully saturated media (Shokri & Or, 2011). This confirms that the liquid bridges can be regarded as effectively isolated, and the effect from film flow is not significant.

From image analysis, as shown in Figure 3b, the propagation of drying front can be identified through comparing the contrast between two consecutive photos (also see Supporting Information Movie S1). It is found that the speed of receding drying front initially decreases, before entering a constant regime after  $t \approx 15$  h, in line with the transition of drying rate. After the end of drying process ( $\sim 42$  h), the drying front cannot be identified. Figure 3c shows the evolution of specimen height  $h$  during drying. The changes in  $h$  is found to be rather discrete, corresponding to individual collapse events. Also, it can be seen that the majority of the decreases in  $h$  occurs near the extreme end of the experiment. To evaluate the packing fraction of the granular medium, the initial packing fraction can be calculated by  $\phi_0 = V_g/V_c$ , with the volume of grains  $V_g$  calculated from the total weight of dry grains divided by the density, and the volume of the container  $V_c$  calculated from its dimension. Then, according to the photos taken during the drying process, the packing fraction at different time can be calculated by  $\phi = \phi_0 h_0/h$ , where  $h_0$  and  $h$  are the initial and current height of the specimen determined from the image. The inset shows the corresponding packing fraction determined from images. The times of collapse events are marked as red-dashed-dotted lines in Figures 3a and 3b.

To ensure the determination of drying front from image analysis actually reflects the saturation profile within the granular medium, and shed light on the liquid distribution during the drying process, drying experiment was conducted using NMR technique under similar experimental conditions. Figure 4a shows the evolution of 1-D saturation profile during NMR experiment, where light yellow color represents early stage and dark red indicates late times with 50 min increments. The saturation, represented by the NMR signal, is found to have similar value along the vertical direction at the start, indicating saturation homogeneity and that the medium is relatively well mixed. As the drying front recedes into the medium, the water content remains unchanged below the drying front, whereas the saturation above the drying front drops to a value smaller than the noise of NMR signal (less than  $\sim 0.05\%$ ). Figure 4a also demonstrates that the saturation gradient at the drying front is relatively sharp (around 2 mm). It is interesting to note that, visually, the spacing between the 1D profiles is relatively the same, indicating a drying front propagating downwards linearly with time, consistent with the drying regime with relatively constant drying rate. Near the end of drying, a transition can be identified (marked by the black-dashed line). After this transition, the drying

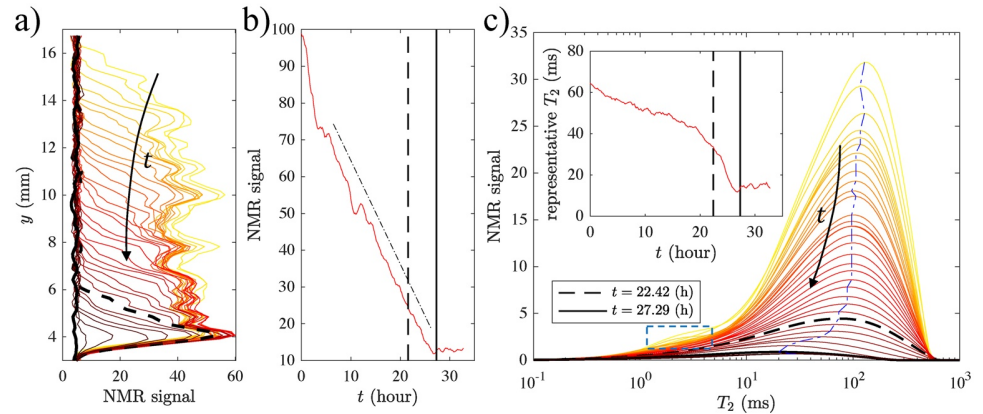


**Figure 4.** (a) Evolution of the 1-D NMR signal (direct indication of water content) profile. The transition from light yellow to dark red indicates snapshots at progressive time intervals. The time increment for each profile is 50 min. (b) Accumulated NMR signal versus time. The black-dashed-dotted line is added only to guide the eye. (c) Evolution of transverse relaxation time  $T_2$  during drying experiment. Blue-dash-dotted line follows the peak value of  $T_2$  at different times. The blue-dashed box marks the location of secondary “peak” (deviation from the gradually decreasing trend of NMR signal for smaller  $T_2$ ). Inset: Evolution of representative  $T_2$ , calculated as the weighted average of the distribution. In all plots, black-dashed lines and black-solid lines denote the same time, that is, 22.42 and 27.29 h, respectively.

region becomes stable in space, and the remaining saturation near the bottom of specimen progressively approaches the end state, which is marked by the black-solid line. Figure 4b plots the accumulated NMR signal as a function of time, which is the sum of area under the curve at different times from Figure 3a. After an initial sharp drop, the decrease in water content again decreases roughly linearly, consistent with the previous observations. Note that the residual NMR signal after the evaporation finishes was found to be non-zero, which could result from the noise of the NMR signal itself and/or from the irreducible water content (the water content at dry state under laboratory conditions). But this should not influence the result as same signal was found for dry specimens.

### 3.2. Evolution of Liquid Distribution

The longitudinal relaxation time  $T_1$ , also known as the spin-lattice relaxation time, characterizes the rate at which the nuclei return to alignment with the magnetic field. The transverse relaxation time  $T_2$ , also called the spin-spin relaxation time, characterizes the time at which the transverse component of the magnetization of the nuclei comes back to the equilibrium in the magnetic field. The value of relaxation times depend on the molecular dynamic. For the liquid water in a porous medium, they depend on the pore size, the saturation, and whether the water is adsorbed on the pore surface. Information on molecular dynamics and water distribution/movement across a very wide range of length and timescales can be obtained by measurements of relaxation times (Valori et al., 2013). Through CPMG (Carr-Purcell-Meiboom-Gill) experiment (Meiboom & Gill, 1958), the transverse relaxation time  $T_2$  during drying can be obtained, which reads as (Valckenborg et al., 2001; Valori et al., 2013):

$$\frac{1}{T_2} \approx \lambda \frac{S}{V} + \frac{1}{T_2^{\text{bulk}}} \approx \lambda \frac{S}{V}, \quad (1)$$

where  $\lambda$  is the surface relaxivity (unit: m/s),  $T_2^{\text{bulk}}$  is the relaxation time of bulk water,  $S$  is the wet surface area, and  $V$  is the volume of water. The term from  $T_2^{\text{bulk}}$  can be neglected in Equation 1 according to Tarr and Brownstein criterion (Brownstein & Tarr, 1979) since the dimensionless parameter  $a\lambda/D$  is found to be much less than 1, corresponding to the fast diffusion region (also denoted as surface limited relaxation), where  $a$  is the characteristic size of liquid cluster, and  $D \approx 2.3 \times 10^{-9} \text{ m}^2\text{s}^{-1}$  is water self-diffusion coefficient at 25 °C (Holz et al., 2000). Figure 4c shows the evolution of  $T_2$  distributions, where the arrow indicates increasing time. At early times, a peak at  $T_2 \approx 100$  ms can be seen. If look closely, a secondary “peak” marked by the blue-dashed box (deviation from the gradually decreasing trend of NMR signal for smaller

$T_2$ ) is also present at  $T_2 \approx 2$  ms, and these two peaks tend to merge as time increases due to the decreasing signal-to-noise ratio. Since liquid in non-saturated granular material can exist in the form of both liquid bridges between grains and thin films on grain surface (Fournier et al., 2005; Scheel et al., 2008a; Tuller & Or, 2005; Wang et al., 2016), it is likely that populations in the vicinities of  $T_2 \approx 100$  ms and  $T_2 \approx 2$  ms correspond to the liquid bridges and thin films, respectively. To test this hypothesis, for given initial volumetric water content, assuming liquid bridges contribute to the majority of liquid volume, we can estimate the average volume of liquid bridge in monodisperse spheres assuming a coordination number  $N \approx 6$  (Liu et al., 1999; Fei & Narsilio, 2020). Then, using the relation (Weigert & Ripperger, 1999):

$$V = 0.12d_p^3 \sin^4(\beta)C_a C_\theta, \quad (2)$$

The half-filling angle  $\beta$  can be obtained, where  $d_p$  is particle diameter,  $C_a = 1$  for particles in contact, and  $C_\theta = 1 + 1.1 \sin \theta$  is the correction factor for contact angle  $\theta$ . Finally, the volume-to-area ratio can be expressed as:

$$\frac{V}{S} = \frac{0.12d_p^3 \sin^4(\beta)C_a C_\theta}{\pi(1 - \cos \beta)}. \quad (3)$$

From Equation 3 and Equation 1, combined with the ratio of  $T_2$  of two populations (2 and 100 ms for liquid films and liquid bridges, respectively) and the constant surface relaxivity  $\lambda$  (composition of solid matrix does not change), the average thickness of thin film, which is simply calculated as  $h = V/S$ , is found to be  $h \in [0.17, 0.25] \mu\text{m}$  for contact angle  $\theta \in [0^\circ, 60^\circ]$ . Past studies have indicated that the film thickness  $h$  is of the same order as roughness of grains (Han et al., 2009). For example, the film thickness is found to be  $h \sim 0.6 \mu\text{m}$  for Fontainebleau sandstone of roughness depth  $1 \mu\text{m}$  (Han et al., 2009). Thus, for typical glass beads of roughness  $\sim 0.5 \mu\text{m}$  (Fournier et al., 2005), the film thickness is expected to be  $\sim 0.3 \mu\text{m}$ , which agrees well with the calculated value. To check the assumption that the total volume of liquid film is much smaller than that of liquid bridges, the volumetric water content under the condition where all surface areas are covered by thin film is found to be  $\sim 0.2\%$ , much smaller than the total initial water content of  $\sim 4.3\%$  in NMR experiment.

Therefore, Figure 4c implies that the liquid exist mainly in the form of liquid bridges (high NMR signal), and the contribution from the thin films can be effectively ignored. The trajectory of  $T_2$  with maximum NMR signal is shown as blue-dot-dashed line. It remains almost constant before the transition marked by black-dashed line, then experiencing a sharp decrease. This is indeed consistent with the previous observation where the drying front recedes into the porous medium, leading to a significant decrease in total volume of liquid (corresponding to decrease in NMR signal), but with no significant change of the geometrical feature of liquid clusters (corresponding to constant  $T_2$ ). The latter is mainly represented by the volume-to-area ratio of the liquid bridges that make up the bulk of liquid volumes (those below the drying front). The volume-to-area ratio only starts to decrease near the end of drying, corresponding to a drying region that is stable in space (Figure 4a after the black-dashed line), during which the representative volume of liquid bridges decreases. Similar tendency can be reflected from the representative  $T_2$  (Inset of Figure 4c), calculated as the weighted average of  $T_2$  distribution at different times, where it decreases slowly before  $t = 22.4$  h due to the weighted averaging process, and a sharp decrease can be observed after the transition. It is interesting to note that the spatial shift of saturation profile (front propagation) in Figure 4a corresponds to the decrease in signal intensity of  $T_2$  distribution in Figure 4c, whereas a spatially stable decrease in saturation after the transition ( $t = 22.4$  h) corresponds to the shift in value of representative  $T_2$ . These observations together reveal the global and local evolution of volume and shape of liquid clusters.

### 3.3. Drying-Induced Collapse

Given the observation of the drying front and sharp saturation gradient propagating downwards continuously, one would expect similar statistics of collapse events that are correlated with the drying front. However, surprisingly, Figure 3c shows that the collapse events (blue dots) occur in a rather discrete manner, with most collapse events occurring at the very end of drying. This has two implications. First, liquid

bridges exist in the dry region above the drying front with corresponding water content that is too small to be detected by NMR technique (less than  $\sim 0.05\%$ ), but sufficient to support the loose structure of the medium. Although we are unable to find past works on the critical liquid content that marks the onset of most drying-induced collapses, the variations of the tensile/shear strength of non-saturated granular materials, as well as the packing fraction of wet grains, should bear the indicative information on the critical liquid content, as the fundamental grain-scale mechanism that controls the aforementioned macroscopic behaviors is the interparticle cohesive forces due to liquid bridges. For spherical grains such as glass beads, the threshold liquid content is indeed found to be rather small ( $<1\%$ ) (Cho & Santamarina, 2001; Feng & Yu, 1998; Scheel et al., 2008a). Particularly, the degree of saturation at maximum shear-wave velocity, which is directly related to the shear modulus, is determined to be  $\sim 0.7\%$  (Cho & Santamarina, 2001), below which the shear modulus plummets with decreasing water content. This critical liquid content can be effectively regarded as an upper bound for the critical saturation for the collapse, since the unstable loosely packed structure will not be able to withstand gravity of particles once the enhancement in interparticle frictional resistance due to liquid bridges (reflected by shear modulus) is reduced. Note that this threshold value is likely to be sensitive to particle shapes and grain size distribution (Cho & Santamarina, 2001; Wu et al., 1984; Zou et al., 2001, 2003), which is worth investigating in future works. Second, contrary to past hypothesis that the liquid in the apparent dry region cannot be further extracted and equals to the air-dry value (Thiery et al., 2017; Wang et al., 2019), it indeed can be further reduced near the end of drying, which is signaled by the collapse events.

To ensure the repeatability of the experiments and gain sufficient statistical information on drying-induced collapse, the specimen height versus time from six experiments are plotted in Figure 5a. Again, concentrated collapses are observed at  $t \approx 40$  h depending on initial water content and minor fluctuations in relative humidity and temperature, and almost no collapse event occurs in the first 30 h even with significant apparent dry region after propagation of drying front (Figure 3c). The corresponding packing fraction  $\rho$  calculated from image analysis is shown in Figure 5b. The solid and dot-dashed lines represent the packing fractions measured at dry condition using pouring method (Wang et al., 2021) and lower limit of random very loose packing (RVLP) (Ciamarra & Coniglio, 2008; Farrell et al., 2010; Jerkins et al., 2008; Onoda & Liniger, 1990), respectively. As can be seen in Figure 5b, the packing fraction increases from  $\sim 0.45$  to  $\sim 0.55$  after collapse, close to the RVLP. Note that there is an underestimation of the packing fraction, as the surface is no longer perfectly smooth after collapse such that the occupied volumes of particles determined from 2D images are typically greater than actual ones. This may explain some of the final packing fractions are still smaller than the RVLP limit.

Apart from the identification of drying front and collapse height, the individual collapse region, characterized by its length  $l_c$  can also be obtained from the image analysis. First, the image contrast (subtraction of image matrix) between every two consecutive images is calculated. Then, the cumulative image contrast along the horizontal direction is calculated, giving an array along the vertical direction. If no collapse event occurs during the time between these two images, the cumulative contrast array should be mainly noise with relatively small values. If, however, a collapse event happens, the image contrast array should contain greater values since there is significant difference between two consecutive images. Figure 5c shows the image contrast array before ( $c_n - 1$ ), at ( $c_n$ ), and after ( $c_n + 1$ ) an individual collapse event. Three distinct regions can be identified: (a) large contrast region with cumulative horizontal contrast above 2,000, which represents the region that is filled before the collapse, but empty after; (b) moderate contrast region with contrast smaller than 2,000 and greater than 300, which represents the region that is filled with initial packing state, but collapses into different (denser) packing state after; (c) small contrast region with contrast less than 300, where there is no change in structure and the fluctuations are mainly from image noise. Note that the changes in image contrast at the boundaries of different regions are relatively sharp, and it is found that minor variations in these empirically selected threshold values do not significantly impact the results. In the case of Figure 5c, the distance between the black-dashed lines is thus  $l_c$ . Note that the individual collapse region length  $l_c$  is calculated as the effective one, that is, it only represents the region that evolves from loose state towards denser state at each individual collapse, without the cumulative effect from previous collapses. The inset shows the photos before and after an initial collapse event, where the region below the white-dashed line remain unaffected. This suggests that even in the apparent dry region, there exists a saturation gradient, which may correspond to a third drying front that separates the specimen by the effectiveness of

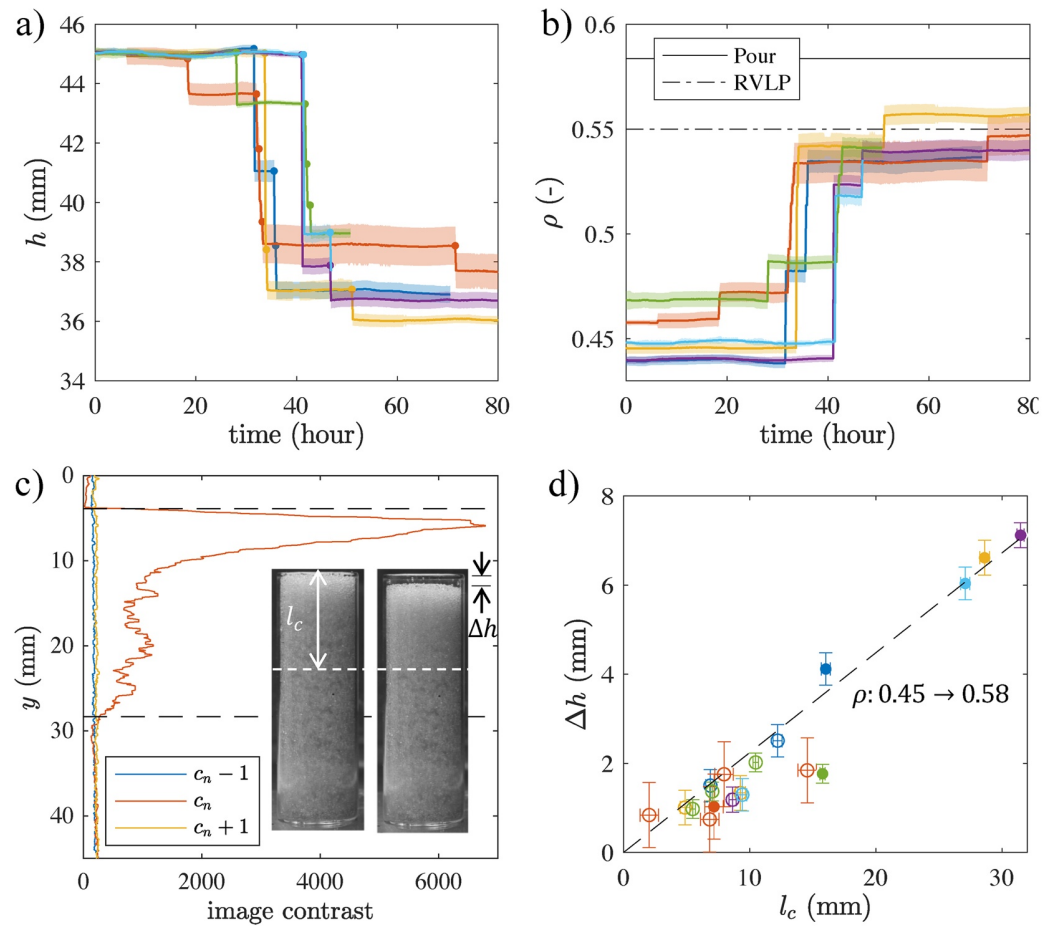


**Figure 5.** (a) Height versus time for six repeated experiments. Concentrated collapse events are observed near the end of drying ( $t \approx 40$  h). (b) Corresponding packing fraction determined from the image analysis. Solid line and dotted-dashed line represent the packing fractions at dry condition using pouring method (0.58) and random very loose packing state (0.55), respectively. (c) Typical data of the sum in the horizontal direction of difference of two consecutive images right before ( $c_n - 1$ ), at ( $c_n$ ), and right after ( $c_n + 1$ ) a collapse event. Distance between the black-dashed lines represents the individual collapse region length  $l_c$ . Inset: photos right before/after a collapse event. The region above the white-dashed line collapses, whereas the region below remains unaffected. (d) Statistics of collapse events for six experiments: change in height  $\Delta h$  versus individual collapse region length  $l_c$ . Filled and hollow symbols represent the first and subsequent collapse events, respectively. Error bars represent the standard deviation of surface profile fluctuation. Black-dashed line shows the theory when packing fraction changes from 0.45 to 0.58 homogeneously.

the capillary bridge through a critical water content. The region below this drying front can withstand the impact of collapse above it and remain intact due to the capillary force. As one of the main findings, this third drying front has not been discovered before. However, a more thorough investigation requires higher resolution of measuring device and more controlled experimental condition, which is beyond the scope of current work.

Figure 5d depicts the correlation between change in height and individual collapse region length. Filled and hollow circles represent initial and subsequent collapse events for each experiment in different colors. Error bars represent the standard deviation of surface profile fluctuations from image analysis. It shows that the initial collapse events tend to have greater region of impact. In addition, most points can be described by a theoretical line assuming the packing fraction changes from 0.45 to 0.58 for each individual collapse event (see appendix for calculation of this line). This again indicates that the nature of collapse is local. Besides, it shows that both the initial packing structure before collapse, and the change in packing fraction for each individual collapse event, are relatively homogeneous.

### 3.4. Transition in Drying Regimes

One possible reason that results in the observed transition in drying regimes, that is, the decreasing rate regime to constant rate regime indicated by the gray region in Figure 3a, could be the theory of enhanced vapor diffusion in non-saturated porous media (Webb & Ho, 1998; Shahraeeni & Or, 2008), that is, in the presence of thermal or capillary gradient, the vapor can condensate on one side of liquid island and subsequently evaporate from the other side, which reduces the effective diffusion path length. Nevertheless, the enhancement factor in this model decreases with decreasing saturation, being close to one at low saturation (Shahraeeni & Or, 2008). Since the initial water content is also low in the current study ( $\sim 2\%$ ), and the transition takes place in later stage of drying (at even lower water content), the enhanced diffusion theory alone cannot explain the observed results.

Besides, the effect from film flow at low water content regime has been explored in the recent years (Tuller & Or, 2001; Tuller & Or, 2005; Wang et al., 2013; Wang et al., 2018; Wang et al., 2016; Wang et al., 2019), where the liquid connectivity is maintained through the thin liquid film at the grain surface. As a result, the drying flux through the film flow is proportional to the specific surface area of the granular medium, which implies that the drying flux at transition in drying regimes, if mainly transported through film flow, should be sensitive to the grain size. However, we did not observe this phenomenon and the critical drying rate at which the transition occurs is similar for  $376 \pm 32 \mu\text{m}$  and  $1,594 \pm 171 \mu\text{m}$  glass beads (Figure A1 in the Appendix).

Actually, it is likely that the observed phenomena is due to Kelvin effect. The Kelvin equation  $\ln p^* = \gamma V_m / rRT$  indicates that the relative vapor pressure at the liquid-gas interface  $p^*$  depends on the capillary pressure  $\gamma/r$ , with  $\gamma$  surface tension,  $V_m$  molar volume,  $r$  the radius of curvature of liquid-gas interface,  $R$  universal gas constant, and  $T$  temperature. As the drying front propagates and the region of the porous medium above it approaches dry condition, the curvature of liquid bridges above the drying front quickly increases (as their volume decreases), causing a drop in vapor pressure at the surface of liquid bridges and slowing down the drying process of those very small liquid bridges in the apparent dry region. Thus, the Kelvin effect explains the delayed evaporation of small liquid bridges that are responsible for supporting the loosely packed granular materials, leading to the observation that the occurrences of most collapse events are concentrated near the very end of the whole drying process. As the evaporation proceeds, the overall drying rate decreases due to greater diffusion distance according to Fick's law, whereas a greater number of menisci are exposed to evaporation, thus leading to a deviation from the theory where Kelvin effect (and thus the presence of liquids above the drying front) is not considered. The enhancement in drying rate due to Kelvin effect is also reported in a recent work using pore-network simulation (Maalal et al., 2021). It is worth noting that this phenomenon can be regarded as an equilibration process (Thiery et al., 2017). However, different from capillary flow where the equilibration takes place within liquid phase due to difference in capillary pressure, it is due to constrain in the vapor pressure according to Kelvin equation. Although without detailed discussion, similar drying enhancement phenomenon at low saturation (less than 5%) is also present in the study by Thiery et al. (2017). In fact, the Kelvin effect can be significant either for very fine particles or very low water content (Thiery et al., 2017; Yang et al., 2020), and the current study demonstrates for the first time the drying enhancement phenomenon due to Kelvin effect for grains with size of hundreds of micrometers.

In this study, glass beads were chosen as the model granular materials for the drying experiment. With careful choice of the particle diameter according to previous studies (Than et al., 2016; Wang et al., 2021), the effect from van der Waals forces can be effectively excluded, and the loosely packed wet granular assembly with packing fraction significantly less than the one at cohesionless state (0.58 in this case) can be generated. For other granular materials, however, depending on the initial state of the granular assembly and particle properties, different behavior can be expected. For example, for finer particles with other cohesive forces apart from capillary force, the resulting packing fraction after collapse due to disappearance of liquid bridges can be some intermediate value between the initial and cohesionless state, depending on the relative significance of the cohesive force to the gravity (Blum & Schröppler, 2004; Dong et al., 2006; Lohse et al., 2005; Parteli et al., 2014; Umbanhowar & Goldman, 2006; Yang et al., 2000, 2007; Yu et al., 2013). Besides, for grains with greater surface roughness, on the one hand, enhanced structural stability might be expected due to greater friction coefficient. On

the other hand, the effectiveness of the small liquid bridges might decrease, that is, increase in surface roughness is associated with smaller capillary force from small liquid bridges as a result of the asperity or roughness regime (Halsey & Levine, 1998), which can consequently lead to an earlier transition towards cohesionless (or less cohesive) state during the drying process. These competing mechanisms originated from change in surface roughness, and other factors such as particle shape and grain size distribution, are worthy of further investigation. In addition, the experimental condition at which the evaporation process occurs is also likely to impact the drying behavior. The drying rate in the current study is relatively slow, that is, it takes about 2 days for the drying of granular materials with 2% initial water content to complete under standard laboratory condition. With faster drying rate due to higher temperature, lower relative humidity, or imposed external airflow in the environment, the influence of Kelvin effect on the drying rate may become less significant even near the end of drying process. The aforementioned aspects, as well as more systematic and quantitative characterization of the drying process with the help of more accurate equipment and thorough control of experimental condition, are some examples of future research directions.

#### 4. Conclusions

The drying of loosely packed granular materials from low initial water content was experimentally studied. The drying rate is found to decrease from the beginning, corresponding to the decreasing rate period controlled by vapor diffusion, which is associated with a propagation of drying front with a sharp saturation gradient identified through image analysis and magnetic resonance imaging. Then, a deviation in drying rate from diffusion limited evaporation is observed. The enhancement of the evaporation at the later stage of drying process is attributed to Kelvin effect.

We also observed the drying-induced collapse of granular medium due to its structural instability as the liquid bridges evaporate and capillary forces decrease. The concentrated collapse at the end of drying suggests the existence of liquid in the form of liquid bridges in the apparent dry region due to Kelvin effect, which can be further extracted near the end of drying process. Through analyzing the collapse statistics, it is found that collapse event is local in space and time, which implies that, apart from previously identified primary and secondary drying fronts, there exists a third drying front in the apparent dry region, which propagates relatively quickly at the end of drying.

#### Appendix A

##### Drying Curves at Different Initial Packing Fractions and Grain Size

Figure A1 shows the drying curves (evolution of specimen weight, drying rate  $\dot{m}$ , and  $\dot{m}^{-2}$ ) for grains at different initial packing fractions (a-c) and larger grain size (d). The black-solid lines are linear fittings based on data at early stages of drying, which represent the theory predicted based on Fick's law. An enhancement in drying rate can be observed in all experiments, which corresponds to a downward deviation from the linear relation. The drying rates at which this transition occurs are  $\sim 3$  g/min for all cases (as in  $\dot{m}$ - $t$  plots).

##### Determination of Theoretical Line Relating $l_c$ and $\Delta h$

The line can be determined based on the idea of conservation of volume, that is, volume occupied by the grains remain the same. For a given volume before collapse, the volume  $V_1 = Al_c$ , with  $A$  the cross-section area,  $l_c$  the height (also the collapse region length). Let  $\phi_1$  be the packing fraction before collapse, leading to the volume occupied by grains  $V_g = \phi_1 V_1$ . After collapse, if the packing fraction is  $\phi_2$ ,  $V_g = \phi_2 V_2$ , with  $V_2 = A(l_c - \Delta h)$  the volume after collapse. So,  $V_g = \phi_1 V_1 = \phi_2 V_2$ , that is,  $\phi_1 Al_c = \phi_2 A(l_c - \Delta h)$ , in other words,  $\Delta h = l_c(1 - \phi_1/\phi_2)$ .

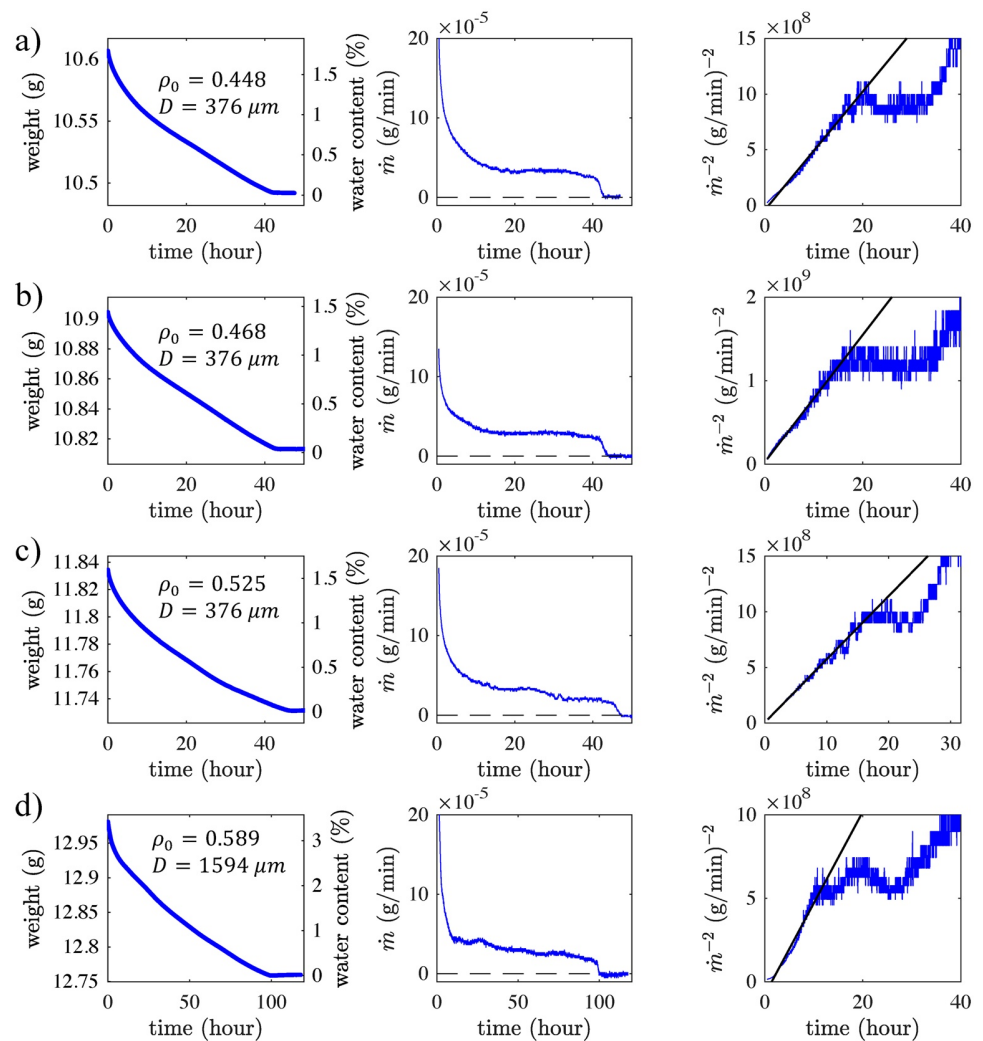


**Figure A1.** Drying curves of unsaturated porous media. (a–c) Glass beads of diameter  $375.5 \pm 31.8$  and different initial packing fractions. (d) Glass beads of diameter  $1,594 \pm 171$ . Solid lines are linear fittings using data at the early stages..

### Data Availability Statement

Data associated with this work are available online (<https://doi.org/10.6084/m9.figshare.14368688>).

### Acknowledgments

This work was financially supported by Australian Research Council (Projects DP170102886) and The University of Sydney SOAR Fellowship. YG acknowledges the financial support of Labex MMCD (ANR-11-LABX-022-01) for his stay at Laboratoire Navier at ENPC. ZW thanks Baptiste Chabot, Xavier Boulay, Loïc Lesueur, and Emmanuel De Laure for the assistance on experiments.

### References

- Ben Abdelouahab, N., Gossard, A., Rodts, S., Coasne, B., & Coussot, P. (2019). Convective drying of a porous medium with a paste cover. *The European Physical Journal E*, *42*(5), 66. <https://doi.org/10.1140/epje/i2019-11829->
- Blum, J., & Schräpler, R. (2004). Structure and mechanical properties of high-porosity macroscopic agglomerates formed by random ballistic deposition. *Physical Review Letters*, *93*, 115503. <https://doi.org/10.1103/physrevlett.93.115503>
- Brownstein, K. R., & Tarr, C. E. (1979). Importance of classical diffusion in nmr studies of water in biological cells. *Physical Review A*, *19*, 2446–2453. <https://doi.org/10.1103/PhysRevA.19.2446>
- Bruchon, J.-F., Pereira, J.-M., Vandamme, M., Lenoir, N., Delage, P., & Bornert, M. (2013). Full 3d investigation and characterization of capillary collapse of a loose unsaturated sand using x-ray ct. *Granular Matter*, *15*(6), 783–800. <https://doi.org/10.1007/s10035-013-0452-6>
- Brutsaert, W., & Chen, D. (1995). Desorption and the two stages of drying of natural tallgrass prairie. *Water Resources Research*, *31*(5), 1305–1313. <https://doi.org/10.1029/95wr00323>
- Butt, H.-J. (2008). Capillary forces: Influence of roughness and heterogeneity. *Langmuir*, *24*(9), 4715–4721. PMID: 18442225 <https://doi.org/10.1021/la703640f>
- Butt, H.-J., & Kappl, M. (2009). Normal capillary forces. *Advances in Colloid and Interface Science*, *146*(1), 48–60. <https://doi.org/10.1016/j.cis.2008.10.002>



- Chiapponi, L. (2017). Water retention curves of multicomponent mixtures of spherical particles. *Powder Technology*, 320, 646–655. <https://doi.org/10.1016/j.powtec.2017.07.083>
- Cho, G. C., & Santamarina, J. C. (2001). Unsaturated particulate materials—Particle-level studies. *Journal of Geotechnical and Geoenvironmental Engineering*, 127(1), 84–96. [https://doi.org/10.1061/\(ASCE\)1090-0241\(2001\)127:1\(84\)](https://doi.org/10.1061/(ASCE)1090-0241(2001)127:1(84))
- Ciamarra, M. P., & Coniglio, A. (2008). Random very loose packings. *Physical Review Letters*, 101, 128001. <https://doi.org/10.1103/physrevlett.101.128001>
- Coussot, P. (2000). Scaling approach of the convective drying of a porous medium. *The European Physical Journal B - Condensed Matter and Complex Systems*, 15(3), 557–566. <https://doi.org/10.1007/s100510051160>
- Coussot, P. (2020). Progress in rheology and hydrodynamics allowed by NMR or MRI techniques. *Experiments in Fluids*, 61(9), 207. <https://doi.org/10.1007/s00348-020-03037-y>
- Dong, K. J., Yang, R. Y., Zou, R. P., & Yu, A. B. (2006). Role of interparticle forces in the formation of random loose packing. *Physical Review Letters*, 96, 145505. <https://doi.org/10.1103/physrevlett.96.145505>
- Farrell, G. R., Martini, K. M., & Menon, N. (2010). Loose packings of frictional spheres. *Soft Matter*, 6, 2925–2930. <https://doi.org/10.1039/c0sm00038h>
- Faure, P. F., & Rodts, S. (2008). Proton nmr relaxation as a probe for setting cement pastes. *Magnetic Resonance Imaging*, 26(8), 1183–1196. <https://doi.org/10.1016/j.mri.2008.01.026>
- Fei, W., & Narsilio, G. A. (2020). Impact of three-dimensional sphericity and roundness on coordination number. *Journal of Geotechnical and Geoenvironmental Engineering*, 146(12), 06020025. [https://doi.org/10.1061/\(asce\)gt.1943-5606.0002389](https://doi.org/10.1061/(asce)gt.1943-5606.0002389)
- Feng, C., & Yu, A. (1998). Effect of liquid addition on the packing of mono-sized coarse spheres. *Powder Technology*, 99(1), 22–28. [https://doi.org/10.1016/s0032-5910\(98\)00086-2](https://doi.org/10.1016/s0032-5910(98)00086-2)
- Fournier, Z., Geromichalos, D., Herminghaus, S., Kohonen, M. M., Mugele, F., Scheel, M., et al. (2005). Mechanical properties of wet granular materials. *Journal of Physics: Condensed Matter*, 17(9), S477–S502. <https://doi.org/10.1088/0953-8984/17/9/013>
- Halsey, T. C., & Levine, A. J. (1998). How sandcastles fall. *Physical Review Letters*, 80, 3141–3144. <https://doi.org/10.1103/physrevlett.80.3141>
- Han, M., Youssef, S., Rosenberg, E., Fleury, M., & Levitz, P. (2009). Deviation from archie's law in partially saturated porous media: Wetting film versus disconnectedness of the conducting phase. *Physical Review E-Statistical Physics, Plasmas, Fluids, and Related Interdisciplinary Topics*, 79, 031127. <https://doi.org/10.1103/PhysRevE.79.031127>
- Holz, M., Heil, S. R., & Sacco, A. (2000). Temperature-dependent self-diffusion coefficients of water and six selected molecular liquids for calibration in accurate 1h NMR pfg measurements. *Physical Chemistry Chemical Physics*, 2, 4740–4742. <https://doi.org/10.1039/B005319H10.1039/B005319H>
- Hueckel, T., Mielniczuk, B., & El Youssoufi, M. S. (2020). Adhesion-force micro-scale study of desiccating granular material. *Géotechnique*, 70(12), 1133–1144. <https://doi.org/10.1680/jgeot.18.P.298>
- Jerkins, M., Schröter, M., Swinney, H. L., Senden, T. J., Saadatfar, M., & Aste, T. (2008). Onset of mechanical stability in random packings of frictional spheres. *Physical Review Letters*, 101, 018301. <https://doi.org/10.1103/physrevlett.101.018301>
- Lehmann, P., Assouline, S., & Or, D. (2008). Characteristic lengths affecting evaporative drying of porous media. *Physical Review E-Statistical Physics, Plasmas, Fluids, and Related Interdisciplinary Topics*, 77, 056309. <https://doi.org/10.1103/PhysRevE.77.056309>
- Liu, L., Zhang, Z., & Yu, A. (1999). Dynamic simulation of the centripetal packing of mono-sized spheres. *Physica A: Statistical Mechanics and its Applications*, 268(3), 433–453. [https://doi.org/10.1016/s0378-4371\(99\)00106-5](https://doi.org/10.1016/s0378-4371(99)00106-5)
- Lohse, D., Rauhé, R., Bergmann, R., & Meer, D. (2005). Creating a dry variety of quicksand. *Nature*, 432, 689–690.
- Maalal, O., Prat, M., & Lasseux, D. (2021). Pore network model of drying with kelvin effect, *Physics of Fluids* 33 (2), 027103. arXiv: <https://doi.org/10.1063/5.0035651>
- Meiboom, S., & Gill, D. (1958). Modified spin-echo method for measuring nuclear relaxation times. *Review of Scientific Instruments*, 29(8), 688–691. <https://doi.org/10.1063/1.1716296>
- Mielniczuk, B., Hueckel, T., & El Youssoufi, M. S. (2015). Laplace pressure evolution and four instabilities in evaporating two-grain liquid bridges. *Powder Technology*, 283, 137–151. <https://doi.org/10.1016/j.powtec.2015.05.024>
- Mielniczuk, B., Hueckel, T., & Youssoufi, M. S. E. (2014). Evaporation-induced evolution of the capillary force between two grains. *Granular Matter*, 16(5), 815–828. <https://doi.org/10.1007/s10035-014-0512-6>
- Mitarai, N., & Nori, F. (2006). Wet granular materials. *Advances in Physics*, 55(1–2), 1–45. <https://doi.org/10.1080/00018730600626065>
- Onoda, G. Y., & Liniger, E. G. (1990). Random loose packings of uniform spheres and the dilatancy onset. *Physical Review Letters*, 64, 2727–2730. <https://doi.org/10.1103/physrevlett.64.2727>
- Or, D., Lehmann, P., Shahraeeni, E., & Shokri, N. (2013). Advances in Soil Evaporation Physics—A Review, *Vadose Zone*. 12(4), vzj2012.0163. <https://doi.org/10.2136/vzj2012.0163>
- Parteli, E., Schmidt, J., Blümel, C., Wirth, K.-E., Peukert, W., & Pöschel, T. (2014). Attractive particle interaction forces and packing density of fine glass powders. *Scientific Reports*, 4, 6227. <https://doi.org/10.1038/srep06227>
- Provencher, S. W. (1982). A constrained regularization method for inverting data represented by linear algebraic or integral equations. *Computer Physics Communications*, 27(3), 213–227. [https://doi.org/10.1016/0010-4655\(82\)90173-4](https://doi.org/10.1016/0010-4655(82)90173-4)
- Rabinovich, Y. I., Esayanur, M. S., & Moudgil, B. M. (2005). Capillary forces between two spheres with a fixed volume liquid bridge: Theory and experiment. *Langmuir*, 21(24), 10992–10997. PMID: 16285763 <https://doi.org/10.1021/la0517639>
- Scheel, M., Seemann, R., Brinkmann, M., Di Michiel, M., Sheppard, A., Breidenbach, B., & Herminghaus, S. (2008). Morphological clues to wet granular pile stability. *Nature Materials*, 7, 189–193. <https://doi.org/10.1038/nmat2117>
- Scheel, M., Seemann, R., Brinkmann, M., Michiel, M. D., Sheppard, A., & Herminghaus, S. (2008). Liquid distribution and cohesion in wet granular assemblies beyond the capillary bridge regime. *Journal of Physics: Condensed Matter*, 20(49), 494236. <https://doi.org/10.1088/0953-8984/20/49/494236>
- Shahraeeni, E., & Or, D. (2008). Pore scale mechanisms for enhanced vapor transport through partially saturated porous media. *Water Resources Research*, 48(5). <https://doi.org/10.1029/2011WR011036>
- Shokri, N., Lehmann, P., & Or, D. (2009). Critical evaluation of enhancement factors for vapor transport through unsaturated porous media. *Water Resources Research*, 45(10). <https://doi.org/10.1029/2009WR007769>
- Shokri, N., & Or, D. (2011). determines drying rates at the onset of diffusion controlled stage-2 evaporation from porous media? *Water Resources Research*, 47(9). <https://doi.org/10.1029/2010WR010284>
- Than, V.-D., Aïmediou, P., Pereira, J.-M., Roux, J.-N., Bornert, M., & Tang, A.-M. (2016). Macro-microscopic one-dimensional compression of wet granular soils by experimental investigation. *E3S Web of Conferences*, 9, 06001. <https://doi.org/10.1051/e3sconf/20160906001>
- Thiery, J., Rodts, S., Weitz, D. A., & Coussot, P. (2017). Drying regimes in homogeneous porous media from macro- to nanoscale. *Physics Review Fluids*, 2, 074201. <https://doi.org/10.1103/PhysRevFluids.2.074201>

- Tuller, M., & Or, D. (2001). Hydraulic conductivity of variably saturated porous media: Film and corner flow in angular pore space. *Water Resources Research*, 37(5), 1257–1276. <https://doi.org/10.1029/2000wr900328>
- Tuller, M., & Or, D. (2005). Water films and scaling of soil characteristic curves at low water contents. *Water Resources Research*, 41(9). <https://doi.org/10.1029/2005WR004142>
- Umbanhowar, P. B., & Goldman, D. I. (2006). Low density fragile states in cohesive powders. *American Journal of Physics*, 74(8), 720–721. <https://doi.org/10.1119/1.2201858>
- Valckenborg, R. M. E., Pel, L., Hazrati, K., Kopinga, K., & Marchand, J. (2001). Pore water distribution in mortar during drying as determined by nmr. *Materials and Structures*, 34(10), 599–604. <https://doi.org/10.1007/BF02482126>
- Valori, A., McDonald, P., & Scrivener, K. (2013). The morphology of c–s–h: Lessons from 1h nuclear magnetic resonance relaxometry. *Cement and Concrete Research*, 49, 65–81. <https://doi.org/10.1016/j.cemconres.2013.03.011>
- Vo, T. T., Nezamabadi, S., Mutabaruka, P., Delenne, J.-Y., & Radjai, F. (2020). Additive rheology of complex granular flows. *Nature Communications*, 11(1), 1476. <https://doi.org/10.1038/s41467-020-15263-3>
- Wang, Y., Jin, M., & Deng, Z. (2018). Alternative model for predicting soil hydraulic conductivity over the complete moisture range. *Water Resources Research*, 54(9), 6860–6876. <https://doi.org/10.1029/2018wr023037>
- Wang, Y., Ma, J., & Guan, H. (2016). A mathematically continuous model for describing the hydraulic properties of unsaturated porous media over the entire range of matric suctions. *Journal of Hydrology*, 541, 873–888. <https://doi.org/10.1016/j.jhydrol.2016.07.046>
- Wang, Y., Ma, J., Zhang, Y., Zhao, M., & Edmunds, W. M. (2013). A new theoretical model accounting for film flow in unsaturated porous media. *Water Resources Research*, 49(8), 5021–5028. <https://doi.org/10.1002/wrcr.20390>
- Wang, Y., Merlin, O., Zhu, G., & Zhang, K. (2019). A physically based method for soil evaporation estimation by revisiting the soil drying process. *Water Resources Research*, 55(11), 9092–9110. <https://doi.org/10.1029/2019wr025003>
- Wang, Z., Pereira, J.-M., & Gan, Y. (2021). Packing of wet monodisperse spheres. *Powder Technology*, 378, 60–64. <https://doi.org/10.1016/j.powtec.2020.09.074>
- Webb, S. W., & Ho, C. K. (1998). Review of enhanced vapor diffusion in porous media, Tech. rep., United States, sAND-98-1819C (1998). URL: [http://inis.iaea.org/search/search.aspx?orig\\_q=RN:30009514](http://inis.iaea.org/search/search.aspx?orig_q=RN:30009514)
- Weigert, T., & Ripperger, S. (1999). Calculation of the liquid bridge volume and bulk saturation from the half-filling angle. *Particle & Particle Systems Characterization*, 16(5), 238–242. [https://doi.org/10.1002/\(sici\)1521-4117\(199910\)16:5<238::aid-ppsc238>3.0.co;2-e](https://doi.org/10.1002/(sici)1521-4117(199910)16:5<238::aid-ppsc238>3.0.co;2-e)
- Whittall, K. P., & MacKay, A. L. (1969). Quantitative interpretation of nmr relaxation data. *Journal of Magnetic Resonance*, 84(1), 134–152. [https://doi.org/10.1016/0022-2364\(89\)90011-5](https://doi.org/10.1016/0022-2364(89)90011-5)
- Wu, S., Gray, D. H., & Richart, F. E. (1984). Capillary effects on dynamic modulus of sands and silts. *Journal of Geotechnical Engineering*, 110(9), 1188–1203. [https://doi.org/10.1061/\(ASCE\)0733-9410\(1984\)110:9\(1188\)](https://doi.org/10.1061/(ASCE)0733-9410(1984)110:9(1188))
- Yang, Q., Sun, P. Z., Fumagalli, L., Stebunov, Y. V., Haigh, S. J., Zhou, Z. W., et al. (2020). Capillary condensation under atomic-scale confinement. *Nature*, 588(7837), 250–253. <https://doi.org/10.1038/s41586-020-2978-1>
- Yang, R., Zou, R., Dong, K., An, X., & Yu, A. (2007). Simulation of the packing of cohesive particles, Computer Physics Communications 177(1) (2007) 206–209, proceedings of the Conference on Computational Physics 2006
- Yang, R. Y., Zou, R. P., & Yu, A. B. (2000). Computer simulation of the packing of fine particles. *Physical Review E-Statistical Physics, Plasmas, Fluids, and Related Interdisciplinary Topics*, 62, 3900–3908. <https://doi.org/10.1103/physreve.62.3900>
- Yang, R. Y., Zou, R. P., & Yu, A. B. (2003). Numerical study of the packing of wet coarse uniform spheres. *AIChE Journal*, 49(7), 1656–1666. <https://doi.org/10.1002/aic.690490706>
- Yiotis, A. G., Salin, D., Tajer, E. S., & Yortsos, Y. C. (2012). Analytical solutions of drying in porous media for gravity-stabilized fronts. *Physical Review E-Statistical Physics, Plasmas, Fluids, and Related Interdisciplinary Topics*, 85, 046308. <https://doi.org/10.1103/PhysRevE.85.046308>
- Yiotis, A. G., Salin, D., Tajer, E. S., & Yortsos, Y. C. (2012). Drying in porous media with gravity-stabilized fronts: Experimental results. *Physical Review E - Statistical Physics, Plasmas, Fluids, and Related Interdisciplinary Topics*, 86, 026310. <https://doi.org/10.1103/PhysRevE.86.026310>
- Yu, A., Feng, C., Zou, R., & Yang, R. (2003). On the relationship between porosity and interparticle forces. *Powder Technology*, 130(1), 70–76. [https://doi.org/10.1016/S0032-5910\(02\)00228-0](https://doi.org/10.1016/S0032-5910(02)00228-0)
- Zou, R., Xu, J., Feng, C., Yu, A., Johnston, S., & Standish, N. (2003). Packing of multi-sized mixtures of wet coarse spheres. *Powder Technology*, 130(1), 77–83. [https://doi.org/10.1016/S0032-5910\(02\)00229-2](https://doi.org/10.1016/S0032-5910(02)00229-2)
- Zou, R.-P., Feng, C.-L., & Yu, A.-B. (2001). Packing density of binary mixtures of wet spheres. *Journal of the American Ceramic Society*, 84(3), 504–508. <https://doi.org/10.1111/j.1151-2916.2001.tb00690.x>

### **6.3 Summary**

We have showed that the proposed theoretical model for predicting the packing fraction of granular assembly formed by falling particles has good agreement with experimental data for different grain sizes and free fall height, which provides an effective approach for generation of granular assembly with tailored packing fraction. Further, the experimental study on drying of loosely packing granular medium at low initial water content reveals the evolution of liquid distribution during the drying process. The existence of liquid in the apparent dry region, although not directly observable with existence technique due to limited resolution, can lead to interesting phenomena, including the enhanced evaporation and concentrated collapse events at the end of drying process.

## Conclusions and Future Work

In this Thesis, the capillary effect on the liquid transport phenomenon in granular media is investigated numerically and experimentally across various length scales (Fig. 7.1). Major conclusions achieved in this Thesis are summarized as the following:

- The sharp edge pinning phenomenon can be utilised to achieve spontaneous droplet movement on patterned surfaces. The proposed model for description of droplet motion on surface with wedge of arbitrary edge shape is validated. Further, it is found that surfaces with convex wedges have the potential of performing better in terms of enhancing total transport distance.

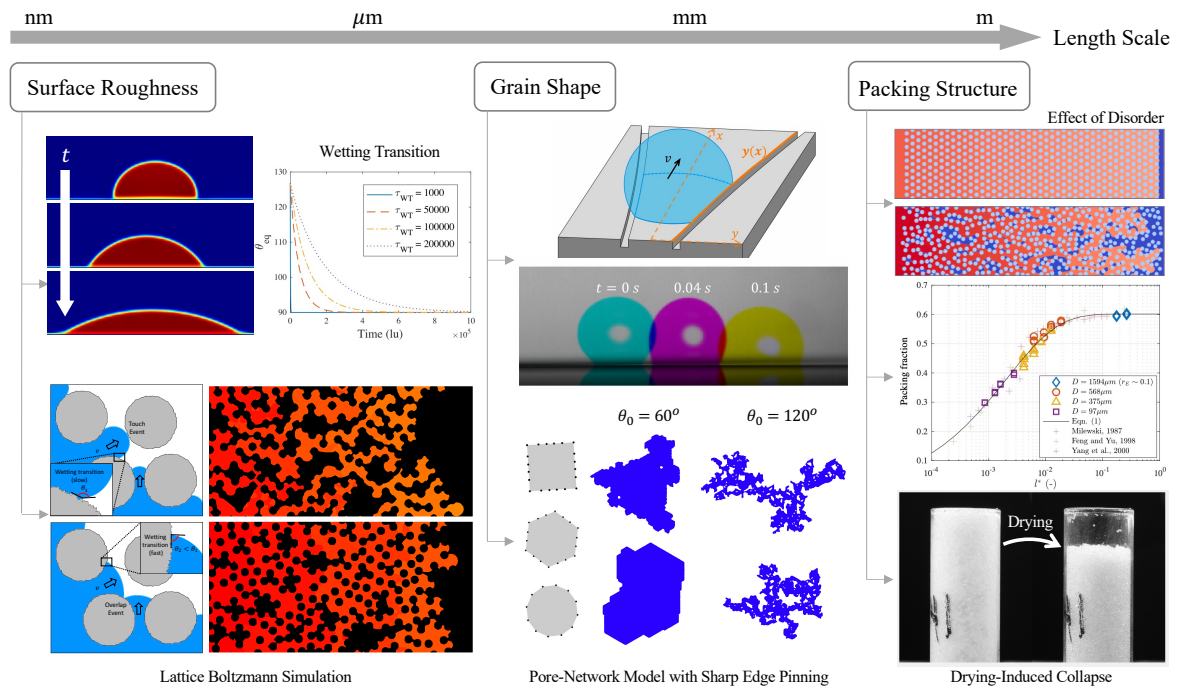


FIGURE 7.1: Summary of investigated topics covered in this Thesis.

- By incorporating the sharp edge pinning effect into the pore-network model, we have extended the existing interface tracking algorithm to simulate multiphase flow in the quasi-static regime for different particle shapes. It is found that increase in angularity not only introduces greater heterogeneity in pore geometry, but also amplifies the effect of menisci pinning at sharp corners. Macroscopically, this leads to an earlier transition from stable displacement toward capillary fingering.
- The time-dependent behaviour of contact angle due to Cassie-Wenzel wetting transition is important and needs to be taken into account for simulations of multiphase flow, especially for porous media where solid surface roughness cannot be neglected. This is because wetting transition can effectively alter the apparent contact angle during displacement process, which determines when, where, and whether a pore-filling event will take place.
- The topological disorder of porous media together with wettability have great impact on the invasion morphology of multiphase flow. Increases in disorder and contact angle promotes fingering, leading to more trapped defending phase. The fluctuations of local critical capillary pressure calculated from pore-scale instability events show agreement with macroscopic observation in displacement efficiency.
- Granular materials with different porosity under same cohesive force and particle size can be generated by controlling the free fall height of particles. The model derived using energy balance has better capability in predicting the final packing fraction of granular media governed by capillary forces or van der Waals forces compared with one derived from force balance.
- Due to Kelvin effect, there exists liquid in the form of liquid bridges in the apparent dry region, which prevents the collapse of loosely packed wet granular materials until the end the drying process when no further liquid can be extracted. The presence of liquid above the secondary drying front also explains the enhanced evaporation of liquid at later stage of drying process.

In summary, these works focusing on the fluid transport phenomena deepens the understanding of the connection between mechanisms at microscale and macroscopic observations, which

provide new insights and contributes to more precise description of the physical phenomena. Several directions for future works following the Thesis include:

- It is promising to apply the developed model for predicting the liquid transport process on patterned surfaces to improve the performance of real-world applications, such as water harvesting and spontaneous water-oil separation.
- The proposed pore-network model can be further extended to consider arbitrary particle shapes such as those directly obtained from scans of realistic granular materials. As both the wettability and pore geometry significantly impact the local capillary resistance, accurately capturing the shapes of granular materials is essential for accurate prediction of the displacement processes. It is also possible to consider viscous effects by introducing the viscous dissipation within different fluid phases, since different instability events, i.e., capillary fingering and viscous fingering, can occur depending on the fluid property and flow condition.
- Although the effect of wetting transition on multiphase flow has been demonstrated through simulations, systematic experimental works are needed to provide more insights. Further, the experimental works on time-dependent behaviour of contact angle due to Cassie-Wenzel wetting transition have been mainly conducted on artificially patterned surfaces. Experiments on random rough surfaces will facilitate the development and validation of the generalised theory of the description of the transition process.
- Currently, the proposed disorder index in characterising porous media is only applicable to monodisperse spheres. Further extensions on the definition of the index for more general porous media with different particle shapes and sizes are needed.
- The parameters experimentally explored during the process of packing of wet granular materials remain limited (particle size and free fall height). Numerical simulations such as discrete element method can provide more information on the effect of other parameters, such as sliding and rolling friction coefficients. Another aspect is to investigate the validity of the treatment of isolating each falling event during the theory development. Currently, it is assumed that each particle falls individually, and the rearrangement of influenced particles has no influence on the process of previous

or next impact event. However, collective falling and impact of multiple particles can introduce more complex physics.

- The evidence on the existence of liquid in the apparent dry region, i.e., enhanced evaporation and concentrated collapse in the end of drying process, are indirect. Actual observation of the liquid would provide more direct evidence, although the required resolution to observe such small liquid cluster (in the order of  $1 \mu\text{m}$ ) is demanding. Further, another important task is to develop a theoretical model to explain the exact transition of water content, below which the observed enhancement in drying rate appears. This will involve more strict control of experimental condition, including temperature and relative humidity, for drying processes with different initial water contents.

## Bibliography

- Wenzel, Robert N. (1936). 'Resistance of solid surfaces to wetting by water'. In: *Industrial & Engineering Chemistry* 28.8, pp. 988–994.
- Cassie, A. B. D. and S. Baxter (1944). 'Wettability of porous surfaces'. In: *Trans. Faraday Soc.* 40 (0), pp. 546–551.
- Crisp, D. J. and W. H. Thorpe (1948). 'The water-protecting properties of insect hairs'. In: *Discuss. Faraday Soc.* 3 (0), pp. 210–220.
- Purcell, W.R. (Aug. 1950). 'Interpretation of Capillary Pressure Data'. In: *Journal of Petroleum Technology* 2.08, pp. 11–12.
- Gibbs, J. Willard (1961). *The scientific papers*. Vol. 1. New York: Dover Publications.
- Oliver, J.F, C Huh and S.G Mason (1977). 'Resistance to spreading of liquids by sharp edges'. In: *Journal of Colloid and Interface Science* 59.3, pp. 568–581.
- Witten, T. A. and L. M. Sander (Nov. 1981). 'Diffusion-Limited Aggregation, a Kinetic Critical Phenomenon'. In: *Phys. Rev. Lett.* 47 (19), pp. 1400–1403.
- Wilkinson, D and J F Willemsen (Oct. 1983). 'Invasion percolation: a new form of percolation theory'. In: *Journal of Physics A: Mathematical and General* 16.14, pp. 3365–3376.
- Wilkinson, David (July 1984). 'Percolation model of immiscible displacement in the presence of buoyancy forces'. In: *Phys. Rev. A* 30 (1), pp. 520–531.
- Wu, Shiming, Donald H. Gray and F. E. Richart (1984). 'Capillary Effects on Dynamic Modulus of Sands and Silts'. In: *Journal of Geotechnical Engineering* 110.9, pp. 1188–1203.
- Cieplak, Marek and Mark O. Robbins (May 1988). 'Dynamical Transition in Quasistatic Fluid Invasion in Porous Media'. In: *Phys. Rev. Lett.* 60 (20), pp. 2042–2045.



- Lenormand, Roland, Eric Touboul and Cesar Zarcone (1988). 'Numerical models and experiments on immiscible displacements in porous media'. In: *Journal of Fluid Mechanics* 189.165-187.
- Lenormand, Roland and Cesar Zarcone (Dec. 1989). 'Capillary fingering: Percolation and fractal dimension'. In: *Transport in Porous Media* 4.6, pp. 599–612.
- Cieplak, Marek and Mark O. Robbins (June 1990). 'Influence of contact angle on quasistatic fluid invasion of porous media'. In: *Phys. Rev. B* 41 (16), pp. 11508–11521.
- Gunstensen, Andrew K., Daniel H. Rothman, Stéphane Zaleski and Gianluigi Zanetti (Apr. 1991). 'Lattice Boltzmann model of immiscible fluids'. In: *Phys. Rev. A* 43 (8), pp. 4320–4327.
- Frette, Vidar, Jens Feder, Torstein Jøssang and Paul Meakin (May 1992). 'Buoyancy-driven fluid migration in porous media'. In: *Phys. Rev. Lett.* 68 (21), pp. 3164–3167.
- Måløy, Knut Jørgen, Liv Furuberg, Jens Feder and Torstein Jøssang (Apr. 1992). 'Dynamics of slow drainage in porous media'. In: *Phys. Rev. Lett.* 68 (14), pp. 2161–2164.
- Meakin, Paul, Jens Feder, Vidar Frette and Torstein Jo/ssang (Sept. 1992). 'Invasion percolation in a destabilizing gradient'. In: *Phys. Rev. A* 46 (6), pp. 3357–3368.
- Blunt, Martin, F.John Fayers and Franklin M. Orr (1993). 'Carbon dioxide in enhanced oil recovery'. In: *Energy Conversion and Management* 34.9. Proceedings of the International Energy Agency Carbon Dioxide Disposal Symposium, pp. 1197–1204.
- Shan, Xiaowen and Hudong Chen (1993). 'Lattice Boltzmann model for simulating flows with multiple phases and components'. In: *Physical Review E* 47.3, pp. 1815–1819.
- Chaouche, M., N. Rakotomalala, D. Salin, B. Xu and Y. C. Yortsos (May 1994). 'Invasion percolation in a hydrostatic or permeability gradient: Experiments and simulations'. In: *Phys. Rev. E* 49 (5), pp. 4133–4139.
- Mason, Geoffrey and Norman R. Morrow (1994). 'Effect of Contact Angle on Capillary Displacement Curvatures in Pore Throats Formed by Spheres'. In: *Journal of Colloid and Interface Science* 168.1, pp. 130–141.
- Brutsaert, Wilfried and Daoyi Chen (1995). 'Desorption and the two Stages of Drying of Natural Tallgrass Prairie'. In: *Water Resources Research* 31.5, pp. 1305–1313.

- Shan, Xiaowen and Gary Doolen (1995). 'Multicomponent Lattice-Boltzmann Model with Interparticle Interaction'. In: *Journal of Statistical Physics* 81, pp. 379–393.
- Swift, Michael R., W. R. Osborn and J. M. Yeomans (July 1995). 'Lattice Boltzmann Simulation of Nonideal Fluids'. In: *Phys. Rev. Lett.* 75 (5), pp. 830–833.
- Furuberg, Liv, Knut Jørgen Måløy and Jens Feder (Jan. 1996). 'Intermittent behavior in slow drainage'. In: *Phys. Rev. E* 53 (1), pp. 966–977.
- Onda, T., S. Shibuichi, N. Satoh and K. Tsujii (1996). 'Super-Water-Repellent Fractal Surfaces'. In: *Langmuir* 12.9, pp. 2125–2127.
- Shan, Xiaowen and Gary Doolen (1996). 'Diffusion in a multicomponent lattice Boltzmann equation model'. In: *PHYSICAL REVIEW E*.
- Shibuichi, Satoshi, Tomohiro Onda, Naoki Satoh and Kaoru Tsujii (1996). 'Super Water-Repellent Surfaces Resulting from Fractal Structure'. In: *The Journal of Physical Chemistry* 100.50, pp. 19512–19517.
- Swift, Michael R., E. Orlandini, W. R. Osborn and J. M. Yeomans (Nov. 1996). 'Lattice Boltzmann simulations of liquid-gas and binary fluid systems'. In: *Phys. Rev. E* 54 (5), pp. 5041–5052.
- Blunt, Martin J. (1998). 'Physically-based network modeling of multiphase flow in intermediate-wet porous media'. In: *Journal of Petroleum Science and Engineering* 20.3, pp. 117–125.
- Feng, C.L. and A.D. Yu (1998). 'Effect of liquid addition on the packing of mono-sized coarse spheres'. In: *Powder Technology* 99.1, pp. 22–28.
- Halsey, Thomas C. and Alex J. Levine (Apr. 1998). 'How Sandcastles Fall'. In: *Phys. Rev. Lett.* 80 (14), pp. 3141–3144.
- Weigert, Tom and Siegfried Ripperger (1999). 'Calculation of the Liquid Bridge Volume and Bulk Saturation from the Half-filling Angle'. In: *Particle & Particle Systems Characterization* 16.5, pp. 238–242.
- Feng, C.L. and A.B. Yu (2000). 'Quantification of the Relationship between Porosity and Interparticle Forces for the Packing of Wet Uniform Spheres'. In: *Journal of Colloid and Interface Science* 231.1, pp. 136–142.

- Nadim, Farhad, George E Hoag, Shili Liu, Robert J Carley and Peter Zack (2000). 'Detection and remediation of soil and aquifer systems contaminated with petroleum products: an overview'. In: *Journal of Petroleum Science and Engineering* 26.1, pp. 169–178.
- Yang, R. Y., R. P. Zou and A. B. Yu (Sept. 2000). 'Computer simulation of the packing of fine particles'. In: *Phys. Rev. E* 62 (3), pp. 3900–3908.
- Cho, Gye Chun and J. Carlos Santamarina (2001). 'Unsaturated Particulate Materials Particle-Level Studies'. In: *Journal of Geotechnical and Geoenvironmental Engineering* 127.1, pp. 84–96.
- Guo, Zhaoli and T. S. Zhao (Sept. 2002). 'Lattice Boltzmann model for incompressible flows through porous media'. In: *Phys. Rev. E* 66 (3), p. 036304.
- Yoshimitsu, Zen, Akira Nakajima, Toshiya Watanabe and Kazuhito Hashimoto (2002). 'Effects of Surface Structure on the Hydrophobicity and Sliding Behavior of Water Droplets'. In: *Langmuir* 18.15, pp. 5818–5822.
- Marmur, Abraham (2003). 'Wetting on Hydrophobic Rough Surfaces: To Be Heterogeneous or Not To Be?' In: *Langmuir* 19.20, pp. 8343–8348.
- He, Bo, Junghoon Lee and Neelesh A. Patankar (2004). 'Contact angle hysteresis on rough hydrophobic surfaces'. In: *Colloids and Surfaces A: Physicochemical and Engineering Aspects* 248.1, pp. 101–104.
- Valvatne, Per H. and Martin J. Blunt (2004). 'Predictive pore-scale modeling of two-phase flow in mixed wet media'. In: *Water Resources Research* 40.7.
- Fournier, Z, D Geromichalos, S Herminghaus, M M Kohonen, F Mugele, M Scheel, M Schulz, B Schulz, Ch Schier, R Seemann and A Skudelný (Feb. 2005). 'Mechanical properties of wet granular materials'. In: *Journal of Physics: Condensed Matter* 17.9, S477–S502.
- Rabinovich, Yakov I., Madhavan S. Esayanur and Brij M. Moudgil (2005). 'Capillary Forces between Two Spheres with a Fixed Volume Liquid Bridge: Theory and Experiment'. In: *Langmuir* 21.24. PMID: 16285763, pp. 10992–10997.
- Zheng, Q.-S., Y. Yu and Z.-H. Zhao (2005). 'Effects of Hydraulic Pressure on the Stability and Transition of Wetting Modes of Superhydrophobic Surfaces'. In: *Langmuir* 21.26, pp. 12207–12212.

- Dong, K. J., R. Y. Yang, R. P. Zou and A. B. Yu (Apr. 2006). 'Role of Interparticle Forces in the Formation of Random Loose Packing'. In: *Phys. Rev. Lett.* 96 (14), p. 145505.
- Lipiec, J., J. Kuś, A. Słowińska-Jurkiewicz and A. Nosalewicz (2006). 'Soil porosity and water infiltration as influenced by tillage methods'. In: *Soil and Tillage Research* 89.2, pp. 210–220.
- Huang, Haibo, Daniel T. Thorne, Marcel G. Schaap and Michael C. Sukop (Dec. 2007). 'Proposed approximation for contact angles in Shan-and-Chen-type multicomponent multiphase lattice Boltzmann models'. In: *Phys. Rev. E* 76 (6), p. 066701.
- Moulinet, S. and D. Bartolo (Nov. 2007). 'Life and death of a fakir droplet: Impalement transitions on superhydrophobic surfaces'. In: *The European Physical Journal E* 24.3, pp. 251–260.
- Nosonovsky, Michael (2007). 'Multiscale Roughness and Stability of Superhydrophobic Biomimetic Interfaces'. In: *Langmuir* 23.6, pp. 3157–3161.
- Sbragaglia, Mauro, Alisia M. Peters, Christophe Pirat, Bram M. Borkent, Rob G. H. Lammertink, Matthias Wessling and Detlef Lohse (Oct. 2007). 'Spontaneous Breakdown of Superhydrophobicity'. In: *Phys. Rev. Lett.* 99 (15), p. 156001.
- Zhao, Xiongce (July 2007). 'Wetting transition of water on graphite: Monte Carlo simulations'. In: *Phys. Rev. B* 76 (4), p. 041402.
- Butt, Hans-Jürgen (2008). 'Capillary Forces: Influence of Roughness and Heterogeneity'. In: *Langmuir* 24.9. PMID: 18442225, pp. 4715–4721.
- Feng, Lin, Yanan Zhang, Jinming Xi, Ying Zhu, Nü Wang, Fan Xia and Lei Jiang (2008). 'Petal Effect: A Superhydrophobic State with High Adhesive Force'. In: *Langmuir* 24.8. PMID: 18312016, pp. 4114–4119.
- Nosonovsky, Michael and Bharat Bhushan (2008). 'Patterned Nonadhesive Surfaces: Superhydrophobicity and Wetting Regime Transitions'. In: *Langmuir* 24.4, pp. 1525–1533.
- Scheel, M, R Seemann, M Brinkmann, M Di Michiel, A Sheppard and S Herminghaus (Nov. 2008a). 'Liquid distribution and cohesion in wet granular assemblies beyond the capillary bridge regime'. In: *Journal of Physics: Condensed Matter* 20.49, p. 494236.

- Scheel, Mario, Ralf Seemann, Martin Brinkmann, M. Di Michiel, A Sheppard, B Breidenbach and Stephan Herminghaus (Apr. 2008b). 'Morphological clues to wet granular pilestability'. In: *Nature materials* 7, pp. 189–93.
- Bahadur, Vaibhav and Suresh V. Garimella (2009). 'Preventing the Cassie-Wenzel Transition Using Surfaces with Noncommunicating Roughness Elements'. In: *Langmuir* 25.8, pp. 4815–4820.
- Butt, Hans-Jürgen and Michael Kappl (2009). 'Normal capillary forces'. In: *Advances in Colloid and Interface Science* 146.1, pp. 48–60.
- Lu, Ning, Tae-Hyung Kim, Stein Sture and William J. Likos (2009). 'Tensile Strength of Unsaturated Sand'. In: *Journal of Engineering Mechanics* 135.12, pp. 1410–1419.
- Peters, A. M., C. Pirat, M. Sbragaglia, B. M. Borkent, M. Wessling, D. Lohse and R. G. H. Lammertink (Aug. 2009). 'Cassie-Baxter to Wenzel state wetting transition: Scaling of the front velocity'. In: *The European Physical Journal E* 29.4, pp. 391–397.
- Bai, Hao, Xuelin Tian, Yongmei Zheng, Jie Ju, Yong Zhao and Lei Jiang (2010). 'Direction Controlled Driving of Tiny Water Drops on Bioinspired Artificial Spider Silks'. In: *Advanced Materials* 22.48, pp. 5521–5525.
- Holtzman, Ran and Ruben Juanes (Oct. 2010). 'Crossover from fingering to fracturing in deformable disordered media'. In: *Phys. Rev. E* 82, p. 046305.
- Zheng, Yongmei, Hao Bai, Zhongbing Huang, Xuelin Tian, Fu-Qiang Nie, Yong Zhao, Jin Zhai and Lei Jiang (2010). 'Directional water collection on wetted spider silk'. In: *Nature* 463.7281, pp. 640–643.
- Mohamad, A.A. (2011). *LBM - fundamentals and engineering applications with computer codes*. Springer.
- Oliveira, Luciana R. de, Daisiane M. Lopes, Stella M. M. Ramos and José C. M. Mombach (2011). 'Two-dimensional modeling of the superhydrophobic behavior of a liquid droplet sliding down a ramp of pillars'. In: *Soft Matter* 7 (8), pp. 3763–3765.
- Shokri, N. and D. Or (2011). 'What determines drying rates at the onset of diffusion controlled stage-2 evaporation from porous media?' In: *Water Resources Research* 47.9.
- Dong, K. J., R. Y. Yang, R. P. Zou and A. B. Yu (2012). 'Settling of particles in liquids: Effects of material properties'. In: *AIChE Journal* 58.5, pp. 1409–1421.

- Szulczewski, Michael L., Christopher W. MacMinn, Howard J. Herzog and Ruben Juanes (2012). 'Lifetime of carbon capture and storage as a climate-change mitigation technology'. In: *Proceedings of the National Academy of Sciences* 109.14, pp. 5185–5189.
- Alheshibri, M. H., N. G. Rogers, A. D. Sommers and K. F. Eid (2013). 'Spontaneous movement of water droplets on patterned Cu and Al surfaces with wedge-shaped gradients'. In: *Applied Physics Letters* 102.17, p. 174103.
- Bandara, U.C., A.M. Tartakovsky, M. Oostrom, B.J. Palmer, J. Grate and C. Zhang (2013). 'Smoothed particle hydrodynamics pore-scale simulations of unstable immiscible flow in porous media'. In: *Advances in Water Resources* 62. Computational Methods in Geologic CO<sub>2</sub> Sequestration, pp. 356–369.
- Bormashenko, Edward and Gene Whyman (2013). 'On the Role of the Line Tension in the Stability of Cassie Wetting'. In: *Langmuir* 29.18, pp. 5515–5519.
- Li, Kan, Jie Ju, Zhongxin Xue, Jie Ma, Lin Feng, Song Gao and Lei Jiang (2013). 'Structured cone arrays for continuous and effective collection of micron-sized oil droplets from water'. In: *Nature Communications* 4.1, p. 2276.
- Lopes, Daisiane M., Stella M. M. Ramos, Luciana R. de Oliveira and José C. M. Mombach (2013). 'Cassie–Baxter to Wenzel state wetting transition: a 2D numerical simulation'. In: *RSC Adv.* 3 (46), pp. 24530–24534.
- Papadopoulos, Periklis, Lena Mammen, Xu Deng, Doris Vollmer and Hans-Jürgen Butt (2013). 'How superhydrophobicity breaks down'. In: *Proceedings of the National Academy of Sciences* 110.9, pp. 3254–3258.
- Bai, Hao, Lin Wang, Jie Ju, Ruize Sun, Yongmei Zheng and Lei Jiang (2014). 'Efficient Water Collection on Integrative Bioinspired Surfaces with Star-Shaped Wettability Patterns'. In: *Advanced Materials* 26.29, pp. 5025–5030.
- Cao, Moyuan, Jie Ju, Kan Li, Shixue Dou, Kesong Liu and Lei Jiang (2014). 'Facile and Large-Scale Fabrication of a Cactus-Inspired Continuous Fog Collector'. In: *Advanced Functional Materials* 24.21, pp. 3235–3240.
- Chen, Li, Qinjun Kang, Yutong Mu, Ya-Ling He and Wen-Quan Tao (2014). 'A critical review of the pseudopotential multiphase lattice Boltzmann model: Methods and applications'. In: *International Journal of Heat and Mass Transfer* 76, pp. 210–236.

- Fall, A., B. Weber, M. Pakpour, N. Lenoir, N. Shahidzadeh, J. Fiscina, C. Wagner and D. Bonn (Apr. 2014). 'Sliding Friction on Wet and Dry Sand'. In: *Phys. Rev. Lett.* 112 (17), p. 175502.
- Lake, Larry W., Russell Johns, Bill Rossen and Gary Pope (2014). *Fundamentals of Enhanced Oil Recovery*. Society of Petroleum Engineers.
- Liu, Haihu, Albert J. Valocchi, Charles Werth, Qinjun Kang and Mart Oostrom (2014). 'Pore-scale simulation of liquid CO<sub>2</sub> displacement of water using a two-phase lattice Boltzmann model'. In: *Advances in Water Resources* 73, pp. 144–158.
- Masson, Yder and Steven R. Pride (Mar. 2014). 'A Fast Algorithm for Invasion Percolation'. In: *Transport in Porous Media* 102.2, pp. 301–312.
- Mielniczuk, Boleslaw, Tomasz Hueckel and Moulay Saïd El Youssoufi (2014). 'Evaporation-induced evolution of the capillary force between two grains'. In: *Granular Matter* 16.5, pp. 815–828.
- Zamuruyev, Konstantin O., Hamzeh K. Bardaweel, Christopher J. Carron, Nicholas J. Kenyon, Oliver Brand, Jean-Pierre Delplanque and Cristina E. Davis (2014). 'Continuous Droplet Removal upon Dropwise Condensation of Humid Air on a Hydrophobic Micropatterned Surface'. In: *Langmuir* 30.33. PMID: 25073014, pp. 10133–10142.
- Babadagli, Tayfun, Xiaojuan Ren and Kayhan Develi (2015). 'Effects of fractal surface roughness and lithology on single and multiphase flow in a single fracture: An experimental investigation'. In: *International Journal of Multiphase Flow* 68, pp. 40–58.
- Bormashenko, Edward (2015). 'Progress in understanding wetting transitions on rough surfaces'. In: *Advances in Colloid and Interface Science* 222. Reinhard Miller, Honorary Issue, pp. 92–103.
- Butt, Hans-Jürgen, Doris Vollmer and Periklis Papadopoulos (2015). 'Super liquid-repellent layers: The smaller the better'. In: *Advances in Colloid and Interface Science* 222, pp. 104–109.
- Holtzman, Ran and Enrico Segre (Oct. 2015). 'Wettability Stabilizes Fluid Invasion into Porous Media via Nonlocal, Cooperative Pore Filling'. In: *Phys. Rev. Lett.* 115 (16), p. 164501.

- Liu, Haihu, Qinjun Kang, Christopher R. Leonardi, Sebastian Schmieschek, Ariel Narvaez, Bruce D. Jones, John R. Williams, Albert J. Valocchi and Jens Harting (2015). ‘Multiphase lattice Boltzmann simulations for porous media applications’. In: *Computational Geosciences* 20.4, pp. 777–805.
- Tani, Marie, Ryuji Kawano, Koki Kamiya and Ko Okumura (June 2015). ‘Towards combinatorial mixing devices without any pumps by open-capillary channels: Fundamentals and applications’. In: *Scientific reports* 5, p. 10263.
- Trojer, Mathias, Michael L. Szulczewski and Ruben Juanes (May 2015). ‘Stabilizing Fluid-Fluid Displacements in Porous Media Through Wettability Alteration’. In: *Phys. Rev. Applied* 3 (5), p. 054008.
- Wang, Ben, Weixin Liang, Zhiguang Guo and Weimin Liu (2015). ‘Biomimetic superlyophobic and super-lyophilic materials applied for oil/water separation: a new strategy beyond nature’. In: *Chem. Soc. Rev.* 44 (1), pp. 336–361.
- Amabili, M, A Giacomello, S Meloni and C M Casciola (Nov. 2016). ‘Intrusion and extrusion of a liquid on nanostructured surfaces’. In: *Journal of Physics: Condensed Matter* 29.1, p. 014003.
- Chen, Huawei, Pengfei Zhang, Liwen Zhang, Hongliang Liu, Ying Jiang, Deyuan Zhang, Zhiwu Han and Lei Jiang (Apr. 2016). ‘Continuous directional water transport on the peristome surface of *Nepenthes alata*’. In: *Nature* 532, p. 85.
- Holtzman, R. (2016). ‘Effects of Pore-Scale Disorder on Fluid Displacement in Partially-Wettable Porous Media’. In: *Sci Rep* 6, p. 36221.
- Jung, Michael, Martin Brinkmann, Ralf Seemann, Thomas Hiller, Marta Sanchez de La Lama and Stephan Herminghaus (Nov. 2016). ‘Wettability controls slow immiscible displacement through local interfacial instabilities’. In: *Phys. Rev. Fluids* 1 (7), p. 074202.
- Matter, Juerg M., Martin Stute, Sandra Ó. Snæbjörnsdóttir, Eric H. Oelkers, Sigurdur R. Gíslason, Edda S. Aradóttir, Bergur Sigfusson, Ingvi Gunnarsson, Holmfrídur Sigurdardóttir, Einar Gunnlaugsson, Gudni Axelsson, Helgi A. Alfredsson, Domenik Wolff-Boenisch, Kiflom Mesfin, Diana Fernandez de la Reguera Taya, Jennifer Hall, Knud Dideriksen and Wallace S. Broecker (2016). ‘Rapid carbon mineralization for permanent disposal of anthropogenic carbon dioxide emissions’. In: *Science* 352.6291, pp. 1312–1314.



- Mishra, Himanshu, Alex M. Schrader, Dong Woog Lee, Adair Gallo, Szu-Ying Chen, Yair Kaufman, Saurabh Das and Jacob N. Israelachvili (2016). ‘Time-Dependent Wetting Behavior of PDMS Surfaces with Bioinspired, Hierarchical Structures’. In: *ACS Applied Materials & Interfaces* 8.12, pp. 8168–8174.
- Prakash, Suruchi, Erte Xi and Amish J. Patel (2016). ‘Spontaneous recovery of superhydrophobicity on nanotextured surfaces’. In: *Proceedings of the National Academy of Sciences* 113.20, pp. 5508–5513.
- Tan, Xianhua, Yiyang Zhu, Tielin Shi, Zirong Tang and Guanglan Liao (2016). ‘Patterned gradient surface for spontaneous droplet transportation and water collection: simulation and experiment’. In: *Journal of Micromechanics and Microengineering* 26.11, p. 115009.
- Zhao, Benzong, Christopher W. MacMinn and Ruben Juanes (2016). ‘Wettability control on multiphase flow in patterned microfluidics’. In: *Proceedings of the National Academy of Sciences* 113.37, pp. 10251–10256.
- Zhu, Hai, Zhiguang Guo and Weimin Liu (2016). ‘Biomimetic water-collecting materials inspired by nature’. In: *Chem. Commun.* 52 (20), pp. 3863–3879.
- Amabili, Matteo, Alberto Giacomello, Simone Meloni and Carlo Massimo Casciola (Mar. 2017). ‘Collapse of superhydrophobicity on nanopillared surfaces’. In: *Phys. Rev. Fluids* 2 (3), p. 034202.
- Blunt, Martin J. (2017). *Multiphase Flow in Permeable Media: A Pore-Scale Perspective*. Cambridge University Press.
- Chen, Z., C. Shu and D. Tan (2017). ‘A simplified thermal lattice Boltzmann method without evolution of distribution functions’. In: *International Journal of Heat and Mass Transfer* 105, pp. 741–757.
- Domingues, Eddy M., Sankara Arunachalam and Himanshu Mishra (2017). ‘Doubly Reentrant Cavities Prevent Catastrophic Wetting Transitions on Intrinsically Wetting Surfaces’. In: *ACS Applied Materials & Interfaces* 9.25, pp. 21532–21538.
- Al-Khayat, Omar, Jun Ki Hong, David M. Beck, Andrew I. Minett and Chiara Neto (2017). ‘Patterned Polymer Coatings Increase the Efficiency of Dew Harvesting’. In: *ACS Applied Materials & Interfaces* 9.15. PMID: 28224792, pp. 13676–13684.

- Kruger, Timm, Halim Kusumaatmaja, Alexandr Kuzmin, Orest Shardt, Goncalo Silva and Erlend Magnus Viggen (2017). *LBM - the principles and methods*. Springer.
- Li, Chuxin, Lei Wu, Cunlong Yu, Zhichao Dong and Lei Jiang (2017). 'Peristome-Mimetic Curved Surface for Spontaneous and Directional Separation of Micro Water-in-Oil Drops'. In: *Angewandte Chemie International Edition* 56.44, pp. 13623–13628.
- Morrisette, Jared M., Pallab Sinha Mahapatra, Aritra Ghosh, Ranjan Ganguly and Constantine M. Megaridis (2017). 'Rapid, Self-driven Liquid Mixing on Open-Surface Microfluidic Platforms'. In: *Scientific Reports* 7.1, p. 1800.
- Tian, Ye, Pingan Zhu, Xin Tang, Chunmei Zhou, Jianmei Wang, Tiantian Kong, Min Xu and Liqiu Wang (2017). 'Large-scale water collection of bioinspired cavity-microfibers'. In: *Nature Communications* 8.1, p. 1080.
- Tinti, Antonio, Alberto Giacomello, Yaroslav Grosu and Carlo Massimo Casciola (2017). 'Intrusion and extrusion of water in hydrophobic nanopores'. In: *Proceedings of the National Academy of Sciences* 114.48, E10266–E10273.
- Zhao, Yan, Hongxia Wang, Hua Zhou and Tong Lin (2017). 'Directional Fluid Transport in Thin Porous Materials and its Functional Applications'. In: *Small* 13.4, p. 1601070.
- Zheng, Yanfen, Jiang Cheng, Cailong Zhou, Haiting Xing, Xiufang Wen, Pihui Pi and Shouping Xu (2017). 'Droplet Motion on a Shape Gradient Surface'. In: *Langmuir* 33.17. PMID: 28398753, pp. 4172–4177.
- AlRatrou, Ahmed, Martin J. Blunt and Branko Bijeljic (2018). 'Wettability in complex porous materials, the mixed-wet state, and its relationship to surface roughness'. In: *Proceedings of the National Academy of Sciences* 115.36, pp. 8901–8906.
- Chatterjee, Souvik, Pallab Sinha Mahapatra, Ali Ibrahim, Ranjan Ganguly, Lisha Yu, Richard Dodge and Constantine M. Megaridis (2018). 'Precise Liquid Transport on and through Thin Porous Materials'. In: *Langmuir* 34.8. PMID: 29377702, pp. 2865–2875.
- Luo, Hu, Yao Lu, Shaohui Yin, Shuai Huang, Jinlong Song, Faze Chen, Fengjun Chen, Claire J. Carmalt and Ivan P. Parkin (2018). 'Robust platform for water harvesting and directional transport'. In: *J. Mater. Chem. A* 6 (14), pp. 5635–5643.
- Primkulov, Bauyrzhan K., Stephen Talman, Keivan Khaleghi, Alireza Rangriz Shokri, Rick Chalaturnyk, Benzhong Zhao, Christopher W. MacMinn and Ruben Juanes (Oct. 2018).

- ‘Quasistatic fluid-fluid displacement in porous media: Invasion-percolation through a wetting transition’. In: *Phys. Rev. Fluids* 3 (10), p. 104001.
- Ran, Hu, Wan Jiamin, Yang Zhibing, Chen Yi-Feng and Tokunaga Tetsu (2018). ‘Wettability and Flow Rate Impacts on Immiscible Displacement: A Theoretical Model’. In: *Geophysical Research Letters* 45.7, pp. 3077–3086.
- Seo, Dongjin, Alex M. Schrader, Szu-Ying Chen, Yair Kaufman, Thomas R. Cristiani, Steven H. Page, Peter H. Koenig, Yonas Gizaw, Dong Woog Lee and Jacob N. Israelachvili (2018). ‘Rates of cavity filling by liquids’. In: *Proceedings of the National Academy of Sciences* 115.32, pp. 8070–8075.
- Si, Yifan, Cunlong Yu, Zhichao Dong and Lei Jiang (2018). ‘Wetting and spreading: Fundamental theories to cutting-edge applications’. In: *Current Opinion in Colloid & Interface Science* 36, pp. 10–19.
- Arunachalam, Sankara, Ratul Das, Jamilya Nauruzbayeva, Eddy M. Domingues and Himanshu Mishra (2019). ‘Assessing omniphobicity by immersion’. In: *Journal of Colloid and Interface Science* 534, pp. 156–162.
- Bakhshian, Sahar, Seyyed A. Hosseini and Nima Shokri (Mar. 2019). ‘Pore-scale characteristics of multiphase flow in heterogeneous porous media using the lattice Boltzmann method’. In: *Scientific Reports* 9.1, p. 3377.
- Bao, Yanyao, Ling Li, Luming Shen, Chengwang Lei and Yixiang Gan (Feb. 2019). ‘Modified smoothed particle hydrodynamics approach for modelling dynamic contact angle hysteresis’. In: *Acta Mechanica Sinica*.
- Blunt, Martin J., Qingyang Lin, Takashi Akai and Branko Bijeljic (2019). ‘A thermodynamically consistent characterization of wettability in porous media using high-resolution imaging’. In: *Journal of Colloid and Interface Science* 552, pp. 59–65.
- From, C. S., E. Sauret, S. A. Galindo-Torres and Y. T. Gu (June 2019). ‘Interaction pressure tensor on high-order lattice Boltzmann models for nonideal fluids’. In: *Phys. Rev. E* 99 (6), p. 063318.
- Hu, Ran, Tian Lan, Guan-Ju Wei and Yi-Feng Chen (2019a). ‘Phase diagram of quasi-static immiscible displacement in disordered porous media’. In: *Journal of Fluid Mechanics* 875, pp. 448–475.

- Hu, Ran, Chen-Xing Zhou, Dong-Sheng Wu, Zhibing Yang and Yi-Feng Chen (2019b). 'Roughness Control on Multiphase Flow in Rock Fractures'. In: *Geophysical Research Letters* 46.21, pp. 12002–12011.
- Ju, Yang, Jiabin Dong, Feng Gao and Jianguo Wang (2019). 'Evaluation of water permeability of rough fractures based on a self-affine fractal model and optimized segmentation algorithm'. In: *Advances in Water Resources* 129, pp. 99–111.
- Mehmani, Ayaz, Shaina Kelly, Carlos Torres-Verdín and Matthew Balhoff (2019). 'Residual oil saturation following gas injection in sandstones: Microfluidic quantification of the impact of pore-scale surface roughness'. In: *Fuel* 251, pp. 147–161.
- Primkulov, Bauyrzhan K., Amir A. Pahlavan, Xiaojing Fu, Benzong Zhao, Christopher W. MacMinn and Ruben Juanes (2019). 'Signatures of fluid–fluid displacement in porous media: wettability, patterns and pressures'. In: *Journal of Fluid Mechanics* 875, R4.
- Wang, Zhongzheng, Kapil Chauhan, Jean-Michel Pereira and Yixiang Gan (Mar. 2019). 'Disorder characterization of porous media and its effect on fluid displacement'. In: *Phys. Rev. Fluids* 4 (3), p. 034305.
- Cho, Yoonkyung and Chung Hee Park (2020). 'Objective quantification of surface roughness parameters affecting superhydrophobicity'. In: *RSC Adv.* 10 (52), pp. 31251–31260.
- From, C. S., E. Sauret, S. A. Galindo-Torres and Y. T. Gu (Mar. 2020). 'Application of high-order lattice Boltzmann pseudopotential models'. In: *Phys. Rev. E* 101 (3), p. 033303.
- Tanino, Yukie, Anelechi Ibekwe and Dubravka Pokrajac (July 2020). 'Impact of grain roughness on residual nonwetting phase cluster size distribution in packed columns of uniform spheres'. In: *Phys. Rev. E* 102 (1), p. 013109.
- Wang, Dehui, Qiangqiang Sun, Matti J. Hokkanen, Chenglin Zhang, Fan-Yen Lin, Qiang Liu, Shun-Peng Zhu, Tianfeng Zhou, Qing Chang, Bo He, Quan Zhou, Longquan Chen, Zuankai Wang, Robin H. A. Ras and Xu Deng (June 2020a). 'Design of robust superhydrophobic surfaces'. In: *Nature* 582.7810, pp. 55–59.
- Wang, Zhongzheng, Jean-Michel Pereira and Yixiang Gan (2020b). 'Effect of Wetting Transition during Multiphase Displacement in Porous Media'. In: *Langmuir* 36.9. PMID: 32070092, pp. 2449–2458.

- Blunt, Martin J., Abdulla Alhosani, Qingyang Lin, Alessio Scanziani and Branko Bijeljic (2021). 'Determination of contact angles for three-phase flow in porous media using an energy balance'. In: *Journal of Colloid and Interface Science* 582, pp. 283–290.
- Liu, Yang, Shuangmei Zou, Ying He, Shuyu Sun, Yang Ju, Qingbang Meng and Jianchao Cai (2021). 'Influence of fractal surface roughness on multiphase flow behavior: Lattice Boltzmann simulation'. In: *International Journal of Multiphase Flow* 134, p. 103497.
- Zhang, Lei, Chao Xu, Yaohao Guo, Guangpu Zhu, Shiyu Cai, Xin Wang, Wenlong Jing, Hai Sun, Yongfei Yang and Jun Yao (Jan. 2021). 'The Effect of Surface Roughness on Immiscible Displacement Using Pore Scale Simulation'. In: *Transport in Porous Media*.
- Zhou, Jian Guo (2021). 'Macroscopic axisymmetric lattice Boltzmann method (MacAxLAB)'. In: *Computer Methods in Applied Mechanics and Engineering* 376, p. 113657.
- Yuan, Chao and Bruno Chareyre (0). 'Transitioning from the funicular to the pendular regime in granular soils'. In: *Géotechnique* 0.0, pp. 1–7.